ISBN 978-82-326-0800-3 (printed version)
ISBN 978-82-326-0801-0 (electronic version)
ISSN 1503-8181

Doctoral Thesis
Andrea Shmueli Alvarado

Doctoral theses at NTNU, 2015:71

Andrea Shmueli Alvarado

# Experiments on the droplet field in multiphase pipe flow

**NTNU**
Norwegian University of
Science and Technology
Faculty of Engineering Science and Technology
Department of Energy and Process Engineering

**NTNU – Trondheim**
Norwegian University of
Science and Technology

Doctoral theses at NTNU, 2015:71

NTNU

**NTNU – Trondheim**
Norwegian University of
Science and Technology

Andrea Shmueli Alvarado

# Experiments on the droplet field in multiphase pipe flow

Thesis for the degree of Philosophiae Doctor

Trondheim, April 2015

Norwegian University of Science and Technology
Faculty of Engineering Science and Technology
Department of Energy and Process Engineering

**NTNU – Trondheim**
Norwegian University of
Science and Technology

**NTNU**
Norwegian University of Science and Technology

Thesis for the degree of Philosophiae Doctor

Faculty of Engineering Science and Technology
Department of Energy and Process Engineering



ISBN 978-82-326-0800-3 (printed version)
ISBN 978-82-326-0801-0 (electronic version)
ISSN 1503-8181

Doctoral theses at NTNU, 2015:71

Printed by Skipnes Kommunikasjon as

# Experiments on the droplet field in multiphase pipe flow

Andrea Shmueli Alvarado
Supervisor: Ole Jørgen Nydal
Co-supervisor: Stein Tore Johansen

Department of Energy and Process Engineering
Norwegian University of Science and Technology
Trondheim
Norway

# Abstract

Gas-liquid flows are very common in industrial applications and many times involve three phases. Experiments are important as basis for development of 1D flow models used for design of multiphase transport systems. The experiments are either used as direct closure relation or for model validation. Currently, there is a lack of three-phase flow data on droplet entrainment. This thesis is focused on two main topics: establish relevant experimental data of the droplet flux profiles, pressure gradient and flow characteristics of three-phase stratified and annular flows and to develop instrumentation suitable for three phase flow measurements.

Experiments in three phase flows at high gas densities were conducted to obtain the magnitude and distribution of the droplet field flux and the effect of the water as a second liquid phase. This was studied by sampling the droplets using an isokinetic sampling probe. An automated probe system was designed and implemented successfully to reach this goal. The probe system is capable to conduct simultaneous measurements of the local droplet flux and gas velocity. Oil and water distribution inside the liquid layer in stratified-annular horizontal flow was studied using a two-energy traversing gamma densitometer and visual observations, using high speed video recordings of the flow. The experiments were performed at the Medium scale loop at SINTEF Multiphase Flow Laboratory using a high density gas at medium pressure conditions, oil and water.

Based on the experimental results, an assessment of the effect of droplet flux distribution over the pipe cross section on the entrainment fraction calculation is discussed. Additionally, the current state of predicting models for liquid droplet concentration profiles is reviewed and new empirical correlations for the droplet concentration at the interface and the concentration decay are proposed.

The effect on the pressure gradient changes due to liquid film at the wall, caused by droplet wetting, was studied on a second experimental setup. The setup was built at the NTNU Multiphase Flow Laboratory and consists of a vertical pipe to promote film symmetry. Two-phase flow experiments using water and air and a viscous oil and air at atmospheric pressure were carried out. The results were compared with predictions of commercial flow simulators.

In addition a new two-energy gamma densitometer is designed and built to obtain cross-sectional measurements of the phase fractions, capture transient flow conditions and for three-phase flow measurements (oil, water and gas) in acrylic pipes. This instrument will be further tested and applied in the future.

# Acknowledgements

I would like to thank my supervisor Ole Jørgen Nydal for giving me the opportunity of being part of his research group. I am very grateful for all his support and guidance during the development of my PhD.

To TOTAL E&P for sponsoring this project, their support and understanding.

To all the staff at the Multiphase Flow Laboratory of SINTEF Petroleum Research at Tiller for allowing me to perform my experiments and helping me with the experimental setup. I would like to thank specially to Tor Erling Unander for being like another supervisor of this thesis.

To my co-supervisor Stein Tore Johansen for your comments during the review of this thesis.

To the Master student Thomas Arnulf, Milad Khatibi and the staff in the Multiphase Flow Laboratory at the NTNU for their help in the developing of the experiments at this facility. Specially, I would like to thank Halvor Haukvik at NTNU for his invaluable contribution to the design, development and assembly of the new gamma densitometer. I would like also to thank the administration department of the EPT-NTNU for their support.

A special thanks to Roel Belt for all the help, all the time he invested helping me during my experiments at SINTEF, good ideas, valuable comments and nice and interesting conversations.

To Prof. Michael Golan for taking care of us since the day we arrive to Norway. Thanks for your advices, guidance and for becoming part of our family.

To my colleagues from the Multiphase Flow group. Thanks for the fun times and sharing the experience that is surviving a PhD. I would like to thank specially to Mariana Diaz, thanks for being more than a friend to me. I enjoyed all our chats, our technical discussions, shopping time, travels and fun together.

I would like to thank to my friends, my old ones and my new ones. Thanks for being there in the good and the bad times.

I would like to thank my parents and my brother for their unconditional support. Thank you also abu for watching and taking care of us from heaven.

Thanks to my dear and fantastic husband, Milan Stanko for cheering me up and making me smile every day, thanks for being my daily inspiration and the love of my life.

# Contents

# List of tables

# List of Figures

# Nomenclature

| | |
|---|---|
| $D$ | Pipe diameter |
| $R$ | Pipe radius |
| $I$ | Measured gamma intensity |
| $Io$ | Initial gamma intensity |
| $Z$ | Horizontal pipe coordinate |
| $y$ | Vertical pipe coordinate |
| $x$ | Axial pipe coodinate |
| $t$ | time |
| $T$ | Temperature |
| $P$ | Pressure |
| $f$ | Darcy friction factor |
| $dp/dx$ | Measured pressure gradient |
| $g$ | Gravity acceleration |
| $q$ | Volumetric flow rate |
| $U$ | Velocity |
| $We$ | Weber number |
| $Re$ | Reynolds number |
| $d$ | Droplet diameter |
| $d_p$ | Probe diameter |
| $R^2$ | Coefficient of determination |
| $A$ | Pipe cross section |
| $d_v$ | Accumulation vessel diameter |
| $\Delta h$ | Increment of liquid in the accumulation vessel |
| $WC$ | Watercut |
| $S$ | Slip ratio |
| $h_w$ | Gas-liquid interface |
| $\dot{m}$ | Mass flow |
| $y_{hw}$ | Vertical distance from the gas-liquid interface |
| $F_{LEn}$ | Local droplet flux of phase “n” |
| $WC_L$ | Local watercut |
| $E_L$ | Total mass flow of entrained droplets |
| $nr$ | Number of rows |
| $nc$ | Number of columns |
| $C$ | Droplet concentration |
| $w$ | Particle settling velocity |
| $C_o$ | Droplet concentration at the gas-liquid interface |
| $C_D$ | Drag coefficient |

| | |
|---|---|
| $Q_d$ | Total droplet flux |
| $u^*$ | Friction velocity |
| $k_D$ | Droplet deposition flux |
| $R_A$ | Atomization rate |
| $R_D$ | Deposition rate |
| $W_{LF}$ | Mass flow in the liquid layer |
| $W_{LFC}$ | Critical flow to onset entrainment |
| $h$ | Film thickness |
| $SF_6$ | Sulphur Hexaflouride |

**Greek letters**

| | |
|---|---|
| $\beta$ | Linear attenuation coefficient of a medium |
| $\alpha$ | Phase fraction |
| $\rho$ | Density |
| $e$ | Pipe roughness |
| $\mu$ | Dynamic viscosity |
| $\sigma$ | Surface tension |
| $N\mu$ | Viscosity number |
| $\varepsilon$ | Particle diffusivity |
| $\tau$ | Shear stress |
| $\zeta$ | Turbulent diffusivity constant |
| $\theta$ | Pipe angle fom horizontal |

**Subscripts**

| | |
|---|---|
| *w* | Water |
| *o* | Oil |
| *g* | Gas |
| *m* | Mixture |
| *L* | Liquid |
| *atm* | Atmospheric conditions |
| *p* | Probe |
| *f* | Front |
| *b* | Back |
| *s* | superficial |
| *i-s* | In-situ |
| *s-o/w* | Slip oil to water |
| *o/w* | Oil to water |
| *n* | Phase, n=o for oil n=w for water |
| *t* | total |
| *nd* | Nodal point |
| *i* | Interfacial |
| *k* | Phase k=w (water), k=o (oil) k=g (gas) |
| *bulk* | Bulk |
| *sampling* | Sampling |

**Superscript**

| | |
|---|---|
| *H* | High energy level |
| *L* | Low energy level |

# Chapter 1

## Introduction

Gas-liquid flows are very common in the oil industry, especially in the gas transportation flowlines and in gas wells. The liquid phase frequently consists of liquid hydrocarbons and water thus constituting a three-phase flow problem. The water can come from a neighboring aquifer or from injection to enhance the oil recovery of an existent reservoir. Depending on the fluid properties, geometrical configurations, system and flow conditions the gas and liquid are distributed within the pipe in different configurations namely flow patterns. The main difference between horizontal and vertical flow is the effect of the gravitational forces. In horizontal flows the heavier phase tends to settle on the pipe bottom. This generates different types of flow arrangements within the pipe. The most common classification for the horizontal and vertical flow patterns in gas-liquid two-phase flows are presented in Figure 1.1 and Figure 1.2 respectively. The flow patterns classification is mainly done by visual inspection of the flow in the pipeline and they are mapped into a flow regime maps.

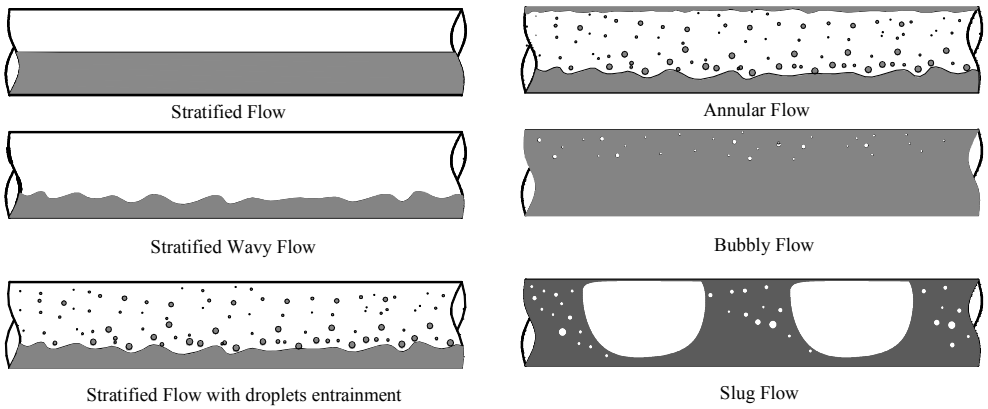


Figure 1.1: Flow pattern for horizontal gas-liquid flows

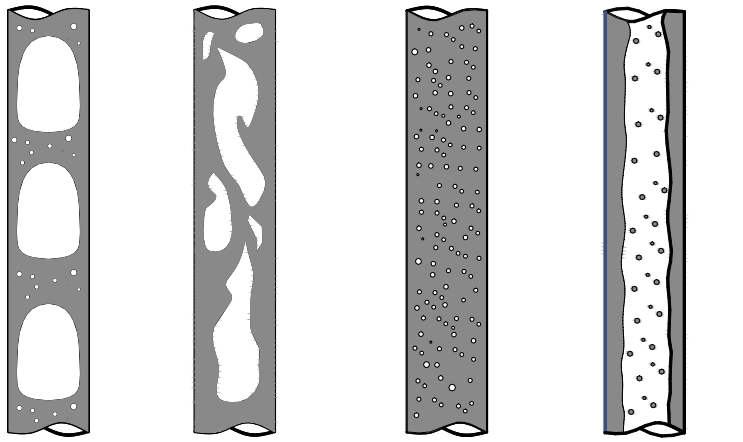


Figure 1.2: Flow pattern for vertical gas-liquid flows

In a simplified way, gas-oil-water three-phase flows can be considered as a case of gas-liquid flows where the liquid phase is described as a non-uniform oil-water mixture (Pan, 1996). This non-uniform liquid distribution, from separated to mixed liquids, is what makes three-phase flows more complicated to study in comparison with two-phase flows. The oil and water can form dispersions which tend to increase the pressure drop increment or flow separation, which tends to give liquid accumulation. There are several flow pattern classifications for three-phase gas-liquid-liquid flows. For horizontal flow, Pan (1996) made a summary of all the proposed classifications as it is shown in Figure 1.3. In this thesis the flow patterns of interest are stratified and annular. Khor (1998) proposed a detailed classification for the flow distribution in stratified and annular three phase flows and it is the one adopted in this study.

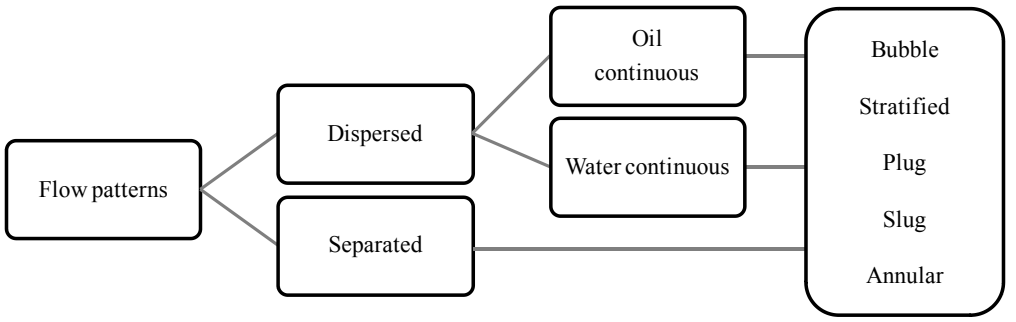


Figure 1.3: Flow pattern classification for three-phase, gas-liquid-liquid flows. (Pan, 1996)

The main focus of this thesis is on the liquid droplets entrained into the gas phase. For low liquid flow rates, as the gas velocity increases the stratified flow structure becomes unstable and waves start to disperse liquid into the gas. Liquid droplets are entrained from the liquid layer and transported as a droplet field in the gas phase. There are two major flow effects coming from an entrained droplet field in the gas phase. The droplet flow can represent a very large fraction of the liquid transport (especially in vertical flows) and even when the entrained fraction is low, the presence of droplets can cause wall wetting and increasing the pressure drop.

Experiments are important as basis for development of 1D flow models used for design of multiphase transport systems. The experiments are either used as direct closure relation or for model validation. These models require closure relationships related to the droplet field. These relationships are usually obtained from experimental measurements under controlled operating conditions. Instrumentation is then needed for measurement of the local droplet flux in the gas core.

Most of the experimental work in the past has been done using water and air at atmospheric pressure. All of these previous studies provide important information about liquid droplets entrainment. However there is still a lack of experimental data in three phase flow and at high pressures. There are a limited number of experiments of the droplet entrainment over the entire pipe cross-section. The uniformity of the droplet flux distribution on the pipe cross section is one assumption in most of the current models.

There are different experimental techniques to measure liquid droplet entrainment in annular flows. It can be done indirectly by withdrawing the liquid film on the pipe wall using a porous pipe section (See Dallman (1978); Laurinat (1982); Mantilla (2008)) or by direct sampling of the droplet flux using a traversing Pitot-type tube under isokinetic conditions. The droplet flux is measured as a liquid flow rate by accumulating the sampled liquid into a vessel for a specific time. (See, Andreussi (1983); Paras et al. (1991); G. J. Zhang et al. (1995); Tayebi et al. (2000); Skartlien et al. (2011)). The droplet volume flux can also be calculated using PDA (Particle Doppler Anemometry) where each droplet is recorded as it crosses a detection volume (See Zhang et al. (2000)).

## 1.1 Scope and Outline

The main objective of the present work is to establish relevant experimental data on the droplet flux in gas-liquid three phase flows and on instrumentation development for this purpose.
From the transport perspective, the droplet entrainment, droplet flux distribution and the effect of the water as a second liquid phase is a main motivation for this study. In addition small droplet

fields can wet the walls and cause an increment in the pressure drop. The framework from this research and main contributions can be summarized in three main activities:

-Instrumentation development: The design and building of a new test section capable of measuring accurately oil and water flux of droplet entrained in gas flow under high pressure conditions. Two isokinetic probes were designed, constructed and tested for this purpose. The measurements are made in an automated manner using a PLC (Programmable logic controller) unit controlling all the involved instrumentation. In Chapter 2 and 3 a detailed explanation of this process and the measuring methodology is shown.

In addition, a new 5 beam two-energy gamma densitometer was designed and built (in collaboration with another PhD student). The new instrument will be capable of measuring phase fractions for three phase flows in pipes up to 90 mm ID. The new gamma densitometer can be rotated around the pipeline and traverse it in order to get measurements over the pipe cross section. The development of this new instrument, its capabilities and limitations are explained in Chapter 8.

-Droplet flux measurements: The developed isokinetic probes are used for liquid droplet flux measurements in horizontal gas-oil-water flows. The experiments extend the available database to improve the current model predictions of the droplet concentration profiles and total liquid entrainment. The experiments were carried out using a high density gas (Sulfur hexafluoride, $SF_6$) at moderate pressures in order to simulate the high pressure conditions of real multiphase transport systems. All the experiments were performed at SINTEF Multiphase Flow Laboratory in Trondheim. The droplet measurements section is subdivided in 3 main Chapters:

- Characteristics of the three-phase stratified-annular flow: A qualitative assessment of the pipe wall film and droplet entrainment is done by studying three different oil with viscosities of 100 cP, 39 cP and 1.8 cP at different watercuts. Video recordings were used to achieve this objective. A two-energy traversing gamma densitometer was used to measure the liquid fraction profiles in horizontal stratified to annular flows. Liquid fraction and gas-liquid interface height is required when calculating the total liquid entrainment fraction and interfacial droplet concentration. Pressure gradient measurements were recorded. Comments on the effect of the added water are given for all the mentioned variables and presented in Chapter 4.

- Gas velocity profiles and pressure drop measurements: In Chapter 5, the velocity profiles of three-phase gas oil and water mixtures were obtained using the isokinetic probe. The measurements are conducted over the gas cross section of a 69 mm horizontal pipe.

- Liquid droplet flux and distribution: The designed isokinetic probe module was used to measure simultaneous oil and water droplet flux along the vertical diameter and on the cross section of a 69 mm horizontal pipe. Three-phase flows systems including oils with two viscosities were tested. The droplet flux distribution over the pipe cross section was analyzed and its consideration has been taken into account on the total liquid entrainment fraction calculation (See Chapter 6). In addition, the available literature on experiments and models for the dispersed phase in annular and stratified horizontal pipe flows are reviewed and compared with the experimental results (See Chapter 7). As a result a new methodology is proposed for the droplet concentration prediction by fitting functions to the experimental data using genetic algorithms.

-Wet wall pressure drop measurements: In Chapter 8, measurements of the pressure drop and liquid hold up in a gas flow with wet walls were carried out in a vertical pipe at NTNU Multiphase Flow Laboratory. For this task a new experimental setup was designed and built. The experiments were performed as a dry-up process, where an initial liquid film becomes thinner with time as it is removed by gas flow. Quick closing valves were used to measure the liquid holdup in the vertical section. Two data sets using Air-Water and Air-Mineral oil (60cP) at atmospheric conditions were obtained and comparisons with commercial flow simulators were performed.

## 1.2 Paper list

***Paper 1:*** *Shmueli, A., Unander, T.E., Nydal, O.J. 2014. Oil and water droplet flux distribution in horizontal separated gas-oil-water flows. To be submitted to International Journal of Multiphase Flow (Based on Chapter 5 and 6)*

Water and oil droplet fluxes and gas velocities have been measured along the vertical diameter and on the cross section of a 0.07 m horizontal pipe using an isokinetic sampling probe. Separated gas-oil and gas-oil-water flows at 4.7 bar pressure conditions were established using Exxsol D80, water and a heavy gas ($SF_6$) to simulate high pressure flows. The entrainment of water and oil droplets depends on the watercut of the liquid mixture. The droplet fluxes on the pipe cross section are non-uniformly distributed. Neglecting the non-uniformity of the droplet flux distribution can give differences up to 40% on the total entrained fraction. The effect of the water addition to an oil-gas system on the total entrained fraction is negligible for the studied flow conditions

***Paper 2:*** *Shmueli, A., Unander, T.E., Nydal, O.J. 2014. Isokinetic sampling probe for cross sectional measurements of droplet entrainment in separated gas-oil-water flows. To be submitted to International Journal of Multiphase Flow (Based on Chapter 2)*

A new isokinetic sampling probe for droplet flux measurements in separated gas-oil-water flows under high pressure conditions is presented. The instrument can sample over the pipe cross section in an automated manner using a PLC (Programmable logic controller) unit controlling all the involved instrumentation. The probe was designed and tested for pressurized horizontal separated flows, using SF6 for the gas phase to simulate high pressure conditions. The probe is demonstrated for a three phase flow case showing non-uniform droplet flux distribution over the flow cross section.

***Paper 3****: Shmueli, A., Borregales, M., Asuaje, M., Nydal, O.J. 2014. Modeling of liquid droplet concentration profiles in horizontal stratified-annular flows. Abstract accepted for submission to the 17$^{th}$ International conference on Multiphase Technology (Based on Chapter 7)*

This paper is focus on the modeling of liquid droplet entrainment in horizontal stratified-annular flows. Two approaches are studied. First a review of the current state of 1D prediction models for liquid droplet concentration profiles is made. The limitations and assumptions are also discussed. Second, a new methodology is proposed as an alternative for the droplet concentration profiles prediction assuming an exponential droplet distribution in the vertical diameter. The methodology is built by obtaining empirical correlations using genetic algorithms. The algorithm implementation is made by using Binary trees and Prüfer encoding. As a result two empirical correlations are presented for the droplet concentration at the gas-liquid interface and the decay coefficient. The correlations are developed for two-phase gas-liquid flows and are expressed in terms of three non-dimensional parameters including the effects of the physical fluid properties and operational conditions. The obtained two-phase flow correlations are extended to the three-phase oil-water-gas flows. The model and correlations are tested against recent experiments and available data from the literature.

***Paper 4:*** *Shmueli, A. Nydal, O.J, Djoric, B. Unander, T.E. 2012. Oil and water droplet entrainment in horizontal gas liquid flows. Proc. 8th North American Conference on Multiphase Flow. BHR Group. Cranfield, U.K pp 199-210.* (Appendix H)

Three oil-water-gas flows experiments have been carried out in a 68 mm ID pipe with a dense gas (simulating high pressure flows) and with oils of different viscosities (1.8-100 cP). Measurements include pressure drop and liquid entrainment using an isokinetic sampling probe. The flow is recorded with a high speed video camera. The tested gas velocities (1-4 m/s) did not

give large entrained droplet fractions. The effect of water is to reduce the entrainment and pressure drop. OLGA predicts the pressure drop quite well.

***Paper 5:*** *Shmueli, A., Unander, T.E., Nydal, O.J. 2013.Liquid droplet entrainment in horizontal three-phase flow. Proc 8th International Conference on Multiphase Flow. ICMF 2013. Jeju, Korea.* (Appendix I)

Liquid entrainment experiments have been performed in a horizontal, 69 mm ID pipe. Exxsol D80 and water were used as liquid phases and $SF_6$ was used as gas phase in order to simulate high pressure flows. A new 4mm ID isokinetic sampling probe was designed to traverse the cross section of the pipe in high pressure systems. This probe has the capability of simultaneous droplet flux sampling and gas mass flow measurement. Two water cuts were tested. A global reduction in the entrainment was observed when the water cut increases when comparing droplet fluxes contour plots. Non uniformities of the droplet profiles on the pipe cross section were found suggesting the existence of secondary flows

***Paper 6:*** *Shmueli, A., Unander, T.E., Nydal, O.J. 2013 Experimental and numerical evaluation and optimization of a non-standard Pitot/sampling probe. Engineering. Vol 5 No. 12. Pp 967-974.* (Appendix J)

An isokinetic sampling probe was design to quantify liquid droplets entrained in gas in horizontal pipes the local gas velocity. This probe has the capability of working as a Pitot probe when the sampling is stopped. The design of the probe is not standard and therefore an evaluation of the device is required. CFD simulations using the commercial software Ansys CFX were carried out using single phase gas and the current probe geometry to analyse the influence of the probe design and on-site installation over the gas velocity measurement and sampling. The predicted results were compared against theoretical profiles from the literature and with gas single phase experimental data acquired in a horizontal 49 m long steel pipeline with an internal diameter of 69 mm. The experiments were done using SF6 at 7 bara. An asymmetry of the experimental velocity profiles was found. This asymmetry was reproduced with the numerical simulations and from them it was possible to predict and correct an installation problem using CFD tools.

***Paper 7:*** *Shmueli, A., Arnul , T., Khatibi, M., Nydal, O.J. 2014. Experiments on gas flow with wet pipe walls. Proc. 9th North American Conference on Multiphase flow. BHR Group. Cranfield, U.K.* (Based on Chapter 9)

Measurements of the pressure drop and liquid hold up in a gas flow with wet walls were carried out on a vertical pipe at NTNU Multiphase Flow Laboratory. The experiments were performed as a dry-up process, where an initial liquid film becomes thinner with time as it is removed by gas flow. Quick closing valves were used to measure the liquid holdup in the vertical section.

Two data sets using Air-Water and Air-Mineral oil were obtained. A significant increase on pressure drop with small amounts of the liquid holdup was observed. Pressure gradient and holdup behavior were reproduced quite well by commercial flow simulators but the flushing time showed discrepancies.

# Chapter 2

## Flow facilities and experimental techniques

### 2.1 Experimental setup I (Rig I)

The medium-scale flow loop at SINTEF Multiphase Flow Laboratory was modified and adapted to measure the local droplet entrainment in a horizontal 49m long steel pipe with an internal diameter of 0.07 m. The flow loop had a transparent 1.95 m section where the flow can be visualized and a traversing single beam gamma densitometer was installed. Oil water and gas enters the loop and are measured individually using Coriolis flow meters. At the end of the clear section an isokinetic sampling droplet module was designed and assembled into the flow loop to measure the local droplets flux entrained in the gas core. A simplified scheme of the rig is shown in Figure 2.1.

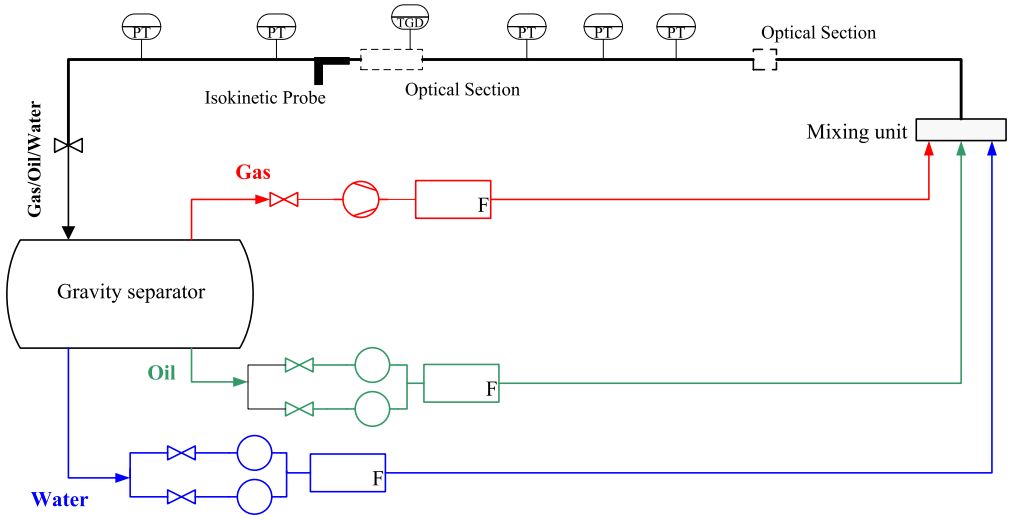


Figure 2.1: SINTEF medium scale loop, simplified flow diagram

## 2.1.1 Instrumentation

#### *2.1.1.1 Pressure gradient measurement*

The pressure gradient is calculated from the measurement of six pressure cells that are installed along the loop (at 99D, 430D, 633D, 865D, 1071D and 1274D). Each differential pressure transducer is connected between a pressure tap on the pipe wall and a reference line. The local absolute pressure is calculated by adding the measured differential pressure to the absolute reference pressure. The pressure gradient was calculated by the estimated slope in the regression line obtained from the dp-cells and their respective positions.

#### *2.1.1.2 High-speed video camera*

Visual observations were performed on the polycarbonate clear pipe in order to classify each flow pattern and to determine the height of the liquid layer (together with the traversing gamma densitometer). All the videos were recorded using a Weinberger SpeedCam MiniVis camera. The camera has a maximum resolution of 512x512 pixels in black and white. Videos were recorded at up to 2500 frames per second in order to capture important characteristics of the flow such as liquid waves. The gas liquid interface location was measured also on the outer pipe perimeter at the clear section using a scale attached to the pipe surface.

#### *2.1.1.3 Isokinetic sampling probe module*

The liquid droplets entrained in the gas phase were sampled using an isokinetic probe. Two probes were design and built during this study. The isokinetic probes were also used to measure the gas velocity profiles. A detailed explanation of the characteristics, capabilities and limitations of this system are discussed in Chapter 4.

#### *2.1.1.4 Traversing gamma densitometer*

Measurements of the time-averaged phase fractions were carried out using an existent traversing two-energy gamma densitometer along the vertical diameter. The gamma densitometer consists of a 3.7 GBq $Am^{241}$ two-energy source (16 keV and 59 keV) and a Cadmium Telluride (CdTe) detector. The $\gamma$ ray is collimated and for each time a 2 mm horizontal pipe slice is measured. The TGD was located on the second transparent polycarbonate pipe (See Figure 2.1) and it is installed such that the beam which contains the collimated gamma emission crosses the pipe horizontally while it is transported from the bottom to the top of the pipe. As the measurements are made stepwise in the pipe it is possible to get average phase fractions in steady state flows. A sketch of the instrument and related instrumentation required for its operation is shown in Figure 2.2.

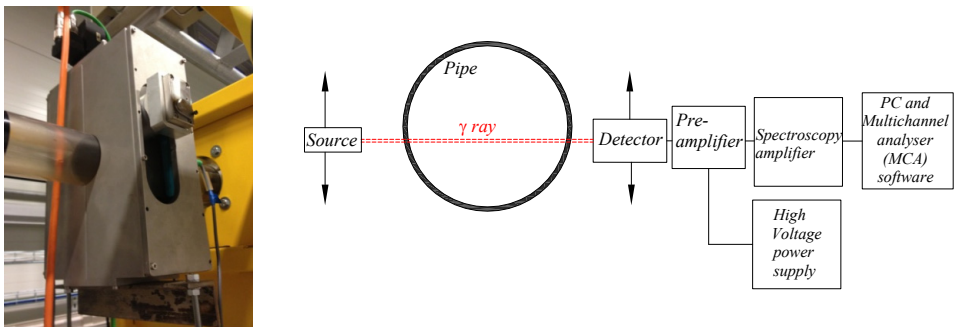


Figure 2.2: Traversing gamma densitometer picture and operating sketch

The measured intensity from a source with an initial intensity $I_0$ traveling through a determined medium at a specific energy level can be written as:

$$I = I_0 \cdot e^{-\beta \cdot Z} \tag{2.1}$$

Where $\beta$ is the attenuation coefficient for the traversed medium and Z is the distance travelled inside the pipe through the traversed medium. The attenuation coefficient is a constant property of the traversed medium for each energy level and can be obtained from the calibration experiments (See calibration section below). The intensity for a three phase mixture (gas-oil-water) at a specific energy level is

$$I_m(y) = I_0 \cdot e^{-\beta_w \cdot Z_w(y)} \cdot e^{-\beta_o \cdot Z_o(y)} \cdot e^{-\beta_g \cdot Z_g(y)} \tag{2.2}$$

$$ln\left(\frac{I_m(y)}{I_0(y)}\right) = -\beta_o \cdot Z_o(y) - \beta_w \cdot Z_w(y) - \beta_g \cdot Z_g(y) \tag{2.3}$$

The sum of the equivalent phase path lengths is equal to the total traversed path length inside the pipe at a specific vertical location (See Figure 2.3).

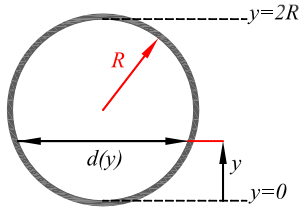


Figure 2.3: Beam traversing the path length inside the pipe

$$d(\mathrm{y}) = \sum_{k=1}^{3} Z_k(y) = 2\sqrt{R^2 - (y-R)^2} \tag{2.4}$$

The gas attenuation coefficient is negligible in comparison to the oil and water coefficient (Frøystein, 2005). This assumption yields that $I_0$=$I_g$ and simplifies equation (2.3) to

$$ln\left(\frac{I_m(y)}{I_g(y)}\right) = -\beta_o \cdot Z_o(y) - \beta_w \cdot Z_w(y) \tag{2.5}$$

Equation (2.5) is valid for each measured energy level and together with equation (2.4) creates a system of three equations with three unknowns (phase path lengths).

$$Z_o(y) = \frac{z\frac{1}{\beta_w^H} ln\frac{I_m^H(y)}{I_g^H(y)} - \frac{1}{\beta_w^L} ln\frac{I_m^L(y)}{I_g^L(y)}}{\frac{\beta_o^L}{\beta_w^L} - \frac{\beta_o^H}{\beta_w^H}} \tag{2.6}$$

$$Z_w(y) = \frac{\frac{1}{\beta_o^H} ln\frac{I_m^H(y)}{I_g^H(y)} - \frac{1}{\beta_o^L} ln\frac{I_m^L(y)}{I_g^L(y)}}{\frac{\beta_w^L}{\beta_o^L} - \frac{\beta_w^H}{\beta_o^H}} \tag{2.7}$$

$$Z_g(y) = d(y) - Z_o(y) - Z_w(y) \tag{2.8}$$

Equation (2.5) can be simplified for two-phase gas-liquid systems by setting $Z_o(y)$ or $Z_w(y)$ equal to zero for oil-gas or water-gas systems respectively. Using just the high energy level the phase path length for two phase flows is

$$\frac{1}{\beta_k} ln\left(\frac{I_g(y)}{I_m(y)}\right) = Z_k(y) \tag{2.9}$$

Where $k=w$ or $k=o$ for water or oil respectively. The volume phase fractions are defined as:

$$\alpha_o(y) = \frac{Z_o(y)}{d(y)} \qquad \alpha_w(y) = \frac{Z_w(y)}{d(y)} \qquad \alpha_g(y) = 1 - \alpha_w(y) - \alpha_o(y)$$

The average phase holdup is calculated by integrating the phase fraction profiles over the pipe area

$$\bar{\alpha}_k = \frac{2}{A}\int_0^D \sqrt{R^2 - (y-R)^2} \cdot \alpha_k(y)\, dy \tag{2.10}$$

*Calibration*

Single-phase calibration experiments were conducted for each fluid at their specific pressure and temperature conditions. These experiments were static and the instrument traversed the pipe to determine the intensities of the phase as function of the pipe location (See Figure 2.4)

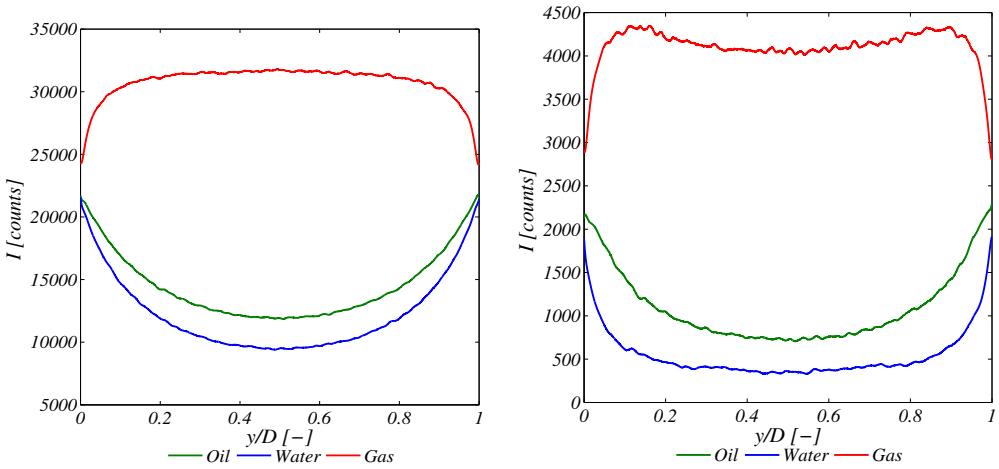


Figure 2.4: Example of the calibration curves (oil=Nexbase, water and gas=$SF_6$)

The attenuation coefficients should be constant for each phase and energy level at the specific experimental conditions. The term $ln\left(I_k(y)/I_g(y)\right)$ varies linearly with the traversed path length inside the pipe. As an example, on Figure 2.5 the logarithm of the relation between intensities is plotted against the path length inside the pipe for the high energy level for Nexbase 3080 and water. The attenuation coefficients are the slopes obtained by fitting a straight line to their respective plotted curve. The non-linear behavior occurs when the collimated beam penetrates both the pipe wall and the inner pipe region. The exponential behavior recovers once around $y$=1.5 mm from the pipe wall.

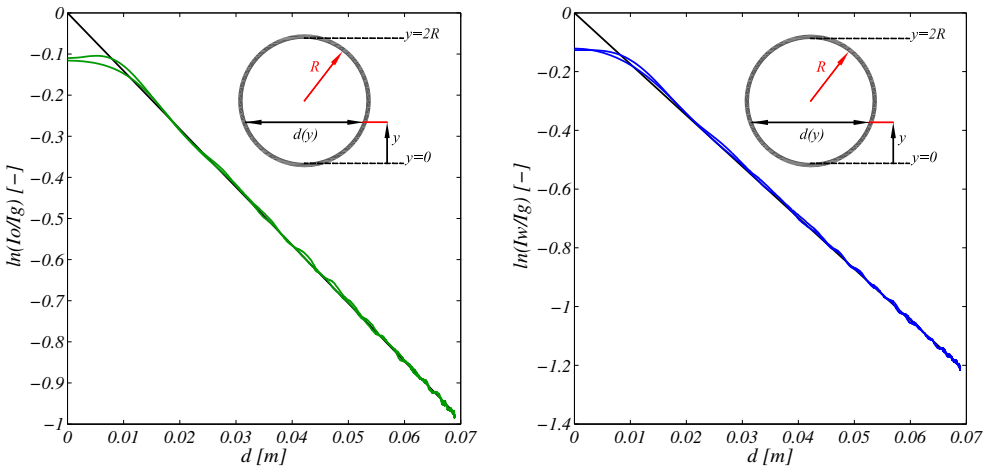


Figure 2.5: Attenuation coefficient calculation procedure, high energy peak (oil=Nexbase)

One limitation of this technology for three phase flow applications is the breakdown of the exponential behavior for the lowest energy peak when handling water. The lowest $Am^{241}$ energy

peak (16 keV) disappears when the water content increases (See Figure 2.6b). The worst case scenario is correspondent to the pipe fully filled with water. The logarithm of the relation between water and gas intensities is plotted against the path length inside the pipe for the lowest energy level (See Figure 2.6a). The exponential behavior breaks down at approximately $y$=4 mm from the pipe wall

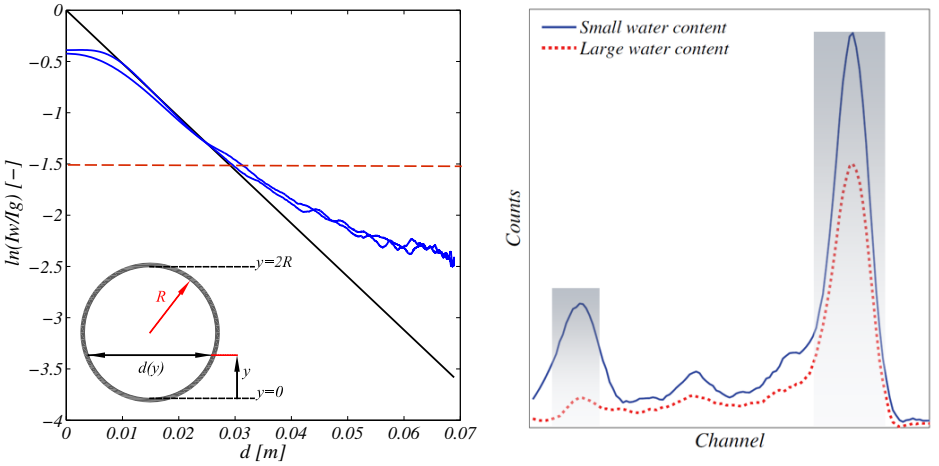


Figure 2.6: Water attenuation for the low energy peak in the Am-241 spectrum (oil=Nexbase)

This limits the usage of the dual energy of the $Am^{241}$ up to certain water cut value. For this reason, a threshold value was established for the three phase flow cases at the lowest energy level on each experimental condition (Red dotted line on Figure 2.6a). Below this limit the phase fractions were calculated as for an oil-water system (neglecting the gas), when the measured intensity places below the oil density profile and oil-gas (neglecting the water) when it is above it (See Figure 2.7). A summary of the obtained attenuation coefficients for the tested conditions is shown in Table 2.1.

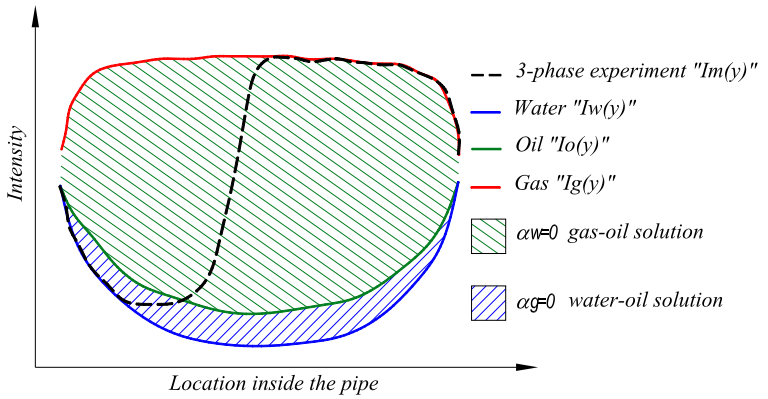


Figure 2.7: Phases considered for the local phase fraction calculations in a three-phase flow mixture when the low energy logarithmic ratio between water and gas is lower than the established threshold

Table 2.1: Attenuation coefficients and selected threashold

| | ***Nexbase-Water-SF6 @ 7bar*** | | ***Mixed oil-water SF6 @4.7 bar*** | | ***Exxsol D80-water-SF6 @4 bar*** | |
|---|---|---|---|---|---|---|
| | ***Water*** | ***Oil*** | ***Water*** | ***Oil*** | ***Water*** | ***Oil*** |
| ***Low energy*** | *-52* | *25.9* | *-58* | *-28.564* | *-66* | *-30.412* |
| ***High Energy*** | *17.44* | *14.123* | *-18.057* | *-14.49* | *-17.54* | *-13.528* |
| ***Threashold*** | *-1.5* | | *-1.6* | | *-1.8* | |

For a stratified wavy flow condition, the gas-liquid and liquid-liquid interfaces will vary in time. However a mean representative value of these interfaces is obtained by using the gamma densitometer (See Figure 2.8)

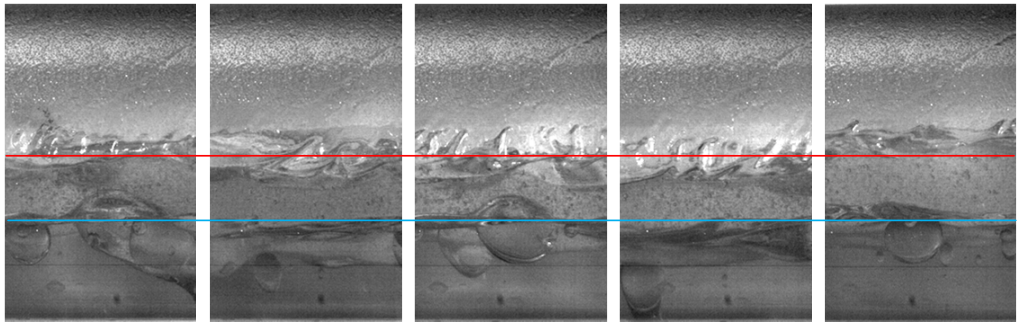

*t=0 ms* *t=61 ms* *t=189 ms* *t=571 ms* *t=1673 ms*

Figure 2.8: Mean value in time for gas-liquid and liquid-liquid interfaces

## 2.1.2 Experimental campaigns and fluid system

Three experimental campaigns were carried out using the Experimental Setup I. Each of them had different scopes and for this reason different results. All of the campaigns involved three-phase flows (gas-oil-water). For all the experiments sulphur hexafluoride ($SF_6$) was used as the gas phase. $SF_6$ is a high density gas that can simulate high pressure conditions. Three oils with different viscosities were used on each campaign. A brief summary of each experimental campaign is given below.

The first campaign was conducted using Nexbase 3080 as the oil phase. Nexbase 3080 is a catalytically hydroisomerized and dewaxed base oil (Neste Oil). This campaign was focused on assessing the behavior of the liquid layer, liquid pipe film and droplet entrainment in three phase flows when a viscous oil is used. In this campaign no direct entrainment measurements were carried out. However by visual observation and gamma densitometer measurements, useful information about the flow patterns, liquid distribution, pipe wall film and entrainment was obtained in addition to pressure gradient measurements.

The second experimental campaign used a different oil (due to flow loop availability). Mixed oil between Nexbase 3080 and Exxsol D80 was used. Exxsol D80 is a de-aromatized, nonflammable hydrocarbon (Exxonmobil, 2010). The mixed oil was obtained by diluting 5600 liters of Nexbase 3080 (79% by volume) with 1500 liters of Exxsol D80 (21% by volume). The performed measurements in this campaign were similar to ones carried out in the first campaign. In addition the 1D isokinetic sampling probe (See Chapter 3) was used and sampling experiments along the vertical diameter were conducted.

The third experimental campaign was carried out using Exxsol D80 as the oil phase. Similar measurements type as the explained earlier were done. In addition cross sectional measurements of the droplets flux were carried out by using a 2D isokinetic sampling probe (See Chapter 3).

A viscosity model for Nexbase 3080 (N3080) as function of temperature and pressure and for the Mixed oil (Moil) as function of temperature were developed by SINTEF using their experimental data base. Where the viscosity will be in Pa·s and $T$ and $P$ are the temperature in Celsius degrees and the absolute pressure in bar respectively.

$$\mu_{N3080} = 0.30477 \cdot e^{-0.054T} \cdot e^{-0.002096414576171 \cdot P} \tag{2.11}$$

$$\mu_{Moil} = \frac{63.57 - 1.39T}{1000} \tag{2.12}$$

The physical properties of the fluids are shown in Table 2.2. Due to the pressure drop in the pipe, the gas density is corrected for the calculations at the probe location.

Table 2.2: Physical properties of the fluids used on the experimental campaigns

| ***Phase*** | ***Fluid*** | ***Campaign*** | ***Pressure [bara]*** | ***Temperature [C]*** | ***Density [Kg/m3]*** | ***Viscosity [cP]*** |
|---|---|---|---|---|---|---|
| *Oil* | *Nexbase 3080* | *M1* | *7.0* | *20* | *847.9* | *101.9* |
| | *Exxsol D80* | *M3* | *4.7* | *20.3* | *813* | *1.8* |
| | *Mixed oil* | *M2* | *4.3* | *20* | *844.5* | *35.9* |
| *Water* | *Water* | | | *20* | *998* | *1* |
| *Gas* | *$SF_6$* | *M1* | *7.0* | *20* | *46.16* | *1.51e-5* |
| | | *M3* | *4.7* | *20.3* | *27.8* | |
| | | *M2* | *4.3* | *20* | *27.17* | |

## 2.1.3 Flow regime classification

The flow pattern classification was made by visual observations and video recordings on the clear section of the flow loop. The criteria established to classify the flow patterns for two-phase flow is shown in Figure 2.9. The pictures correspond to water and $SF_6$ experiments working at 18°C and 7 bar at different superficial gas velocities. Stratified flow was considered when gas and liquid phases are separated. Depending on the gas velocity the liquid interface can be smooth (SS) or wavy (SW). Depending on the liquid phase, the onset of liquid droplets atomization can occur on the stratified wavy flow regime. When the gas velocity increases, entrained liquid

droplets and unstable waves are swept around the pipe wall wetting it and creating a film. (Barnea et al., 1980). This flow pattern is classified as Stratified-Wavy-Annular "SW-AT". Stratified-annular flow occurs when the gas velocity rises. A large liquid droplets rate is entrained in the gas core wetting the top of the pipe and together with the waves create a film which covers all the pipe walls. No slugs or pseudo slugs are present in the flow when annular flow is considered (Lin, (Lin et al., 1986). The liquid level in the pipe will increase at low gas and high liquid flow rates. The waves can block the pipe cross-section creating intermittent flow.

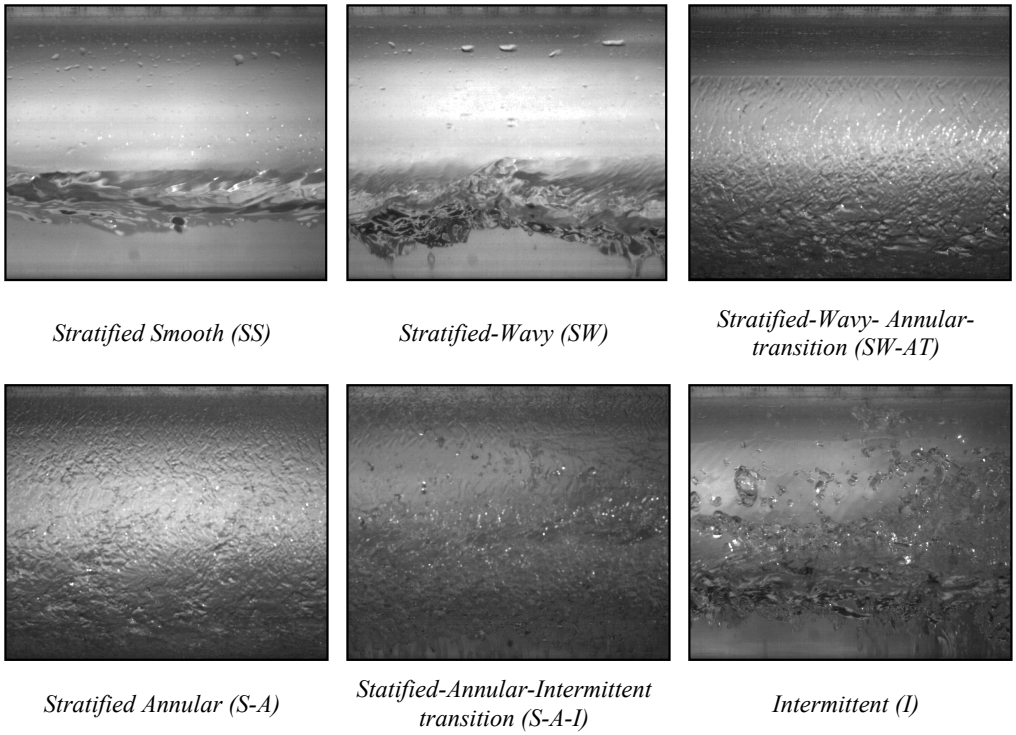


Figure 2.9: Classification criteria for flow Pattern in horizontal gas-liquid two-phase flow

The flow patterns for three-phase gas-water-oil system were classified following the proposed classification by Khor (1998) and the visual criteria used in this work are shown in Figure 2.10. The pictures correspond to water-Nexbase 3080 and $SF_6$ experiments working at 18°C and 7 bar at different superficial gas velocities and water cut 0.5.

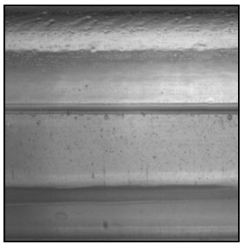

*Stratified Smooth (SS)*

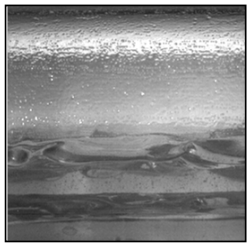

*Gas-oil stratified wavy; Oil-water stratified wavy (SW)*

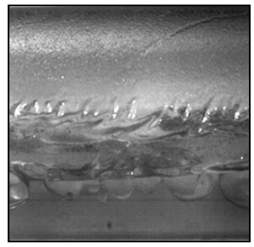

*Gas-oil stratified wavy; Oil-water partially mixed (PDSW)*

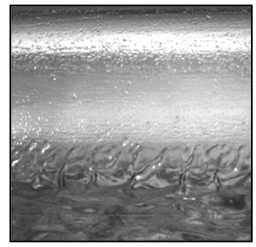

*Gas-liquid stratifed wavy; Oil-water mixed, , dry upper tube (DSW)*

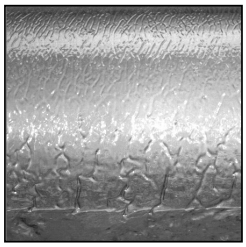

*Gas-liquid stratifed wavy; Oil-water mixed, oil wetted upper tube (DSW-WW)*

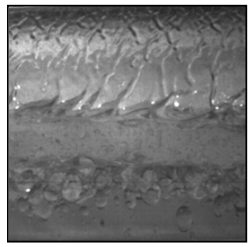

*Oil-water stratified wavy with interface dispersion and oil-wetted upper tube (SW-A)*

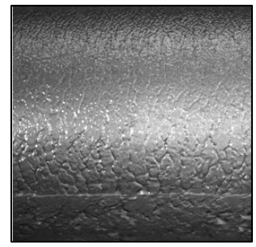

*Oil-water mixed, annular flow (D-A)*

Figure 2.10: Classification Criteria for Flow patterns. Three phase flow. Following Khor, 1998

## 2.2 Experimental setup II (Rig II)

The experiments were performed at the Multiphase Laboratory located in the department of Energy and Process Engineering at NTNU in Trondheim, Norway. The facility consists of a 90° riser-pipeline formed by a horizontal 13 m length 50 mm ID hose and a 6 m height 60 mm ID riser (See Figure 2.11). There is a transparent 0.5 m vertical section that was used to visualize the flow.

At the inlet of the flow loop air is injected into a buffer tank with an equivalent volume of $0.26m^3$. This is done to simulate a larger upstream pipe. Air is supplied from the workshop to the laboratory at 7 bara and it is reduced to 4 bara in the fluid feed line and then reduced again by a control valve located upstream the buffer tank. Oil, water and air are independently injected to the setup. A manifold was used to mix the single phases at the inlet. Water and oil are stored together in a large gravity separator in the basement of the laboratory. Each phase is independently transported to the flow loop floor using centrifugal pumps and measured using an electromagnetic and a Coriolis flow meter for water and oil respectively. Oil, water and air flow rates are controlled using control valves.

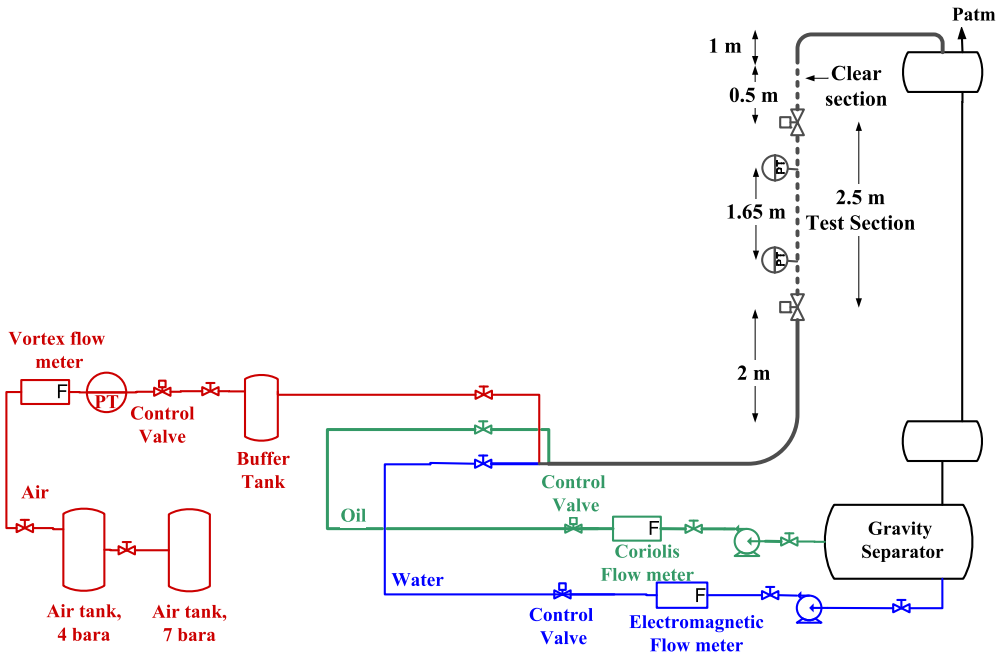


Figure 2.11:Setup at NTNU Multiphase Laboratory

### 2.2.1 Fluid system

Two sets of two-phase gas-liquid experiments were carried out using a viscous mineral oil and water as the liquid phase and air as the gas phase. The properties of the fluids at 20°C and 1 bar are shown in Table 2.3. The oil density was measured by filling up measuring flask with the oil and then weighting this on a precision scale. The dynamic viscosity of the mineral oil was measured using a rheometer.

Table 2.3:Liquid and Gas Properties @20 °C, 1 bar

| *Fluid* | *Density [Kg/m3]* | *Viscosity [Pa s]* |
|---|---|---|
| *Mineral oil* | *840* | *0.061* |
| *Water* | *998* | $1.002 \cdot 10^{-3}$ |
| *Air* | *1.2* | $1.3 \cdot 10^{-5}$ |

### 2.2.2 Pressure gradient calculation

The pressure gradient is obtained from the measurement of two absolute pressure transducers separated 1.65 m. The precision uncertainty of the measurements for a confidence level of 95% was estimated to be 18 Pa/m for steady state annular flow at the selected experimental condition. In order to verify the ΔP measurements, single-phase air measurements of the pressure drop were carried out comparing the results from a differential pressure transducer (±1 KPa) to the absolute

transducers used in the drying experiments. From the pressure gradient measurements the gas velocity was calculated using Equation 1, where D is the riser *ID,* $\rho_g$ is the air density, *dp/dx* is the measured pressure gradient*,* $g$ is the gravity acceleration and $f$ is the Darcy friction factor (Equation 2)

$$U_g = \sqrt{\frac{2 \cdot D}{f \cdot \tilde{\rho}_g}\left(\tilde{\rho}_g \cdot g + \frac{dp}{dx}\right)} \tag{1}$$

$$\frac{1}{\sqrt{f}} = -2 \cdot log_{10}\left(\frac{e}{3.7D} + \frac{2.51}{Re\sqrt{f}}\right) \tag{2}$$

Values for the air flow rate are measured by a vortex flow meter located on the high pressure side of the rig. A pressure transducer is located next to the flow meter so that the measured flow rates can be pressure corrected to the atmospheric values used in the reported superficial gas velocity (See Equation 3) The gas velocity values obtained from the differential and absolute pressure transducers and the Vortex flow meter are shown in Figure 2.12. There is a fair agreement in both techniques for high gas velocities. In general the absolute pressure transducers under predict the velocity value.

$$U_{g,atm} = \frac{1}{A} q_{Vortex} \frac{P_{@Vortex}}{P_{atm}} \tag{3}$$

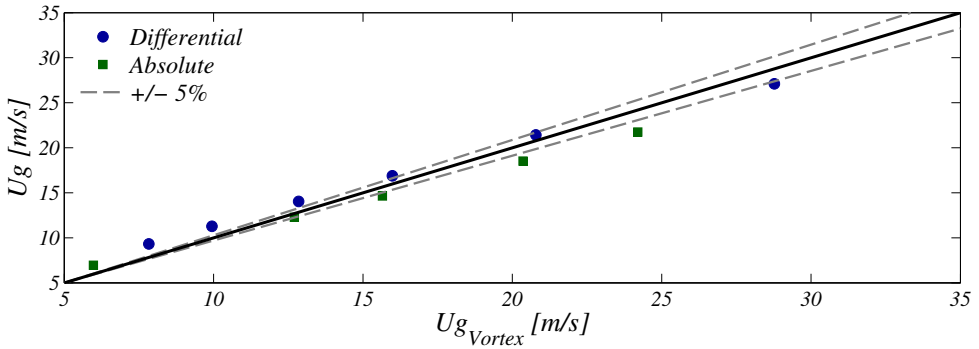


Figure 2.12. Comparison between air velocity calculation using a Vortex flow meter and a differential and absolute pressure transducers.

### 2.2.3 Liquid holdup measurements

Quick closing valves are installed at the vertical steel test section. After each experiment, the test section can be disconnected from the rest of the setup together with the bottom valve in a closed position. By opening the bottom valve, the liquid fills a graded glass (accuracy 1 ml). The liquid stuck to the pipe walls is removed using a simple cleaning piston (See Figure 2.13). Accurate holdup measurements can be obtained by measuring the collected liquid volume and dividing it by the total volume of the test section. The total uncertainty of the holdup measurements was determined by error propagation method as 1e-4.

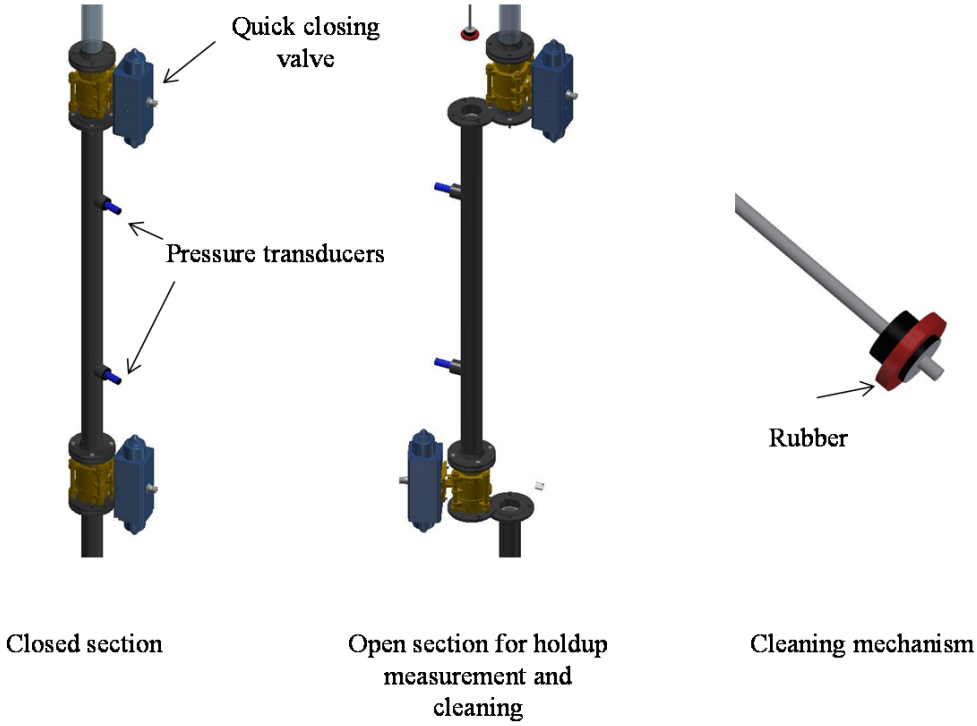


Figure 2.13: Cleaning mechanism

# Chapter 3

# Isokinetic sampling probe module design and operation

## 3.1 Introduction

The flux of liquid droplets entrained in the gas phase was sampled using an isokinetic probe. Two probes were design and built during this study. First, a probe which was capable of traversing and sampling the flow along the vertical pipe diameter and second, a more sophisticated probe was designed and built in order to sample in the full pipe cross section. The characteristics, capabilities and limitations of this technique are commented in this chapter while the results of the sampled oil and water droplet fluxes are presented in Chapter 6.

An isokinetic probe is a Pitot type sampling tube that is designed to operate under isokinetic conditions. Isokinetic conditions are achieved when the total pressure at tip of the probe is equal to the static pressure at the specific probe location and at a constant gas mass flow. Failing in withdraw the correct gas flow can lead to generate oversampling or under sampling of the flow (See Figure 3.1).

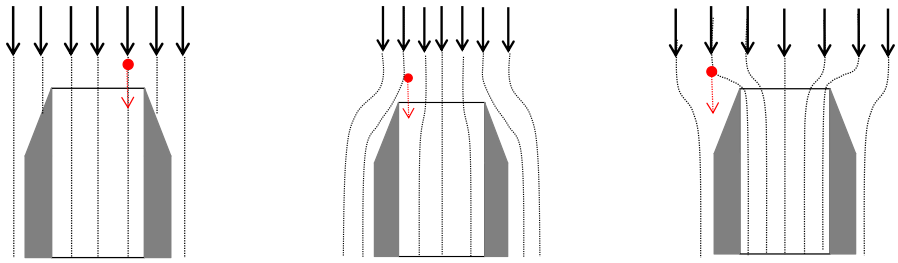

***Isokinetic sampling*** $U_{sampling}=U_{bulk}$

***Oversampling*** $U_{sampling}<U_{bulk}$

***Under sampling*** $U_{sampling}>U_{bulk}$

Figure 3.1: Effect of the gas withdraw into the flow sampling

Most of the sampling probe design considerations employed in this work follow the proposed ones by Tayebi (1994). The probe should be designed to avoid any disturbance in the flow. Wicks et al. (1960) and Williams (1990) have demonstrated that the effect of the sampling tube diameter on the measured droplet flux is negligible. However in this study the criteria used to select the probe diameter was associated to the maximum possible droplet size and for this purpose, two correlations were compared. Kocamustafaogullari et al. (1994) presented a correlation for the maximum droplet diameter in annular flows. The correlation is a function of the fluid properties and of the local energy dissipated by the turbulence.

$$\frac{d_{max}}{d_h} = 2.609 \cdot C_w^{-4/15} \cdot We_m^{-3/5} \cdot \left( \frac{Re_g^{\,4}}{Re_l} \right)^{1/15} \cdot \left[ \left( \frac{\rho_g}{\rho_L} \right) \cdot \left( \frac{\mu_g}{\mu_L} \right) \right]^{4/15} \tag{3.1}$$

$$Cw = \begin{cases} 0.028(N\mu)^{-4/5} & for \;\; N\mu \le 1/15 \\ 0.25 & for \;\; N\mu > 1/15 \end{cases} \tag{3.2}$$

Where the viscosity number $N\mu$ is defined by,

$$N\mu = \frac{\mu_f}{\sqrt{\rho_l \cdot \sigma \cdot \sqrt{\frac{\sigma}{g} \cdot \Delta\rho}}} \tag{3.3}$$

Kubie et al. (1977) developed a correlation for maximum droplet size in liquid/liquid systems. This correlation gives larger droplet diameter between the two tested correlations.

$$\left( \frac{d_{\max} \cdot \rho_c \cdot \overline{U}^{\,2}}{\sigma} \right) \cdot \left( \frac{f \cdot d_{\max}}{D} \right)^{\frac{2}{3}} = 0.369 \tag{3.4}$$

$$f = 0.076 \cdot (Re)^{-0.25} \tag{3.5}$$

### 3.1.1 1D Isokinetic sampling probe

The probe diameter was selected using the oil-water-gas fluid system to be used afterwards in the multiphase flow experiments. The probe has a 4 mm inner diameter, a 0.2 mm wall thickness. It is possible to measure within 4.2 mm of the pipe wall. To avoid flow disturbance, the opening of the sampling probe extends 50 mm upstream (≈11.4$d_p$).The dynamic pressure is read at 3.75$d_p$ and the static pressure sensed at the pipe wall on the probe stem plane. Three static pressure taps were connected together in order to get an appropriate average static pressure and avoid pressure fluctuations inside the pipe. The probe head has 4 orifices connected to a common chamber and from it two hoses (one from the probe top and one from the bottom) were connected to transmit the dynamic pressure from the holes to the differential pressure transducer. The probe can traverse the vertical pipe diameter using a linear actuator and has the ability to work as a sampling and Pitot probe when a manual ball valve connected to the sampling line is

closed. The 1D isokinetic sampling probe used in this study is schematically shown in Figure 3.2.

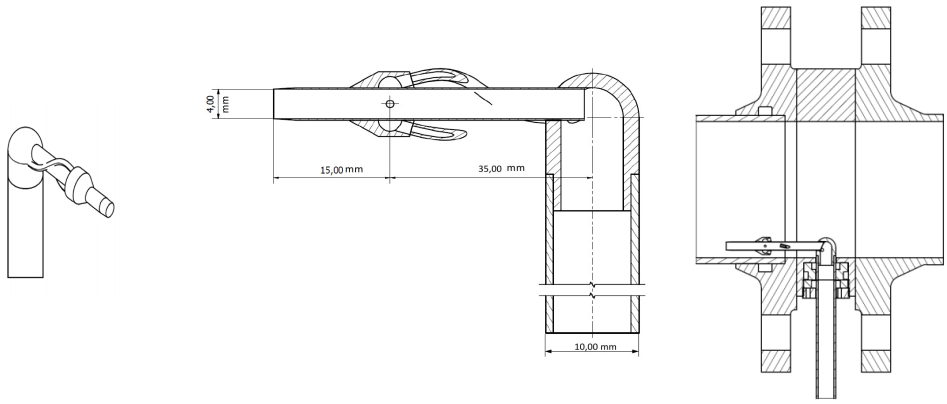


Figure 3.2: 1D Isokinetic sampling probe sketch

CFD simulations using Ansys CFX were carried out to study the effect of the probe presence on the flow and to detect and correct possible installation problems. The CFD analysis was validated by comparing the model predictions against experimental measurements. The CFD simulations made it possible to verify the design and predict and correct an installation problem related with the axial position of the static pressure port. Details of this study can be found in A. Shmueli et al. (2013)

### 3.1.2 2D Isokinetic sampling probe

A 4mm ID. Isokinetic sampling probe was designed and built. The probe can be positioned at different locations inside the pipe using simultaneously a linear and a rotary actuator. A real picture of the probe with a description of its components is shown in Figure 3.3a and the operating principle of the probe moving system is described on Figure 3.3b.

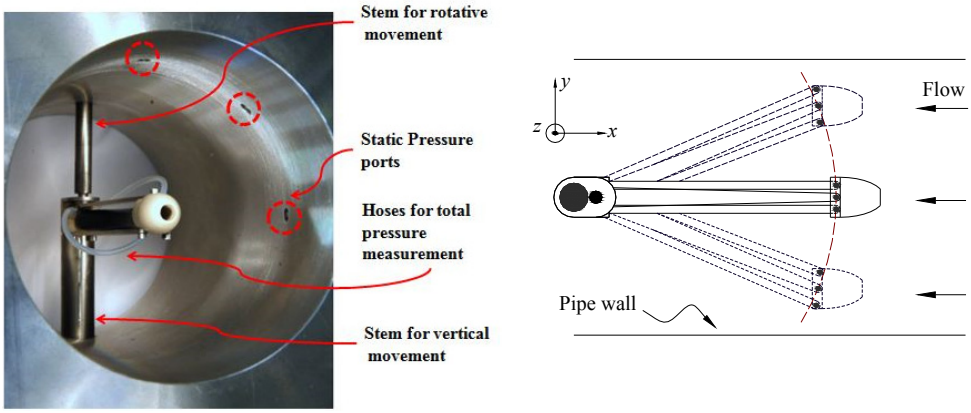


*(a)* *(b)*

Figure 3.3: (a)Isokinetic probe, (b) Probe operating principle

The dynamic pressure is read at $1.375d_p$ and the static pressure sensed at the pipe wall on the probe tip plane. Three static pressure taps were connected together in order to get an appropriate average static pressure and avoid pressure fluctuations inside the pipe. The probe head has 5 orifices on the top side connected to a common chamber and from it two hoses were connected to transmit the dynamic pressure from the holes to the differential pressure transducer (See Figure 3.4).

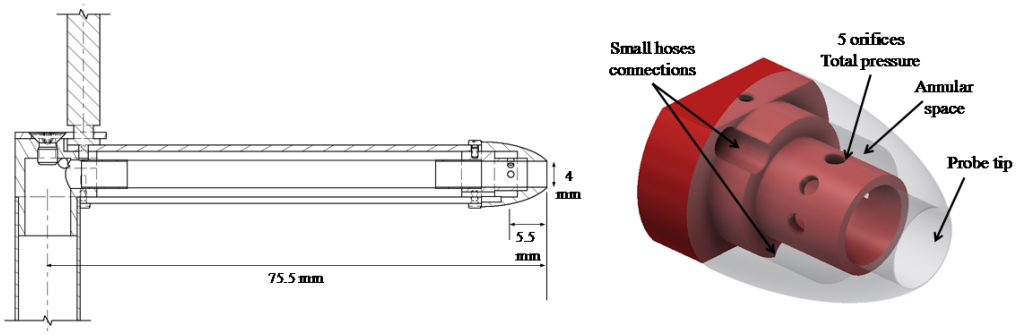


Figure 3.4: 2D Isokinetic probe dimensions and details of probe head

The location given by the PLC unit was verified and calibrated by the following procedure. Two fixed spatial references were used, one in front of the probe spool piece (black lines in Figure 3.5) and another one behind it (red lines in Figure 3.5) The test consisted on setting a desired location of probe inside the pipe using the PLC unit and checking afterwards the real location obtained by the visualization technique.

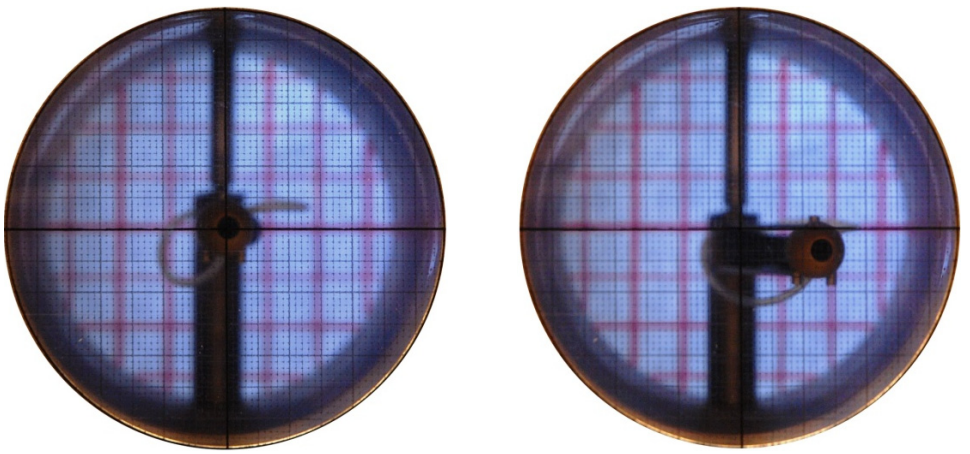

Figure 3.5: Probe location calibration

The real location of the probe was calculated using the methodology explained in Figure 3.6 and below. Where $H_p$ is the spool piece length, $h_i$ is the length from the spool piece entry to the probe vertical traversing stem. The instantaneous location of the probe is describe by the coordinates

$X_p$, $Y_p$ and $Z_p$. Due to the camera angle of view this location is observed as $X_f$, $Y_f$, $Z_f$, in front of the probe and $X_b$, $Y_b$, $Z_b$ on the reference plane behind the probe. By geometrical relations is possible to define the location of the probe (See equations (3.6)to (3.8))

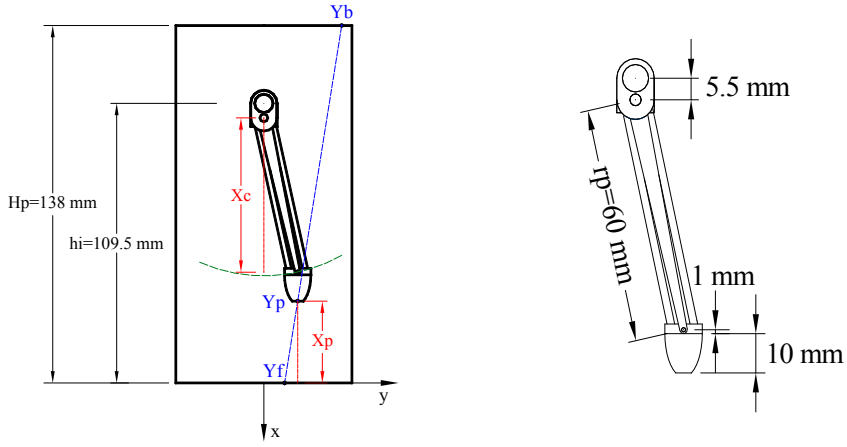


Figure 3.6: Coordinates for probe location calibration

$$X_p = h_i - X_c - 11 - 5.5 = h_i - 5.5 - \sqrt{rp^2 - Y_p^2} \tag{3.6}$$

$$Y_p = \frac{-2K_1K_2 \pm \sqrt{(2K_1K_2)^2 - 4(K_2^2+1)(K_1^2 - rp^2)}}{2(K_2^2+1)} \qquad \text{Where} \quad K_1 = -h_i + 5.5 - \frac{H_P \cdot (Y_f)}{Y_b - Y_f}, \quad K_2 = \frac{H_P}{Y_b - Y_f} \tag{3.7}$$

$$Z_p = \left(\frac{Z_b - Z_f}{H_p}\right) X_P + Z_f \tag{3.8}$$

The correspondence between the locations set using the PLC and the current location inside the pipe is shown in Figure 3.7

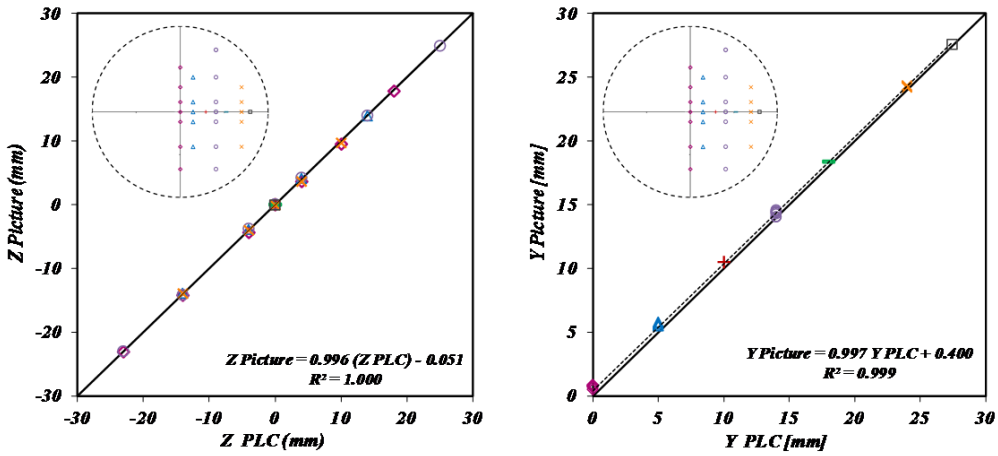


Figure 3.7: Correspondence between the set probe location by the PLC and real probe location

### 3.1.3 Sampling Methodology

The measurement of the total and static pressure are made at the probe tip and at the inner pipe wall respectively. The sampled flow goes through the probe to a gas-liquid transparent separator. From the separator, the gas flows through a Coriolis flow meter (Micromotion CMFS010) and then to a pneumatic control valve (Samson 3510). The liquid falls by gravity and is accumulated in a clear and graded vessel. Two clear and graded vessels with 69mm and 17mm ID were used depending on the sampling location inside the pipe. To obtain the isokinetic condition it was required to generate sufficient suction between test section and the loop separator. For this reason, two Danfoss gas compressors were connected in parallel between the control valve and the gas flow meter. A linear and a rotary actuator from Oriental Motors were used to position the probe vertically and on the pipe cross section respectively.

The total pressure sensing hoses can be blocked by oil after a certain sampling time and wrong pressure values would be sensed. For this reason, the little hoses were flushed and cleaned with pressurized $SF_6$ at the beginning of each sampling measurement.

All the signals from the pressure transmitter, the valve, Coriolis flow meter and the actuators are sent to a PLC unit with a built-in HMI operator panel (Unitronics vision 1040-T20B). A Ladder code was developed to control all the desired variables. On the touch screen it is possible to set the desired probe location and to visualize the average values from the instrumentation in the probe module. The pressure signal from the probe, gas mass flow, valve opening and tank pressure is plotted in real time on the screen. The sampling rate was set to $2s^{-1}$. By using the PLC unit it was possible to control automatically the isokinetic condition (See Figure 3.8a and Figure 3.8b). Figure 3.9 shows the probe module used during this study

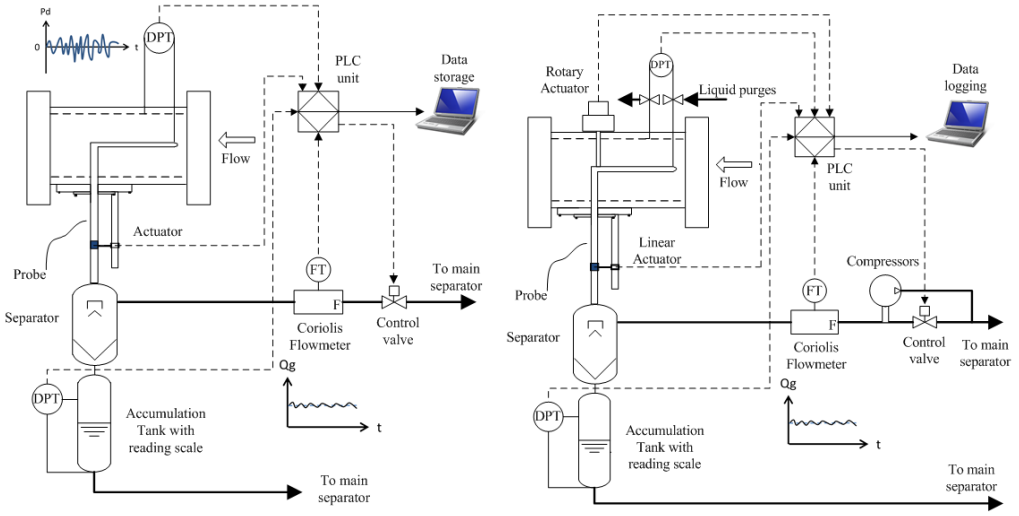


*(a)PID 1D isokinetic probe* *(b) PID 2D isokinetic probe*

Figure 3.8:Control process of the isokinetic probe modules using the 1D and 2D probes

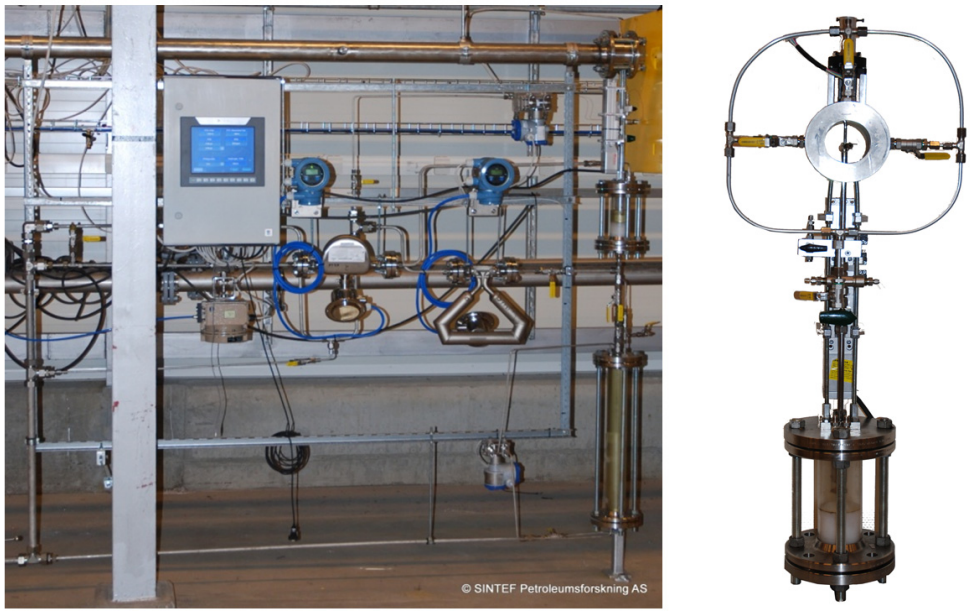


Figure 3.9: Isokinetic probe Module

A sampling test started by changing the probe location to the desired one and flushing the pressure hoses with pressurized gas. The control was developed such that the flow will be controlled by opening or closing the pneumatic valve until the measured dynamic pressure on the probe be closed to 0 Pa (Isokinetic condition). Once the value of the dynamic pressure is close to the desired condition, the control is more precise and the valve opening changes are smaller. During the sampling period the control is maintained, keeping a stable gas mass flow and dynamic probe pressure. In general the stabilization time to reach the sampling the sampling period vary between experiments and the probe location in the pipe (See Figure 3.10)

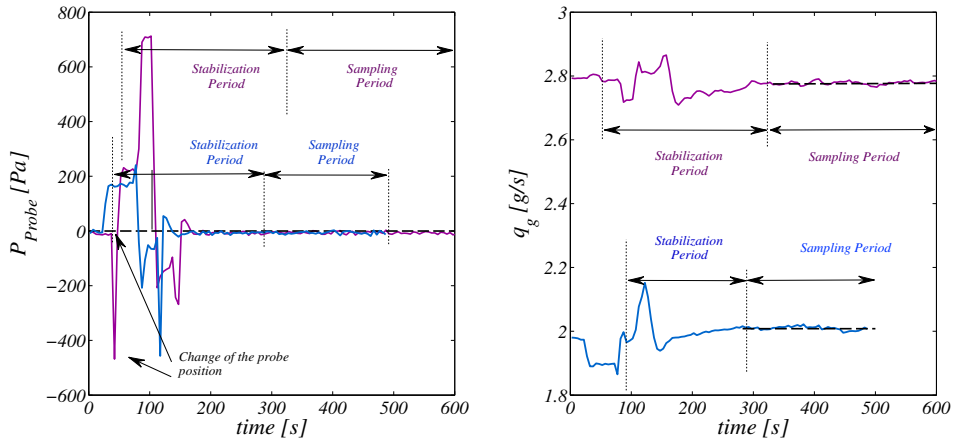


Figure 3.10: Sampling methodology. Stabilization of isokinetic condition and sampling period

The increment of oil and water level in the tank $\Delta h$ is used to calculate the local oil and water droplet flow rates. For the two-phase flow experiments, $\Delta h$ can be calculated using two methods: From the record of the differential pressure transducer installed in the tank (calculating the equivalent hydrostatic liquid column) or $\Delta h$ can be also estimated visually using a scale attached to the clear vessel.

For the three-phase flow experiments, the increment of the water level in the tank $\Delta h_w$ was visually estimated using a scale attached to the clear vessel (See Figure 3.11) and the oil level increment $\Delta h_o$ was obtained using the recorded tank pressure together with the obtained $\Delta h_w$. Videos of the oil-water interface in the tank were recorded to facilitate the interface reading process.

The oil and water local volumetric flow rate are calculated using equations (3.9) and (3.10) respectively

$$q_o(y) = \Delta h_o(y) \cdot \frac{A_v}{\Delta t(y)} = \left( \frac{\Delta Pt(y) - \rho_w \cdot g \cdot \Delta h_w(y)}{\rho_o \cdot g} \right) \cdot \frac{\pi \cdot d_v^{\,2}}{4 \cdot \Delta t(y)} \tag{3.9}$$

$$q_w(y) = \Delta h_w(y) \cdot \frac{A_v}{\Delta t(y)} = \Delta h_w(y) \cdot \frac{\pi \cdot d_v^{\,2}}{4 \cdot \Delta t(y)} \tag{3.10}$$

As an example, the read $\Delta h_w$ and oil droplet flux is compared to the calculated ones from the pressure difference for an oil-gas system. The error bars are calculated by propagation as explained in Appendix A (See Figure 3.12).

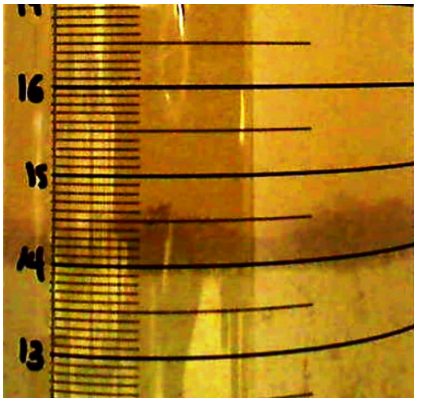


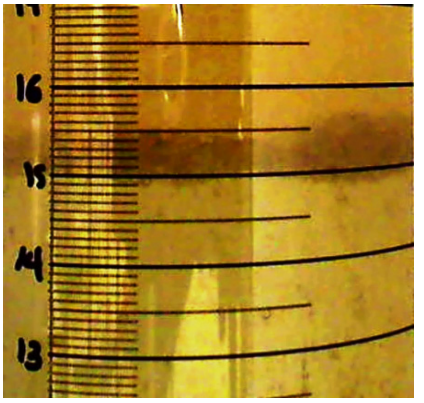


*hw@$t_1$=14 cm* *hw@$t_2$=15 cm*

Figure 3.11: Example of the measurement of the collected water droplets

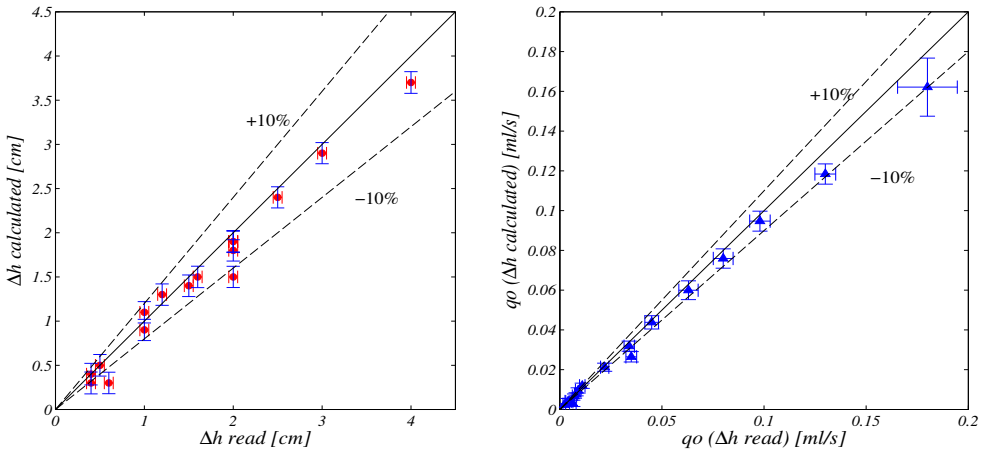


Figure 3.12: Example of the obtained Δh and droplet flow rate for oil-gas. Usl=0.1 m/s and Usg=6.6m/s (Mixed oil-$SF_6$)

The total sampling time depends on the location of the probe in the pipe and on the tested global watercut value. Most of the experiments were carried out at low watercuts values so the required sampling time to collect enough water to be measured in the vessel is higher than for two-phase flow conditions.

## 3.1.4 Velocity Calculations

The probe was designed to work as a sampling probe and as a Pitot tube. The local gas velocity is necessary to determine the local droplet concentration and to understand the flow physics. Two kinds of experiments were run to guarantee the results from the probe. Single phase experiments using $SF_6$ were carried with the two isokinetic probes and then compared to theoretical profiles.

### *3.1.4.1 Gas single phase velocity profiles*

The power law velocity profile for fully developed turbulent pipe flow can be written as:

$$\frac{U_g}{U_{max}} = \left(1 - \frac{r}{R}\right)^{1/n} \tag{3.11}$$

$$r = \sqrt{y^2 + z^2} \tag{3.12}$$

The value of the exponent n will depend and increase with the Reynolds number (Cengel et al., 2004) . There are many suggested empirical values for this coefficient and a summary of most of them are shown in Afzal et al. (2007). On Figure 3.13 a comparison of experiments and the theoretical velocity profile are shown for the 1D and 2D probes showing a good agreement between them.

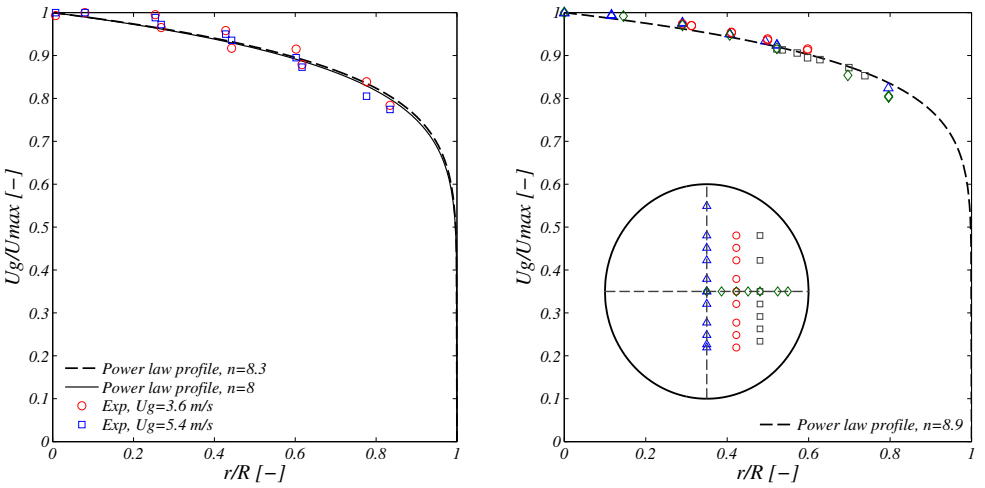


*(a). M2 gas experiments. 1D probe*

*(b) M3 gas experiments. Usg=7.5 m/s. 2D probe*

Figure 3.13: Comparison between Power-law velocity profile and the local gas velocity profiles for two experimental campaigns (M2, M3)

### *3.1.4.2 Multiphase velocity profiles*

In order to measure the local gas velocity using the probe as a Pitot tube it is assumed that the stagnation pressure will be the same as the kinetic energy of the mixture. Following Skartlien et al. (2011)

$$U_g = \sqrt{\frac{2 \cdot P_d}{\rho_m}} \tag{3.13}$$

$$\rho_m = K_o \cdot \rho_o + K_w \cdot \rho_w + K_g \cdot \rho_g \tag{3.14}$$

$$K_n = \frac{q_n}{U_g \cdot A_p} \tag{3.15}$$

The value for the constants $K_i$ will correct the velocity profile distortion due to the existence of liquid droplets.

For the measurements carried out in the experimental campaign M3, the velocity was calculated using the local measured gas flow rate under isokinetic conditions. Assuming non-slip conditions between the droplets and the gas, the local gas velocity can be calculated using the mixture velocity definition.

$$U_g(y) = Um(y) = Usg(y) + Uso(y) + Usw(y) \tag{3.16}$$

$$U_g(y) = \frac{1}{A_p}\left(\frac{\dot{m}_g(y)}{\rho_g} + q_o(y) + q_w(y)\right) \tag{3.17}$$

# Chapter 4

## Characteristics of horizontal three-phase stratified-annular flow

Three-phase gas-oil-water flows in horizontal pipes were studied in this Chapter and characteristics of the flow such as flow patterns, phase fractions, liquid height and pressure gradient were measured. Three oils with different viscosities, watercuts and operative conditions were studied. The measurements were focused on stratified and annular flow regimes. The flow patterns where classified based on high speed video recordings of the flow. Visual observations of the flow allowed measuring the liquid height together with an existent two-energy traversing single beam gamma densitometer. Liquid fraction and gas-liquid interface height is required when calculating total liquid entrainment fraction and interfacial droplet concentration. In addition comments on the pipe wall film and droplet entrainment are presented.

### 4.1 Introduction

Three-phase flows are treated sometimes as gas-liquid flows with average properties on the liquid phase. However this assumption might not be correct in all cases as slip can cause deviations from the homogenous liquid-liquid behavior. Experimental studies on three phase flows have been conducted in the past. Sobocinski (1955), Açikgöz et al. (1992), Pan (1996) and Khor (1998) proposed classifications for the flow regimes based on visual observations of their oil-water-air experiments.

Several authors have studied the effect of the fluid properties on gas-liquid flow in horizontal pipes. Most of them focused their work on the effect of the liquid viscosity (Hoogendoorn (1959); Weisman et al. (1979)). Phase fractions in two-phase gas-liquid flow have been studied in the past using gamma densitometers, x-rays, conductance and capacitance probes or quick closing valves. However, studies on the characteristics of three phase stratified-annular flows are more limited (See Nuland et al. (1993); Chen et al. (1997); Pan (1996); Hoffmann et al. (2011); among others).

## 4.2 Experimental conditions

The experiments were conducted starting from an oil-gas system and increasing the water cut at a constant superficial liquid and gas velocity as it is shown in Table 4.1. The water cut and superficial liquid velocity are defined as *WC=Usw/Usl, Usl=Usw+Uso* respectively. The flow regimes in all the experiments are ranged from stratified wavy flow with small amplitude waves to annular flow with atomization. Three different oils were used to study the influence of the viscosity on the behaviour of the flow.

Table 4.1 Experimental matrix

| ***Fluids*** | ***Pressure (bar)*** | ***Usl (m/s)*** | ***Usg (m/s)*** | ***WC (-)*** |
|---|---|---|---|---|
| *(N3080/W/SF6)*<br>*Nexbase 3080*<br>*Water*<br>*SF6* | *7.0* | *0.11* | *0.7*<br>*2.6*<br>*5.3*<br>*8.0* | *0.75* |
| | | *0.2* | *1.3* | *0*<br>*0.49*<br>*1* |
| | | | *2.6* | *0*<br>*0.5*<br>*1* |
| | | | *5.3* | *0*<br>*0.5*<br>*1* |
| | | | *8.0* | *0*<br>*0.5*<br>*1* |
| | | *0.40* | *2.6*<br>*5.3* | *0*<br>*0.5* |
| | | *0.79* | *1.3*<br>*2.6*<br>*8.0* | *0.5* |
| *(MO/W/SF6)*<br>*Mixed oil*<br>*Water*<br>*SF6* | *4.3* | *0.1* | *6.6* | *0*<br>*0.1*<br>*0.21*<br>*0.72* |
| *(E80/W/SF6)*<br>*Exxsol D80*<br>*Water*<br>*SF6* | *4.5* | *0.1* | *8.8* | *0*<br>*0.2*<br>*0.8* |
| | | *0.2* | *6.1* | *0*<br>*0.05*<br>*0.1*<br>*0.2* |
| | | | *7.5* | *0*<br>*0.1*<br>*0.2* |
| | | | *8.9* | *0*<br>*0.05*<br>*0.1*<br>*0.2*<br>*0.4* |

## 4.3 Flow maps

The flow pattern maps were obtained based on the high speed video recordings of the flow and following the classification criteria explained in Chapter 2. The flow pattern maps are shown for two oils: Nexbase 3080 and the mixed oil. The conditions using Exxsol D80 were limited to stratified-annular flow where oil and water where mixed in the liquid layer.

### 4.3.1 Nexbase-Water-SF6

The flow pattern maps for a two-phase water-gas and Nexbase-gas system are summarized in Figure 4.1a and Figure 4.1b respectively. Where the abbreviations SW: Stratified wavy; SW-AT: Stratified wavy transition to annular. SW-DW-Ent: Stratified wavy with dry pipe walls droplet atomization; S-A: Stratified annular; S-A-I: Stratified annular to intermittent and I: Intermittent flow. Gray dashed lines are drawn on the plots to illustrate the possible flow regime transitions.

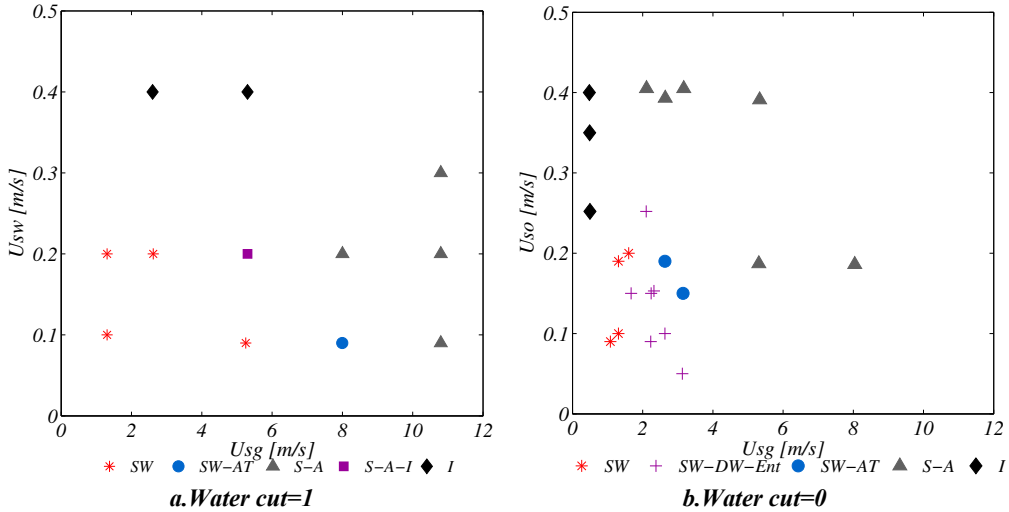


Figure 4.1: Flow pattern map for water-gas (a) and Nexbase 3080(100 cP)-gas (b) at 7 bara

The transitions from stratified wavy to annular flow occur considerably earlier for the oil-gas system than for the water-gas system. One explanation may be the reduction on the surface tension of the liquid phase (Water has almost three times the oil surface tension). These observations are in agreement with the experimental work from Tzotzi et al. (2011). According to previous studies the effect of the liquid viscosity was found to be negligible over the stratified to annular flow transition (See Gokcal et al. (2008); Weisman et al. (1979)). The onset of liquid droplet entrainment occurs around *Usg*=2 m/s for Nexbase-$SF_6$ and between *Usg*=7 m /s and 9 m/s for the water-gas system.

The transition from stratified to intermittent flow is later for the oil-gas system. Tzotzi et al. (2011) did not find any effect of the surface tension on the stratified-intermittent flow transition for low gas velocities. However, for high gas velocities (close to the annular flow region) they found later transitions for systems with low surface tension liquids. A small region with

intermittent flow was found at low gas and liquid velocities for the Nexbase-gas system. Previous experiments on the same setup and conditions were carried out by Smith et al. (2011). They found a transition from stratified to slug flow at $Uso \geq 0.1$ m/s and low gas superficial velocities, defining all flow patterns which not fully close the pipe cross section as stratified flow.

The flow pattern results for a three-phase flow system (water-Nexbase 3060-$SF_6$) at watercuts 0.5 and 0.75 are shown in Figure 4.2 together with a scheme of the observed flow configuration. The onset of droplet entrainment for the water cut 0.5 case is around $Usg$=2.6 m/s.

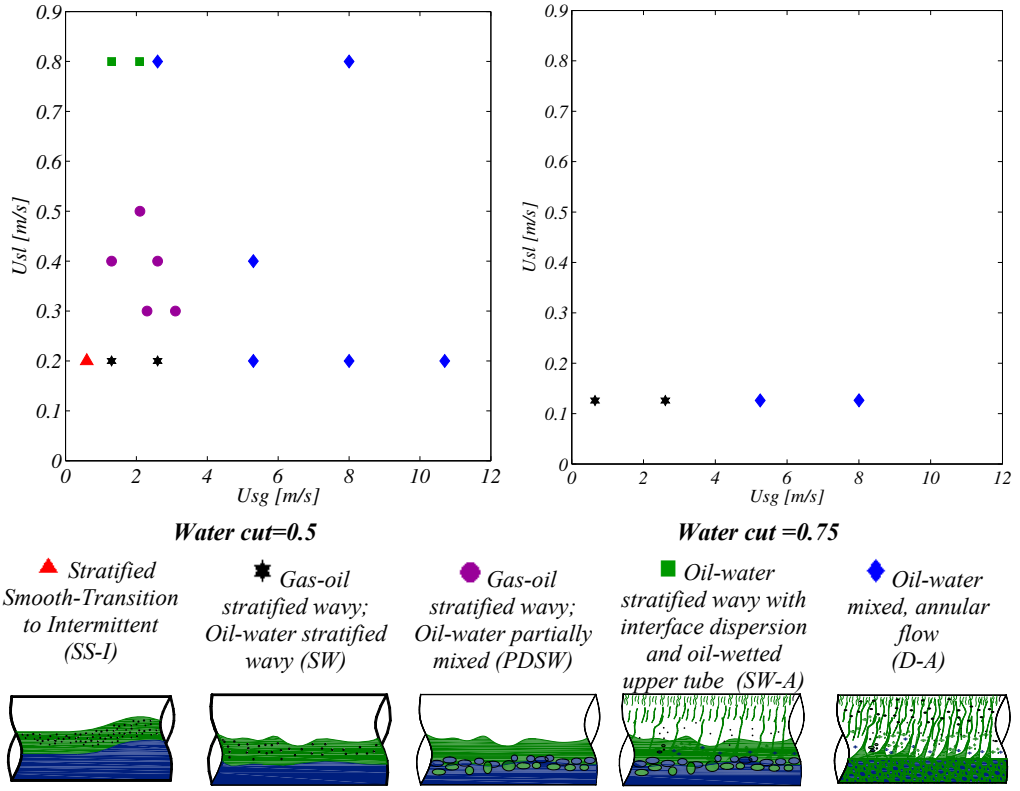


Figure 4.2: Flow maps for Nexbase 3080(100 cP) 7 bara, WC=0.5 and WC=0.75

## 4.3.2 Mixed oil-Water-SF6

The flow pattern map for two-phase Mixed oil-gas is shown in Figure 4.3. The pressure in this case is lower than for the Nexbase-gas case. The comparison between the flow maps is not straightforward as both the gas density and the viscosity are different in this case. The stratified flow region is reduced in comparison to the Nexbase 3080-gas system and the transition to intermittent flow occurs earlier ($Usl$<0.15 m/s).The transition from stratified to annular flow occurs at higher $Usg$ values ($Usg$> 6 m/s). The three-phase flow experiments were carried out at a constant gas and liquid superficial velocity where the flow pattern was always Oil-water mixed, annular flow.

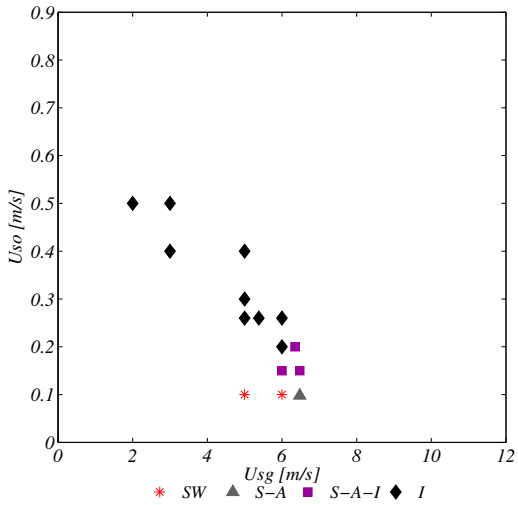


Figure 4.3: Flow pattern map for Mixed oil(35 cP)-gas at 4.3 bara

## 4.4 Phase fractions

The phase fractions profiles are measured using a traversing gamma densitometer. The average phase holdup is calculated by integrating the local phase fractions over the pipe area. The integration is made as:

$$\bar{\alpha}_k = \frac{2}{A}\int_0^{2R} \sqrt{R^2 - (y-R)^2}\cdot \alpha_k(y)\,dy \tag{4.1}$$

Here the sub index $k$=$g,o,w$ as gas, oil or water respectively and $y$, $R$ and $A$ are vertical location in the pipe, the pipe radius and the pipe cross section respectively. On Figure 4.4 a summary of the experiments using the highest viscosity oil (Nexbase) at $Usl$=0.2 m/s is presented. The total liquid and phase profiles for the rest of the experiments listed in Table 4.1 can be found in Appendix B. Stratified wavy flow with small amplitude waves was visually observed at the lowest gas superficial velocities ($Usg$=1.3 m/s, See Figure 4.4a) for water cut values 0 (oil and gas) and 1 (water-gas). For the three-phase case at watercut 0.5 and the same $Usg$, three-layer stratified wavy flow is present. There was a large amount of small gas bubbles entrained in the oil layer. At $Usg$=2.3 m/s the liquid layer is still stratified but partially mixed at the interface between oil and water (See Figure 4.4b). The gas-liquid interface becomes wavier and some droplets are entrained on the gas phase. When increasing the superficial gas velocity to 5.3 m/s (See Figure 4.4c), the flow pattern becomes stratified-annular. Droplets from the liquid layer waves wet the top of the pipe wall creating a thick and wavy film. A thick, continuous and homogenous liquid film climbs up the pipe wall and a delimited border between the two film regions is observed. This behavior is very similar to the oil-gas system. No visual oil and water stratification was observed in the liquid layer for these conditions. This is confirmed by the gamma densitometer measurements where oil is dispersed in water (See Figure 4.4i-k).

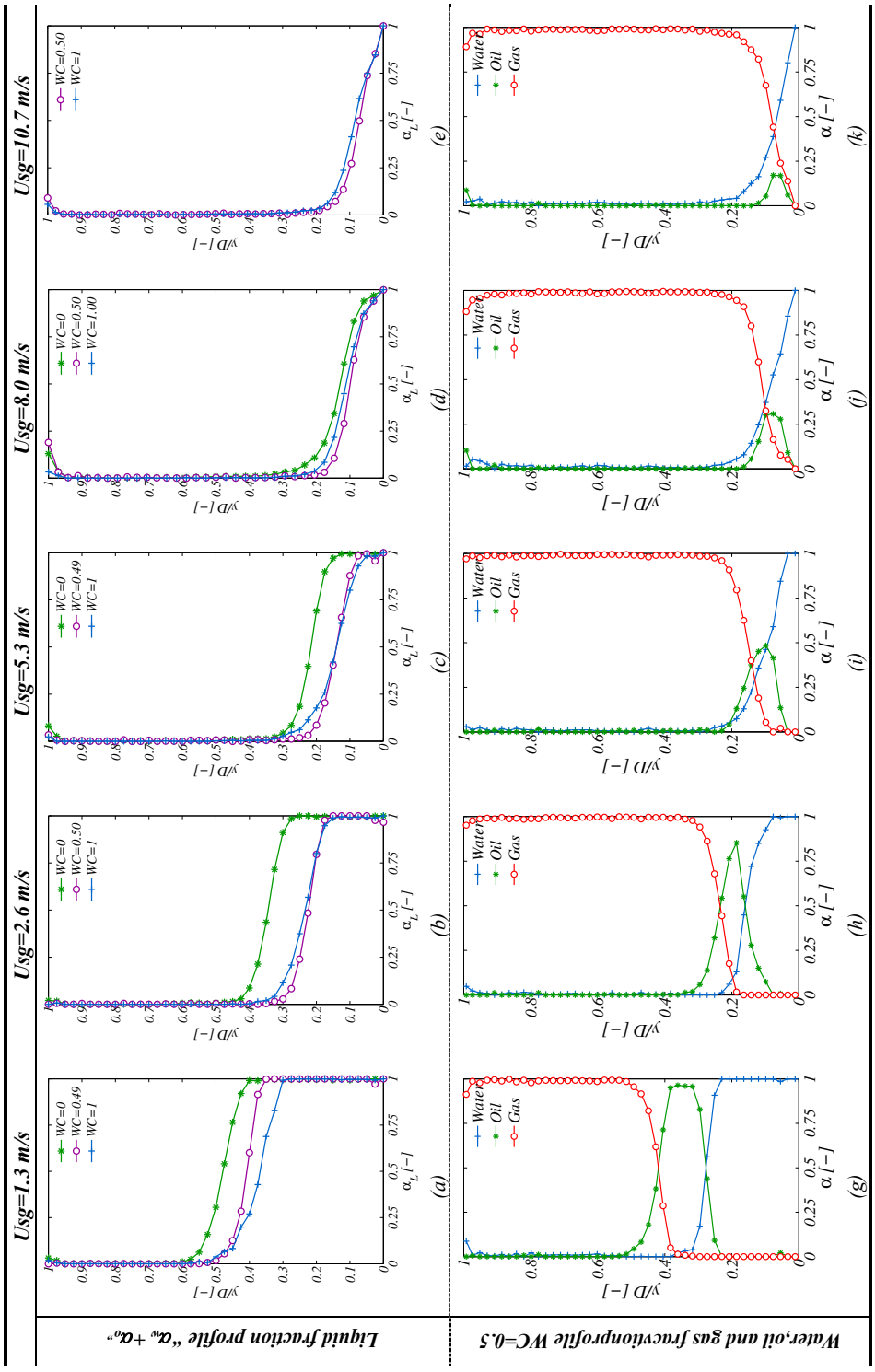


Figure 4.4: Liquid and phase profiles for Nexbase 3080(100 cP), water and gas at 7 bara. WC=0.5. Usl=0.2 m/s



38

When the liquid phases are mixed they can be approximated as homogenous flow, meaning that there is no slip between them. One might expect that the oil and water phase fraction profiles to be overlapped as the watercut value in these experiments is 0.5. However, this is not observed in these experiments as the oil content in the liquid layer becomes considerably smaller than the water as the superficial gas velocity increases. The in-situ watercut $WC_{i\text{-}s}$ defined by the ratio of water to total liquid holdup $(WC_{i\text{-}s}=\alpha_w/\alpha_L)$ is plotted in Figure 4.5 The in-situ water is always larger than the input water cut (0.5) for these conditions.

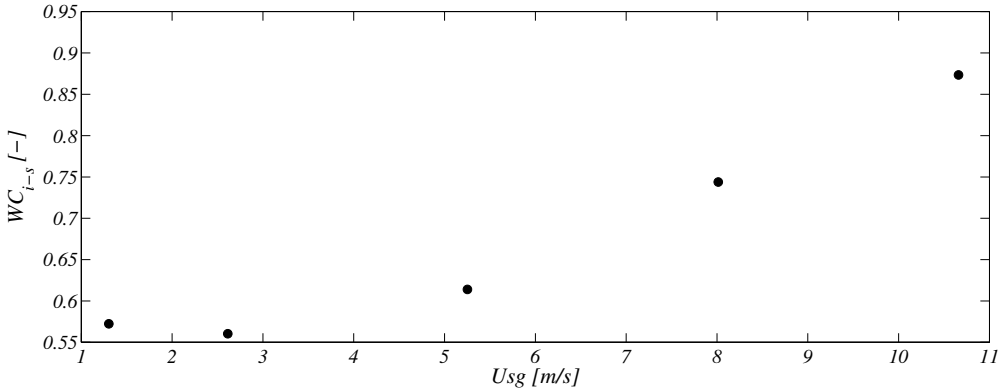


Figure 4.5:In-situ water cut vs superficial gas velocity. Oil: Nexbase 3080. WC=0.5. Usl=0.2 m/s

Two possibilities can explain this behavior: (a) There is a large slip between oil and water layers (See Figure 4.6) (b) A large amount of oil is redistributed from the liquid wall film and atomized to the gas phase as droplets (See Figure 4.8).

***(a) Large slip between oil and water:*** Assuming this premise, water and oil have different velocities on the liquid layer ($U_w \neq U_o$). As a simplified approach, neglecting the gas entrained in the oil layer and the liquid entrained as droplets in the gas phase the mass conservation equations for the three phases are written as

$$q_g = U_{sg} \cdot A = U_g \cdot A_{gu} \tag{4.2}$$

$$q_w = U_{sw} \cdot A = U_w \cdot A_{wd} \tag{4.3}$$

$$q_o = U_{so} \cdot A = U_o \cdot A_{od} \tag{4.4}$$

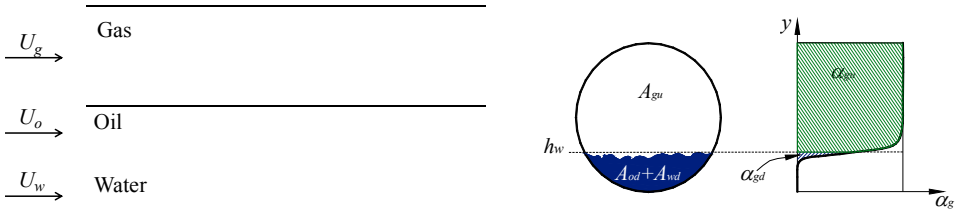


Figure 4.6: First possibility sketch

Here $A_{gu}$, $A_{wd}$ and $A_{od}$ are the area occupied by the gas over the gas-liquid interface and the areas occupied by water and oil below the gas liquid interface respectively. These areas are calculated by establishing a gas-liquid interface based on the phase fraction profiles (See a detailed explanation in section 4.5). The gas, oil and water phase fraction profiles are integrated from the pipe bottom to the gas-liquid interface in the oil and water phases and from the gas-liquid interface to the pipe top for the gas phase.

$$A_{ku} = \alpha_{ku} \cdot A_u = 2\int_{hw}^{D} \sqrt{R^2 - (y-R)^2} \cdot \alpha_k(y)dy \tag{4.5}$$

$$A_{kd} = \alpha_{kd} \cdot A_d = 2\int_{0}^{hw} \sqrt{R^2 - (y-R)^2} \cdot \alpha_k(y)dy \tag{4.6}$$

Here the sub index $k=g,o,w$ as gas, oil or water respectively. For oil-water flows the slip ratio and slip velocity between the phases are respectively estimated by:

$$S_{o/w} = \frac{U_o}{U_w} = \frac{q_o \cdot \alpha_o}{q_w \cdot \alpha_w} \tag{4.7}$$

$$U_{s-o/w} = U_o - U_w \tag{4.8}$$

The slip ratio and oil water slip velocity obtained from using the approach described above are plotted in Figure 4.7. Both variables increase with the gas superficial velocity and numerically could explain the behavior on Figure 4.4. However physically there is no reason to expect an increment on the slip when increasing *Usg*. The relative velocities are also very large.

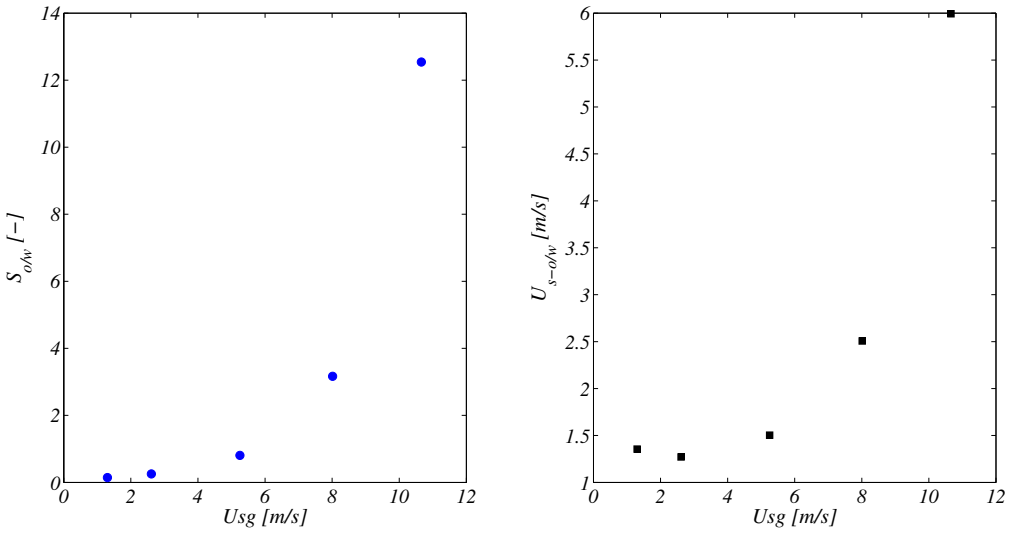


Figure 4.7: Slip ratio and oil water slip velocity

***(b) Oil redistribution as droplets and film***: The gas flow generates a shear stress on the oil stratified layer. Due to the large oil viscosity, the gas-oil shear stress might not be high enough to promote a proper mixing between the liquid phases but rather cause entrainment of the oil to the

gas phase. The majority of oil is then entrained in the gas and the remaining can be mixed with the water resulting in the situation shown in Figure 4.4i-k. The gamma densitometer does not have the accuracy to measure the entrained liquid droplet fractions in the gas phase so a different approach to the first possibility is followed.

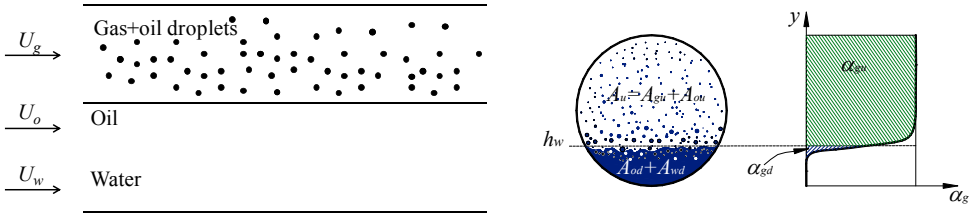


Figure 4.8: Second possibility sketch

Assuming a non-slip condition between the oil droplets and the gas and no gas entrainment in the oil layer, the gas phase velocity is calculated as:

$$U_g = \frac{U_{sg} \cdot A}{A_{gu}} \tag{4.9}$$

As an extreme case it is assumed that all the oil is transported in the gas phase as droplets or as the liquid wall film. The area occupied by the oil over the gas-liquid interface $A_{ou}$ is calculated as

$$A_{ou} = \frac{U_{so} \cdot A}{U_g} \tag{4.10}$$

For the dispersed cases ($Usg \geq 5.3$ m/s), the percentage of the gas area $A_{gu}$ that should be occupied by oil if all of it is entrained to the gas phase is no larger than 1.7%. This suggests that this possibility is feasible and can explain the fraction profiles shown in Figure 4.4.

The phase fraction profiles obtained when using Exxsol D80 as an oil phase (P=4.7 bara) are shown in Figure 4.9. The liquid fraction profile of the three-phase flow tends to be similar to the water-gas system at high gas velocities (for stratified-annular flow) so the differences between the liquid fraction profiles of the two-phase or three-phase flows are small. (See Figure 4.4d-e). There is a distribution of the oil and water phases inside the liquid layer when increasing the input watercut value. The general trend is a reduction on the oil fraction and an increment on the water fraction as the watercut value rises (See Figure 4.10). The in-situ water cut is generally larger but close to the input water cut. However using Exxsol D80 at the presented conditions, the differences between the input and the in-situ watercut are not as large as in the Nexbase 3080 cases.

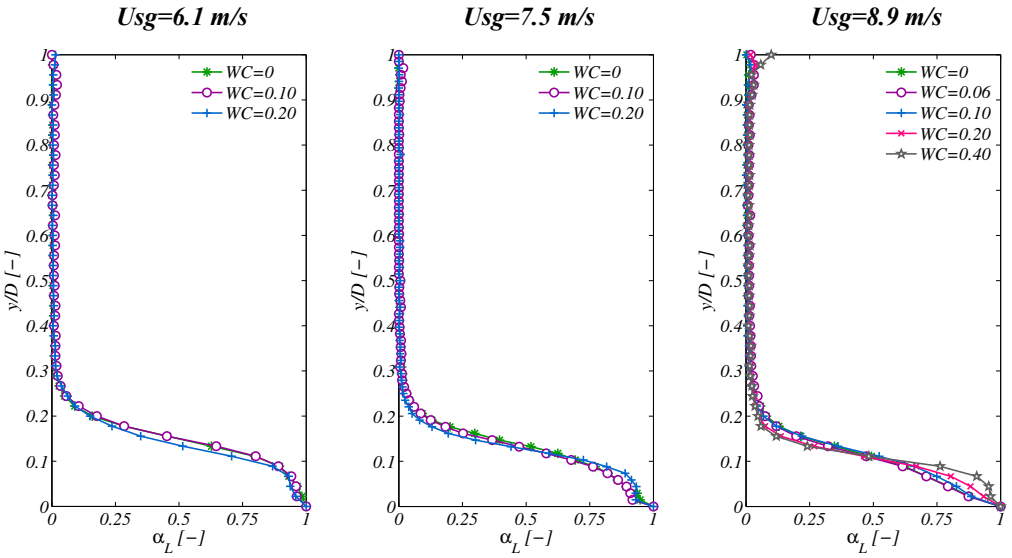


Figure 4.9: Liquid phase profiles for Exxsol D80-water and gas at Usl=0.2 m/s

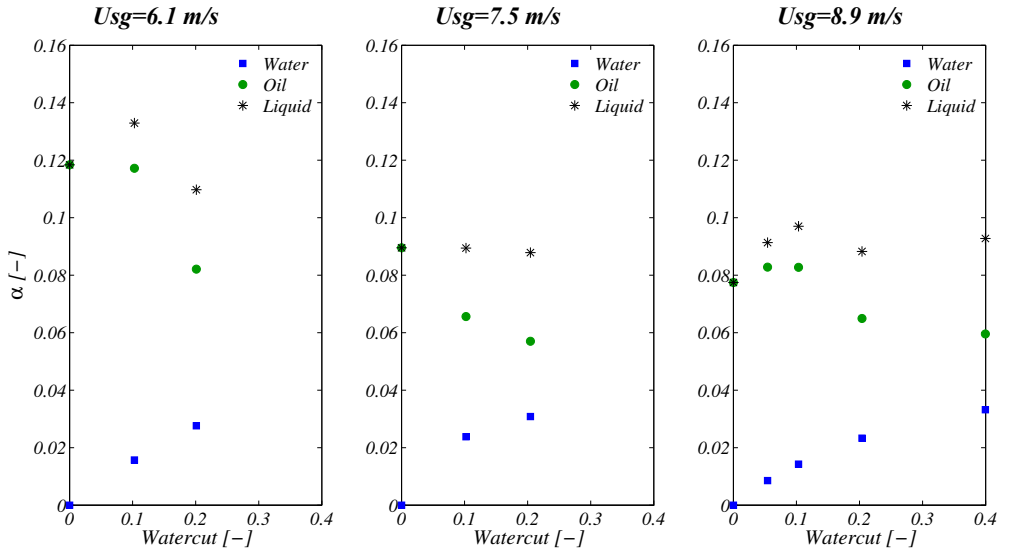


Figure 4.10: Oil, water and liquid phase fraction for Exxsol D80-water and gas at Usl=0.2 m/s

The phase fraction profiles obtained when using the Mixed oil as an oil phase ($P$=4.3 bara) are shown in Figure 4.11. Similar to the results using Nexbase as an oil phase, there is a reduction on the liquid holdup of the three-phase flow cases in comparison to the two-phase flow case. There is a redistribution of the oil and water phases inside the liquid layer when increasing the input watercut value. A reduction on the oil fraction and an increment on the water fraction as the watercut value rises are observed. Similar to the previous results, the in-situ water cut is in most cases larger than the input water cut.

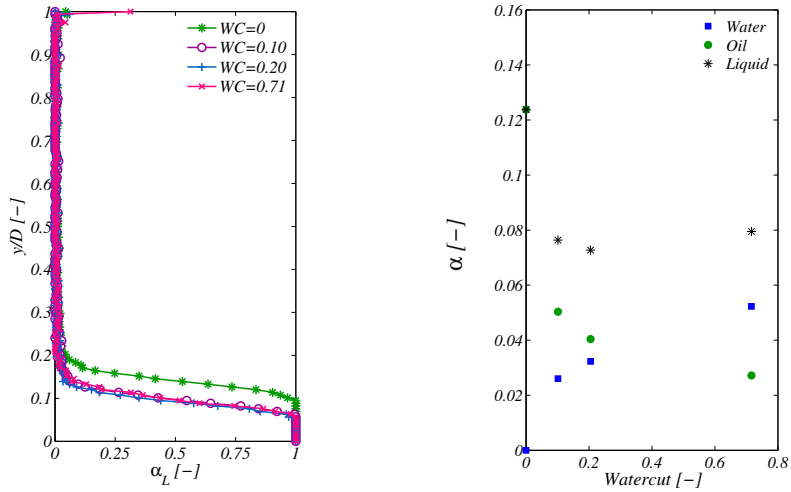


Figure 4.11: Liquid phase fraction for Mixed oil-water and gas at Usl=0.25 m/s, Usg=6.6 m/s

## 4.5 Gas-liquid interface

The gas-liquid interface height $h_w$ is a parameter required in the integration of the measured liquid droplet flux (See Chapter 6). Due to the wavy interface, a proper selection of its location will be uncertain. For the integration purposes, $h_w$ should be selected in the location just above the largest observed wave. For this reason different strategies were followed: First a scale was attached to the outer pipe diameter on the clear section. Using the high speed videos and direct visual observations the interface can be located. Second, the interface location can be obtained from the measured gamma profiles. The first guess was to select the interface at $\alpha_L$=0.5. In this case, the entrainment fraction is overestimated as it includes the wavy region. It was decided to assumed that the maximum top wave will occur when the liquid fraction in the pipe was set to $\alpha_L$=0.05. A summary of the gas-liquid interface height $h_w$ measured from the pipe bottom and using the approaches explained before is shown in Table 4.2and Table 4.3. For each set of *Usl* and *Usg and* a specific *hw* estimation methodology, the liquid height keeps relatively constant with the variation of the watercut value.

Table 4.2: Gas liquid interface height. Mixed oil-water-$SF_6$

| ***Fluids*** | ***Pressure (bar)*** | ***Usl (m/s)*** | ***Usg (m/s)*** | ***WC (%)*** | ***$h_w$ (mm)*** | | |
|---|---|---|---|---|---|---|---|
| | | | | | ***Visual*** | ***Gamma*** $\alpha_L$=*0.5* | ***Gamma*** $\alpha_L$=*0.05* |
| *(MO/W/SF6) Mixed oil Water SF6* | *4.3* | *0.1* | *6.6* | *0* | *13.7* | *11.97* | *16.27* |
| | | | | *0.1* | *14.0* | *6.92* | *10.85* |
| | | | | *0.21* | *13.3* | *6.56* | *9.51* |
| | | | | *0.72* | *13.1* | *5.85* | *11.30* |

Table 4.3: Gas liquid interface height. Exxsol D80 -water-$SF_6$

| *Fluids* | *Pressure (bar)* | *Usl (m/s)* | *Usg (m/s)* | *WC (%)* | $h_w$ *(mm)* | | |
|---|---|---|---|---|---|---|---|
| | | | | | *Visual* | *Gamma* $\alpha_L$=*0.5* | *Gamma* $\alpha_L$=*0.05* |
| *(E80/W/SF6) Exxsol D80 Water $SF_6$* | *4.7* | *0.1* | *8.8* | *0* | *15.3* | *5.68* | *10.69* |
| | | | | *0.2* | *15.3* | *5.69* | *9.24* |
| | | | | *0.8* | *14.5* | *4.70* | *10.33* |
| | | *0.2* | *6.1* | *0* | *22.6* | *11.11* | *17.94* |
| | | | | *0.05* | *24.4* | - | - |
| | | | | *0.1* | *21.8* | *10.94* | *18.48* |
| | | | | *0.2* | *27.1* | *9.82* | *18.96* |
| | | | *7.5* | *0* | *22.4* | *9.74* | *16.13* |
| | | | | *0.1* | *24.4* | *9.34* | *15.91* |
| | | | | *0.2* | *24.4* | *9.21* | *14.99* |
| | | | *8.9* | *0* | *21.2* | *8.12* | *16.04* |
| | | | | *0.05* | *23.8* | *8.05* | *16.08* |
| | | | | *0.1* | *22.9* | *8.38* | *16.24* |
| | | | | *0.2* | *21.2* | *8.71* | *15.35* |
| | | | | *0.4* | *22.4* | *8.21* | *13.62* |

As mentioned before, the droplet sampling probe was not available for experiments using Nexbase 3080. However some interesting and relevant information was observed and comments about it are made below.

From the high speed videos, the thick liquid layer height seems to increase (See Figure 4.12) while the *Usg* value rises from 5.3 m/s to 8 m/s and later to 10.7 m/s being contradictory to previous studies (Paras and Karabelas (1991); Williams. et al. (1996); among others). However from the gamma densitometer measurements it is verified that the layer decreases with the increment of *Usg*. A possible explanation for this behavior might be the existence of a curved gas-liquid interface. Curved gas-liquid interfaces are commonly reported for small diameters (less than 0.05 m), low viscosity liquids or low-liquid loading gas-liquid stratified and annular flow (Hart et al. (1989); Chen et al. (1997); Meng et al. (2001); Vlachos (2003); Tzotzi et al. (2011). For high liquid holdups, there is not much experimental evidence of this phenomenon as in gravity dominated systems the liquid surface tends to be flat (Gorelik et al. (1999)). The oil viscosity and surface tension in this case help the oil to climb up the pipe wall.

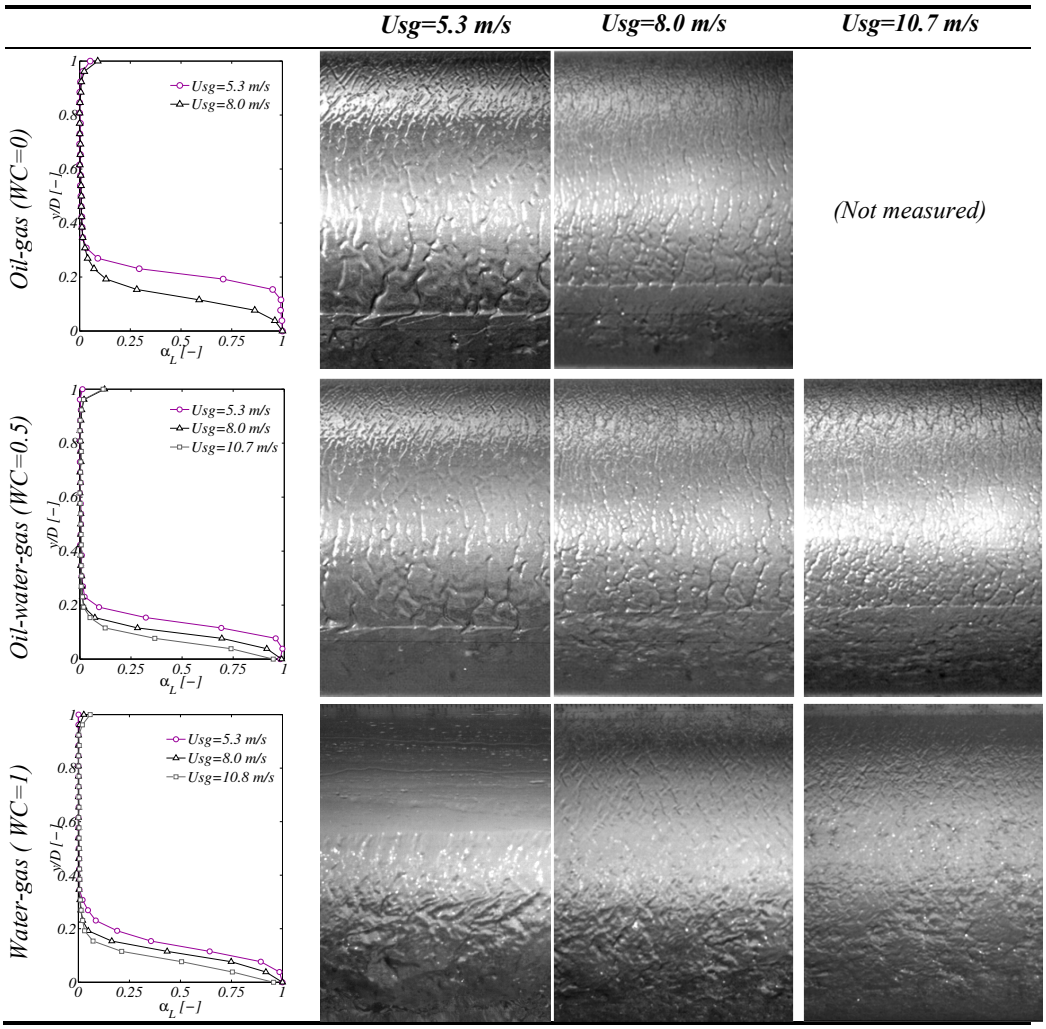


Figure 4.12: Pictures from high speed videos. Oil=Nexbase 3080(100 cP) 7 bara, Usl=0.2 m/s.WC=0.5

## 4.6 Axial pressure drop

The pressure gradient at different watercuts for all the studied fluid systems and operational conditions are shown in Figure 4.13 for all the studied cases from Table 4.1. The pressure gradient increases with the superficial gas velocity for a constant watercut and superficial liquid velocity. For the cases using Nexbase 3080 as the oil phase the three phase pressure gradient (*WC*=0.5) is in between the value for an oil-gas (*WC*=0) and water-gas system (*WC*=1). For the Mixed oil case it was observed a slight increment on the pressure drop at 0.7 watercut. More experiments are needed to confirm this trend. For the Exxsol D80 cases the pressure gradient remains relatively constant for the studied watercuts up to 0.4. There is an increment on the pressure gradient for *WC*=0.7 and *Usl*=0.1 m/s, *Usg*= 8.8 m/s. This increment is caused by the

dispersions formed by the oil-water mixture as shown in the picture on Figure 6.6 in Chapter 6. Comparisons between the experimental data and predictions from models in the literature and commercial a flow simulator was shown in Shmueli et al. (2012) (See Paper I). The uncertainty was estimated using the methodology shown in Appendix A. Using this methodology the maximum and average errors in the pressure gradient were 8 Pa/m and 4 Pa/m respectively.

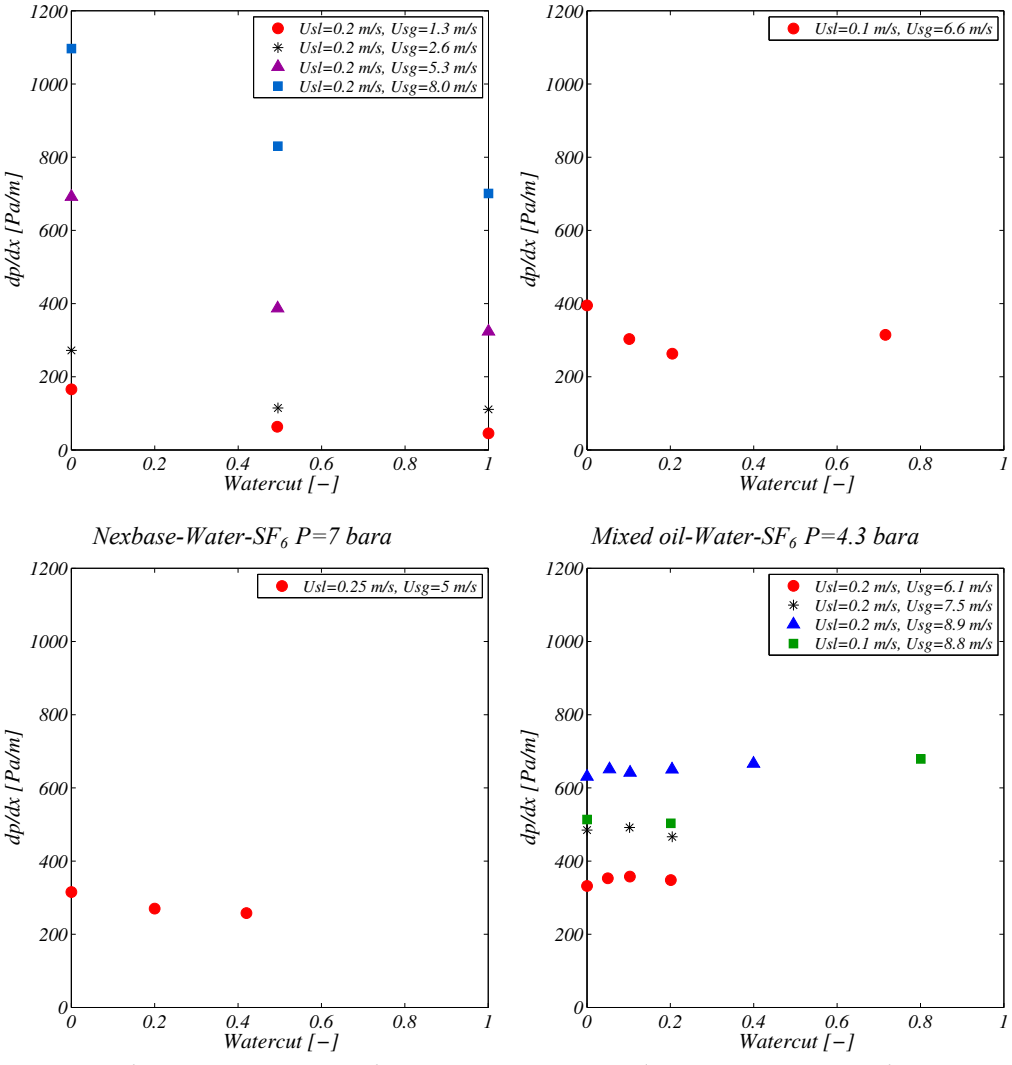


*Nexbase-Water-$SF_6$ P=7 bara*

*Mixed oil-Water-$SF_6$ P=4.3 bara*

*Exxsol D80-Water-$SF_6$ P=7.7 bara*

*Exxsol D80-Water-$SF_6$ P=4.5 bara*

Figure 4.13: Pressure drop vs. Water cut at a constant Usl=0.2 m/s

## 4.7 Summary

In this chapter the experimental data obtained for flow regime maps, phase fraction profiles, liquid layer heights and pressure gradients in horizontal three phase flows were presented. The test matrix was limited by the loop access.

For the high viscous oil used it was shown that there is oil deficiency in the liquid layer compared to water for a case with WC=0.5. This might be due to increased oil entrainment in the gas phase when the superficial gas velocity is increased. The three-phase ($WC$=0.5) liquid layer decreases from $WC$=0 to $WC$=1, especially at low gas velocities. However, for low viscous systems, the liquid layer height relatively constant for fixed values of the superficial liquid and gas velocities and varying the watercut meaning that the oil and water phases redistribute inside the mixed liquid layer.

At the studied conditions the pressure gradient decreases systematically with the increase of the watercut for all the gas velocities and for the high viscosity oil. There are no significant differences on the pressure gradient measurements for the low viscous system at the studied conditions.

For low viscosity oils and high gas velocities, the holdup profiles are quite independent on the watercut. The three-phase pressure drop values are, for most cases, quite independent on the watercut.

For the viscous oils, the holdup profile with pure gas-oil shows higher values than for the three-phase profiles, which are again quite independent on the watercut. The oil and water holdup profiles show water accumulation with respect of no-slip conditions. This is due to more oil than water being entrained as droplets into the gas core. The three-phase pressure drop values are in between the gas-oil and gas-water values. For the viscous oils, when comparing visual liquid heights with holdup measurements, there are indications that the shape of the gas-liquid interface may be curved.

# Chapter 5

## Gas velocity profiles in stratified-annular three-phase horizontal flow

Measurements of the vertical and cross sectional gas velocity were carried out for stratified/annular gas-oil and gas-oil-water flows under high pressure conditions. Exxsol D80, water and a dense gas ($SF_6$) were used as fluids in the experiments. Secondary flows were observed for all tested conditions. The addition of water modifies the distribution of droplets inside the pipe caused by a modification of the secondary flows nature in the gas core.

### 5.1 Introduction

The study of the droplet characteristics in stratified-annular flows is essential for designing and calibrating flow models. The gas velocity profiles gives information about the distribution effects on the pipe cross section. In horizontal gas-liquid separated flows, observations indicate an asymmetry of the liquid film and a non-uniform entrained droplet concentration distribution along the vertical axis. (See Williams. et al. (1996); Tayebi et al. (2000), experiments in Chapter 6). The existence of a liquid film on the pipe wall may be due to a combination of several flow effects. Van't Westende et al. (2007) listed possible involved mechanisms such as entrainment and deposition of droplets, surface tension effects (mainly for small pipe diameters), wave-spreading where liquid from the layer climbs-up to the pipe walls and secondary flows in the gas core. Secondary flows are counter rotating cells which contribute to drag the liquid in the spanwise direction, towards the pipe top (See Figure 5.1).

The existence of secondary flows has been proven in the past by experimental measurements by Darling et al. (1968); Flores et al. (1995); Williams. et al. (1996); Dykhno et al. (1994). Secondary flows are promoted by the non-uniform pipe roughness product of the non-uniform liquid film between the pipe wall and the gas-liquid interface (See Flores et al. (1995); Belt (2007)) and the non-uniform droplet concentration distribution along the vertical axis due to gravity.

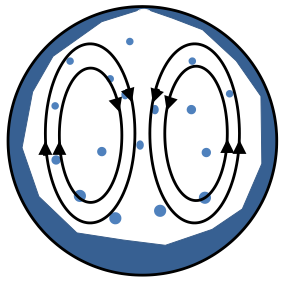

Figure 5.1. Illustration of secondary flow in the gas core

Belt (2007) suggested that secondary flows occur due to an anisotropy in the Reynolds stress tensor in the pipe cross section. This anisotropy is caused either by the effect of a non-circular geometry or due to a non-uniform wall roughness effect. He suggested that two effects can be present in the gas core depending on the distribution of the liquid film:

- Roughness effect: The non-uniform pipe roughness product of the non-uniform liquid film between the pipe wall and the gas-liquid interface cause higher tangential stresses on the bottom of the pipe than in the top promoting an upwards gas flow along the pipe wall. The maximum mean axial velocity is shifted to the bottom compared to a single-phase flow case (See Figure 5.2a)
- Blockage effect: Particles far from the pipe wall and close to the gas-liquid interface can block the flow. In this case the tangential stresses are larger on the top of the pipe than on the bottom promoting a downwards gas flow. The maximum mean axial velocity is shifted to the top compared to a single-phase flow case. See Figure 5.2b)

These two effects can often be combined and obtaining in some cases two secondary flow cells which are symmetric with respect to the vertical pipe axis See Figure 5.2c). Van 'T Westende (2007) conducted numerical simulations using LES and concluded that secondary flows help to increase the droplet concentration in the gas core and the deposition rate in the pipe top. In his simulations the particle concentration distribution was not uniform on the pipe cross section and he attributed it to the presence of secondary flows.

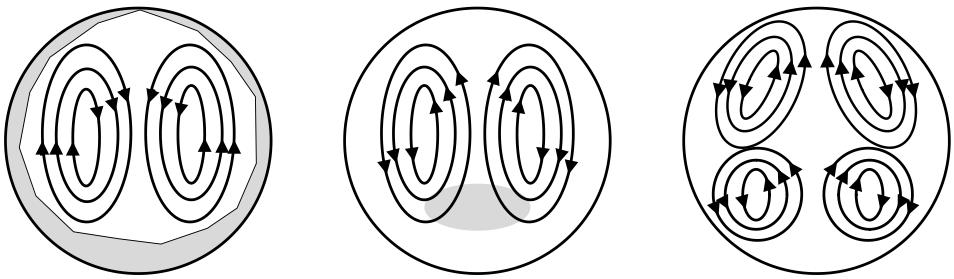

(a) Roughness effect (b) Blockage effect (c) Combined effect

Figure 5.2. Effects that promotes secondary flows within the gas core in a horizontal pipe

In oil, water and gas flows, the presence of a second liquid phase can modify the behavior of the flow characteristics (as shown in Chapter 4). At certain flow conditions, adding water to a two-phase oil-gas system can diminish the liquid film at the wall or it can reduce the liquid droplet entrainment (See Shmueli et al. (2012)). The effect of the added water on the behavior of secondary flows is also unknown. The current study provides some experimental data on gas velocity profiles in stratified-annular three-phase pipe flow and aimed to analyze the effect of the added water on the velocity profiles of a two-phase gas-liquid system.

## 5.2 Experimental conditions

The experiments were performed using the experimental setup explained in Chapter 2. The experiments were carried out by starting from two-phase flow (oil-gas) system and then adding water at a constant liquid and gas superficial velocity. Gas velocity measurements were performed along the vertical diameter and over the pipe cross section. The watercut for the water-oil mixture is calculated as the relation of the water superficial velocity to the liquid velocity. The gas-liquid interface is determined using a two-energy gamma densitometer and following the procedure explained in Chapter 4. A summary of the tested flow conditions is shown in Table 5.1.

Table 5.1: Experimental tested conditions

| *Fluid* | *Pressure [bar]* | *$\rho_g$ [Kg/m$^3$]* | *Usl [m/s]* | *Uso [m/s]* | *Usw [m/s]* | *Usg [m/s]* | *WC [-]* | *Case* | *Sampling Type* |
|---|---|---|---|---|---|---|---|---|---|
| *(E80/W/SF6) Exxsol D80 Water SF6* | *4.3* | *25.8* | *0.1* | *0.1* | *0* | *8.8* | *0* | *1* | *1D* |
| | | | | *0.08* | *0.02* | | *0.2* | *2* | |
| | | | | *0.02* | *0.08* | | *0.8* | *3* | |
| | *4.5* | *26.8* | *0.2* | *0.2* | *0* | *6.1* | *0* | *4* | *1D/2D* |
| | | | | *0.19* | *0.01* | | *0.05* | *5* | *1D* |
| | | | | *0.18* | *0.02* | | *0.1* | *6* | *1D/2D* |
| | | | | *0.16* | *0.04* | | *0.2* | *7* | |
| | | | | *0.2* | *0* | *7.5* | *0* | *8* | *1D/2D* |
| | | | | *0.18* | *0.02* | | *0.1* | *9* | |
| | | | | *0.16* | *0.04* | | *0.2* | *10* | |
| | | | | *0.2* | *0* | *8.9* | *0* | *11* | *1D/2D* |
| | | | | *0.19* | *0.01* | | *0.05* | *12* | *1D* |
| | | | | *0.18* | *0.02* | | *0.1* | *13* | *1D/2D* |
| | | | | *0.16* | *0.04* | | *0.2* | *14* | |
| | | | | *0.12* | *0.08* | | *0.4* | *15* | *1D* |

## 5.3 Results

On Figure 5.3 the vertical gas velocity profiles for the tested cases are shown. Each plot corresponds to a constant gas and liquid superficial velocity and different watercut values. The profiles are plotted against the distance from the gas-liquid interface to the top of the pipe $y_{hw}$. Where the interface height $h_w$ are summarized in Table 4.3. The tested conditions shown on the plots correspond to stratified flow with atomization to stratified-annular flow. For the studied

cases, the addition of water as a third phase does not show a significant effect on the on the mean gas velocity profiles in shape or magnitude. Small differences are noted between the vertical profiles. However, these differences are mainly within the magnitude of the measurement error (See Appendix A). Reducing the superficial liquid velocity to *Usl*=0.1 m/s gives the same trends. The shape or magnitude of the vertical velocity profiles are not affected by the water addition even for the largest tested watercut value (*WC*=0.8). For all the cases the maximum of the velocity profile is found to be close to the center of the of the gas area.

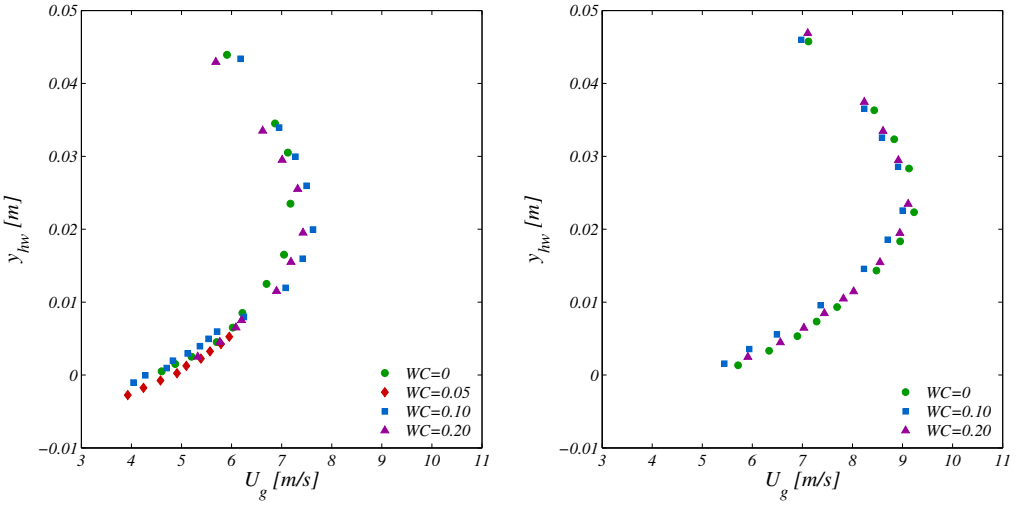


a.Usl=0.2 m/s, Usg=6.1 m/s

b.Usl=0.2 m/s, Usg=7.5 m/s

c.Usl=0.2 m/s, Usg=8.9 m/s

d.Usl=0.1 m/s, Usg=8.8 m/s

Figure 5.3: Gas velocity profiles. Oil: Exxsol D80.

The gas velocity was measured on the pipe cross section for cases 4,6-11,13-14 (See Table 5.1). To generate the gas velocity contour plots, a boundary condition on the gas-liquid interface was

imposed if the velocity value was not measured. In this case, the waves celerity at the gas-liquid interface, using Kumar et al. (2002) model, Equation (5.1) was used. The velocity values outside the measured boundaries (pipe wall) were interpolated between the measured and an imposed zero velocity condition on the pipe wall above the liquid film.

$$U_{waves} = \frac{\Psi \cdot U_{sg} + U_{sl}}{\Psi + 1} \tag{5.1}$$

Where

$$\Psi = 5.5 \cdot \left( \frac{\mathrm{Re}_{sl}}{\mathrm{Re}_{sg}} \right)^{0.25} \cdot \sqrt{\frac{\rho_g}{\rho_L}} \tag{5.2}$$

The oil-water liquid layer in three-phase flow experiments was assumed to be mixed (and confirmed by the phase fraction profiles and visual observations). For this reason mixture properties of oil and water where used. The viscosity of the liquid mixture was considered as the continuous phase viscosity.

The velocity contours are shown for constant watercut and each tested superficial gas velocities are shown in Figure 5.4 and Figure 5.5. The velocity values are normalized by the maximum velocity. All the sampled points are shown as a red cross on the plots. The gas-liquid interface is shown as a dotted black line and the white dotted line represents the condition for *U(y)/Umax*=0.98.

For *WC*=0, the flow pattern is stratified-annular flow for all the tested gas velocities. For all the conditions the maximum velocity is found around *y/D*≈0.6. As the gas superficial velocity increases the liquid layer height at the pipe bottom decreases suggesting a slight upward shifting of the maximum velocity value, which is in accordance to the measurements of Dykhno et al. (1994) and the simulations from Van 'T Westende (2007). There is a small deflection on the velocity profile towards the pipe centre and on the region close to the gas-liquid interface. This deflection accentuates when increasing the superficial gas velocity to 8.9 m/s.

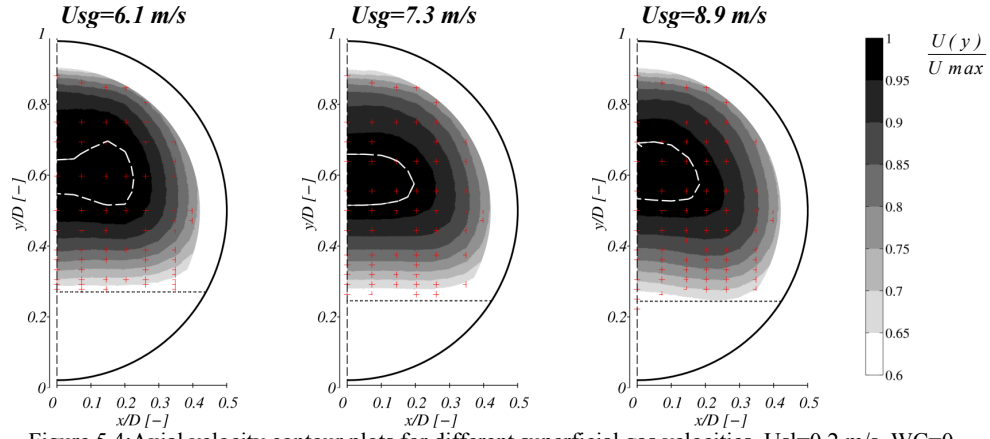


Figure 5.4:Axial velocity contour plots for different superficial gas velocities. Usl=0.2 m/s, WC=0

The deflection of the velocity profiles in the bottom area close to the gas-liquid interface is related to the redistribution of the liquid droplets entrained in the gas core. As the gas velocity increases, more liquid droplets are entrained. The effect of more droplets travelling close to the gas-liquid interface is to block the mean flow reducing the Reynolds stresses in the bottom in comparison to the top of the pipe and creating a blockage effect, (Belt, 2007), Van 'T Westende (2007)).

The results for watercut values of 0.1 and 0.2 are shown in Figure 5.5. The addition of water at the lowest gas velocity (6.1 m/s) has a small effect on the velocity contour shape. This behaviour is expected for the watercut value 0.1 as the oil and water droplet distribution is not strongly affected by the addition of water (See Chapter 6). On the contrary, a change on the velocity profile was expected for *WC*=0.2. In this case, the film on the top is not sustained, meaning that the droplet deposition rate and the strength of the secondary flows are not enough to promote the deposition of particles. For higher velocity values a deflection in the bottom region is found for both watercuts studied. This is in agreement with the observed increment of the droplets close to the interface (See Chapter 6).

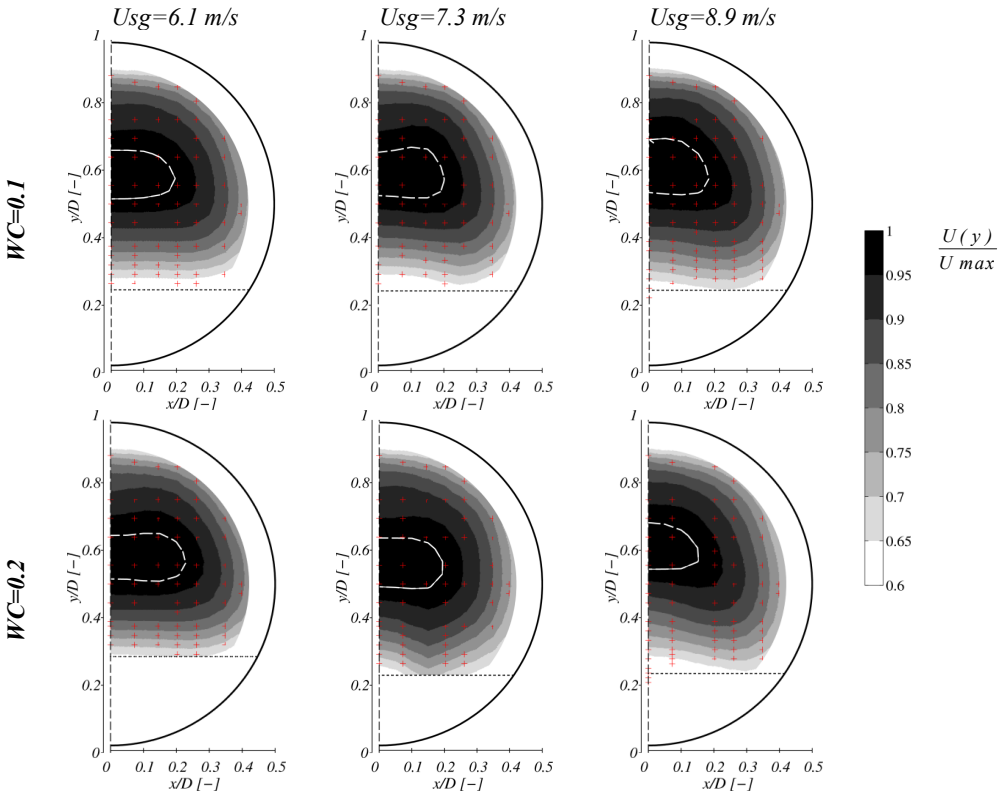


Figure 5.5: Axial velocity contour plots for different superficial gas velocities. Usl=0.2 m/s.

## 5.4 Summary

Gas velocities profiles have been measured in stratified three-phase flows, under conditions were droplet entrainment exists. A sampling probe was used under isokinetic conditions to measure the gas velocity profiles on the pipe cross section. Even for high entrainment conditions, the maximum of the velocity profiles were observed to be close to the centre of the gas area.

Along the interface the gas velocity profile is deflected with lower values towards the pipe wall, indicating secondary flows.

The deflection increases with increasing the gas velocity. For the tested watercut values, the gas velocity profiles are not sensitive to the input watercut.

# Chapter 6

## Oil and water droplet flux distribution in horizontal gas-liquid-liquid flows

*This chapter will be submitted for publication in Int. J. Multiphase Flow and has been partially published at Proc. 8th North American Conference on Multiphase flow. BHR Group*

Water and oil droplet fluxes have been measured along the vertical diameter and on the cross section of a 0.07 m horizontal pipe using an isokinetic probe. Stratified-annular gas-oil and gas-oil-water flows under high pressure conditions were established using Exxsol D80, a more viscous oil, water and a heavy gas ($SF_6$) to simulate high pressure flows. The entrainment of water and oil droplets depends on the global watercut of the liquid mixture. The droplets on the pipe cross section are non-uniformly distributed. Neglecting the non-uniformity of the droplet distribution can give differences up to 40% on the total entrained fraction. The effect of the water addition to an oil-gas system on the total entrained fraction is negligible for the studied flow conditions.

### 6.1 Introduction

Gas-liquid flows are very common in the industry and in many cases the liquid phase is hydrocarbons and water. The droplet entrainment fraction in the gas phase and the pressure drop in the pipeline are important variables to predict when designing multiphase flow lines and equipment.

In separated flows, droplets can be entrained from the liquid layer and transported as a droplet field in the gas phase. There are two major flow effects resulting from an entrained droplet field in the gas phase. The droplet flow can represent a very large fraction of the liquid transport. Even when the entrained fraction is low, the presence of droplets can be important because droplets cause wall wetting and thus contribute to increased pressure drop.

It is common practice to use 1D flow models to describe the behavior of multiphase flow. These models require closure relationships related to the droplet field. These relationships are usually obtained from experimental measurements under controlled operating conditions. Most of the reported experimental work in the past has been made using water and air at atmospheric

pressure. All of these previous studies provide important information about liquid droplets entrainment. However there is still a lack of experimental data in three phase flow and at high pressures and large diameters. A summary of the available data in the literature is shown in Table 6.1.

Table 6.1: Summary of experimental data in droplet entrainment in horizontal flows

| ***Author*** | ***Measurement technique*** | ***Fluids*** | ***D [cm]*** | ***Usg [m/s]*** | ***WL [kg/s]*** | ***WC [-]*** | ***$\rho_g$ [Kg/m3]*** |
|---|---|---|---|---|---|---|---|
| *Dallman (1978)* | *Film withdrawal (Porous section)* | *Air-Water* | *2.31* | *15-88* | *0.003–0.250* | *1* | *1.26–2.75* |
| *Laurinat (1982)* | *Film withdrawal (Porous section)* | *Air-Water* | *5.08* | *11-131* | *0.033–0.970* | *1* | *2.05* |
| *Williams (1986 & 1990)* | *Isokinetic Sampling* | *Air-Water* | *9.53* | *26-88* | *0.12–0.86* | *1* | *1.3–1.85* |
| *Paras & Karabelas (1991)* | *Isokinetic Sampling* | *Air-Water* | *5.08* | *31-66* | *0.04–0.39* | *1* | *1.3–2.3* |
| *Tayebi (2000)* | *Isokinetic Sampling* | *SF6-Water SF6-Exxsol D80* | *10* | *3.5-7* | *1.96* | *0/1* | *22-47* |
| *Mantilla (2008)* | *Film withdrawal (Porous section)* | *Air-Water Air-Water/Butanol Air-Water/Glycerin* | *5.08* | *20-80* | *0.0035-0.1* | *1* | *100* |
| *Boulesteix (2010)* | *High speed camera* | *Air-Water* | *5* | *4.5-30* | *0.04-1.38* | *1* | *1.18-1.23* |
| *Skartlien (2011)* | *Isokinetic Sampling* | *SF6-Water-ExxsolD80* | *10* | *5-9.5* | *0.031-3.275* | *5/0.2/0.4/0.6* | *54* |
| *Kjølaas et al (2011)* | *Isokinetic Sampling* | *Naphta-Nitrogen* | *20.32* | *3.03-10.19* | *0.574-4.696* | *0* | *23.4-102.5* |
| *Magrini et al (2012)* | *Isokinetic Sampling/ Film withdrawal (Porous section)* | *Air- water* | *7.62* | *40-80* | *0.016-0182* | *1* | *1.2* |
| *Gawas (2013)* | *Isokinetic Sampling* | *Air- Isopar LTM-Water* | *15* | *1.93-2.02* | *0.13-0.35* | *0/0.1/0.2/0.4/1/* | *23.4-102.5* |

Dallman (1978) studied the liquid entrainment in annular air-water flow in horizontal and vertical pipes. He performed measurements in a horizontal pipeline 2.54 cm in diameter, collected data from the literature and proposed models for the entrainment fraction in fully developed flows for vertical and horizontal systems. To measure the entrainment fraction he used a porous section of a pipe to withdrawn the liquid film on the walls and also a pitot-type sampling probe. Good agreement was obtained for the entrainment fraction with both techniques (5%).

The results obtained by Dallman (1978) indicate that the entrained fraction is negligible if the gas velocity is below a critical value for initiation of atomization. However if the gas velocity exceeded the threshold value for atomization the entrainment fraction increases with the third power of the gas velocity. The entrainment value would typically reach a maximum and then change less with increasing the gas velocity.

The effect of the pipe size on entrainment in horizontal pipes was studied first by Laurinat (1982) and afterwards by Williams (1990). In his research, Laurinat (1982) used a similar setup and flow conditions as Dallman (1978) but using a 5.08 cm I.D pipe. He withdrew the wall film through a porous pipe section to measure the entrained droplet flux. He compared the pressure drop, film thickness and entrainment fraction measurements with the results obtained by Dallman (1978) and correlated the results using a modified form of the correlation developed by Dallman (1978).

The test facility used by Dallman (1978) and Laurinat (1982) was modified by Williams (1990). The local entrained droplet flux was measured using an isokinetic sampling probe. The probe module he designed was able to sample droplets in different locations of the pipe cross section. He studied the effect of the sampling tube diameter on the measured droplet flux showing that there was not a big difference on the results. As a main conclusion of his work, he found that increasing the pipe diameter in horizontal annular flows will change the droplet concentration distribution and liquid film considerably. He pointed out that the entrainment fraction correlations developed in small diameter pipes will over predict the entrainment fraction in large diameter pipes. Williams et al. (1996) studied the effect of the pipe diameter in horizontal annular flow. He measured the local liquid droplet flux in the gas core using a sampling probe in a 9.53 cm i.d horizontal pipe using air and water at atmospheric conditions. The test section was constructed from a Plexiglas pipe. He found that when increasing the pipe diameter at a constant gas velocity, the distribution of the liquid film around the pipe will become more symmetric. Comparing the entrainment fraction results with previous data from literature they did not found a significant effect of the pipe diameter, contrary to his previous work.

Mantilla (2008) carried out measurements in stratified and annular flow in a 2-inch and 6-inch diameter flow loop, to estimate the entrainment fraction a liquid film extractor was used. The working fluids were air-water-butanol and air-water-glycerin. Additionally he developed a mechanistic model to predict the entrainment fraction in horizontal gas-liquid systems.

Boulesteix (2010) used visual techniques to describe the atomization mechanisms in stratified and annular air-water flow at atmospheric conditions. In addition he measured the local droplet flux, diameters and velocity.

The pressure effect on the liquid droplet entrainment fraction has been studied by Tayebi et al (2000). The experiments were performed using a high density gas ($SF_6$) at moderate pressures to simulate pressure conditions closer to the real transport conditions. The local droplet flux was measured using an isokinetic sampling probe. He explained that the liquid flux distribution along the vertical axis above the film behaves as an exponential function. The experiments were performed using water and Exxsol D80 as liquid phases to study the effect of the surface tension.

Skartlien et al. (2011) used the same configuration as Tayebi et al. (2000) to measure the local flux of droplets across the vertical diameter. They developed a 1D cross sectional droplet concentration profile model and suggested that that the entrainment phenomena in three phase flows is controlled by the dominant liquid in the system.

Azzopardi (1997) and Boulesteix (2010) summarize all the experimental techniques that has been used to measure liquid droplet entrainment in stratified flow with atomization and annular flow.

There are a limited number of experiments of the droplet entrainment over the entire pipe cross-section. Paras and Karabelas (1991) found the liquid droplet entrainment to be fairly constant along the horizontal axis for low liquid rates. However there were no uniformities of the droplet concentration distribution at high liquid rates and the authors attribute this to the measuring technique uncertainty. Williams et al (1996) studied two cases: stratified flow with dry top wall and stratified-annular flow. On his cross section measurements he found non uniformities along the horizontal direction in the droplet concentration profiles. He proposed that this could be caused by the effect of secondary flows, which in their study will appear when the concentration of droplets was high. This fact is consistent with the observations from Van 'T Westende (2007) who states that the existence of secondary flows in the gas core of stratified-annular flow can modify the droplet distribution and its deposition on the wall. Belt (2007) stated that an anisotropy of the Reynolds stress tensor will modify the pattern of the secondary flow. This anisotropy is caused either by the effect of a non-circular geometry, non-uniform particles distribution or due to a non-uniform wall roughness effect. The particle distribution can promote a blockage effect when they are far from the pipe wall and a roughness effect when they are close to the pipe wall and can act on the viscous stresses. A more detailed explanation about secondary flows has been given in Chapter 5.

The uniformity of the droplet flux and droplet concentration distribution over the pipe cross section is one assumption in most of the current models and no proper validation has been done to confirm if the droplet distribution can be considerable when calculating the total liquid entrained.

The objectives of this Chapter are to describe the effect of the addition of a second liquid phase on the total liquid entrainment fraction, to quantify and understand cross sectional distributions

effects and estimate and quantify the differences associated in the total liquid entrained calculations when the cross section droplet flux distribution in the pipe is not considered in the integration.

## 6.2 Experimental conditions

The experiments were performed using the experimental setup explained in detailed in Chapter 2. The experiments were carried out by starting from two-phase flow (oil-gas) system and then adding water at a constant liquid and gas superficial velocity. Isokinetic sampling experiments along the vertical diameter and over the pipe cross section were performed. A summary of the tested flow conditions is shown in Table 6.2. The water cut and superficial liquid velocity are defined as *WC=Usw/Usl, Usl=Usw+Uso* respectively.

Table 6.2: Experimental tested conditions

| ***Fluid*** | ***Pressure [bar]*** | ***Usl [m/s]*** | ***Uso [m/s]*** | ***Usw [m/s]*** | ***Usg [m/s]*** | ***WC [-]*** | ***Case*** | ***Sampling Type*** |
|---|---|---|---|---|---|---|---|---|
| *(E80/W/SF6) Exxsol D80 Water $SF_6$* | *4.7* | *0.1* | *0.1* | *0* | *8.8* | *0* | *1* | *1D* |
| | | | *0.08* | *0.02* | | *0.2* | *2* | |
| | | | *0.02* | *0.08* | | *0.8* | *3* | |
| | | *0.2* | *0.2* | *0* | *6.1* | *0* | *4* | *1D/2D* |
| | | | *0.19* | *0.01* | | *0.05* | *5* | *1D* |
| | | | *0.18* | *0.02* | | *0.1* | *6* | *1D/2D* |
| | | | *0.16* | *0.04* | | *0.2* | *7* | |
| | | | *0.2* | *0* | *7.5* | *0* | *8* | *1D/2D* |
| | | | *0.18* | *0.02* | | *0.1* | *9* | |
| | | | *0.16* | *0.04* | | *0.2* | *10* | |
| | | | *0.2* | *0* | *8.9* | *0* | *11* | *1D/2D* |
| | | | *0.19* | *0.01* | | *0.05* | *12* | *1D* |
| | | | *0.18* | *0.02* | | *0.1* | *13* | *1D/2D* |
| | | | *0.16* | *0.04* | | *0.2* | *14* | |
| | | | *0.12* | *0.08* | | *0.4* | *15* | *1D* |
| *(MO/W/SF6) Mixed oil Water $SF_6$* | *4.3* | *0.1* | *0.1* | *0* | *6.6* | *0* | *16* | *1D* |
| | | | *0.09* | *0.01* | | *0.1* | *17* | |
| | | | *0.08* | *0.02* | | *0.21* | *18* | |
| | | | *0.03* | *0.07* | | *0.72* | *19* | |

## 6.3 Droplet flux

The local droplet flux for each liquid phase "*n*" (*n=o* for oil and *n=w* for water) is defined as

$$F_{LEn}(x,y) = \frac{q_n(x,y)\cdot \rho_n}{A_p} \tag{6.1}$$

Where $q_n(x,y)$ is the sampled volumetric flow rate of phase "$n$" droplets, $\rho_n$ is the density of the phase "$n$" and $A_p$ is the probe cross section opening area. The effect of the gas velocity is shown in Figure 6.1 where the total droplet fluxes vertical profiles are presented for a constant watercut, liquid velocity and fluid properties. The profiles are plotted against the distance from the gas-liquid interface to the top of the pipe $y_{hw}$. Where the interface height $h_w$ values are summarized in Table 4.3The total local droplet local flux is defined by the addition of the water and oil droplet fluxes profiles ($F_{LEo+w}=F_{LEo}+F_{LEw}$). In general for all the studied cases, there is an increment on the water and oil droplet fluxes when the gas velocity increases for all the tested watercuts. This is in line with previous observations from Williams et al. (1996), Paras & Karabelas (1991), Tayebi et al. (2000), among others. The water and oil droplet fluxes are very low and fairly constant in the top of the pipe indicating that gravity does not have a strong effect on the droplet distribution in this pipe region. Williams et al. (1996) attribute this to the droplet size distribution in the pipe where smaller droplets travel on the top and larger ones close to the gas-liquid interface. Measurements of the droplet sizes made by Gawas (2013) in three different pipe locations confirm this hypothesis. An increment in the gas superficial velocity increases the droplet fluxes.

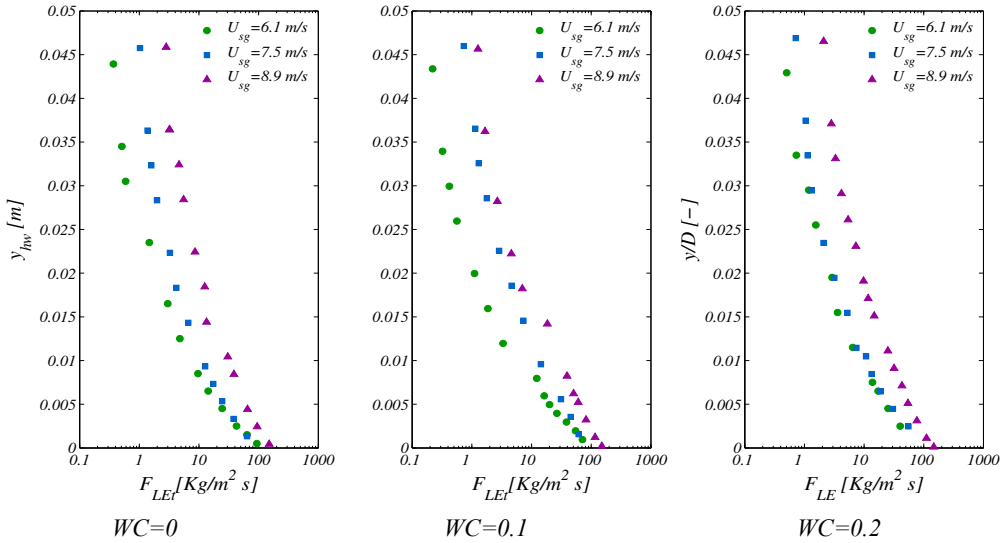


Figure 6.1: Total local droplet flux at constant watercut. Oil: Exxsol D80.

The subsequent results are organized in the following manner: In Figure 6.2a-b to Figure 6.4a-b, the vertical profiles of local water and oil droplet fluxes are shown for a constant superficial gas and liquid velocity and fluid properties and are plotted against the distance $y_{hw}$ from the gas-liquid interface to the top of the pipe. The water and oil droplet fluxes are shown as filled and non-filled markers respectively on the plots. Plots on the right hand side shown the total local

droplet local flux. The contours of water and oil droplets flux are displayed in Figure 6.2c to Figure 6.4c. All the sampled points are displayed as blue crosses on the contour plots. Please note the logarithmic scale on the plots.

Figure 6.2a-b show a comparison of the droplet fluxes for *Usg*=6.1 m/s and watercuts varying from 0 to 0.2 (cases 4-7). For *WC*=0, a continue oil film covering the entire pipe wall was present. Increasing the water cut to 0.05 and gradually to 0.2 yields to an increase on the transported water droplet flux and on a reduction on the liquid wall film thickness especially on the top of the pipe. This behavior was previously reported by Shmueli et al. (2012). At the highest watercut, some droplets were deposited on the top of the pipe and travelling along it. Close to the interface, the oil droplets fluxes are relatively constant between the tested water cuts and decrease to the top of the pipe following an exponential behavior.

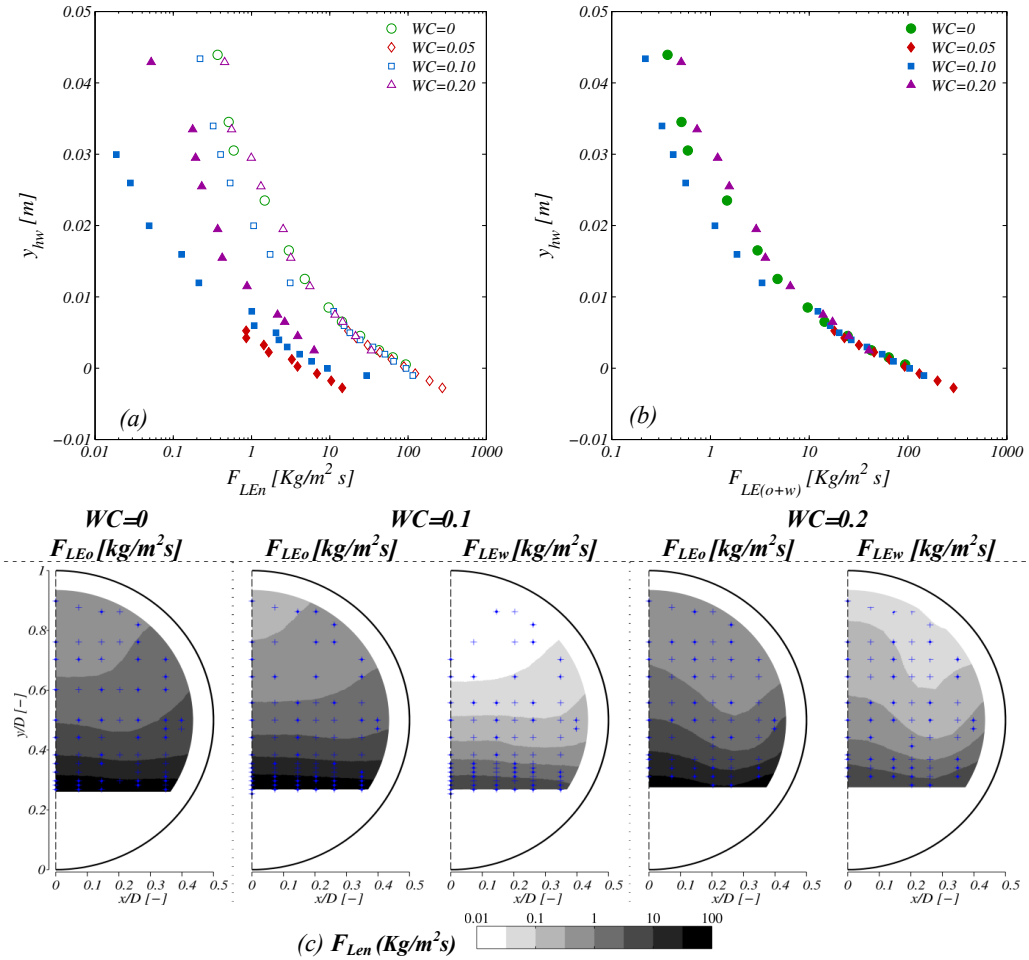


Figure 6.2: (a) 1D- Oil (empty markers) and water (filled markers) local droplet fluxes. (b) 1D-Total local droplet flux. (c) 2D- cross section droplet flux. Usl=0.2 m/s, Usg=6.1 m/s. Oil: Exxsol D80.

The distribution of oil and water droplets over the cross section are fairly uniform for $x/D<0.2$ and $y/D<0.5$ for both $WC=0$ and 0.1 (Figure 6.2c). There is not a significant effect on the cross section droplets flux distribution shape when increasing the watercut to 0.1. These contours give an indication of the presence of secondary flows promoted by roughness. The roughness effect is accentuated when increasing to $WC=0.2$. Increasing the watercut also promotes to get more water droplets which are heavier than oil droplets and they tend to be closer to the interface due to gravity. This creates a blockage effect that combined with the roughness effect generates two secondary flows cells in the gas core. One cell is promoting droplet transport counterclockwise from the pipe wall bottom to the center and a second cell supporting the transport clockwise from the center close to the gas liquid interface to the top of the pipe. Thanks to this effect, both the oil and total droplet flux for this watercut condition is larger than in the top of the pipe.

Increasing the *Usg* to 7.5 m/s shows a similar trend (cases 8-10, see Figure 6.3a-b). For $WC=0$ there is a continuous film on the entire pipe wall and while the watercut value is increasing the film thickness become thinner. However, in this case the film is still existent at $WC=0.2$. The existence of annular-stratified flow at this flow conditions is possible due to the gas velocity. As the gas velocity increases oil and water droplets become smaller after their atomization from the liquid wavy layer. Their transport to the top of the pipe is easier in this case and so it is their deposition on the pipe wall to maintain the liquid wall film. Similar to the lower gas velocity, the vertical oil droplet flux profiles are relatively constant close to the interface and both water and oil droplet fluxes decrease to the top of the pipe following an exponential behavior. The total local droplet flux is very similar between the three watercuts tested at this superficial gas velocity.

On Figure 6.3c, the contour plots have a similar shape for all the tested water cuts and it is a clear presence of at least one secondary flow cell promoted by the roughness effect. There is a small secondary flow cell promoted by particle blockage close to the gas-liquid interface in all the tested conditions. This blockage might exist due to the increment of waves and wave pumping at this gas velocity.

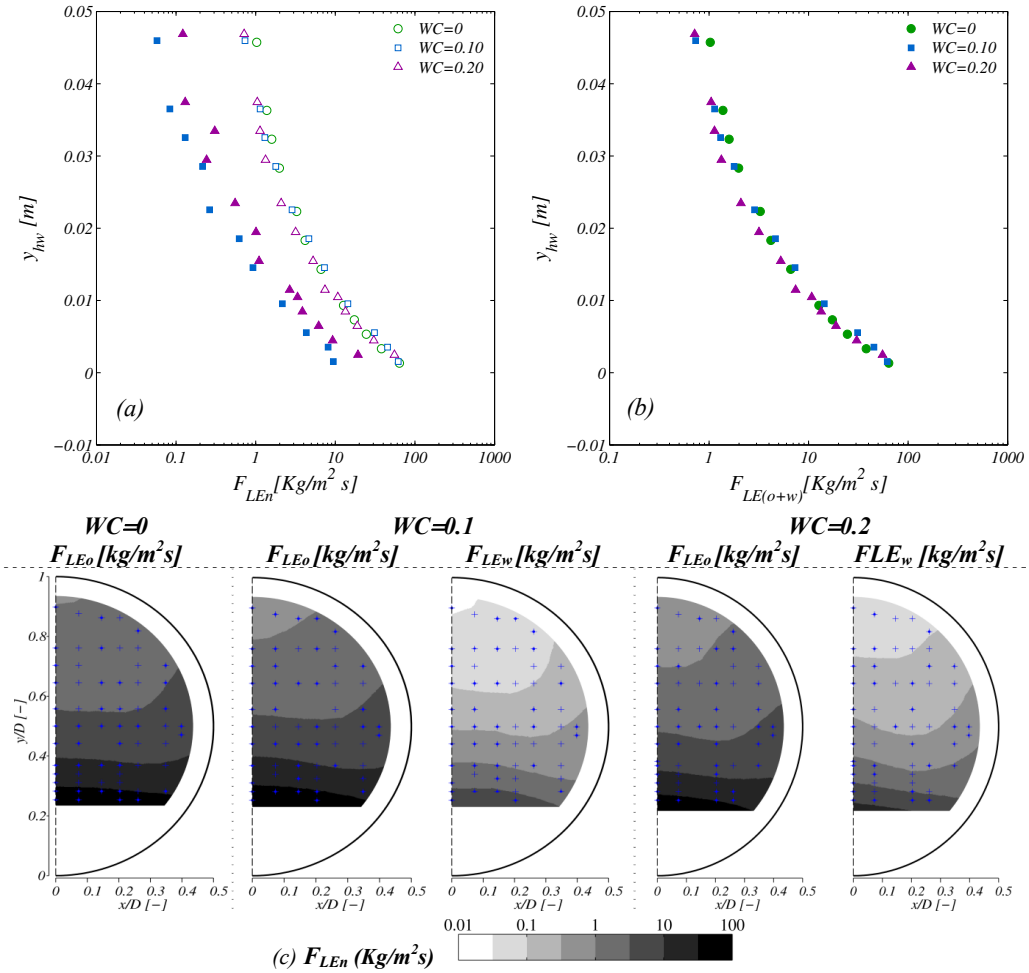


Figure 6.3: (a) 1D-Oil (empty markers) and water (filled markers) local droplet fluxes. (b) Total local droplet flux . (c) 2D- cross section droplet flux. Usl=0.2 m/s, Usg=7.5 m/s. Oil: Exxsol D80.

For the highest gas velocity *Usg*=8.9 m/s (cases 11-15) annular-stratified flow is present for all the watercut values studied at this gas and liquid velocity (See Figure 6.4a). There are not visible differences on the liquid pipe wall thickness when varying the watercut value. As a general trend, the water droplet fluxes increase and oil droplet fluxes decrease in a systematic way to the increment of the watercut value. This is consistent with the observations by Gawas (2013). As the gas superficial velocity increases the droplet flux distribution on the pipe cross close to the gas-liquid interface are less uniform.

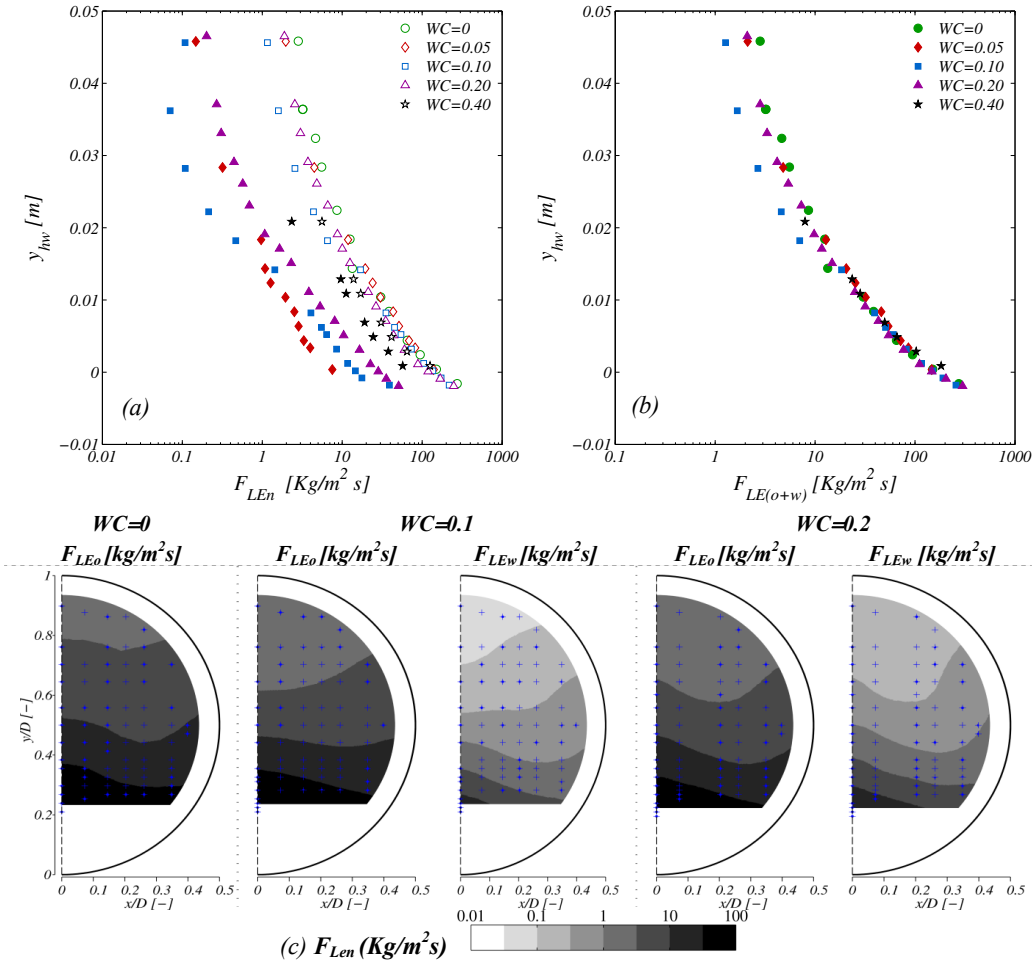


Figure 6.4: (a) 1D-Oil (empty markers) and water (filled markers) local droplet fluxes. (b) Total local droplet flux. (c) 2D- cross section droplet flux. Usl=0.2 m/s, Usg=8.9 m/s. Oil: Exxsol D80.

Stratified -annular flow pattern is still present for all the studied watercut values when reducing the superficial liquid velocity to 0.1 m/s at *Usg*=8.9 m/s. The total droplet flux decreases with decrease in the liquid superficial velocity for all the tested watercuts. This has been previously stated on the studies by Paras & Karabelas (1991), Williams et al. (1996) and Gawas (2013). However, the flow structure changes when the systems goes from oil continuous to water continuous. The liquid layer height decreases and an oil-water emulsion is created and makes the wall film waves to become thicker and having a foamy appearance (See Figure 6.6 ). On the top of the pipe a very thin film is present with some droplets traveling faster than the film itself. Close to the interface there is symmetry between the profiles for *WC*=0.2 and *WC*=0.8.

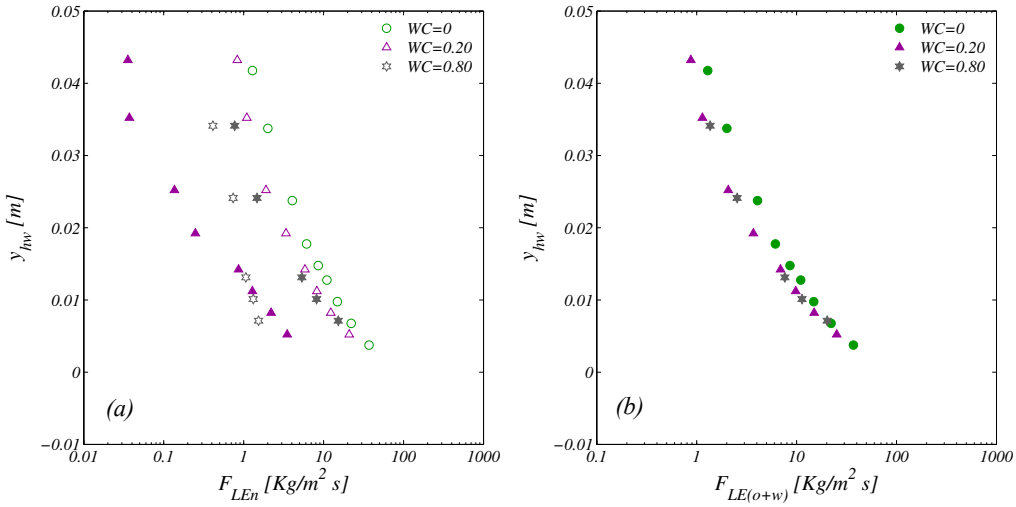


Figure 6.5: (a) Oil (empty markers) and water (filled markers) local droplet fluxes. (b) Total local droplet flux .Usl=0.1 m/s, Usg=8.8 m/s. Oil: Exxsol D80.

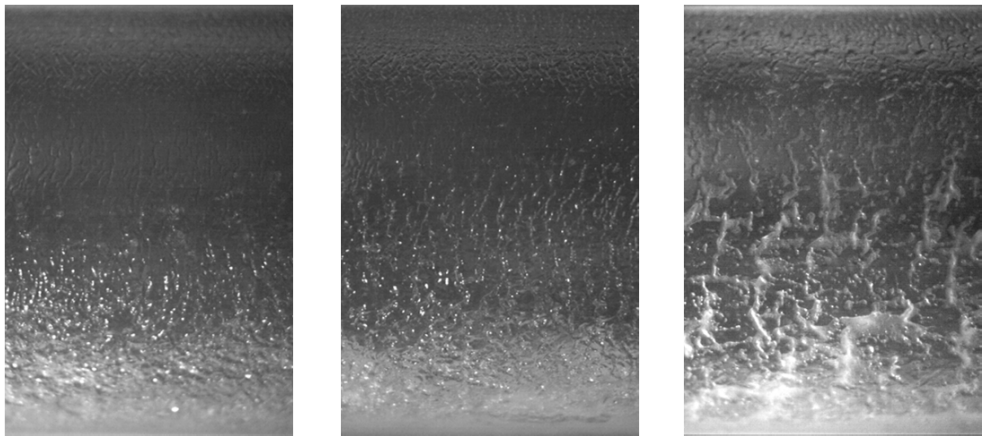

*WC=0* *WC=0.2* *WC=0.8*

Figure 6.6: Variation of the Usg and watercut at constant Usl=0.1 m/s and Usg=8.8 m/s. Oil: Exxsol D80.

The effect of the oil viscosity was studied in cases 16-19. Case 16 started as a stratified-annular flow. However, the liquid film on the top of the pipe disappears by increasing the watercut to 0.077 and continues to thinning itself while the watercut increases (Shmueli et al. (2012)).The decrement on the oil droplet fluxes while the watercut value increases is also observed when using the viscous oil (See Figure 6.7). In this case the measured water droplet fluxes are very scattered to give a clear tendency about their behavior with the watercut. By increasing the watercut the total droplet flux decreases faster than for the cases using Exxsol D80 as oil phase.

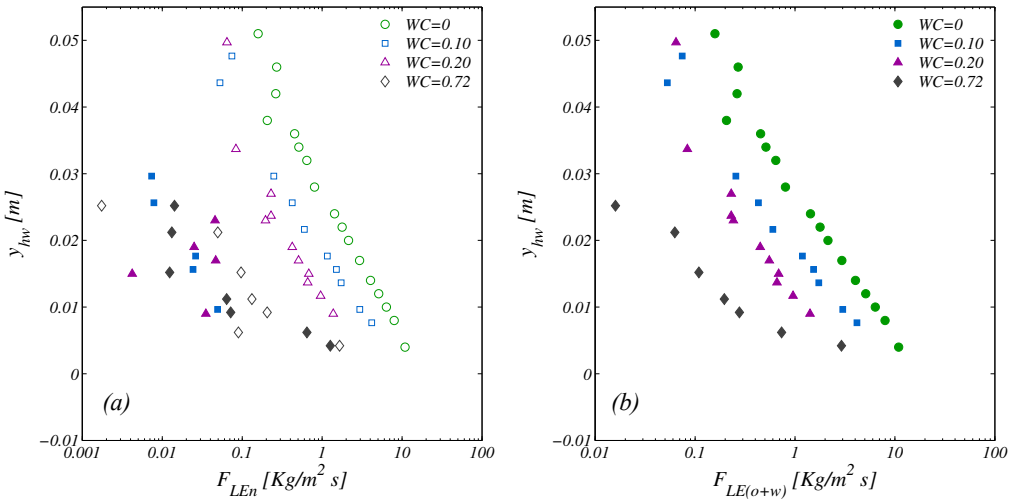


Figure 6.7: (a) Oil (empty markers) and water (filled markers) local droplet fluxes. (b) Total local droplet flux .Usl=0.1 m/s, Usg=6.49 m/s. Oil: Mixed oil.

The total local fluxes show a general decrement with the increment on the water cut. This reduction is more significant in the cases 16-19 where the mixed oil was used. The oil droplets show an exponential behavior from the interface to the top of the pipe.

## 6.4 Oil and water droplet concentrations

The dimensional droplet concentration is defined as

$$C(y) = \frac{F_{LEn}(y)}{U_g(y)} \tag{6.2}$$

Where $F_{LEn}$ is the local droplet fluxes, $U_g$ is the local gas velocity (presented in Chapter 5). Vertical droplets concentration profiles are presented in Figure 6.8 for Exxsol D80-water and $SF_6$ (Cases 1-15) for a fixed liquid superficial velocities of *Usl*=0.2 m/s and *Usl*=0.1 m/s respectively. The oil and water droplets concentration are shown as filled and non-filled markers on the plots. For all the tested water cuts an exponential concentration behavior is observed closed to the gas-liquid interface for water and oil droplets. For most of the cases, close to the upper pipe wall, the concentration values become to a fairly constant asymptotic value as observed before by Kjølaas et al. (2011), Skartlien et al.(2011) and Gawas (2013).

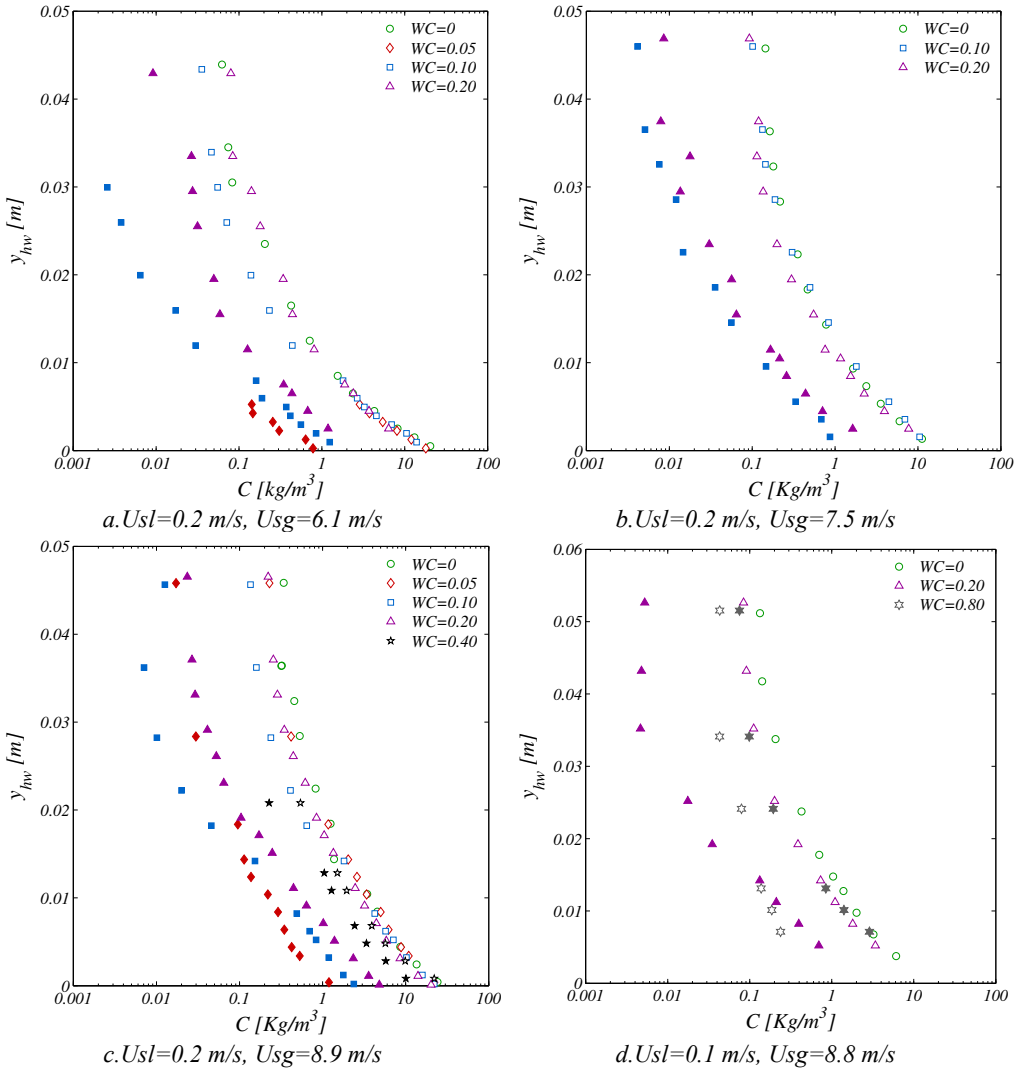


Figure 6.8: Droplet concentration profiles. Oil: Exxsol D80. The measured oil and water droplet concentration profiles are shown as filled and non-filled markers respectively.

The oil and water droplet concentrations were normalized by their interface concentration value and plotted against the distance from the gas-liquid interface (See Figure 6.9). The shapes of the oil and water profiles are very similar for a constant watercut value, especially close to the interface. The distribution of water and oil droplets in the gas seems to be governed by their concentration value on the interface. However some differences between the curves are expected (and represented by the data) as the terminal velocity for water and oil droplets is different. For watercut values 0.8 the differences between the oil and water profiles are large, suggesting that for this case oil and water droplets might be atomized to the gas phase in a separate way (in agreement with the separate entrainment hypothesis from Skartlien et al., 2011).

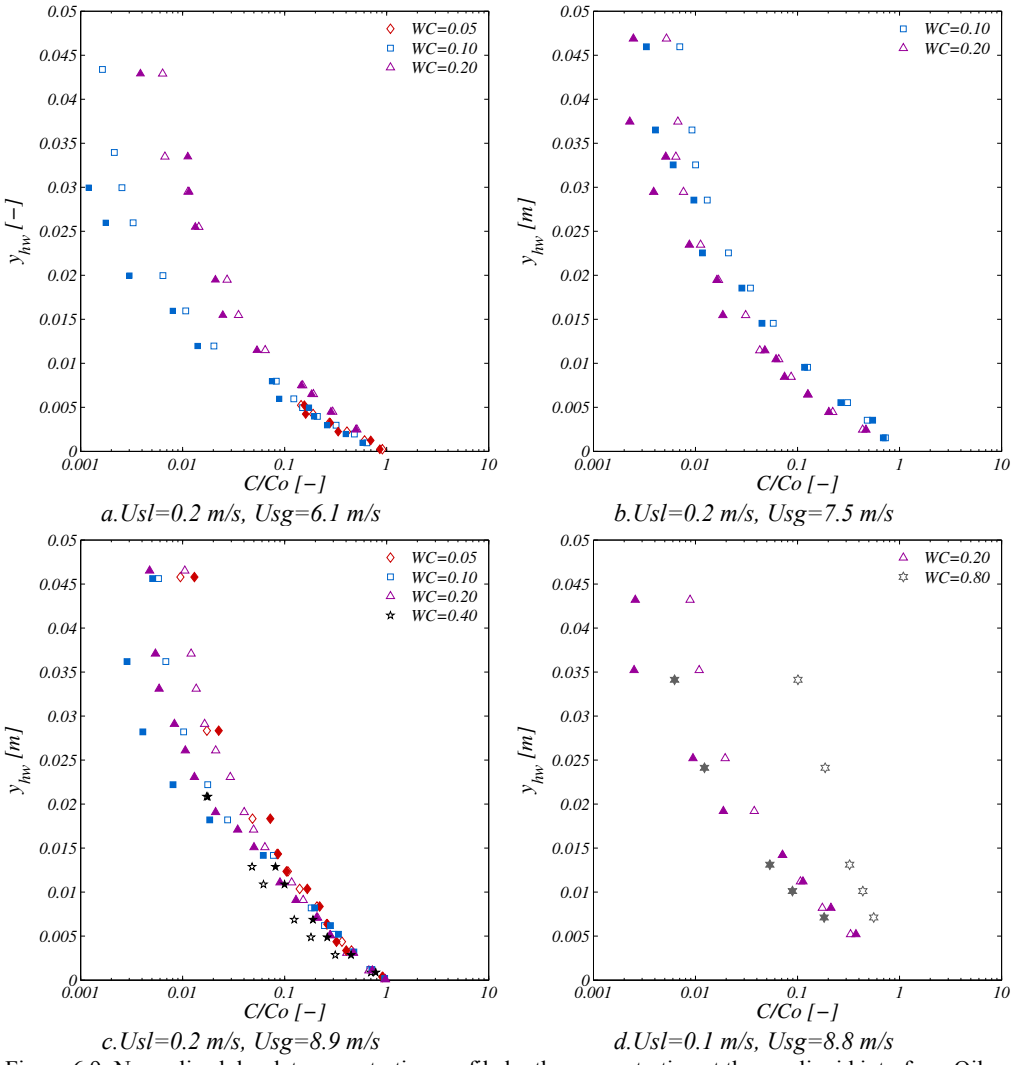


Figure 6.9: Normalized droplet concentration profile by the concentration at the gas-liquid interface. Oil: Exxsol D80. The measured oil and water droplet concentration profiles are shown as filled and non-filled markers respectively.

## 6.5 Local watercut

The local watercut is defined as

$$WC_L(x,y) = \frac{q_w(x,y)}{q_w(x,y) + q_o(x,y)} \tag{6.3}$$

The local watercut is plotted on the pipe cross section (Cases 4, 6-11,13,14) in Figure 6.10. For most of the cases (with exception of *WC*=0.2 *Usg*=6.1 m/s). The local watercut decreases along the pipe diameter from the gas-liquid interface to the top of the pipe. The local watercut values are lower but very close to the input watercut value in close proximity to the gas-liquid interface,

being an indication of a well-mixed liquid layer. There is a redistribution of the water droplets in the pipe cross section when the gas superficial velocity increases at constant watercut. The distribution of the local watercut for the case of *WC*=0.2 and *Usg*=6.1 m/s is affected by the secondary flow cells present for this case as explained before.

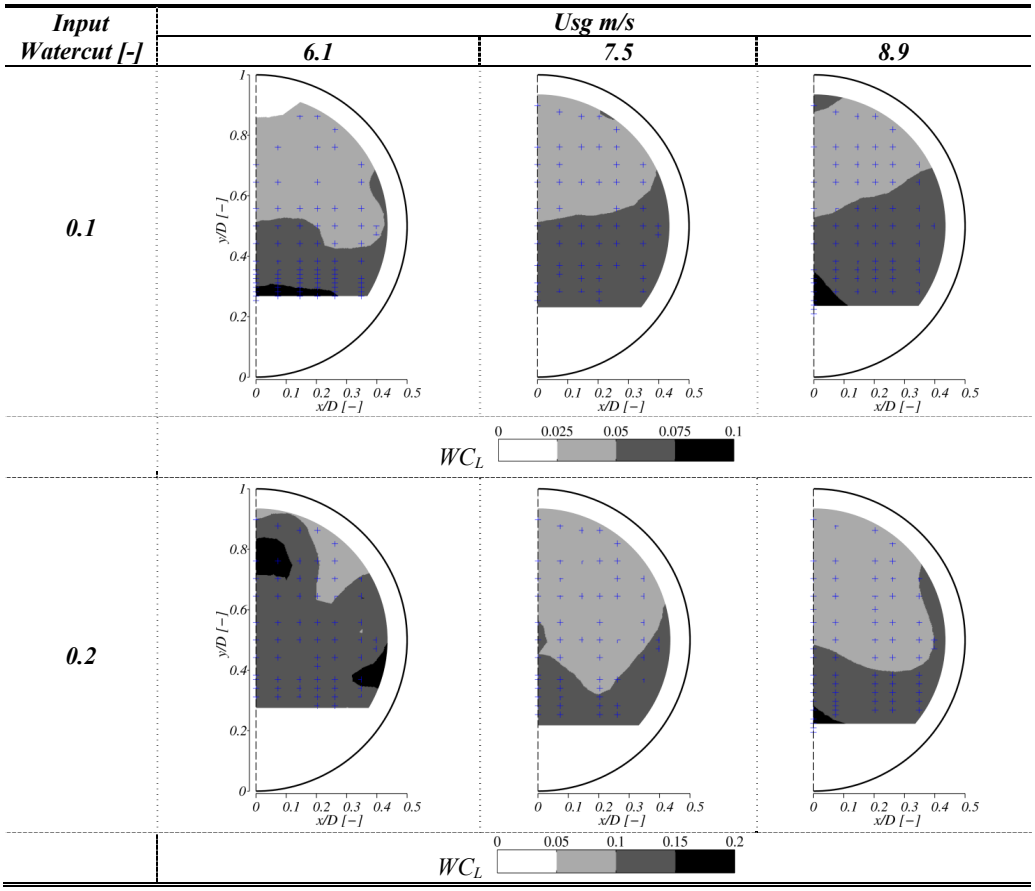


Figure 6.10: Local watercut cross sectional contours

## 6.6 Total liquid entrained fraction

The total mass flow of droplets is calculated by integrating the local liquid flow of droplets from the gas liquid interface to the top of the pipe. For the 1D sampling experiments it was assumed a uniform distribution of the droplet fluxes on the gas phase cross section, meaning that the droplet flux just vary on the vertical diameter. This is a common approach used in the current flow simulators and utilized by previous authors (Paras & Karabelas 1991, Williams 1996, Tayebi 2000, Gawas 2013, among others). For the integration a flat gas-liquid interface is assumed. (See Figure 6.11a)

$$\overline{E}_L = A \cdot \overline{F}_{LE_i} = \frac{2A}{A_g} \int_{hw}^{D} \sqrt{R^2 - (y-R)^2} \cdot F_{LE_i}(y)dy \tag{6.4}$$

The 1D integration was performed numerically using the trapezoidal rule of the experimental data. The data was discretized and interpolated using a piecewise cubic hermite interpolating polynomial. The experimental data was extrapolated or interpolated when required to get the values at the top of the pipe and at the interface (See Figure 6.11b). A grid dependency study was performed and the integration results were not dependent on the used discretization (from 10 to 1000 elements, the maximum relative error found in comparison to the finer grid was 0.3%).

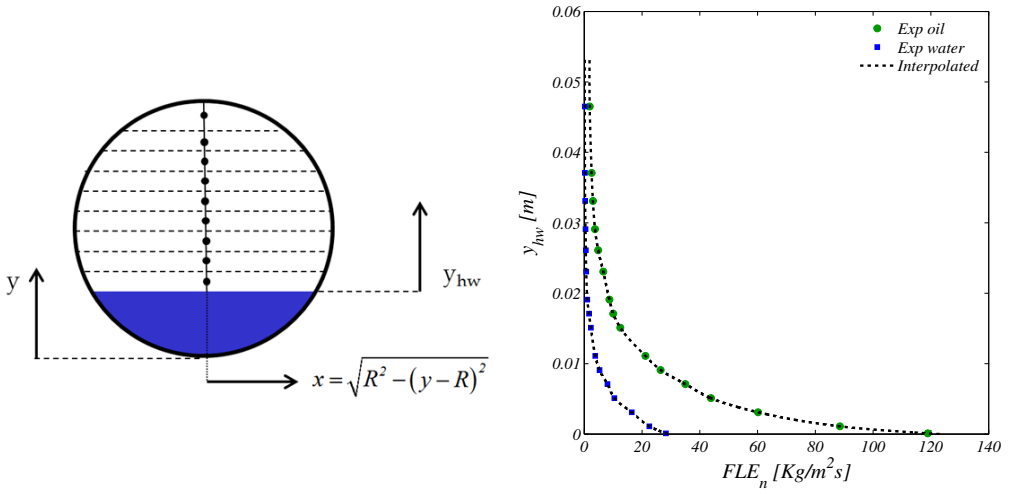


(a) (b)

Figure 6.11: (a) Sketch for 1D integration of the droplet fluxes. (b) Example of the interpolation and extrapolation result on the droplet profiles. Usl=0.2 m/s, Usg=8.9 m/s, WC=0.2 (Case 14)

The 2D integration was performed based on a different approach. In this case, the sampled droplet fluxes are scattered within the pipe cross section. To facilitate the visualization of the results and subsequent integration the sampled points were fitted to a rectangular grid. This task was performed by using a surface modeling tool developed in Matlab (Gridfit, 2006). This also allows refining the measured mesh and getting a better discretization for the integration process (See Figure 6.12a). The data outside the measured boundaries was extrapolated without considering any particular boundary condition. Every cell or element of the grid used for the droplet flux integration on the pipe cross section was classified depending on its location inside the pipe and has four nodes. A total of 15 different element types were found (See Figure 6.12b). A detailed summary is available on Appendix D. The identification of each element type was set according to its location in reference to the pipe wall. A methodology was created to identify every element type where each one will have a unique identification vector (See Appendix D).

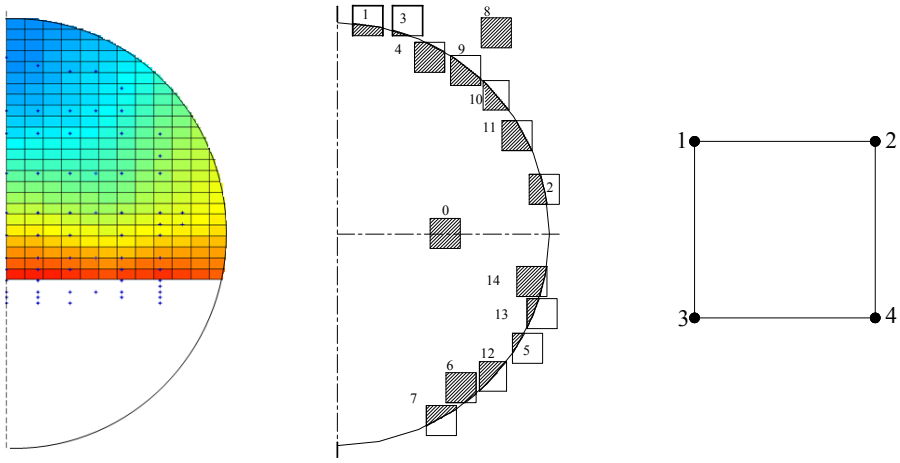


*(a)* *(b)* *(c)*

Figure 6.12: (a) Rectangular grid and fitted surface to the experimental data (b) Element types on the cross section (c) Possible nodes configuration

Fitting a surface to a rectangular grid provides information of droplet fluxes in the 4 nodes of each element, however the surface equation is not known. There are several approaches one can chose to perform the 2D integration, two examples of them are shown in Figure 6.13. In this work the methodology in Figure 6.13a was applied. Considering that the fitted surface can be described as multiple planes which contains three of the four nodes of each element, the equation of each plane is given by

$$F_{LEn\_calc}(x,y) = \frac{n_1 \cdot (x + x_{np}) + n_2 \cdot (y + y_{np}) + n_3 \cdot F_{LEn}(x_p, y_{np})}{n_3} \tag{6.5}$$

Where $n_1$, $n_2$ and $n_3$ are the components of the vector normal to the plane and $x_{np}$ and $y_{np}$ are the spatial coordinates of any of the three selected points in the plane.

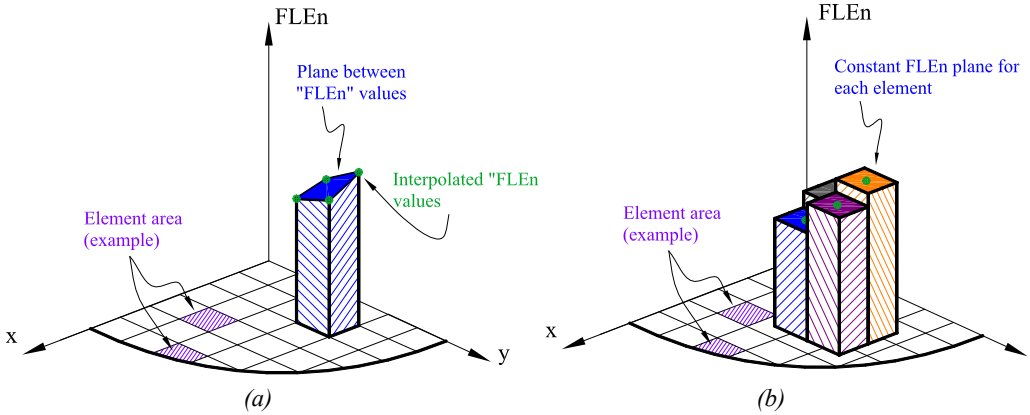


*(a)* *(b)*

Figure 6.13: (a) Representation of the interpolated data.(a) Plane between node. (b) Plane using one representative node value.

A grid dependence study was performed and an example is shown in Figure 6.14a. The vertical discretization was set to be the double of the horizontal one. Using 12 divisions in the horizontal, the relative error in comparison with the finest grid is 0.7%. It was considered that from this point the results are not dependent of the grid. On Figure 6.14b an example of the obtained fitted planes is shown together with experimental data (shown as red circles). The maximum, minimum and average fitting errors in this case are 27%, 0.3% and 8% respectively. The maximum error occurs for low droplet fluxes mainly in the top of the pipe (See Figure 6.14c)

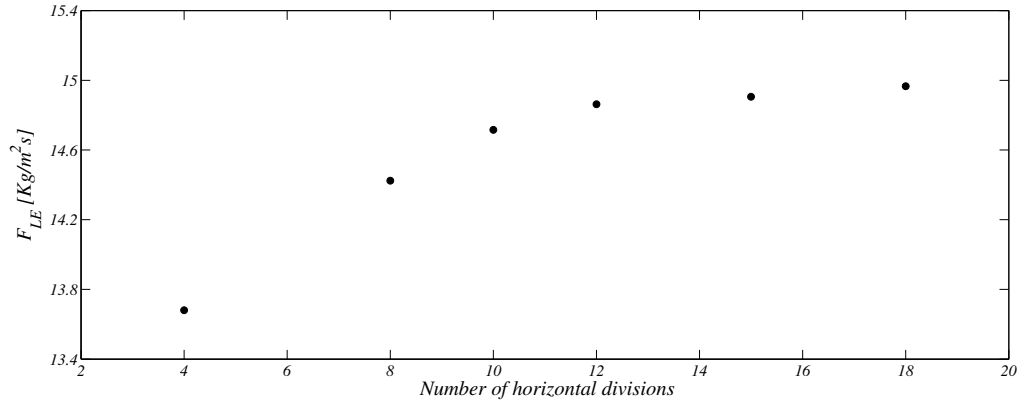


(a)

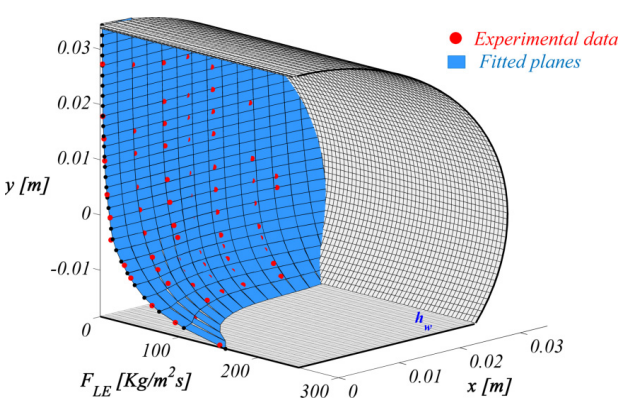


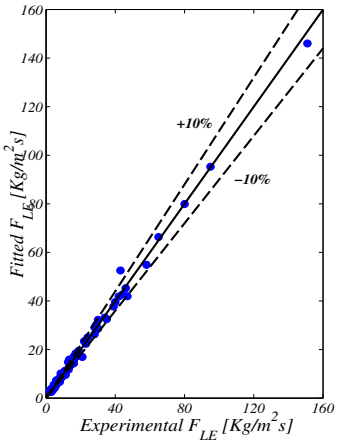


(b) (c)

Figure 6.14: (a) Grid dependency study (b)Fitted planes over the droplet flux experimental data (c)Comparison of the experimental droplet flux with the predicted flux by the fitted planes. All the examples are for Case 11

The total droplet flux of water and oil is calculated by adding all the volumes of the solids formed by the element area and the height of the flux plane.

$$\overline{F}_{LEn} = \frac{\left( \sum_{i}^{nr} \sum_{j}^{nc} \int_{x\min}^{x\max} \int_{y\min}^{y\max} \int_{0}^{q_n(x,y)} dz dy dx \right) \cdot \frac{\rho_n}{A_p}}{A_g} \tag{6.6}$$

The droplet entrainment fraction is defined by the relation between the entrained oil droplet mass flow rate ($E_L$) and the total liquid mass flow rate in the system ($W_L$)

$$f_e = \frac{E_L}{W_L} = \frac{\left(\overline{F}_{LEo} + \overline{F}_{LEw}\right) \cdot A}{A \rho_L U_{sl}} \tag{6.7}$$

Figure 6.15 shows the oil, water and total entrainment fraction obtained for cases 4-15 (Oil: Exxsol D80, *Usl*=0.2 m/s). The general tendency is that the water entrainment increments and the oil entrainment decreases with the rise in the watercut. In this way the total entrainment fraction (oil + water) keeps relatively constant, similar to what was reported previously by Gawas (2013). The entrainment fraction increases with the gas superficial velocity in line to previously reported results from by Ishii et al. (1989), Paras & karabelas (1991), Williams et al. (1996), Tayebi et al. (2000).

The total entrainment fraction is not strongly dependent on the added water for the studied cases using Exxsol D80 as an oil phase. A different perspective was observed when using the viscous oil (See Shmueli et al. (2012)). The total entrainment fraction decreases while adding water to the system. In this work visual support from the high speed videos confirm this tendency. However, further experimental work needs to be done in order to confirm the reduction in liquid entrainment when adding water to the gas-liquid system in high viscosity systems.

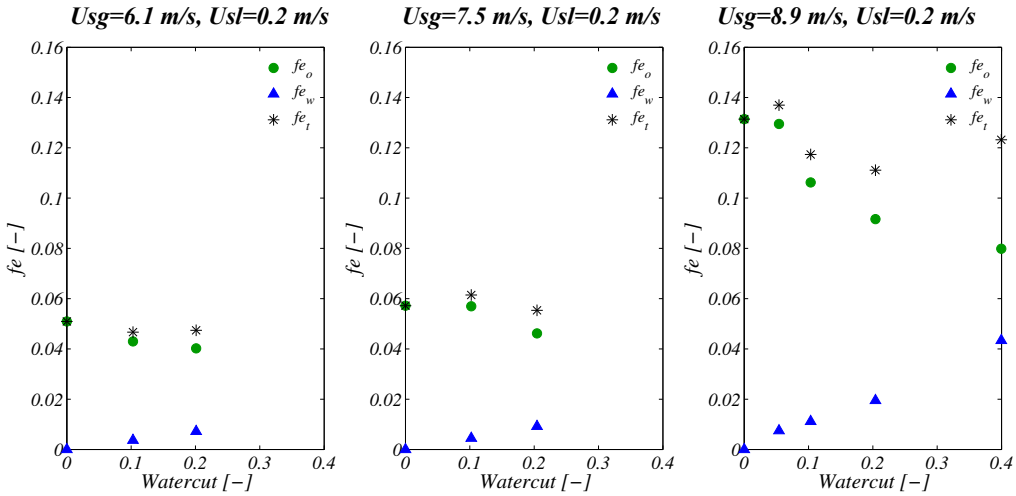


Figure 6.15: Water, oil and total entrainment fraction. Exxsol D80-Water-$SF_6$ (Cases 4-15)

A comparison between the two integration methodologies to calculate the total entrainment fraction is presented in Figure 6.16. There is an over prediction of the entrainment fraction when

using the 1D integration methodology. The relative error when using the 1D approach in comparison to the 2D approach increases with the gas superficial velocity from 10% to 43%. The majority of the liquid transported as droplets occurs close to the gas-liquid interface. As presented on the droplet flux cross sectional plots, at lower gas velocities the droplets are more uniform distributed close to the interface mainly due to the less wavy flow. Secondary flows have a strongly effect on the distribution of droplets on the top of the pipe even at low gas superficial velocities. However the total entrained fraction is not strongly influenced by them at the lowest gas superficial velocities.

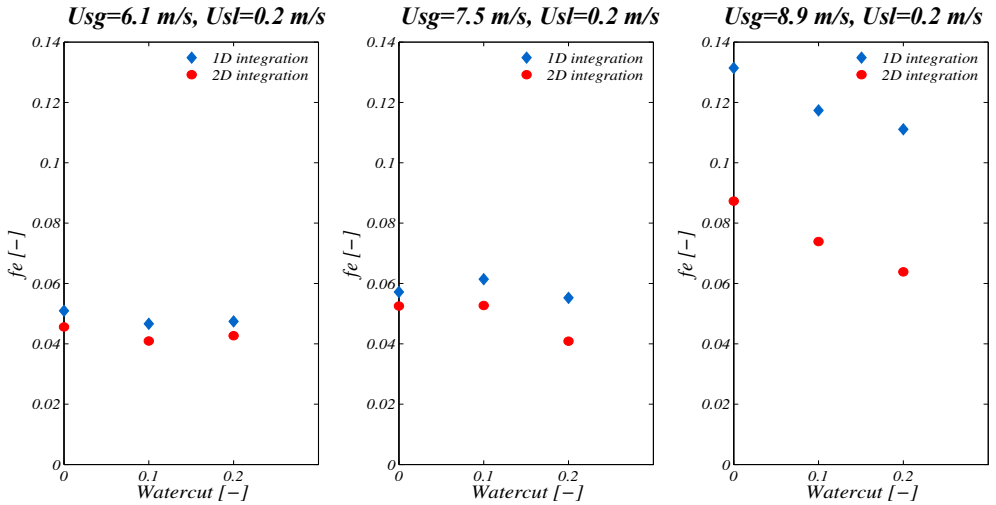


Figure 6.16: Comparison of total liquid entrained fraction using 1D and 2D integration methodologies. Oil=Exxsol D80

## 6.7 Effect of the interface selection

The droplet entrainment fraction calculated by the integration of the droplet profiles will depend mainly on the correct measurement of the droplet profiles and on the correct estimation of the gas-liquid interface. Ideally the integration should be done from the location of the highest wave top to the pipe top and sometimes the selection of the interface could be quite uncertain. Different approaches can be followed to select the gas liquid interface.

The interface location can be estimated as well from the frames extracted from the high-speed videos on the pipe diameter on the clear section. This technique might have a large associated uncertainty as the location could be affected by the camera location, pipe wall effect, film around the pipe or just human errors when discriminating between a wave and a very large droplet just expulsed from the wave. Using this technique the interface height will be overestimated and in consequence the entrainment fraction underestimated.

In the previous section, the total entrained fraction was calculated using the measurements from the liquid fraction profiles (See Chapter 4) obtained using a two-energy gamma densitometer.

The fraction profiles from the gamma densitometer showed, for some of the studied cases, a steep slope in the profiles which is a characteristic of a wavy flow (See Hu et al. 2013). This complicates the selection of the "real" gas-liquid interface. As a first guess, it can be assumed that the gas liquid interface is located at $\alpha_L$=0.5. The entrainment fraction will be overestimated by selecting this interface as it includes the wavy region. Being more conservative, it can be assumed that the maximum top wave will occur when the liquid fraction in the pipe was set (arbitrarily) to $\alpha_L$=0.05. On Figure 6.17 it is shown the effect of the interface selection in the total entrainment fraction calculation. The differences between the lowest and largest interface locations ($\Delta h_w$) are between 1 cm and 1.8 cm. This difference can lead to a large effect on the total entrainment fraction calculation. The results from the visual observations and the gamma densitometer at $\alpha_L$=0.05 are closest to each other.

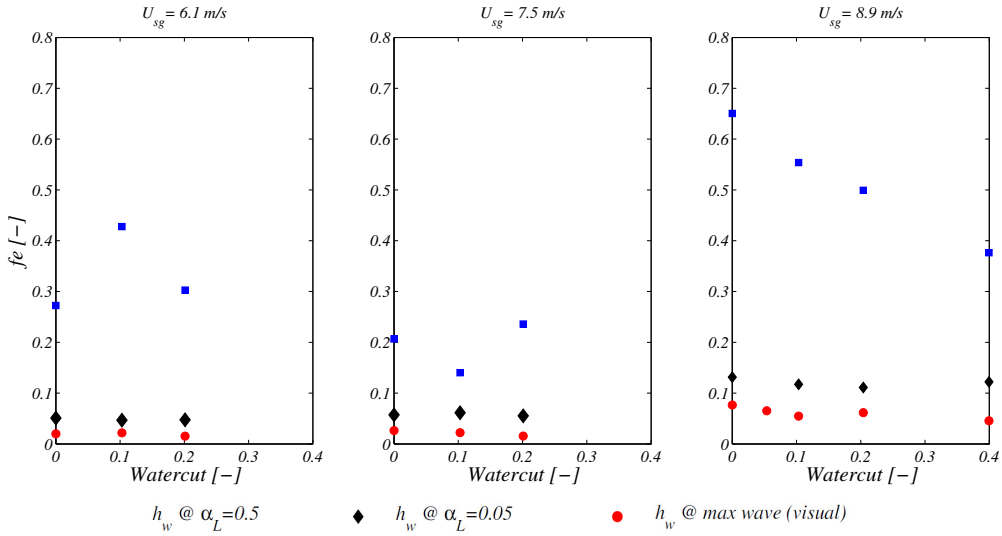


Figure 6.17: Effect of the interface height selection on the *fe* calculation. Oil=Exxsol D80

## 6.8 Summary

A new instrument was designed and built for isokinetic sampling of gas flow with droplets at high pressure flow conditions. The sampling probe can traverse over the pipe cross section.

Using the new 2D probe it is therefore possible to measure simultaneously the gas local velocity and the liquid droplet flux in the gas core. An experimental campaign on droplet flux measurement was carried out and results for the liquid droplet local fluxes are presented for two and three phase flows.

A general increment of the droplet fluxes were observed when the gas velocity increases at constant water cut.

The droplet distribution in the pipe cross section is not uniform over the horizontal axis for both water and oil and all the studied cases. The droplet distribution shape and the magnitude of the non-uniformity depend on the particular flow conditions.

In addition, in horizontal stratified-annular flow there is a non-uniform droplets distribution on the vertical diameter due to gravity. Larger and heavier droplets travel closer to the gas-liquid interface while smaller and lighter droplets travel closer to the top of the pipe. This support the creation of a non-uniform liquid film on the pipe wall, which is thicker close to the gas-liquid interface and thinners at to the top of the pipe. The existence of a non-uniform film causes a non-uniform pipe wall roughness and its effect is to promote the occurrence of secondary flows in the gas core.

The integration of the 1D profiles gives an over prediction of the total entrainment fraction in comparison to the 2D profiles. The total entrainment fraction from the integration of the droplet flux profiles is very sensitive to the definition of the interface position. The maximum relative error found for the highest gas velocity was 43%. The effect of the water addition to an oil-gas system on the total entrainment fraction is negligible for the studied conditions.

# Chapter 7

## Modeling of liquid droplets concentration profiles in stratified-annular flows

The current state of prediction models for liquid droplet concentration profiles is reviewed in this Chapter. The limitations and assumptions are discussed. The model is tested against the experiments from this work and data from the literature. Despites the non-uniformities on the droplets distribution on pipe the cross section found in last chapter a 1D modeling approach is followed. Empirically based relations for the concentration profiles are derived using genetic algorithms on the available experimental data.

### 7.1 Introduction

Most of the current models for prediction the droplets concentration profiles are based on a 1D approach (Paras and Karabelas (1991), Pan et al. (2002), Kjølaas et al. (2011), Skartlien et al. (2011)). Following Paras and Karabelas (1991), a diffusion-type equation is used to estimate the droplet concentration

$$\varepsilon \frac{dC}{dy_n} + w \cdot C(1-C) = a(y_{hw}) \tag{7.1}$$

Where $\varepsilon$ is the particle diffusivity, $w$ is the terminal settling velocity of the particles. For dilute suspensions $C(1\text{-}C) \approx C$ (Paras et al. (1994)). $y_{hw}$ represents the distance from the gas-liquid interface to the top of the pipe. The term $a(y_{hw})$ in the rhs represents a net upwards flux of droplets in the horizontal plane. Some authors neglect this term and consider that the droplet concentration is just affected by gravity forces and the droplets inertia (Pan and Hanratty (2002), Kjølaas et al. (2011), Skartlien et al. (2011)). If the turbulent diffusion, terminal velocity of droplets and location in the pipe are independent variables, the solution from equation (7.1) is:

$$C = C_o \cdot exp(-{}^{w}\!/_{\varepsilon} \cdot y_{hw}) \tag{7.2}$$

In order to model the droplets concentration profiles it is required to estimate three parameters: The droplet settling velocity $w$, the droplet diffusivity $\varepsilon$ and the interface concentration $C_o$. The assumptions taken in the model are:

- Equal diffusivities of gas and particles (small particles sizes).
- For simultaneous oil and water flow the droplets do not interact between each other after atomization (Skartlien, 2011)
- No effect of secondary flows on the cross sectional droplet distribution (1D approach)

## 7.2 Droplet settling velocity "*w*"

The droplet settling velocity is considered as the terminal velocity and can be obtained from a force balance on a single particle (Kjølaas et al, 2011)

$$w = u_T = \sqrt{\frac{4 d_d g\left(\rho_l - \rho_g\right) cos(\theta)}{3 C_D \rho_g}} \tag{7.3}$$

Where $d_d$ is the droplet diameter and $C_D$ is the drag coefficient. Kjølaas et al (2011) estimates the drag coefficient using the correlation proposed by (Clift et al., 1978) and together with particle Reynolds number, the terminal velocity can be calculated

$$C_D = 24 \frac{1 + 0.15\, Re_d^{0.687}}{Re_d} \qquad Re_d = \frac{\rho_g u_T d_d}{\mu_g} \tag{7.4}$$

Similarly, Skartlien et al. (2011) calculate the terminal velocity from an iterative procedure using the drag coefficient equation developed by Rivkind et al. (1976) and the particle Reynolds number. In this case the approach from Kjølaas et al (2011) is followed.

The droplet diameter is computed from the available experimental information. Kjølaas et al, (2011) tuned the droplet diameter to fit the experimental data. Skartlien et al. (2011) assumed that the droplet sizes follow a gamma distribution. Two parameters in the gamma distribution are tuned to fit the experimental data.

Previous studies showed an improvement on the droplet concentration profiles prediction when the droplet diameter distribution is taken into account (See Skartlien et al. (2011) and Gawas (2013)). The main effect of considering the droplet size distribution in the pipe is to predict more accurately the droplet concentration distribution on the top of the pipe. From the transport point of view, most of the liquid entrained as droplets travel close to the gas-liquid interface where the droplet size distribution does not strongly affect the current model predictions. Nevertheless in the context of "top of line corrosion" (See Skartlien, (2011)), predicting accurately the droplet fluxes in the top of the pipe can be a major topic. Gawas (2013) show a comparison between the predictions of the droplet concentration profiles by the models from Skartlien et al. (2011), Pan and Hanratty (2002), Gawas (2013) and an experimental dataset. The liquid velocity and interface height of this experimental condition is unknown. However, a total entrained droplet

flux was obtained for each model and experiments by integrating them over a commonly assumed interface value ($h_w$= 0.01 m). The relative error between the prediction and experimental total droplet flux are 8% ($Qd$= 0.0045 Kg/s), 11% ($Qd$= 0.0037 Kg/s) and 15% ($Qd$=0.0047 Kg/s) for the models of Gawas (2013), Skartlien et al. (2011) and Pan and Hanratty (2002) respectively.

## 7.3 Turbulent Diffusivity "ε"

The turbulent diffusivity can be estimated based on the normalized diffusivity in pipe flow (Vames and Hanratty, 1988).

$$\zeta = \varepsilon / R \cdot u^* \tag{7.5}$$

Where $R$ is the pipe radius and $u^*$ is friction velocity in the gas zone. Kjølaas et al (2011) used the hydraulic diameter concept $(D_{hg}/2)$ and Skartlien et al. (2011) used one half of the height of the gas volume from the interface to the top of the pipe instead of the pipe radius $R\ ((D-z_i)/2)$.
The friction velocity can be estimated following Skartlien et al. (2011). In single phase pipe flow $u^*$ is defined as

$$u^* = \sqrt{\frac{\tau_w}{\rho_g}} \tag{7.6}$$

Where $\tau_w$ is the wall shear stress and $\rho_g$ is the gas density. For stratified flow, the averaged momentum equation in the gas phase gives.

$$\tau_w S_w + \tau_i S_i - A_g \left( \frac{dP}{dx} + \rho_g g \sin(\theta) \right) = 0 \tag{7.7}$$

Where $S_g$ and $S_i$ are the gas and interface perimeters respectively, $\tau_i$ is the interface stresses and $A_g$ is the gas area. An average shear stress that takes into account the interface and wall perimeters replaces the wall shear stress in equation (Skartlien et al, (2011)).

$$u^* = \sqrt{\frac{\langle \tau \rangle}{\rho_g}} \tag{7.8}$$

Blending the definition of the average perimeter stress and equation the momentum equation in the gas phase, the average shear stress is written as:

$$\langle \tau \rangle = \frac{\tau_g S_g + \tau_i S_i}{S_g + S_i} = \frac{A_g}{S_g + S_i} \left( \frac{dP}{dx} + \rho_g g \sin(\theta) \right) \tag{7.9}$$

On previous studies, the value of $\zeta$ has been varied to fit the experimental data. Pan and Hanratty (2002) suggest a decrement of $\zeta$ with the increment of the pipe diameter. In their work values of $\zeta$ =0.08 and $\zeta$ =0.04 were used for fitting the data of pipe diameters of 0.05 m and 0.095 m respectively. Kjølaas et al (2011) fitted their experimental data using a value of $\zeta$ =0.026 for a 0.189 m pipe diameter. Skartlien et al. (2011) did not adjust the value of $\zeta$ to fit their experimental data but adopted a value of $\zeta$=0.074 (following Vames et al. (1988)). Pan and

Hanratty (2002) stated that $\zeta$ is not constant because the assumption of $a(y_n)=0$. This coefficient represents a weak point of the model as it should be constantly changed depending on the desired operational conditions.

Considering the modeling approach presented by Kjølaas et al (2011) and assuming a known value for the droplet concentration at the interface $C_o$ (obtained directly from the experimental data), the model was run and multiple feasible solutions were obtained. In the light of these results, a sensitivity analysis was performed using different droplet diameter values (from 2 μm to 300 μm) and for different normalized turbulent diffusion coefficients (from 0.02 to 0.08). It is possible to study how the variation of the droplet diameter and the dimensionless turbulent diffusivity affects the results from the predictions. The droplet concentration profiles were well predicted in all the cases independently of the initial values for the two adjusted variables $\zeta$, $d_p$. The quality of the fitting was tested by verifying the coefficient of determination ($R^2$) of the fitting for each pair of $\zeta$, $d_p$. On Figure 7.1 a contour plot of the $R^2$ for each pair of the adjusted variables is shown as an example for the cases of *Usg*=6.1 m/s, *Usl*=0.2 m/s, WC=0 and *Usg*=8.9 m/s, *Usl*=0.2 m/s, WC=0. Similar results were observed when testing the model for the rest of the experimental data from this work and data from Tayebi et al. (2000) and Paras et al. (1991). Combinations of $\zeta$ and $d_p$ can give similar predictions illustrating that models with several parameters can give compensating errors when tuned to data. Given this observation, the suggested trend of the normalized diffusion coefficients with the pipe diameter from the work from Pan and Hanratty (2002) and Kjølaas et al (2011) might be just a coincidence given by the model and not a physical behavior of the data itself.

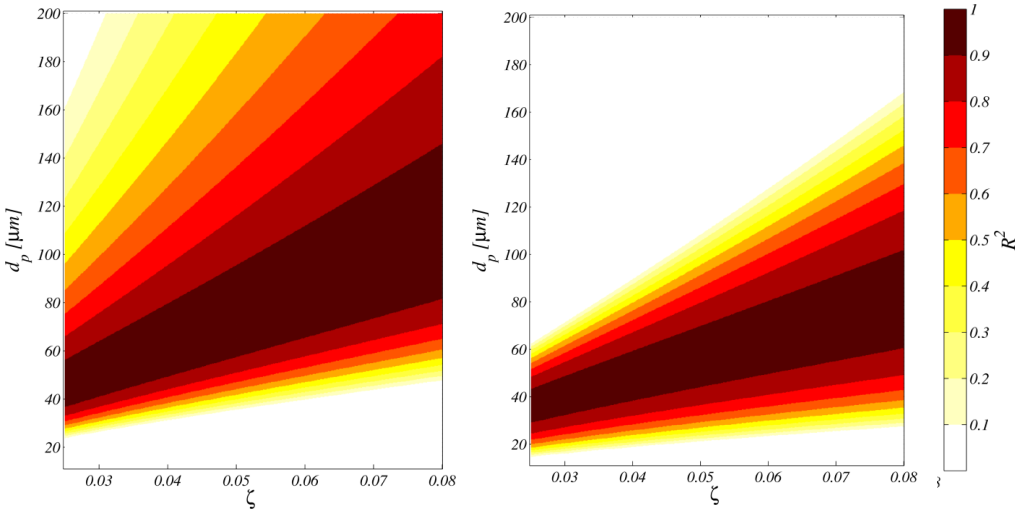


*Usg=6.1 m/s, Usl=0.2 m/s* *Usg=8.9 m/s, Usl=0.2 m/s*

Figure 7.1:Wellness of the predictions. Sensitivity analysis of the droplet diameter and ζ

To predict the turbulent diffusivity based on this simplified model, two main assumptions about the normalized diffusion coefficient and the droplet sizes should be made. In this case, the value $\zeta$=0.074 used by Skartlien et al. (2011) and previously proposed by Vames and Hanratty (1988) is adopted. For predicting the droplet diameter in annular flows, different correlations are available in the literature. Pan and Hanratty (2002) proposed a model for the Sauter droplet diameter based on the theory from Tatterson et al. (1977)

$$\left(\frac{\rho_g u_g^2 d_{32}}{\sigma}\right)\left(\frac{d_{32}}{D}\right) = 0.0091 \tag{7.10}$$

Azzopardi (1985) reported an empirical correlation for the Sauter droplet diameter. This correlation was modified by Skartlien et al. (2011) by neglecting the term due to coalescence.

$$\frac{d_{32}}{\lambda} = \frac{15.4}{We^{0.58}} \tag{7.11}$$

Where We is the Weber number and in this case is defined as

$$We_\lambda = \frac{\rho_l U_G^2 \lambda}{\sigma}, \quad \lambda = \sqrt{\frac{\sigma}{\rho_l g}} \tag{7.12}$$

Where $\sigma$ is the gas liquid interfacial tension

Al-Sarkhi et al. (2002) proposed a simplified correlation for the Sauter droplet diameter based on experimental data from different pipe diameters (0.0254 m and 0.0953 m)

$$\left(\frac{\rho_g U_{sg}^2 d_{32}}{\sigma}\right)^{0.55}\left(\frac{d_{32}}{D}\right)^{0.36} = 0.154 \tag{7.13}$$

Gawas (2013) measured droplet diameter distribution in annular horizontal and inclined pipe flow with 0.15 m pipe diameter and compared his results with correlations from the literature finding that the correlation from Al-Sarkhi and Hanratty (2002) gives the closest prediction to the measured Sauter diameter from his experiments. In this study the droplet sizes were not measured. The three mentioned correlations for the droplet diameter were tested in the model and it was verified which of them gives the best fitting of the experimental data. On Figure 7.2 the predictions are plotted against the distance from the gas liquid interface $y_{hw.}$ For the low viscosity cases, Pan and Hanratty (2002) correlation gives the best fitting to the data while for the case using the viscous oil, Al-Sarkhi and Hanratty (2002) correlation gives the closest prediction.

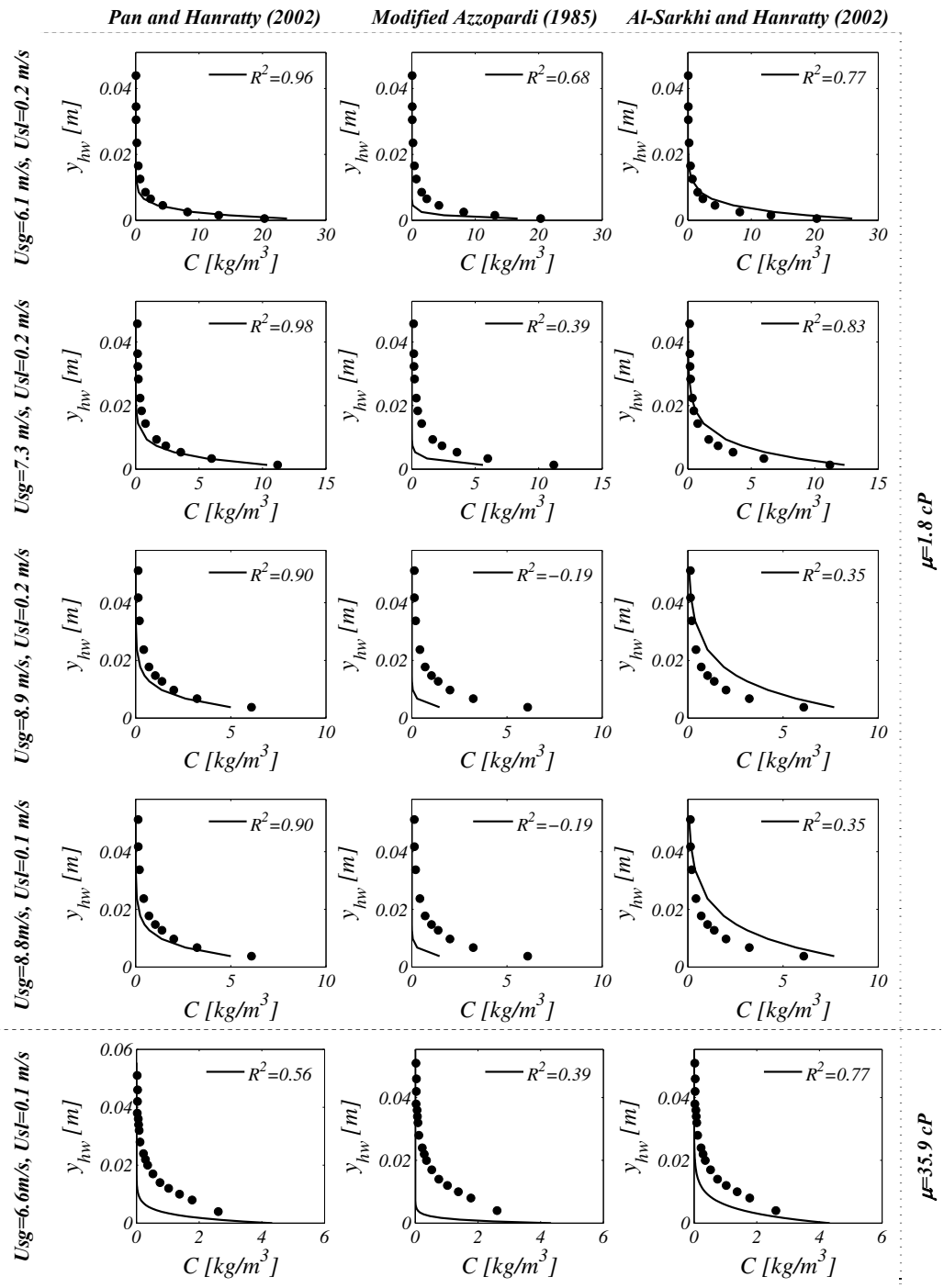


Figure 7.2: Comparison of the model prediction using different correlations for droplet diameter

When three-phase flows (oil-water-gas) are flowing simultaneously, additional information about the third phase is required to model the oil and water droplet concentrations. The term $\varphi=\varepsilon/w$ in equation (7.2) represents the shape of the droplets profile. If the normalized diffusion coefficient is considered constant, the term $\varphi$ mainly depends on the droplet sizes (through the calculation of the terminal velocity).

The log-plots with the experimental data presented in Chapter 6 showed similar shapes between the oil and water droplet concentration profiles for constant and low watercut values (up to 0.2). Considering the concentration at the interface known, the coefficient $\varphi_o$ and $\varphi_w$ is calculated using the correlation from Pan and Hanratty (2002) for the droplet diameter.

On Figure 7.3 and Figure 7.4 the predicted profiles for water and oil are plotted against the location over the gas-liquid interface normalized by the pipe diameter are shown for *Usl*=0.2 m/s, gas superficial velocities from 6.1 m/s and 8.9 m/s and watercut values 0.1 and 0.2 respectively. The experimental data is also plotted (where circles and stars are the oil and water experimental data respectively). The predictions for the rest of the studied cases are shown in Appendix E. The fitting quality is expressed using again the coefficient of determination $R^2$ as a reference. In general, good agreement is obtained between the predictions and experiments.

The correlation of Al-Sarkhi and Hanratty (2002) gave better predictions for the case where the highest tested watercut value (0.8) and for all the cases where the Mixed oil (39 cP) were used as an oil phase.

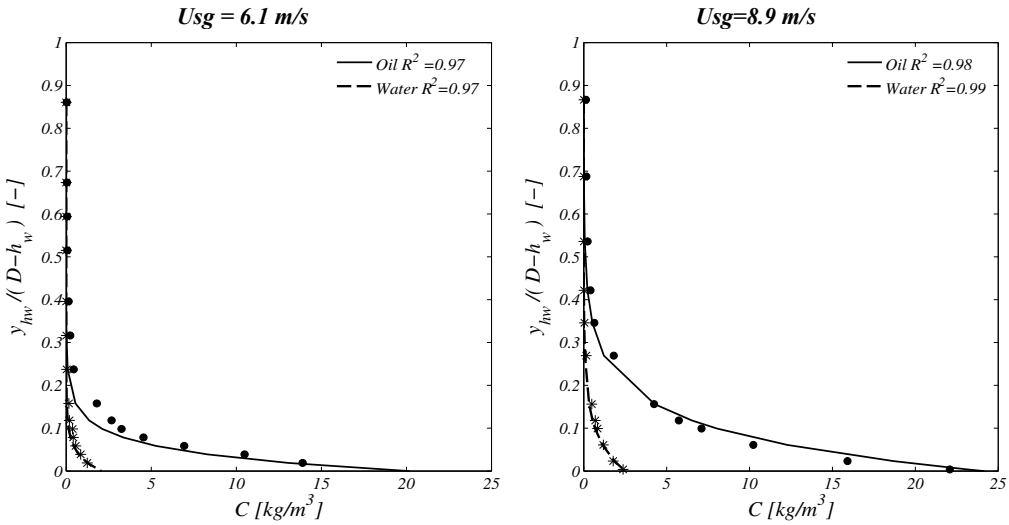


Figure 7.3 Predicted oil and water concentration profiles using the correlation from Pan and Hanratty (2002) for the droplet diameter. WC=0.1

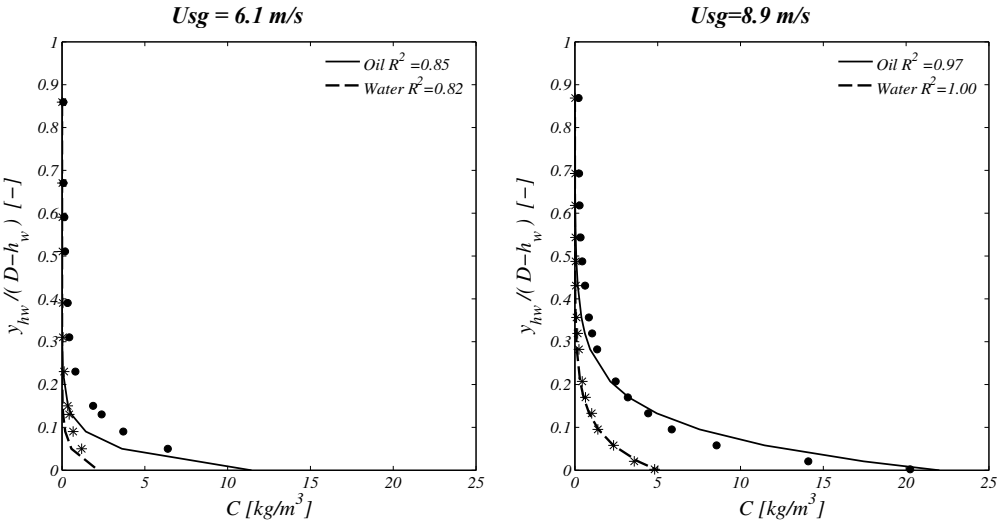


Figure 7.4 Predicted oil and water concentration profiles using the correlation from Pan and Hanratty (2002) for the droplet diameter. WC=0.2.

## 7.4 The interface concentration "$C_o$"

The interface concentration is a critical parameter of the profile model and when experimental data is available, the interface concentration is estimated as earlier, from the interpolation/extrapolation of the experimental concentration profiles to the specific interface location. This approach is valid for testing the predictions of the model to a current set of data. However it limits the model applicability range.

An empirical correlation for predicting $C_o$ in gas-oil systems was built by Kjølaas et. al (2011). The correlation is dependent of the liquid volume fraction, gas density, liquid density, gas velocity, liquid film velocity and critical velocity. The correlation is part of the LedaFlow development so the shape of it is unknown.

To predict the droplet concentration at the interface, Skartlien et al (2011) assumed that the deposition and entrainment fluxes balances at the interface so $C_o=R_A/k_D$. This being valid for steady state conditions where the atomization rate $R_A$ is equal to the deposition rate $R_D$ (Paras and Karabelas, 1991) Here, $k_D$ is the deposition flux. Pan and Hanratty (2002) model the atomization rate based on a single phase "thin-film" entrainment correlation as

$$R_A = \frac{k_A' U_G^2 \sqrt{\rho_g \rho_L}}{\sigma} \frac{\left(W_{LF} - W_{LFC}\right)}{P} \tag{7.14}$$

Where $W_{LF}$ is the mass flow of liquid in the liquid layer, $W_{LFC}$ is the critical film flow to onset entrainment, $\sigma$ is the gas-liquid surface tension, $\rho_L$ and $\rho_g$ are the liquid and gas densities respectively, $U_G$ is the gas velocity, $P$ is the pipe perimeter (Skartlien et al. (2011) used the interfacial perimeter $S_i$ instead of the pipe perimeter) and $k'_A$ is a proportionality factor $k'_A$ which has to be tuned to match the experimental data. Values for the proportionality factor $k'_A$ has been

proposed by Pan & Hanratty (2002) to be $3x10^{-6}$ for tuning air-water experimental data at low pressures and by Skartlien et al. (2011) to be $6x10^{-6}$ for tuning $SF_6$-Exssol D80-water at high pressures. The requirement of data tuning inside the model weakens the proposed approach.

The critical film flow to onset entrainment was calculated by Skartlien et al. (2011) using $W_{LFC} = \mu_L \, Re_c \, S_i / 4$ where $Re_c$ is the critical Reynolds number for the entrainment onset defined as (Hewitt et al. (1990))

$$Re_c = exp\left( 5.85 + 0.4249 \frac{\mu_g}{\mu_L} \sqrt{\frac{\rho_g}{\rho_L}} \right) \tag{7.15}$$

For vertical annular flows, the rate of deposition $k_D$ can be considered constant and is approximated as (See Binder et al. (1992))

$$k_D = \sqrt{\frac{1}{2\pi}} \sqrt{\overline{v^2}} \tag{7.16}$$

Where the mean-square of the particle velocity fluctuation can be approximated to $\sqrt{\overline{v^2}} \approx u^*$ (See Williams et al. (1996), Skartlien et al. (2011)). For horizontal flows both the gravity and turbulence contribute to the droplets deposition (Williams et al. (1996), Mols et al. (1998); Pan and Hanratty, (2002)). Williams et al. (1996) considered both effects and proposed a correlation for the droplets deposition rate in horizontal flows

$$k_D = \frac{C_w}{C_B} \left[ \sqrt{\frac{1}{2\pi}} \sqrt{\overline{v^2}} + w cos\,\theta \right] \tag{7.17}$$

Where $C_w$ is the concentration at the wall, $\theta$=0 is the pipe bottom

$$C_B = \frac{1}{D - hw} \cdot \int_0^{D-hw} exp\left(\frac{-w \cdot y_{hw}}{\varepsilon}\right) dy_{hw} \tag{7.18}$$

The deposition rate requires a droplet sizes model (through the settling velocity term). This gives a dependence between the prediction of the interface concentration and the previously discussed constant $\varphi = \varepsilon / w$.

The local concentration of oil and water at the pipe wall can be obtained by extrapolating the cross sectional data to the pipe wall for the 2D sampled cases or as it is considered a uniform distribution of droplets in the cross section $C_w$ is obtained from the vertical profiles. An average deposition rate can be calculated as

$$\langle k_D \rangle = \frac{1}{\pi - \theta} \left[ \int_\theta^\pi \frac{C_w}{C_B} \sqrt{\frac{1}{2\pi}} u^* d\theta + \frac{C_w}{C_B} w cos\,\theta d\theta \right] \tag{7.19}$$

If the experimental data is available for validate the model, the concentration at the wall can be obtained from the experiments as shown in Figure 7.4. However if the model is used for predictions the calculation of the concentration at the interface needs to be solved in an implicit way. It is still required a good model for the droplet sizes and to select empirically the proportionality factor $k'_A$. Under all this considerations the model is capable to give fairly good predictions of the droplet concentration profiles. However it is limited to the available

experimental data ranges. In the light of these results and limitations, a second approach is proposed. In this case an initial attempt of finding a unique fitted correlation for $C_o$ and $\varphi$ and is presented in the following section.

## 7.5 Correlation for $C_o$ and $\varphi$

A new methodology is proposed to find correlations for the interface droplet concentration $C_o$ and the constant $\varphi$ that fit the exponential droplet concentration profile of a set of experimental data. The main advantage of this approach is that the implementation is simple and it does not required either a model for the droplet sizes or to tune a specific $k'_A$ to each data set. Also gives more flexibility to improve the model and expand the applicable model ranges when new experimental data becomes available. The main drawback is that similar to the previous approach, the correlations are limited to the experimental range. The range of the correlations is also limited to a good selection of independent variables related to the fitted parameters.

The correlations are built using genetic algorithms and the implementation is done based on binary trees and Prüfer encoding. The methodology and implementation is based on the work from Borregales, Capelleto, et al. (2014) and Borregales, Cappelletto, et al. (2014). An advantage of utilizing this methodology is that it allows finding a model or correlation regardless of the number of independent variables to be used and without having previous information on the data behavior. A simplified scheme of the methodology is presented in Figure 7.5 and Figure 7.6 .


Figure 7.5: Steps required to build correlations using the methodology from Borregales et al. (2013)

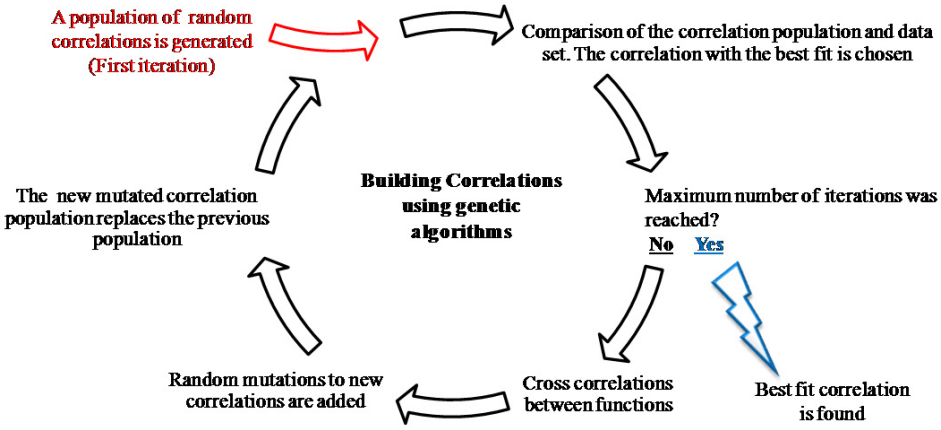


Figure 7.6: Summary of the genetic algorithm methodology for building correlations.

The experimental data has been described in this and previous Chapter and in the literature. The experimental data can be represented using the exponential model mentioned in equation (7.2). Two correlations are required to fit the theoretical model $C_o$ and $\varphi$. To analyze the dependence between variables, the available data from the literature on the liquid droplet concentration profiles was gathered together with the current experimental results. (40 two-phase flow experimental profiles at different conditions). Reference values for $C_o$ and $\varphi$ for each individual experiment were obtained by fitting a curve with the shape $C = C_o \cdot exp(-\varphi \cdot y_{hw})$ in Matlab. The effect of the physical variables and operational points ($Usg$, $U_{sl}$, $h_w$, $\rho_l$, $\rho_g$, $D$, $\alpha_g$, $\mu_g$, $\mu_l$ and $\sigma$) on the predicted $C_o$ and $\varphi$ can be studied and trends of them could be found. However these variables can interact and a more appropriate way of foreseeing the effect of them is through non-dimensional numbers. In this case, the superficial liquid and gas Reynolds number and the liquid height based Weber number are adopted and defined below.

$$Re_{sl} = \frac{\rho_l UslD}{\mu_l} \qquad Re_{sg} = \frac{\rho_g UsgD}{\mu_g} \qquad We_{hw} = \frac{\rho_l U_G^2 h_w}{\sigma}$$

The selected non-dimensional numbers have different magnitude orders so in order to facilitate the correlation building process the non-dimensional numbers were balanced as:

$$\delta_1 = \frac{Re_{sl}}{10000} \qquad \delta_2 = \frac{Re_{sg}}{100000} \qquad \delta_3 = \frac{We_{hw}}{1000}$$

The experimental data selected for the correlation is limited to the available high pressure experimental profiles (from Tayebi, (2000) and the current data sets for the lower oil viscosity) and the low pressure profiles (from Williams (1990) and Paras and Karabelas (1994)). Different gas densities, liquid phases, three pipe diameters and different flow velocities are included in this correlation and they are summarized in Table 7.1.

Table 7.1: Summary of experimental conditions used in the correlations building process

| | |
|---|---|
| *Number of experiments* | *40* |
| *Liquid phase* | *Water, Exxsol-D80* |
| *Gas phase* | *Air, $SF_6$* |
| *Gas density* | *1.2 Kg/m$^3$ - 46.5 Kg/m$^3$* |
| *Diameter* | *0.0508 m, 0.0689m,0.0953 m, 0.1m* |
| *Liquid density* | *813 Kg/m$^3$-998 Kg/m$^3$* |
| *Liquid viscosity* | *0.001Pa s-0.0018 Pa s* |
| *Surface tension* | *0.02-0.06 N/m* |
| *Superficial gas velocity* | *3.35 m/s - 61.5 m/s* |
| *Superficial liquid velocity* | *0.03 m/s-0.25 m/s* |

The proposed methodology delivered the following expressions for the interface concentration $C_o$ and the constant $\varphi$.

$$\lambda = 0.2 \cdot \delta_1^{0.3} \cdot log_{10}\left[0.1098 + \delta_2 \cdot \left(exp\left(\frac{1.6\delta_3 + 0.2863}{exp(\delta_3) + ln\left(\delta_3\left(\delta_3 + 0.0314\right)\right)}\delta_3\right)\right)\right] \tag{7.20}$$

$$C_o = \frac{10 \cdot \left[ 0.05\delta_1 + 1.5\delta_2 + \left(\delta_3^{0.9}\right) \right] \delta_1^3}{\delta_3 + \left( exp\left(1.36\delta_1 - 0.86\delta_3 - 0.1216\right)\right)^{1.6}} \tag{7.21}$$

Five examples of the predictions with the correlations are presented in Figure 7.7. To show their capabilities under different flow conditions and experimental setups it is shown: 1 set from the current experiments (Case 1,*WC*=0, *Usg*=7.3 m/s, *Usl*=0.2 m/s), 2 sets from Tayebi (Case 2, *WC*=0 and Case 3,*WC*=1, *Usg*=7 m/s, *Usl*=0.25 m/s, *P*=3.6 bar), one set from Williams (1990) (Case 4, *WC*=1, *Usg*=31 m/s, *Usl*=0.03 m/s, *P*=1 bar) and one set from Paras and Karabelas (1994) (Case 5, *WC*=1, *Usg*=31.6 m/s, *Usl*=0.06 m/s, *P*=1 bar). A good agreement is found between most of the experiments and predicted values. However the correlation performance for the data using the more viscous oil (39 cP) is not satisfactory and more work should be done to obtain a better function to fit this case.

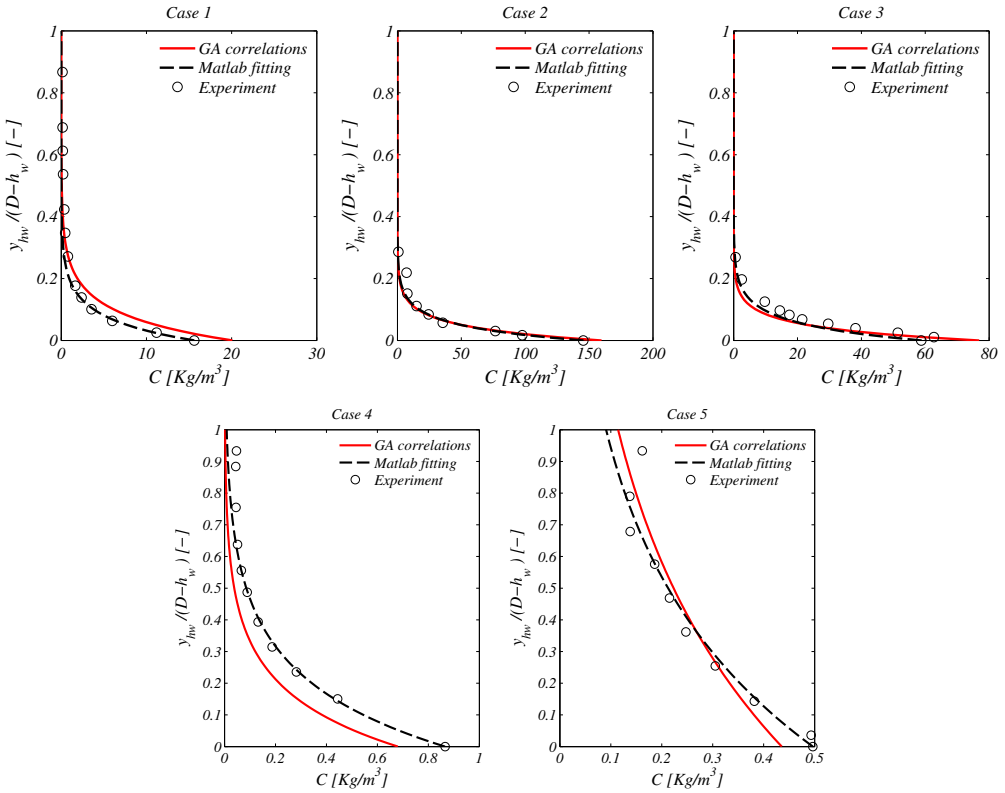


Figure 7.7: Predicted concentration profiles with Genetic algorithm correlations for $C_o$ and $\varphi$ and comparison with fitted curves using Matlab

The mean droplet concentration in the gas phase can be calculated from the gas liquid interface to the top of the pipe assuming a flat gas-liquid interface as

$$\langle C \rangle = \frac{2}{A_g} \int_{hw}^{D} \sqrt{R^2 - (y-R)^2} \cdot C(y)\, dy \tag{7.22}$$

The performance of the correlations is presented as the comparison of the mean droplet concentration obtained from the fitting curve from Matlab and the predicted by the correlations for *Co* and $\varphi$. The 1D integration was performed numerically using the trapezoidal rule. Most of the predictions for the two-phase flow date are below 30% difference with the Matlab (Figure 7.8).

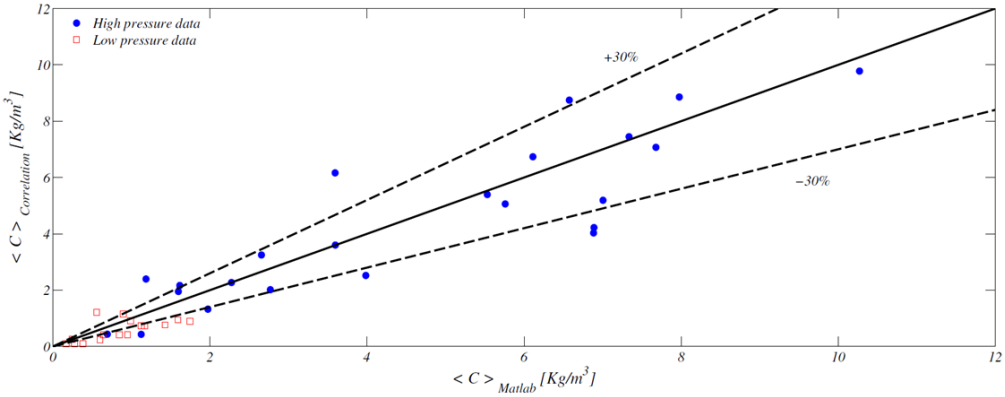


Figure 7.8: Comparison between mean droplet concentration predictions from correlation and Matlab fitting

The presented correlations were developed for two-phase gas-liquid flows. However their extent and performance on the concentration profiles prediction for three-phase flows is unknown and for this reason it is tested below. Following the assumption proposed by Skartlien et al. (2011), the oil and water phases are considered as a mixture as they entrain into the gas phase. Once there, the oil and water droplets separate. The entrainment is considered to be controlled by the majority phase. Based on the experimental results presented in Chapter 6, the shapes of the oil and water profiles are very similar for a constant watercut value, especially close to the interface ($\varphi_o = \varphi_w$). In addition, the local watercut at the interface was observed to be similar than the input watercut. For these reasons the prediction of the water droplet concentration profiles is obtained from the oil droplet concentration profiles. The local watercut at the interface can be written in terms of the interfacial water and oil droplet concentrations as

$$WC_{interface} \approx WC = \frac{q_{winterface}}{q_{winterface} + q_{ointerface}} = \frac{C_{o,w}/\rho_w}{C_{o,w}/\rho_w + C_{o,o}/\rho_o} \tag{7.23}$$

Where $C_{o,w}$ and $C_{o,o}$ are the water and oil droplet concentrations at the interface respectively. The water concentration can be calculated from the expression above as

$$C_{o,w} = \left[\frac{WC}{1-WC}\left(\frac{\rho_w}{\rho_o}\right)\right]\cdot C_{o,o} \tag{7.24}$$

In Figure 7.9, the predicted profiles for simultaneous oil and water droplet concentrations are shown for Exxsol D80-water-$SF_6$ at 4.7 bar, *Usl*=0.2 m/s, *Usg*=8.9 m/s and different watercut

values. On the plot the circles and stars symbols represent the oil and water concentrations respectively. There is a good agreement between the experiments and the predictions. Comparisons between predictions and experiments for the rest of the experimental data from this work are shown in Appendix E. Even though the oil correlation was not designed to predict three-phase flows it gives a good performance against the tested data from this work. The correlations were also tested against the data from Skartlien et al. (2011) and for most of the cases under predict the concentration profiles. However it gives the correct order of magnitude of the predicted $C_o$. The effect of the watercut seems to be well described by the use of equation (7.24).

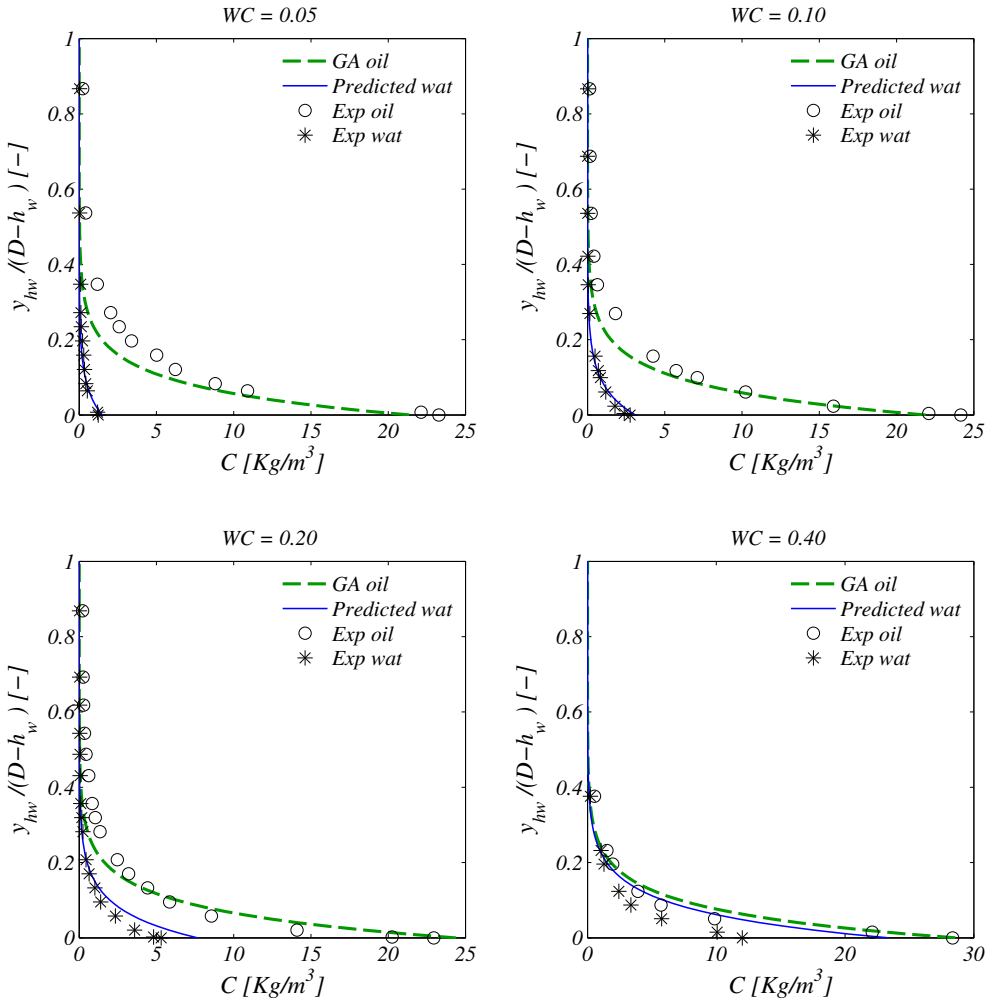


Figure 7.9: Predicted concentration profiles obtained with the Genetic algorithm correlations for $C_o$ and $\lambda$ (Exxsol D80-water-$SF_6$ at 4.7 bar, *Usl*=0.2 m/s, *Usg*=8.9 m/s, D=0.069 m)

## 7.6 Summary

The current state of the models available in the literature for the prediction of droplet concentration profiles is reviewed. The models depend on tuning the proportionality factor $k'_A$ and on having a good correlation for the prediction of the droplet diameter. In contradiction with previous studies, it was not found any trend of the normalized diffusivity value with the current pipe diameter. However it was noted that fairly good predictions were obtained when using a normalized pipe diffusivity of $\zeta$=0.074 and the droplet diameter correlation from Pan and Hanratty (2002).

Genetic algorithms were applied to obtain correlations for the interface concentration and the constant $\varphi$. These correlations are expressed in terms of three non-dimensional parameters including the effects of the physical fluid properties and operational conditions. The correlations give a fairly good prediction for all the tested experimental data at low liquid viscosities but fails on the case of 39cP oil viscosity. The use of the obtained two-phase flow correlations is extended to the three-phase flows cases where the oil droplets concentration profiles are predicted by the correlation and the water droplet concentration profiles are predicted by the interfacial watercut and the oil interfacial concentration. This methodology allows for improving the correlations for $C_o$ and $\varphi$ while more experimental data is gathered. The correlations might be improved in the future by using different non-dimensional numbers to the chosen in this study.

# Chapter 8

# Development of a two energy 5 beams gamma densitometer

## 8.1 Introduction

The main objective of this study is to develop a two-energy multiple beam gamma densitometer. The instrument is designed to obtain cross-sectional measurements of the phase fractions, capture transient flow conditions and for three-phase flow measurements (oil, water and gas) in acrylic pipes. This is an ongoing project lately developed together with the PhD student Mariana Diaz and Halvor Haukvik. This work is done in cooperation with SINTEF Petroleum Research and FACE and as the continuation of the work from Plasencia (2013).

## 8.2 Previous work

Plasencia (2013) studied the feasibility of using Americium ($Am^{241}$) and Barium ($Ba^{133}$) as gamma sources for the densitometer. In his work, a summary of the global pros and cons related to each source is shown (See Table 8.1). Tests using an existent $Am^{241}$ and $Ba^{133}$ source were performed using different pipe sizes and fluids and possible CdTe detectors from Eurorad. Due to the higher counting rate and resolution seen from the obtained spectrograms the CdTe 5x5x2$mm^3$ detector model S.5.5.2.U was decided to be used on the instrument. The detector is mounted in an aluminum casing with a BNC connector and tested with a PR16-H charge sensitive preamplifier.

Two possible source-detector configurations were suggested in his work. The first one is considering one collimated source and 8 collimated detectors. The main limitation of this configuration is the required source activity due to the distance between the sources and detectors. The second suggested configuration is 8 sources and 8 detectors. In this option special

care should be taken when designing the collimators in order to avoid gamma rays from a neighbor source.

Table 8.1:Pros and cons chart for Americium ($Am^{241}$) and Barium ($Ba^{133}$) from Plasencia (2013).

| *Source* | *Advantages* | *Disadvantages* |
|---|---|---|
| *Barium ($Ba^{133}$)* | *Higher energy levels (≈ 400 keV, better penetration)* | *Shorter lifetime (10 years)*<br>*Higher cost (≈ 7300€ each)*<br>*Thicker shielding* |
| *Americium ($Am^{241}$)* | *Longer lifetime (432 years)*<br>*Lower cost (≈ 3600€ each)*<br>*Lower energy level peaks (18 and 60 keV)*<br>*Up to 11 Gbq* | *Lower energy levels (≈ 100 keV, bad penetration)* |

## 8.3 Gamma source selection

There are two important aspects to take into account when selecting the gamma source. One of the challenges is the liquid-liquid discrimination and low gamma ray energies are preferred to achieve this task. The second one is a high sampling speed to capture transient flows. The spectrograms from Plasencia (2013) were integrated over their respective energy windows and the total counting rates were compared for $Am^{241}$ and $Ba^{133}$. (See Table 8.2 and Table 8.3). $Am^{241}$ provides with higher counting rates than $Ba^{133}$ for all energy levels. The counting rates of $Am^{241}$ are high enough to get a high sampling speed in contrary to $Ba^{133}$. The oil-water contrast seems to be better for $Ba^{133}$ than for $Am^{241}$. Limitations on the use of $Am^{241}$ for three-phase flow applications have been discussed in Chapter 2.

The number of sources will be limited to the minimum size of the pipe it is planned to be used. Even though the instrument is designed for pipes up to 90 mm ID, it will be used mostly in 60 mm ID. For this reason and due to the source and detector dimensions it was decided to reduce the number of sources to 5. $Am^{241}$, 3.7 GBq sources (Eckert and Ziegel. Model: AM132330100M) were requested from Gammadata. A scheme of the selected source is shown in Figure 8.1.

Table 8.2:Summary of the integrated values from Spectrum. $Am^{241}$

| *Energy Level* | | *ID60-Air* | *ID60-Oil* | *ID60-Water* | *ID90-Air* | *ID90-Oil* | *ID90-Water* | *Empty Pipe* |
|---|---|---|---|---|---|---|---|---|
| ***18 keV*** | ***Total counting (counts/s)*** | *51307* | *19627* | *12529* | *50204* | *13673* | *11509* | *80085* |
| | ***Fluid/Empty*** | *0.64* | *0.25* | *0.16* | *0.63* | *0.17* | *0.14* | *1.00* |
| ***60 keV*** | ***Total counting (counts/s)*** | *358865* | *187226* | *150347* | *358384* | *135044* | *102457* | *405397* |
| | ***Fluid/Empty*** | *0.89* | *0.46* | *0.37* | *0.88* | *0.33* | *0.25* | *1.00* |

Table 8.3:Summary of the integrated values from Spectrum. Ba 133

| *Energy Level* | | *ID60-Air* | *ID60-Oil* | *ID60-Water* | *ID90-Air* | *ID90-Oil* | *ID90-Water* | *Empty Pipe* |
|---|---|---|---|---|---|---|---|---|
| ***31 keV*** | ***Total counting (counts/s)*** | *9867* | *3497* | *1932* | *9670* | *2064* | *894* | *13118* |
| | ***Fluid/Empty*** | *0.75* | *0.27* | *0.15* | *0.74* | *0.16* | *0.07* | *1.00* |
| ***81 keV*** | ***Total counting (counts/s)*** | *3256* | *1511* | *1249* | *3285* | *1021* | *821* | *3877* |
| | ***Fluid/Empty*** | *0.84* | *0.39* | *0.32* | *0.85* | *0.26* | *0.21* | *1.00* |

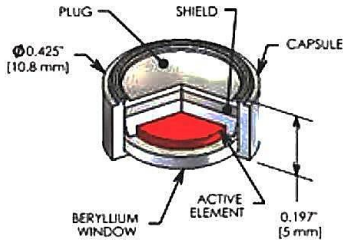


Figure 8.1: $Am^{241}$ source with beryllium window for Gammadata (Eckert and Ziegler, 2006)

## 8.4 General design

The five sources and detectors are arranged in the configuration shown in Figure 8.2. The detectors are connected to their respective pre-amplifiers and energized by a high power supply unit. Each of the preamplifiers is connected to a spectroscopy amplifier and from there to a computer with multichannel analyzer software. The sources, detectors and preamplifiers should move as a unit inside holders and they should have the capability to rotate around the pipe or traverse it linearly.

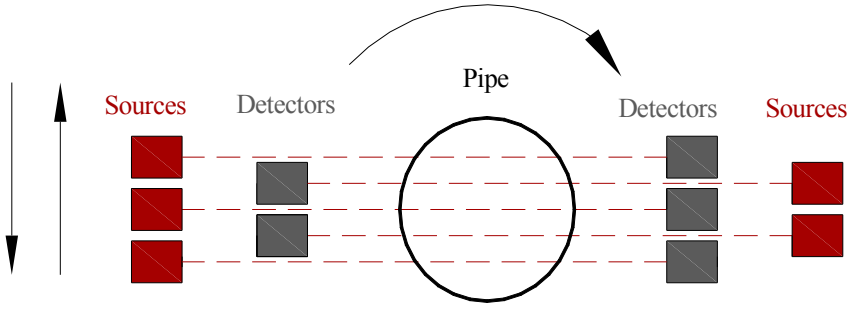


Figure 8.2: Simplified scheme of the gamma densitometer

Different mechanical parts needed to be designed and built: Gamma sources holder, detectors holder and collimation unit, rotary and linear movement mechanisms and additional safety mechanisms. A picture of the instrument showing the main parts is shown in Figure 8.3 and

details about them are given in the following sections. All the main parts of the gamma are built in an independent way in order to accommodate future modifications, if desired. The source holder is the only part of the instrument that does not allow major changes in order to ensure the integrity of the radiation container. Most of the mechanical parts of the instrument were built in stainless steel due to its attenuation coefficient and corrosion resistance.

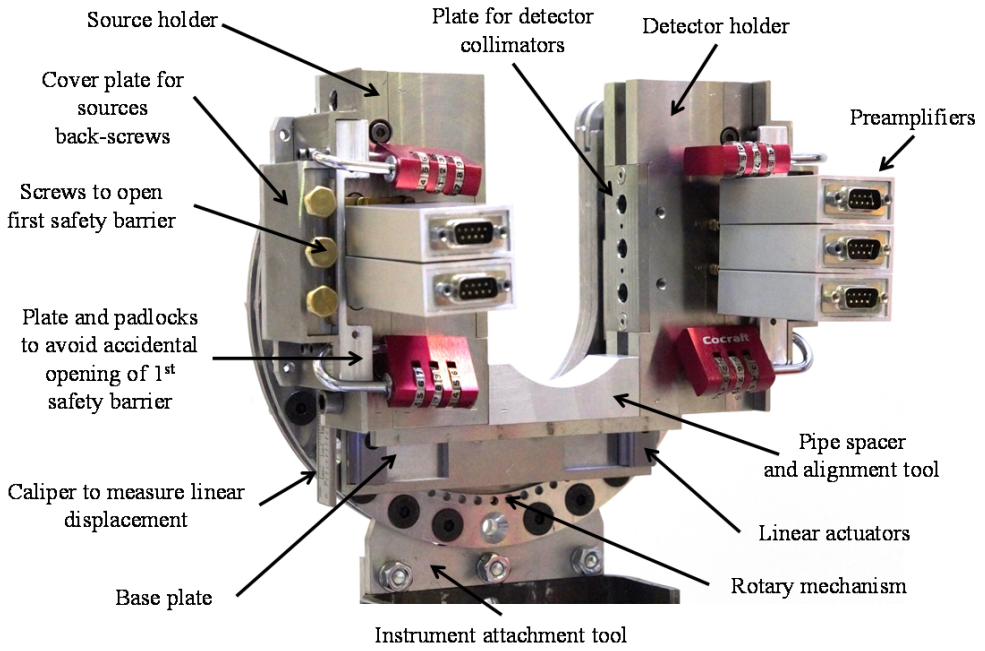


Figure 8.3: Main parts of the gamma densitometer

## 8.5 Sources holder and main safety mechanisms

The sources holder is the unit where the sources are stored and where the first and second safety mechanisms are located. Two holders were designed, one for each side of the instrument. The sources where safely installed inside the holders at the Institute for energy Technology (IFE) and they are shielded following the Norwegian law regulations for handling radiation. The shielding calculations are detailed in Appendix F. The holder is made in stainless steel needing a minimum material distance of 5.82 mm from the source to the outside. A lead 1.1 mm thick ring surrounding each source together with a 1 mm thick lead disc on the back of them give extra shielding to the holder. Each source has independent access given by a stainless steel 11 mm long screw. The screws were sealed by using glue to avoid opening them (it is still possible to open them in the future, if desired). As a safety measure, a plate is located covering the sources screws. In the source holder there are cavities where the detectors assembly is supported. The sources are located behind these cavities. It might occur that radiation from these sources is

detected from the back side of the detectors assembly. This should be tested in the future. However in case of back-reading there is available space to add a lead cover to provide extra shielding. A 3D representation of the source holder (for the 3 sources side) is shown in Figure 8.4. The detailed mechanical drawings of the source holder and it parts are shown in Appendix G

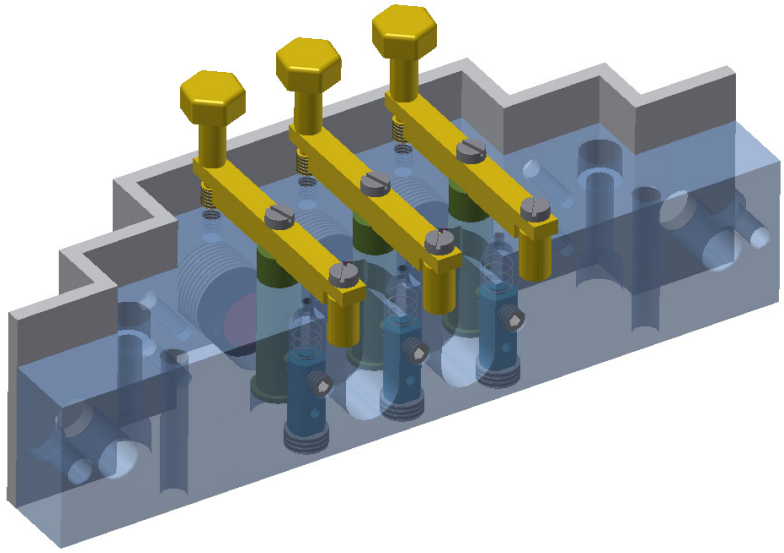

Figure 8.4: Source holder 3D representation (3 sources)

The source holder should be safely shielded when is not in operation. For this reason, two independent barriers safety mechanisms were designed. The first safety barrier is manually closing and works as a gate. This gate allow to shut down the instrument when is not in use. Each source has an independent gate. The mechanism consists of a tungsten heavy alloy rod connected to a bar. When the mechanism is open a cylindrical 2.2 mm channel traversing the tungsten pin is aligned to the collimators allowing the radiation to go out. A screw should be removed to allow pulling up the bar and the tungsten pin. When the source holder is connected to the detector holder (as in normal operation), the first safety barrier is kept open by the action of a spring.

The second safety mechanism is normally closed by the action of a spring that pushes down a small tungsten heavy alloy pin. Similar to the first safety mechanism the pin has a small cylindrical 2.2 mm diameter hole to allow the radiation out. The barrier opens when the source holder is located, during operation, over the base plate which is equipped with three or two small pins (depending on the side of the instrument) that push the tungsten rods up. A sketch of the source holder safety mechanisms is shown in Figure 8.5.

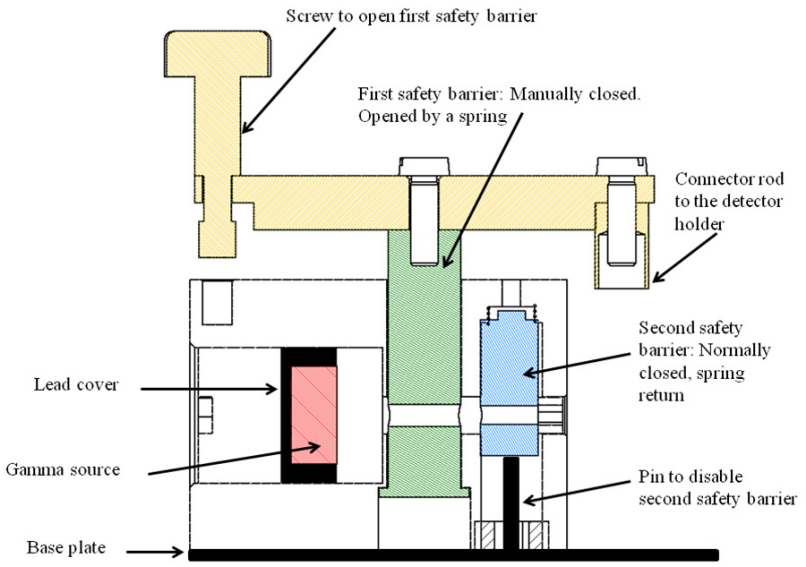


Figure 8.5: Details of parts in sources holder (Showing the configuration for one source and open safety mechanisms)

The two safety mechanisms have four possible operational configurations (See Figure 8.7). Two views of the source holder are presented in Figure 8.7 from the sections shown in Figure 8.6. In all the configurations the material in the source holder is enough to keep the radiation dose under the maximum allowed by the Norwegian law.

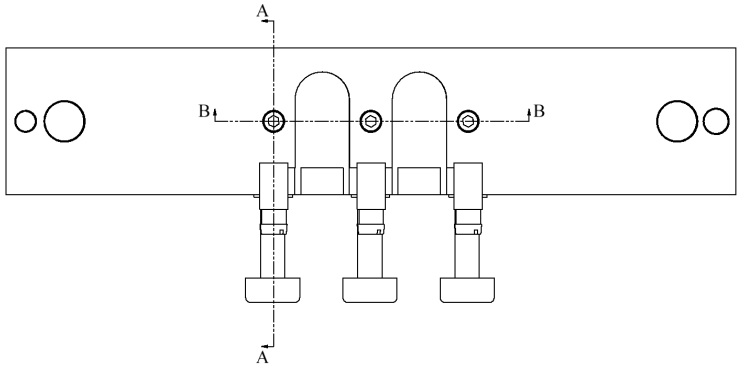


Figure 8.6: Sections on the source holder

The radiation dose was measured at IFE before shipping the instrument to the NTNU. Instantaneous readings of the radiation with the two safety mechanisms closed at the wall in front of sources open area was less than 2 μSv/h. On the same location and with one of the safety mechanisms open the obtained readings were 5 μSv/h. The efficiency of the safety mechanisms was tested by tests conducted at IFE and by the NTNU HSE division (See NTNU HSE division (2014))

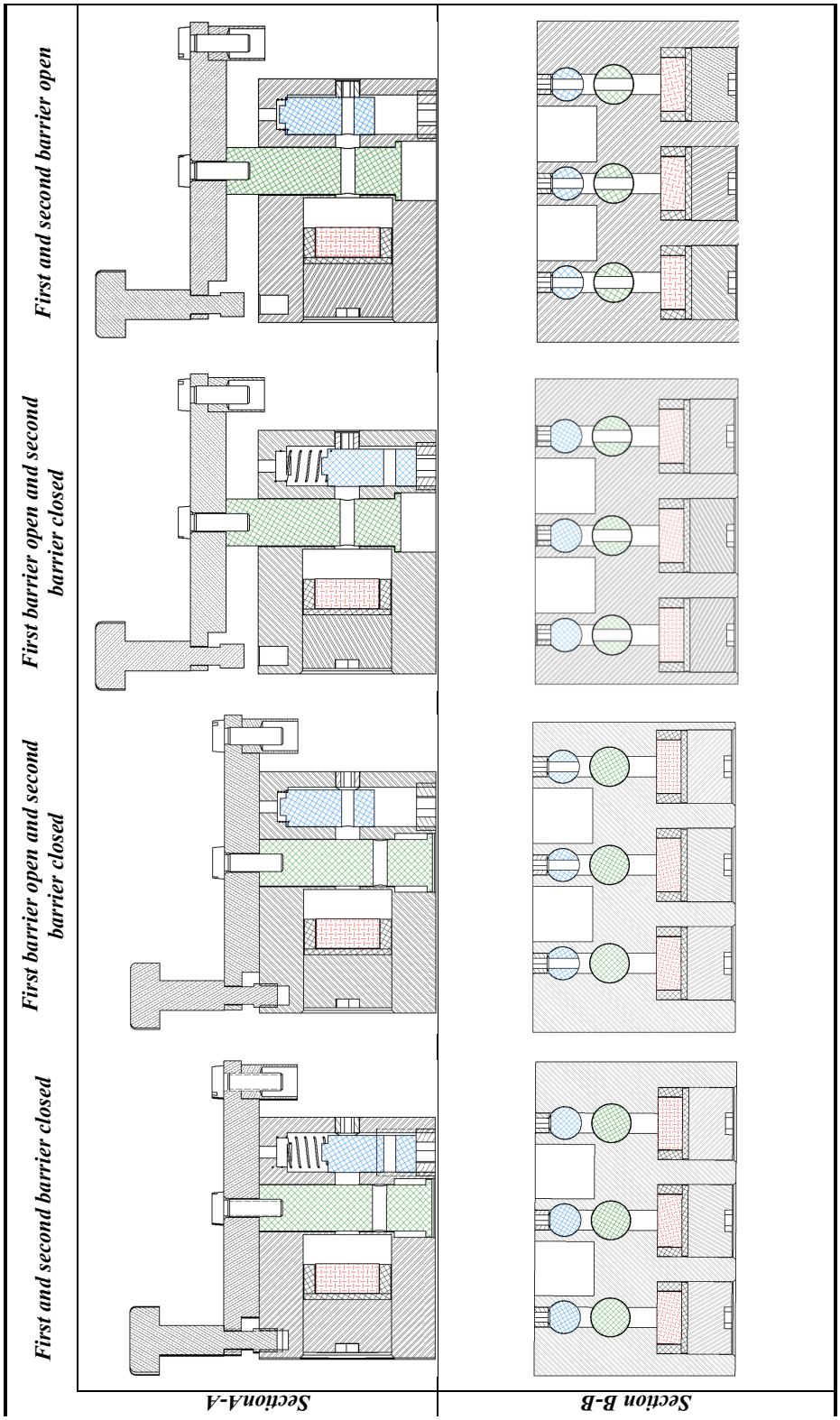


Figure 8.7: Operational configurations of the source holder

## 8.6 Detectors holder and collimation unit

The instrument has two detector holders, one in each side of it. This part is attached to the source holder by the connector rod in the safety mechanism, as explained earlier. The main purpose of this part is to provide support and proper alignment of the detectors with it correspondent source in front and to allocate the collimators of the sources at the back. The collimators are used in the instrument for different reasons: To define the direction of the gamma rays from each source, to limit the region to be measured and the region to be seen by each detector and to prevent gamma rays from neighboring sources to be seen by the detector. The detector holder dimensions will be limited by the length of the detectors and also by the required size of the collimators. A plate is located in the front of the holder where the detectors collimators are placed. A 3D representation of the detectors holder (for the 3 sources side) is shown in Figure 8.8 together with a simplified detector-preamplifier assembly. The detailed mechanical drawings of these parts are shown in Appendix G.

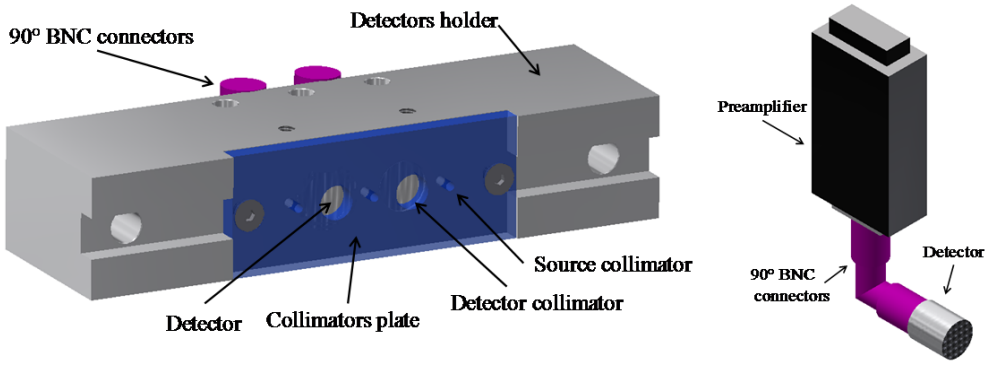


Figure 8.8: (a) Detectors holder and collimation unit (b) Detector-preamplifier assembly

The sources are collimated by 70 mm long cylindrical channels of 2.2 mm of diameter. In front of the detectors a small plate is attached including 5.5 mm long cylindrical collimators of 8.5 mm of diameter. The total attenuated photon flux with an empty pipe was estimated to be 36878.52 counts/s and 192963.45 counts/s for 13.9 KeV and 59.5 KeV respectively.

## 8.7 Rotary and linear movement mechanism

A rotary mechanism was designed to allow the instrument to freely rotate around the pipe. Every 5°, fixed locations are available to fix the densitometer. The linear movement is adjusted by sliding the instrument using a pair of linear bearings. A rack and pinion system is used to precisely locate the instrument at the desired position. A modified digital caliper is attached to the moving linear mechanism to know exactly the position of the instrument. Attached to the

linear bearings a base plate is located were the holders and rest of the parts will be placed. A 3D representation of the rotary and linear mechanism is shown in Figure 8.9. The detailed mechanical drawings of these two mechanisms are shown in Appendix G.

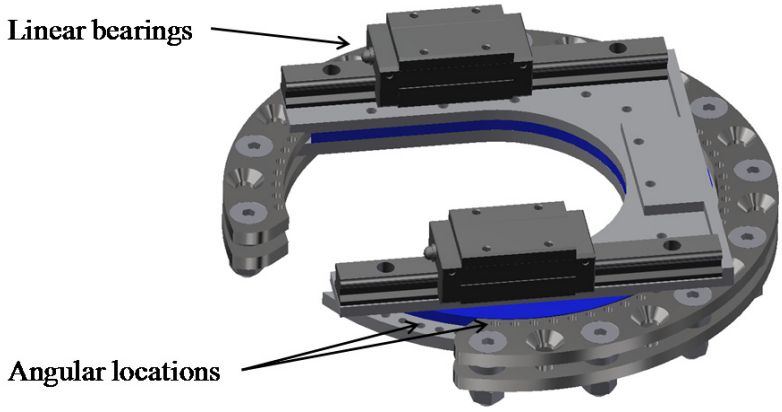


Figure 8.9: Rotary and linear movement mechanism

## 8.8 Electronic system

The gamma rays from the sources are received by the CdTe detectors at the opposite side of the instrument. At the detector, the gamma ray photons interact with the material. A high voltage supply is required to give the electric field to collect the charge produced by the interaction between the gamma ray and the detector. The Canberra 3106D power supply was selected for this application as is specially designed for operation with semiconductor detectors requiring up to 6 kV bias and up to 300 μA of current.

The output from the detector is then an amount of energy proportional to the absorbed amount of gamma ray energy by the detector (Gilmore (2008)). The preamplifier connected to the detector collects the produced energy and supplies it to the amplifier. Different types of preamplifiers are available. However, as the detectors are high-resolution ones, the selected preamplifiers are charge sensitive type (PR-16 from Eurorad). The detector and preamplifier are connected as close as they can be in the fixture. This maximizes the signal-to-noise ratio of the output pulse and preserves the gamma ray energy information (Parker (1991)).

The pulses leaving the preamplifier are sent to the amplifier. The main function of the amplifier is to shape the pulse and convert it into a suitable signal for the pulse-height analysis instrumentation afterwards. This is done by filtering the signal electronically. One spectroscopy amplifier is required for each detector in the system. For this instrument a Canberra amplifier model 2022 was selected.

The amplified pulses are sent now to a multichannel analyzer. This analyzer comprises a digitizer (Spectrum model M2I.3122-EXP 12 bit) and a PC with analysis software which will be designed by SINTEF Petroleum Research.

## 8.9 Further work

The design, building and assembly of the new gamma densitometer parts is finished. All the electronic parts are in place and the following activities comprises the development of the analysis software by SINTEF Petroleum Research and the testing stage in the Multiphase flow lab at NTNU. The design of the collimators and efficiency of the process should be evaluated during this experimental campaign. This work will be continued by a PhD student and a Post Doc from the multiphase flow group at NTNU.

# Chapter 9

## Experiments on gas flow with wet pipe walls

*This chapter was partially published in the 9th North American Conference on Multiphase flow. BHR Group*

Measurements of the pressure drop and liquid hold up in a gas flow with wet walls were carried out in a vertical pipe at NTNU Multiphase Flow Laboratory. The experiments were performed as a flushing process, where an initial liquid film becomes thinner with time as it is removed by gas flow. Quick closing valves were used to measure the liquid holdup in the vertical section. Two data sets using Air-Water and Air-Mineral oil were obtained. A significant increase in pressure drop with small amounts of the liquid holdup was observed. Pressure gradient and holdup behavior were reproduced quite well by commercial flow simulators but the flushing time showed discrepancies.

### 9.1 Introduction

Annular flow is a common flow pattern found in many industrial applications. This type of flow occurs at high gas and low liquid velocities. The liquid is transported as a film on the walls and as droplets entrained in the gas phase (Hanratty (1991)).The entrained droplet field in the gas core of separated gas-liquid flows in pipelines affects the flow in two ways: the droplet field provides efficient liquid transport and the droplets can deposit on the wall and enhance the wall friction and pressure drop. For horizontal flows, stratification of the liquid occurs due to gravity, the flow symmetry disappears and the film thickness is larger on the bottom than on the top making the analysis difficult (Chupin (2003)). For this reason in this study a vertical pipe configuration was used.

To predict the phase distribution in a pipe, the mass and force balance on the film and the gas core should be written and an estimation of the interfacial shear-stress is needed (Belt et al. (2009)). This estimation is given in terms of the interfacial friction factor *fi*, the gas density and velocity. For the estimation of *fi,* several correlations have been proposed in the literature (See Wallis (1969); Henstock et al. (1976), Belt et al. (2009), L. B. Fore et al. (2000), Asali et al. (1985)) Most of them are modifications of the Wallis correlation (1969) which treats the liquid

film as a wall roughness. The modifications to this correlation are mainly done to fit a certain experimental data set. Pressure drop and film thickness are parameters of interest when developing interfacial friction factor correlations.

The principal objective of this study is to provide new experimental data on pressure drop and holdup values for low liquid flows and evaluate the predictions from flow simulators as LedaFlow® V1.4 and OLGA® 7.1 under film thinning experimental conditions.

## 9.2 Experimental conditions

Several tests were made in order to find appropriate experimental conditions. Two different experimental procedures were used in each case as the required oil flow rate was too small for the pump to operate. When using water as the liquid phase, the initial liquid film was established, in steady two-phase flows. The flow in each test was then observed visually in the acrylic pipe section as the film was drained by the gas flow.

In the case of oil, the film tests were done by introducing oil at a specified liquid valve opening for different amounts of time, and then the following film thinning process was observed in the acrylic pipe section. The air flow rate was selected to be the same as in the water case. The oil valve was kept open for 30 seconds and shut down afterwards. Air was injected at a constant rate from this moment and a uniform film was created after 2 minutes.

### 9.2.1 Experimental procedure

A Lab-view program was developed to control the different start up procedures. At a given time, a test section was closed with quick closing valves at each end. When closing the valves on each side of the test section, the air supply was closed 500 ms in advance, in order to avoid an upstream pressure build-up. The quick closing valves could also be opened and closed individually.

#### *9.2.1.1 Water case procedure*

Air and water was introduced simultaneously at $Usg$=37.3 m/s and $Usw$=0.006 m/s and run for 10 min in order to reach two-phase flow steady-state conditions (constant pressure gradient on the test section). The logging started and after 30 seconds the liquid supply was shut off and the dry-up process was initiated. At specific times, the air flow was shut down and the quick closing valves were simultaneously closed. The liquid holdup was measured by dividing the measured liquid volume in the test section to the total test section volume. Pressure drop was recorded from the logging files at the desired shutting time. (See Figure 9.1) Air was run for several minutes in order to clean the complete setup after each measurement.

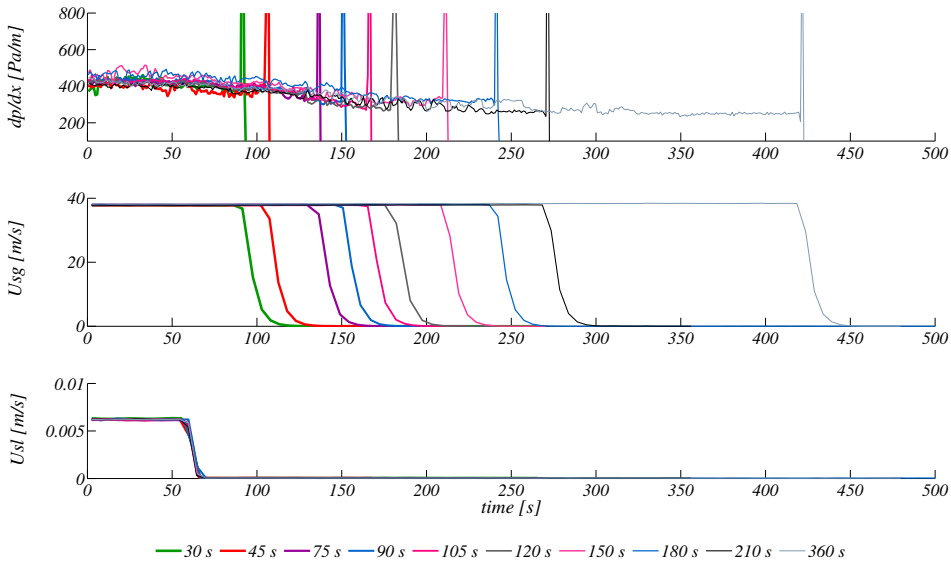


Figure 9.1:Description of the water experiments and repeatability of flow conditions for different shutting times

### *9.2.1.2 Oil case procedure*

The procedure for the oil experiments was different than the water case due to limitations on the oil pump operational range. No steady two-phase flow was present at the start of the dry-up process. A small oil volume was introduced into the horizontal section by setting the oil valve opening to 18% and closing it again after 30 seconds. Then the film thinning process was started by increasing the air velocity to *Usg*=37.3 m/s Time was measured from the instant at which the desired air flow rate was reached and a constant pressure drop value was obtained. The method was tested by repeating the mentioned procedure different times. An example of two oil-air runs is shown in Figure 9.2 to describe the repeatability.

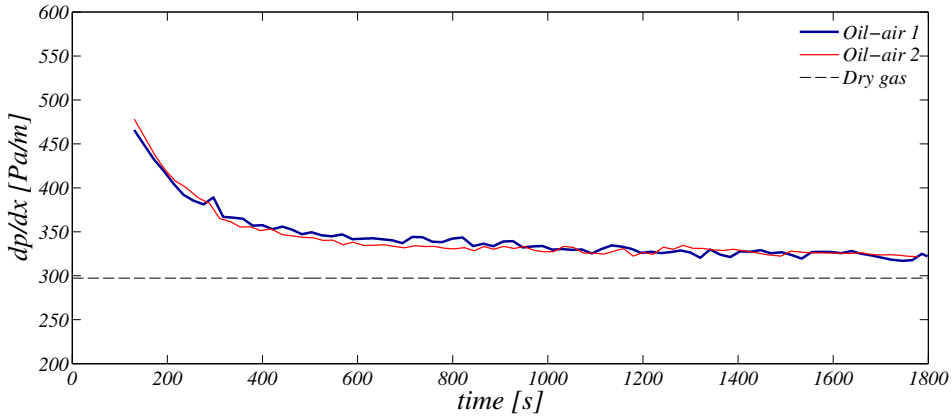


Figure 9.2: Repeatability of method used for Oil-Air experiments.

At specific times from the initial time (where the starting pressure drop was obtained) the air flow was shut down and the quick closing valves were simultaneously closed. From this point the remaining water experimental procedure was followed.

## 9.3 Results

Flow visualization of the dry-up process was done for each experiment through the acrylic pipe section (located on the top of the test section). The film breaking-down time was estimated by visual inspection on this clear section. The experiments started from a concurrent upwards annular flow. For the water case, the liquid film appears to be uniformly and covering the entire pipe. When the water source was shut down and air was kept constant, the film thinning started and for 75 seconds the flow regime was still annular flow. After this time the film breaks down and the pipe is partially covered by the film and ripples traveling upwards. At later times large single droplets move along the pipe wall. At 360 seconds the pipe was completely dry (See Figure 9.3). This behavior was similar to the one previously reported in (Chupin (2003)).

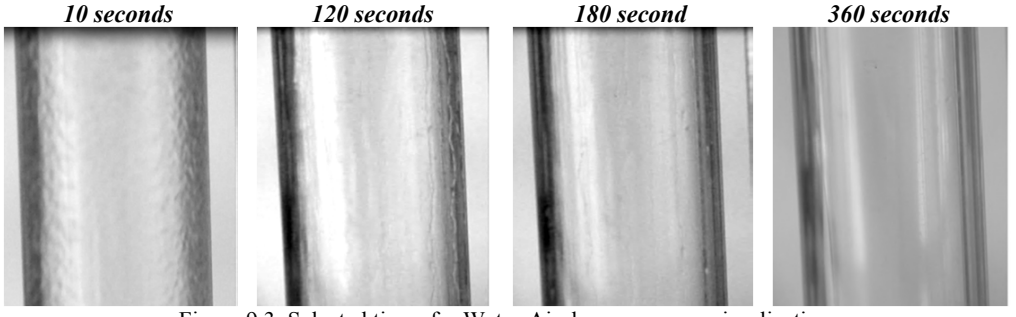


Figure 9.3: Selected times for Water-Air dry-up process visualization

For the oil case, the liquid film was initially observed to be equally distributed around the pipe. When the thinning process has started, the wave and film thickness are reduced. In this case no rivulet flow was observed as the film thins gradually. At later times (around 1300 seconds) a non-symmetrical thin film covered the pipe wall. Single-phase conditions could not be reached even after 30 min after the drying process has started (See Figure 9.4). Using the mineral oil which is sixty times more viscous than water the dry-up process takes considerable longer time.

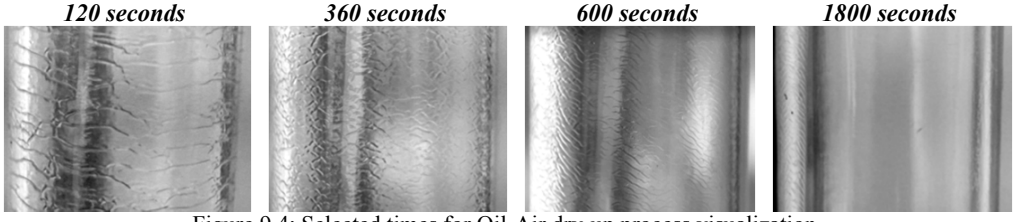


Figure 9.4: Selected times for Oil-Air dry-up process visualization

The pressure gradient and holdup measured during the drying experiments is shown in Figure 9.5a-b for the water case and on Figure 9.5c-d for the oil case. For the water case the pressure

gradient and the liquid holdup drop rapidly until reaching the value correspondent to the single phase. For water as liquid phase, the pressure gradient drops slightly under the single phase value. However, this is considered to be within the measurement accuracy. On the oil-air case the pressure gradient and holdup decrease smoother than in the water case.

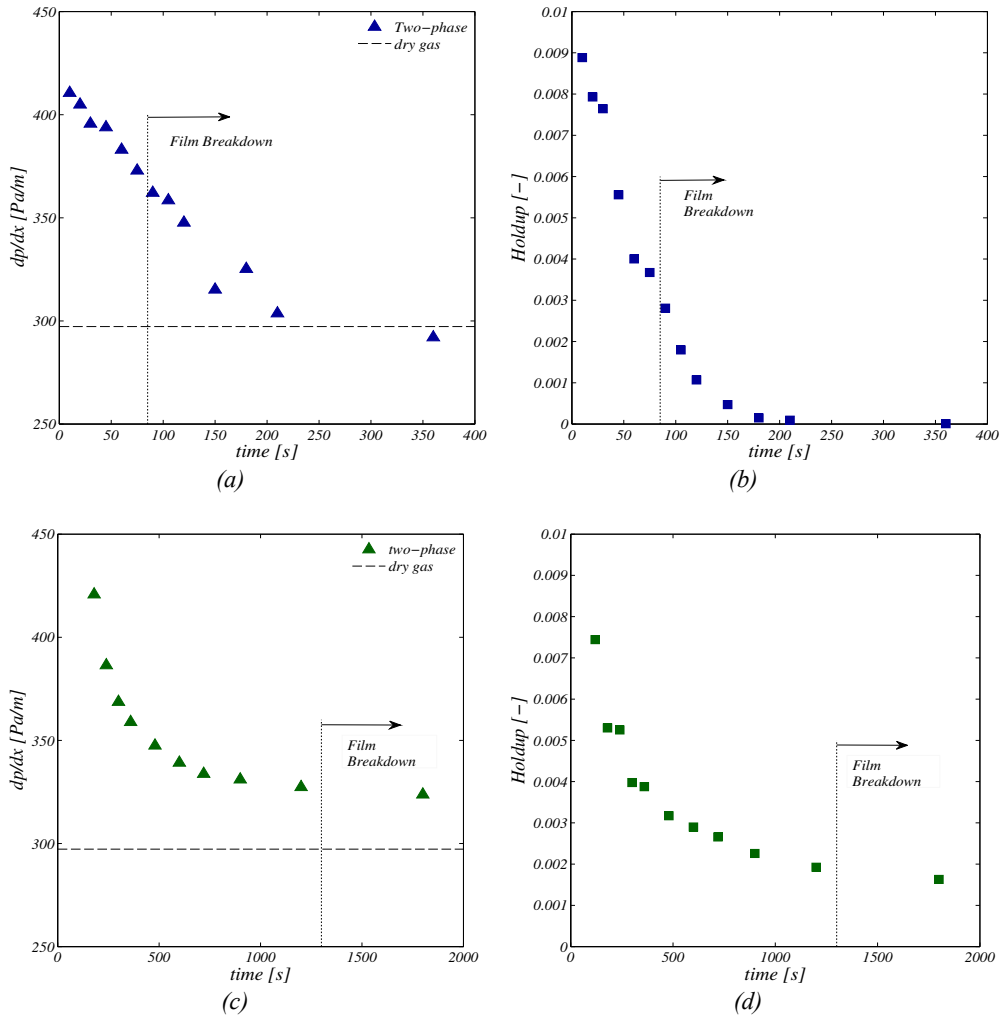


Figure 9.5 Pressure gradient and liquid holdup for the drying experiments. (a),(b)Air-Water. (c),(d) Air-Oil

In this study the film thickness was not measured. An average film thickness was calculated using the measured liquid holdup, assuming a uniform film distribution on the pipe wall and neglecting the liquid droplets. ($H = A_l / A = (R^2 - (R-h)^2) / R^2$, (See Figure 9.6). This assumption is only valid for the cases before the film breakdown.

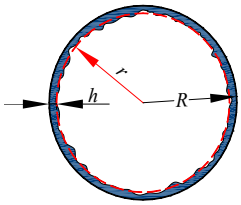


Figure 9.6: Thickness calculation, uniform liquid film distribution

$$h = R\left(1-\sqrt{1-H}\right) \tag{9.1}$$

Where R is the pipe radius and H is the liquid holdup. The film thicknesses for the water and oil experiments are between 42μm and 133 μm and 29μm and 112 μm respectively. Below this point the film has broken down and the uniform film distribution assumption is not valid (See Figure 9.7).

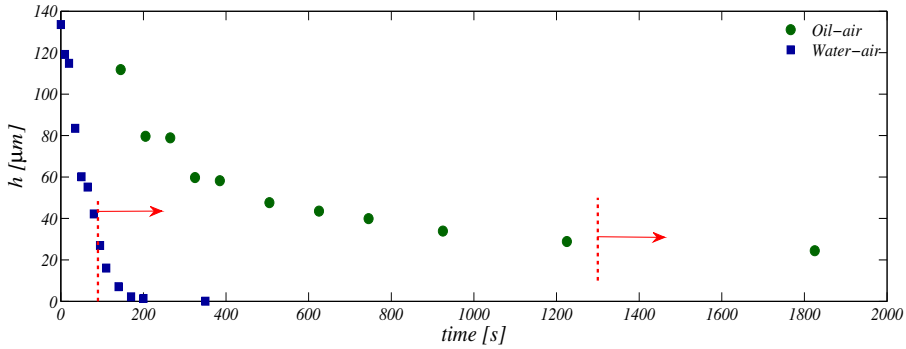


Figure 9.7: Average film thickness for both experimental setup

For vertical annular flow a correlation for the interfacial friction factor was proposed by Wallis (1969)

$$\left(C_f\right)_i = 0.005\cdot\left(1+300\frac{h}{D}\right) \tag{9.2}$$

The interfacial shear stress in annular flow is defined by (See Fore 2000)

$$\tau_i = \frac{\left(C_f\right)_i \rho_g U_g^2}{2} \tag{9.3}$$

Assuming no droplet entrainment conditions, the pressure gradient can be obtained by simplifying the momentum balance of the gas core presented by Fore et al. (1995)

$$-\frac{dp}{dz} = \frac{4\tau_i}{D-2h} + \rho_g g \tag{9.4}$$

A comparison between the pressure gradient and the film height for both experimental setups is shown together in Figure 9.8. The pressure gradient increases sharply with small increments on the film height for both studied cases. For low holdup ranges both experimental data sets gives

approximately the same pressure gradient values even though the oil viscosity it is considerably larger than water viscosity. At larger holdup values the difference between oil and water pressure gradient increases. However this is not conclusive as there is just one point on high holdup for the oil case and must be checked in further work.

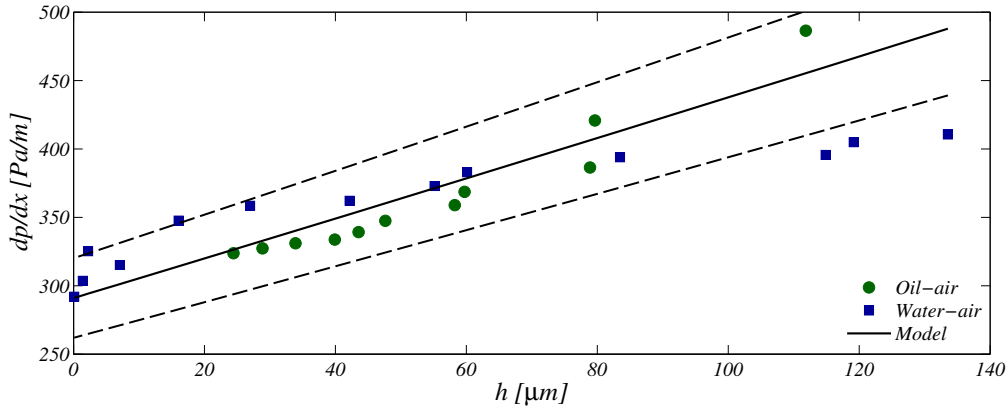


Figure 9.8 Relation between the pressure gradient and film thickness for both experimental setups

## 9.4 Comparisons with commercial flow simulators

Simulations in LedaFlow® v1.4 and OLGA® 7 were carried out using the same geometry, fluid properties (.tab file), and boundary conditions. The buffer tank was modeled as an equivalent pipe with the diameter 0.2 m and length of 8.125 m. Pressure in the outlet was kept atmospheric pressure. Temperature of the flow environment was the indoor at about 20°C.

Similar to the experiments, the procedure for the water case was different from the oil case. When having water as a liquid film, air and water were injected together, creating a steady two-phase flow. This flow was kept running for 600 seconds to make sure that steady state conditions were reached. Then the dry-up process was initiated by shutting off the liquid source. The predicted steady state pressure gradient using the experimental water flow rate is lower than the measured one for LedaFlow® V1.4. For this reason, the simulated water flow rate was set to a higher value for both simulations ($\dot{m}_w$ =0.056 Kg/s). This modifies the initial condition for the simulation (pressure drop, holdup values) but not the dry-up process itself which is the main point of interest in this study. (See Figure 9.9).

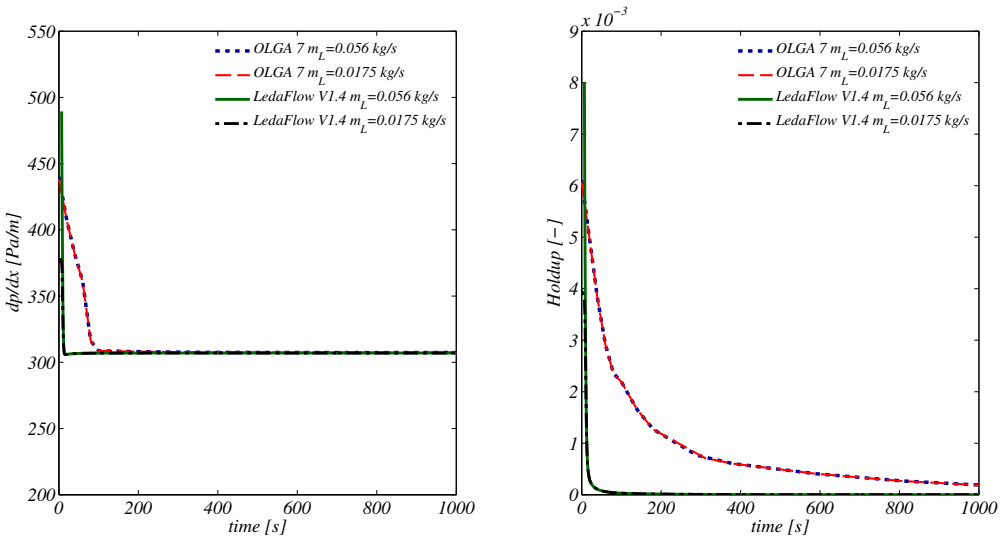


Figure 9.9: Sensibility to the water inlet mass flow rate

When having oil as a liquid film, the oil was injected for 30 seconds and at that time air flow started. For both water and oil cases, the simulations were run for 9000 seconds to reach either fully dry condition on the pipe or single phase gas flow. Particular attention has been given to the flow direction for both simulated cases and it was always verified that gas and liquid were flowing upwards and concurrent.

The holdup and pressure gradient predictions in LedaFlow® V1.4 and OLGA® 7 are shown in Figure 9.10. For the oil case, both simulators do not fully dry up the pipe before achieving gas single-phase conditions and for the water case OLGA® 7 repeat the same behavior. The pressure drop will keep constant from this point until the liquid holdup is finally zero up at 4000 seconds for the oil case and at 1500 seconds for the water case in OLGA® 7. The transition between two-phase flow with very low holdup and single phase flow is done as a jump in OLGA® 7 while it is smoother in LedaFlow® V1.4.This transition is correspondent with the occurrence of the experimental film breakdown and from this moment annular flow models are not applicable anymore. In general both simulators gives a fairly good prediction of the pressure drop and holdup for the oil case but over predicts the pressure drop for the water case. The film thinning behavior is represented by both simulators. However, in comparison to the experiments, the liquid flushing occurs very rapidly in LedaFlow® v1.4 and very slow in OLGA®7. For the water case and for low liquid holdups, both simulators under predict the pressure gradient and over predict it for the higher holdup values. For the oil case, both flow simulators over predict the pressure gradient.

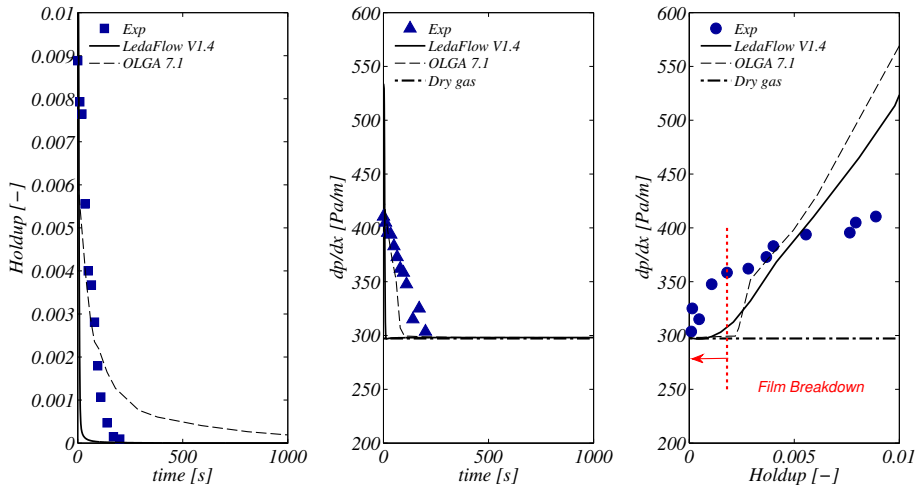


*(a)Water-Air case*

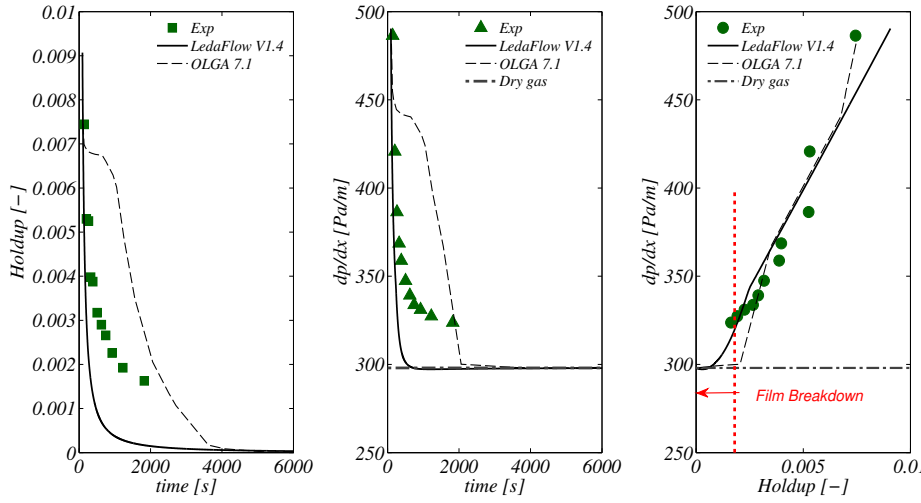


*(b) Oil-Air case*

Figure 9.10: Holdup and pressure gradient predictions in LedaFlow® V1.4 and OLGA® 7. (a) water-air case, (b) oil-air case

A sensitivity analysis was carried out to see the effect of the gas velocity (See Figure 9.11). For the tested configuration and flow conditions, the gas velocity is the parameter which influences the most on the film thinning process. The liquid viscosity, affects the transition between the film breakdown-annular and annular-annular mist flow and the flushing rate. These regions are observed on the OLGA® 7 plots for both oil and water cases.

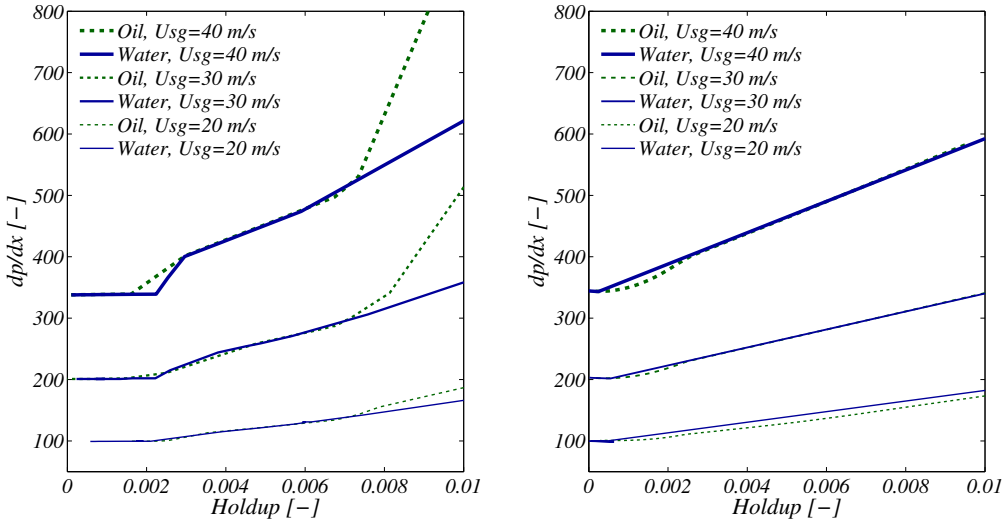


Figure 9.11: Sensibility analysis to the gas velocity for oil and water cases.

## 9.5 Summary

A study of pressure drop and holdup evolution in gas flow with wet walls has been carried out. This has been done by using an experimental setup in a vertical pipe to achieve symmetry. Two experimental data sets were obtained using water- air and a mineral viscous oil-air.

The pressure drop is very sensitive to small changes in the liquid holdup. The slope of this relation does not vary significantly with the liquid viscosity for low holdup values while for larger values in presence of droplets this difference grows.

The cases were simulated in the multiphase flow simulators OLGA 7.1 and LedaFlow V1.4. The pressure and holdup predictions for oil-air are reasonably well for the oil case. However the flushing time predictions are not accurate in comparison with the experimental cases and these results should be used with caution when using either flow simulators for this purpose.

# Chapter 10

## Conclusions

This thesis reports the experimental work on gas-oil-water flow with focus on droplet entrainment measurements and on instrumentation development for three-phase flows. Experiments in two-phase and three-phase flow were conducted in two laboratories. The main contributions and conclusions from this work are described below.

New instrumentation was developed to measure the droplet fluxes in the gas core of separated flows. The system consists of an isokinetic sampling probe to measure liquid droplet fluxes and the gas mass flow. The isokinetic condition sampling conditions are adjusted automatically and the effect on the sampling of possible pressure fluctuations in the pipe flow is avoided. The probe can traverse the whole pipe cross section. CFD studies of the probe were made to optimize and asses the design and installation.

Sampling of simultaneous oil and water droplets and gas were performed for 19 flow conditions and local droplet fluxes and gas velocities were obtained along the vertical diameter (1D) and over the gas cross section (2D). A methodology for the integration of the measured variables on the pipe cross section was presented and implemented. Non uniform droplet distribution in the pipe cross section was observed in all the tested experimental cases for two-phase or three-phase flows. The total entrainment fraction was calculated using two approaches: A 1D and 2D profile integration. The 1D approach yields, in general, larger fractions than the 2D. The maximum relative difference was 43% corresponding to the highest gas velocity.

The existence of secondary flows was detected by inspection of the gas velocity profiles plots for the tested flow conditions. The addition of water as a second liquid phase modifies the distribution of droplets flux in the gas region due to a modification of the secondary flows in the gas core. However, for the current experiments, the addition of water does not have a significant effect on the total entrainment fraction. The local watercut value close to the gas-liquid interface is similar to the input watercut. In the three-phase flow experiments it was found that the water droplet

concentration profile can be estimated by multiplying the oil droplet concentration profile by the interfacial watercut.

The calculation of the total entrainment fraction is very sensitive to the definition of the position of the gas-liquid interface. A variation of the interface height of 20% gives in average, a variation of 40% in the total entrainment fraction. It is therefore recommended to use a consistent methodology to define the interface for a given set of experiments.

A comparison of the droplet concentration profiles was carried out between the current experimental data set, data from the literature and an exponential model from the literature. A sensitivity analysis showed that it is possible to obtain a good prediction by using multiple combinations of two key input parameters to the model (Normalized diffusivity and droplet diameter). This multiplicity in solutions hints that the trend suggested in the literature for the normalized diffusion coefficients versus the pipe diameter might not be strictly physical but just a coincidence.

Two empirical correlations for the input variables of the exponential model were developed by using a genetic-algorithms-based methodology. The correlations were developed using all available two-phase flow data from the literature and the current experimental data set. The input variables are the droplet interface concentration and the decay rate and are expressed in terms of non-dimensional numbers.

The characteristics of separated gas-liquid flows were studied using a dense gas, high and low viscosity oil or water for 40 flow conditions. The phase distribution and pressure gradient were measured using gamma densitometry and pressure transducers. The existence of droplets was observed by using high speed video recordings. An algorithm and a methodology were developed and implemented to solve three-phase volume fractions using the available gamma sources on the existing traversing gamma densitometer.

For two-phase gas-liquid flows using a viscous oil (90 cP), the onset of entrainment occurs at a lower gas velocities than for a water-gas system.

The observed droplet entrainment and pressure gradient decrease significantly when adding water as a second liquid phase to a two-phase high viscous oil and gas system. This behavior was not observed for low viscosity systems and more experiments should be carried out in the future to confirm this behavior.

For two-phase gas-liquid flow using a viscous oil (90 cP), the onset of entrainment occurs at a lower gas velocities than for a water-gas system. The droplet entrainment and pressure gradient decreases significantly, for systems using high viscous oil, when adding water as a third phase.

An experimental setup was built using a vertical pipe to study the pressure gradient in gas flows with wet pipe walls. The two-phase experiments were carried out using air and two liquids: a viscous oil (60 cP) and water. The pressure gradient increases with the liquid film thickness. The flushing time for the viscous oil is very long in comparison with the water case (approximately eight times longer). Models from the literature for the pressure gradient versus the film thickness were compared against the current experiments showing a good agreement between them.

A new two-energy five beams gamma densitometer was designed and built. The instrument can measure three-phase flow fractions. The densitometer can rotate so cross sectional measurements can be performed. Even though the instrument is ready to use, the first calibration experiments are not part of this work due to time limitations and this work is followed up by a PhD student and a Post Doc at NTNU.

# APENDIXES

# Apendix A-Uncertainty calculations

**Error in the pressure gradient calculation**

The pressure gradient is calculated from the measurement of six pressure cells that are installed along the loop (at 99D, 430D, 633D, 865D, 1071D and 1274D). Each differential pressure transducer is connected between a pressure tap on the pipe wall and a reference line. The local absolute pressure is calculated by adding the measured differential pressure to the absolute reference pressure. The pressure gradient was calculated by the estimated slope in the regression line obtained from the dp-cells and their respective positions. The uncertainty of the pressure gradient calculation is the error of the slope obtained by fitting a straight line to their respective plotted curve. (See example in figure below). Using this methodology the maximum and average errors in the pressure gradient were 8 Pa/m and 4 Pa/m respectively.

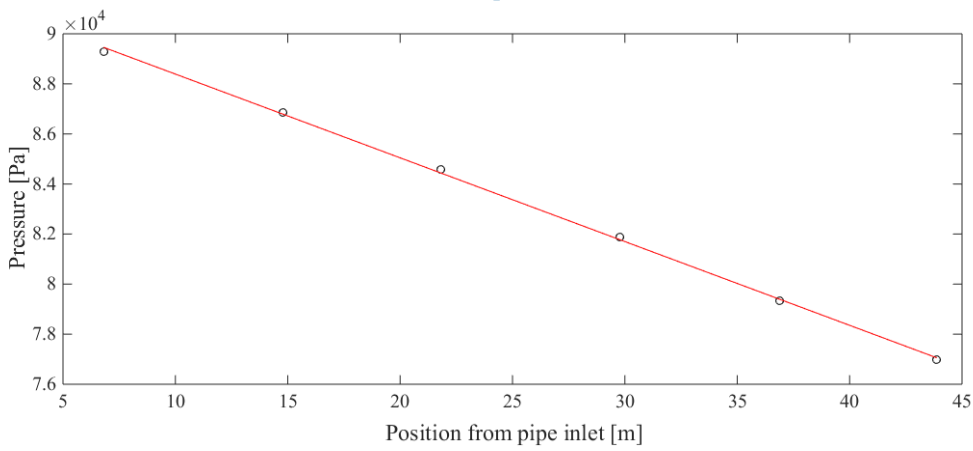


**Error in the sampling tank pressure**

The pressure in the sampling tank was measured using a dp-cell with a Bias limit of 6.5 Pa. The initial and ending sampling pressure conditions were estimated by a linear regression of the tank pressure time traces (See example in the figure below). The standard error of the regression was calculated using

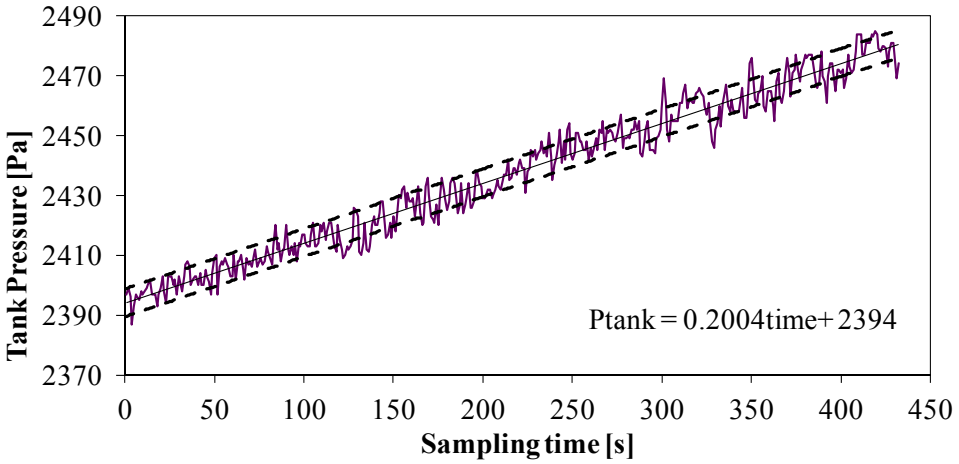


$$S_{P\tan k} = \sqrt{\frac{\sum\left(P_{\tan k(measured)} - P_{\tan k(\text{predicted})}\right)^2}{N-2}}$$

The uncertainty of a single measurement with 95% confidence level is

$$w_{\text{Pt}} = \sqrt{B_{Pt}^2 + 2S_{Pt}^2}$$

The uncertainty of the pressure difference in the tank can be calculated using the square root of the sum of squares (RSS)

$$w_{\Delta Pt}^2 = w^2_{\text{Pt@t1}} \cdot \frac{\partial \Delta Pt}{\partial Pt_{@t1}} + w^2_{\text{Pt@t2}} \cdot \frac{\partial \Delta Pt}{\partial Pt_{@t2}} = w^2_{\text{Pt@t1}} + w^2_{\text{Pt@t2}}$$

**Uncertainty in the liquid level in the sampling tank**

There are two ways of estimating the liquid level inside the tank. It can be estimated visually using a scale attached to the clear tank wall ($B_h$=0.0005 m) or it can be determined by the static column measured with the dp-cell s. When the experiments involved just two phases (oil-gas) these two methodologies can be compared.

$$\Delta h(y) = h_{@t_2}(y) - h_{@t_1}(y)$$

The uncertainty of the visually estimated liquid level difference in the tank can be calculated using the square root of the sum of squares (RSS)

$$w_{\Delta h}^2 = w^2_{\text{h@t1}} \cdot \frac{\partial \Delta h}{\partial h_{@t1}} + w^2_{h@t2} \cdot \frac{\partial \Delta h}{\partial h_{@t2}} = w^2_{h@t1} + w^2_{\text{h@t2}}$$

For the two-phase gas-oil system:

$$\Delta h_o(y) = \left( \frac{P_{t@t_2}(y) - P_{t@t_1}(y)}{\rho_o \cdot g} \right)$$

For three-phase flow system (water-oil-gas)

$$\Delta h_o(y) = \left( \frac{\Delta Pt(y) - \rho_w \cdot g \cdot \Delta h_w(y)}{\rho_o \cdot g} \right)$$

The uncertainty of the oil level in the tank can be calculated using the square root of the sum of squares (RSS)

$$w_{\Delta ho}^2 = \left( \frac{\partial \Delta ho}{\partial \rho_o} \right)^2 w_{\rho_o}^2 + \left( \frac{\partial \Delta ho}{\partial \Delta Pt} \right)^2 w_{\Delta Pt}^2 + \left( \frac{\partial \Delta ho}{\partial \Delta h_w} \right)^2 w_{\Delta h_w}^2 + \left( \frac{\partial \Delta ho}{\partial \rho_w} \right)^2 w_{\rho_w}^2$$

**Uncertainty in local droplet flux calculation**

The local droplet flux for each liquid phase "n" is defined as

$$F_{LEn}(y) = \frac{q_n(y) \cdot \rho_n}{A_p}$$

Where $q_n$ is calculated as:

$$q_n = \Delta h_n \cdot \frac{\mathrm{A_v}}{\Delta \mathrm{t}} = \Delta h \cdot \frac{\pi \cdot d_v^{\,2}}{4 \cdot \Delta \mathrm{t}}$$

$$F_{LEn}(y) = \Delta h_n(y) \cdot \frac{d_v^{\,2}}{d_p^{\,2} \Delta \mathrm{t(y)}} \cdot \rho_n$$

$$F_{LEw}(y) = \Delta h_o(y) \cdot \frac{d_v^{\,2}}{d_p^{\,2} \Delta \mathrm{t(y)}} \cdot \rho_o = \frac{\Delta Pt(y) - \rho_w \cdot g \cdot \Delta h_w(y)}{g} \cdot \frac{d_v^{\,2}}{d_p^{\,2} \Delta \mathrm{t(y)}}$$

$$F_{LEw}(y) = \Delta h_w(y) \cdot \frac{d_v^{\,2}}{d_p^{\,2} \Delta \mathrm{t(y)}} \cdot \rho_w$$

The diameter of the sampling vessel and the probe were measured using a caliper ($B_{dv}$=0.005 cm). The oil density was measured by manually noting the value from a coriolis meter located before the mixing section ($B_{\rho n}$=0.5 Kg/m$^3$). The uncertainty on the water measurement is assumed to be the same as for the oil density. The sampling time was measured using a chronometer ($B_{\Delta t}$=0.1 s). The total uncertainty is written as:

$$w_{FLEo}^2 = \left( \frac{\partial FLE_o}{\partial \Delta Pt} \right)^2 w_{\Delta Pt}^2 + \left( \frac{\partial FLE_o}{\partial \Delta hw} \right)^2 w_{\Delta hw}^2 + \left( \frac{\partial FLE_o}{\partial d_v} \right)^2 w_{d_v}^2 + \left( \frac{\partial FLE_o}{\partial \Delta t} \right)^2 w_{\Delta t}^2 + \left( \frac{\partial FLE_o}{\partial \rho_w} \right)^2 w_{\rho_w}^2 + \left( \frac{\partial FLE_o}{\partial d_p} \right)^2 w_{d_p}^2$$

$$w_{FLEw}^2 = \left( \frac{\partial FLE_w}{\partial \Delta h_w} \right)^2 w_{\Delta hw}^2 + \left( \frac{\partial FLE_w}{\partial d_v} \right)^2 w_{d_v}^2 + \left( \frac{\partial FLE_w}{\partial \Delta t} \right)^2 w_{\Delta t}^2 + \left( \frac{\partial FLE_w}{\partial \rho_w} \right)^2 w_{\rho_w}^2 + \left( \frac{\partial FLE_w}{\partial d_p} \right)^2 w_{d_p}^2$$

**Uncertainty in the gas velocity**

$$U_g(y)=\frac{1}{A_p}\left(\frac{\dot{m}_g(y)}{\rho_g}+q_o(y)+q_w(y)\right)$$

$$Ug(y)=\frac{\dot{m}_g(y)}{\rho_g}+\left(\frac{\Delta Pt(y)-\rho_w\cdot g\cdot\Delta h_w(y)}{\rho_o\cdot g}\right)\cdot\frac{\pi\cdot d_v^{\,2}}{4\cdot\Delta\mathrm{t(y)}}+\Delta h_w(y)\cdot\frac{\pi\cdot d_v^{\,2}}{4\cdot\Delta\mathrm{t(y)}}$$

The total uncertainty is written as:

$$w_{Ug}^2=\left(\frac{\partial Ug}{\partial\Delta Pt}\right)^2 w_{\Delta Pt}^2+\left(\frac{\partial Ug}{\partial\Delta hw}\right)^2 w_{\Delta hw}^2+\left(\frac{\partial Ug}{\partial d_v}\right)^2 w_{d_v}^2+\left(\frac{\partial Ug}{\partial\Delta t}\right)^2 w_{\Delta t}^2+\left(\frac{\partial Ug}{\partial\rho_w}\right)^2 w_{\rho_w}^2+$$
$$+\left(\frac{\partial Ug}{\partial\rho_o}\right)^2 w_{\rho_o}^2+\left(\frac{\partial Ug}{\partial\rho_g}\right)^2 w_{\rho_g}^2+\left(\frac{\partial Ug}{\partial\dot{m}_g}\right)^2 w_{\dot{m}_g}^2$$

For all the studied cases the error of the gas velocity is 2% of the measured value

**Uncertainty in local droplet concentration calculation**

The droplet concentration is defined as:

$$C(y)=\frac{F_{LEn}(y)}{U_g(y)}$$

Where the gas velocity is calculated as

$$U_g(y)=\frac{1}{A_p}\left(\frac{\dot{m}_g(y)}{\rho_g}+q_o(y)+q_w(y)\right)$$

$$C_o(y)=\frac{\dfrac{\Delta Pt(y)-\rho_w\cdot g\cdot\Delta h_w(y)}{g}\cdot\dfrac{d_v^{\,2}}{d_p^{\,2}\Delta\mathrm{t(y)}}\cdot A_p}{\dfrac{\dot{m}_g(y)}{\rho_g}+\left(\dfrac{\Delta Pt(y)-\rho_w\cdot g\cdot\Delta h_w(y)}{\rho_o\cdot g}\right)\cdot\dfrac{\pi\cdot d_v^{\,2}}{4\cdot\Delta\mathrm{t(y)}}+\Delta h_w\cdot\dfrac{\pi\cdot d_v^{\,2}}{4\cdot\Delta\mathrm{t(y)}}}$$

The total uncertainty is written as:

$$w_{Coil}^2=\left(\frac{\partial C_{oil}}{\partial\Delta Pt}\right)^2 w_{\Delta Pt}^2+\left(\frac{\partial C_{oil}}{\partial\Delta hw}\right)^2 w_{\Delta hw}^2+\left(\frac{\partial C_{oil}}{\partial d_v}\right)^2 w_{d_v}^2+\left(\frac{\partial C_{oil}}{\partial\Delta t}\right)^2 w_{\Delta t}^2+\left(\frac{\partial C_{oil}}{\partial\rho_w}\right)^2 w_{\rho_w}^2+\left(\frac{\partial C_{oil}}{\partial\rho_o}\right)^2 w_{\rho_o}^2+$$
$$\left(\frac{\partial C_{oil}}{\partial\rho_g}\right)^2 w_{\rho_g}^2+\left(\frac{\partial C_{oil}}{\partial\dot{m}_g}\right)^2 w_{\dot{m}_g}^2+\left(\frac{\partial C_{oil}}{\partial d_p}\right)^2 w_{d_p}^2$$

A summary of the errors in the local concentration for all sampled points obtained with the described methods are presented in the Figure below. For the oil concentrations the most significant value is 4% of the measured value. Larger errors were obtained but mainly for sampled locations close to the top of the pipe where the droplet flux is very small. For the water cases the errors are larger as the water fluxes are smaller than oil and the most typical error is 52%.

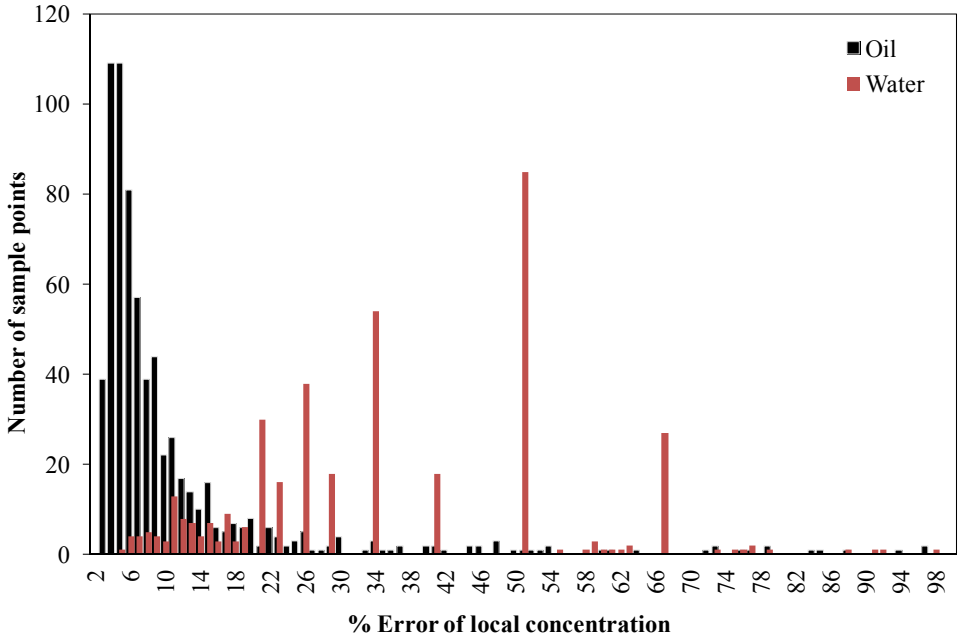


**Uncertainty in total entrainment fraction**

$$\bar{E}_L = A \cdot \bar{F}_{LE} = \frac{2A}{A_g}\int_{hw}^{D}\sqrt{R^2-(y-R)^2}\cdot F_{LE,}(y)dy$$

$$fe_n = \frac{A\cdot\bar{F}_{LEn}}{\rho_L U_{sl}} = \frac{2A}{A_g\rho_L U_{sl}}\int_{hw}^{D}\sqrt{R^2-(y-R)^2}\cdot\frac{q_n(y)\cdot\rho_n}{A_p}dy$$

The gas area is calculated as

$$\theta = 2a\cos\left(\frac{R-h_w}{R}\right)$$

$$A_g = A-0.5R^2(\theta-sin(\theta)) = \pi R^2-0.5R^2(\theta-sin(\theta)) = \pi R^2-0.5R^2\left(2a\cos\left(\frac{R-h_w}{R}\right)-sin\left[2a\cos\left(\frac{R-h_w}{R}\right)\right]\right)$$

The total entrainment fraction of each phase is calculated as

$$fe_n = \frac{A\cdot\bar{F}_{LEn}}{\rho_L U_{sl}}$$

For each phase the entrainment fraction can be written as

$$fe_w = \frac{A\cdot\bar{F}_{LEw}}{\rho_L U_{sl}} = \frac{2\pi R^2}{\rho_L U_{sl}\left(\pi R^2-0.5R^2\left(2a\cos\left(\frac{R-h_w}{R}\right)-sin\left[2a\cos\left(\frac{R-h_w}{R}\right)\right]\right)\right)}\int_{hw}^{D}\sqrt{R^2-(y-R)^2}\cdot\Delta h_w(y)\cdot\frac{d_v^{\,2}}{d_p^{\,2}\Delta t(y)}\cdot\rho_w dy$$

$$fe_o = \frac{A\cdot\bar{F}_{LEo}}{\rho_L U_{sl}} = \frac{2\pi R^2}{\rho_L U_{sl}\left(\pi R^2-0.5R^2\left(2a\cos\left(\frac{R-h_w}{R}\right)-sin\left[2a\cos\left(\frac{R-h_w}{R}\right)\right]\right)\right)}\int_{hw}^{D}\sqrt{R^2-(y-R)^2}\cdot\frac{\Delta Pt(y)-\rho_w\cdot g\cdot\Delta h_w(y)}{g}\cdot\frac{d_v^{\,2}}{d_p^{\,2}\Delta t(y)}dy$$

For simplicity, the variable $K_1$ is defined as

$$K1 = \frac{2\pi R^2}{\rho_L U_{sl}\left(\pi R^2 - 0.5R^2\left(2a\cos\left(\frac{R-h_w}{R}\right) - \sin\left[2a\cos\left(\frac{R-h_w}{R}\right)\right]\right)\right)}$$

The uncertainty in the liquid height was assumed to the differences between the liquid height visually estimated and the measured by the gamma at $\alpha_L$=0.05 for the upper level error and the difference between the height measured by the gamma at $\alpha_L$=0.05 and the height measured by the gamma at $\alpha_L$=0.5. The total uncertainty is written as:

$$w_{fe}^2 = w_{fe_o}^2 + w_{fe_w}^2$$

$$w_{fe_o}^2 = \left(\frac{\partial fe_o}{\partial \Delta Pt}\right)^2 w_{\Delta Pt}^2 + \left(\frac{\partial fe_o}{\partial \Delta hw}\right)^2 w_{\Delta hw}^2 + \left(\frac{\partial fe_o}{\partial d_v}\right)^2 w_{d_v}^2 + \left(\frac{\partial fe_o}{\partial \Delta t}\right)^2 w_{\Delta t}^2 + \left(\frac{\partial fe_o}{\partial \rho_w}\right)^2 w_{\rho_w}^2 +$$
$$+\left(\frac{\partial fe_o}{\partial \rho_o}\right)^2 w_{\rho_o}^2 + \left(\frac{\partial fe_o}{\partial R}\right)^2 w_R^2 + \left(\frac{\partial fe_o}{\partial U_{sl}}\right)^2 w_{U_{sl}}^2 + \left(\frac{\partial fe_o}{\partial h_w}\right)^2 w_{h_w}^2$$

$$w_{fe_w}^2 = \left(\frac{\partial fe_w}{\partial \Delta hw}\right)^2 w_{\Delta hw}^2 + \left(\frac{\partial fe_w}{\partial d_v}\right)^2 w_{d_v}^2 + \left(\frac{\partial fe_w}{\partial \Delta t}\right)^2 w_{\Delta t}^2 + \left(\frac{\partial fe_w}{\partial \rho_w}\right)^2 w_{\rho_w}^2 + \left(\frac{\partial fe_w}{\partial \rho_o}\right)^2 w_{\rho_o}^2 +$$
$$+\left(\frac{\partial fe_w}{\partial R}\right)^2 w_R^2 + \left(\frac{\partial fe_w}{\partial U_{sl}}\right)^2 w_{U_{sl}}^2 + \left(\frac{\partial fe_w}{\partial h_w}\right)^2 w_{h_w}^2$$

The partial derivatives with respect to each of the variables "var" on the equations above are calculated using the chain rule as

$$\frac{\partial fe_o}{\partial \mathrm{var}} = K1 \cdot \frac{\partial}{\partial \mathrm{var}}\left(\int_{hw}^{2R} \sqrt{R^2 - (y-R)^2} \cdot \frac{\Delta Pt(y) - \rho_w \cdot g \cdot \Delta h_w(y)}{g} \cdot \frac{d_v^{\,2}}{d_p^{\,2}\Delta \mathrm{t(y)}} dy\right) + \frac{\partial K_1}{\partial \mathrm{var}} \int_{hw}^{2R} \sqrt{R^2 - (y-R)^2} \cdot \frac{\Delta Pt(y) - \rho_w \cdot g \cdot \Delta h_w(y)}{g} \cdot \frac{d_v^{\,2}}{d_p^{\,2}\Delta \mathrm{t(y)}} dy$$

$$\frac{\partial fe_w}{\partial \mathrm{var}} = K1 \cdot \frac{\partial}{\partial \mathrm{var}}\left(\int_{hw}^{2R} \sqrt{R^2 - (y-R)^2} \cdot \Delta h_w(\mathrm{y}) \cdot \frac{d_v^{\,2}}{d_p^{\,2}\Delta \mathrm{t(y)}} \cdot \rho_w dy\right) + \frac{\partial K_1}{\partial \mathrm{var}} \int_{hw}^{2R} \sqrt{R^2 - (y-R)^2} \cdot \Delta h_w(\mathrm{y}) \cdot \frac{d_v^{\,2}}{d_p^{\,2}\Delta \mathrm{t(y)}} \cdot \rho_w dy$$

To obtain the partial derivatives it is required to solve the derivatives of an integral. The integral limits and/or the integer might depend on the desired variable "var". The Leibniz rule is used where the function *f* is the integer on the expressions above.

$$F'(\mathrm{var}) = \left(\int_{g(\mathrm{var})}^{h(\mathrm{var})} f(\mathrm{y}, \mathrm{var}) dy\right)' = \int_{g(\mathrm{var})}^{h(\mathrm{var})} \frac{\partial f}{\partial \mathrm{var}} dy + f(h(\mathrm{var})) \cdot h'(\mathrm{var}) - f(g(\mathrm{var})) \cdot g'(\mathrm{var})$$

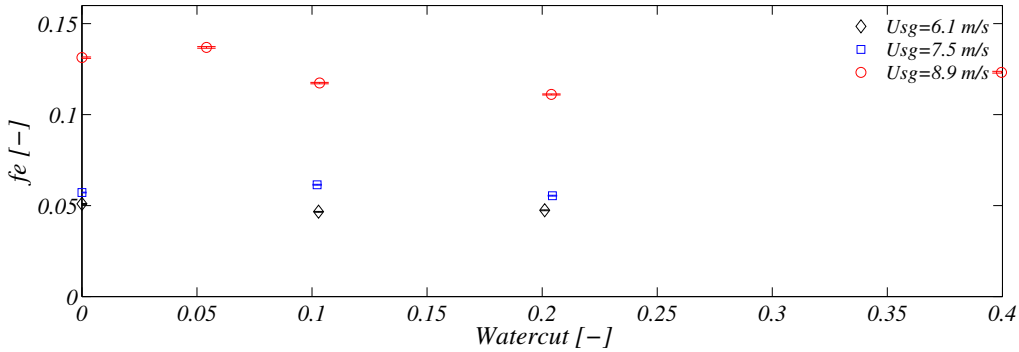


Water, oil and total entrainment fraction. Exxsol D80-Water-$SF_6$ (Cases 4-15)

**Error in the probe location (y and z) inside the pipe**

The location of the probe inside the pipe is controlled by a linear actuator (vertical movement) and a rotary actuator (horizontal movement). The error sources related to location of the probe inside the pipe are:

- Accuracy of the linear actuator (Bias ±0.02 mm)
- Accuracy of the rotary actuator (Bias ± 0.004°or ±0.0042 mm)
- Installation of the probe inside the pipe.

$$w_z = \sqrt{\left(B_z\right)^2 + \left(t \cdot S_z\right)^2}$$

$$w_y = \sqrt{\left(B_y\right)^2 + \left(t \cdot S_y\right)^2}$$

Bias millimeter paper ±1 mm

$$w_y = \sqrt{(0.02e-3)^2 + (0.5e-3)^2 + (0.5e-3)^2} = 0.0009m$$

$$w_R = 0.01e-3m$$

**Uncertainty on the phase fraction profiles measured by the gamma densitometer**

The volume phase fractions are defined as:

$$\alpha_o(y) = \frac{Z_o(y)}{d(y)} \qquad \alpha_w(y) = \frac{Z_w(y)}{d(y)} \qquad \alpha_g(y) = 1 - \alpha_w(y) - \alpha_o(y)$$

$$\alpha_k(y) = \frac{Z_k(y)}{d(y)} = \frac{\frac{1}{\mu_k} ln\left(\frac{I_g(y)}{I_m(y)}\right)}{2\sqrt{R^2 - (y-R)^2}}$$

$$\alpha_g(y) = 1 - \frac{Z_o(y)}{d(y)} - \frac{Z_w(y)}{d(y)} = 1 - \frac{ln\left(\frac{I_g(y)}{I_m(y)}\right)}{2\sqrt{R^2-(y-R)^2}}\left(\frac{1}{\mu_o}+\frac{1}{\mu_w}\right)$$

The total uncertainty of the oil or water fraction profile will be given by

$$w_{\alpha_k}^2 = \left(\frac{\partial \alpha_k}{\partial \mu_k}\right)^2 w_{\mu_k}^2 + \left(\frac{\partial \alpha_k}{\partial I_g}\right)^2 w_{I_g}^2 + \left(\frac{\partial \alpha_k}{\partial I_m}\right)^2 w_{I_m}^2 + \left(\frac{\partial \alpha_k}{\partial R}\right)^2 w_R^2 + \left(\frac{\partial \alpha_k}{\partial y}\right)^2 w_y^2$$

Similar for the gas phase

$$w_{\alpha g}^2 = \left(\frac{\partial \alpha_g}{\partial \mu_o}\right)^2 w_{\mu_o}^2 + \left(\frac{\partial \alpha_g}{\partial \mu_w}\right)^2 w_{\mu_w}^2 + \left(\frac{\partial \alpha_g}{\partial I_g}\right)^2 w_{I_g}^2 + \left(\frac{\partial \alpha_g}{\partial I_m}\right)^2 w_{I_m}^2 + \left(\frac{\partial \alpha_g}{\partial R}\right)^2 w_R^2 + \left(\frac{\partial \alpha_g}{\partial y}\right)^2 w_y^2$$

The attenuation coefficients were calculated by fitting a straight line to the curved $ln\left(I_k(y)/I_g(y)\right)$ vs *d*. Where k=w or k=o for water or oil respectively and $d = 2\sqrt{R^2-(y-R)^2}$. The uncertainty on the attenuation coefficient calculation is the error of the slope obtained by fitting a straight line to their respective plotted curve as:

$$S_\mu = \frac{\sqrt{\frac{\sum\left(f_{\mu(measured)} - f_{\mu(\text{predicted})}\right)^2}{N-2}}}{\sqrt{\sum(d-\bar{d})^2}} \qquad ()$$

# Apendix B- Traversing gamma profiles

***Nexbase 3080(100 cP) 7 bara, Usl=0.4 m/s, WC=0.5***

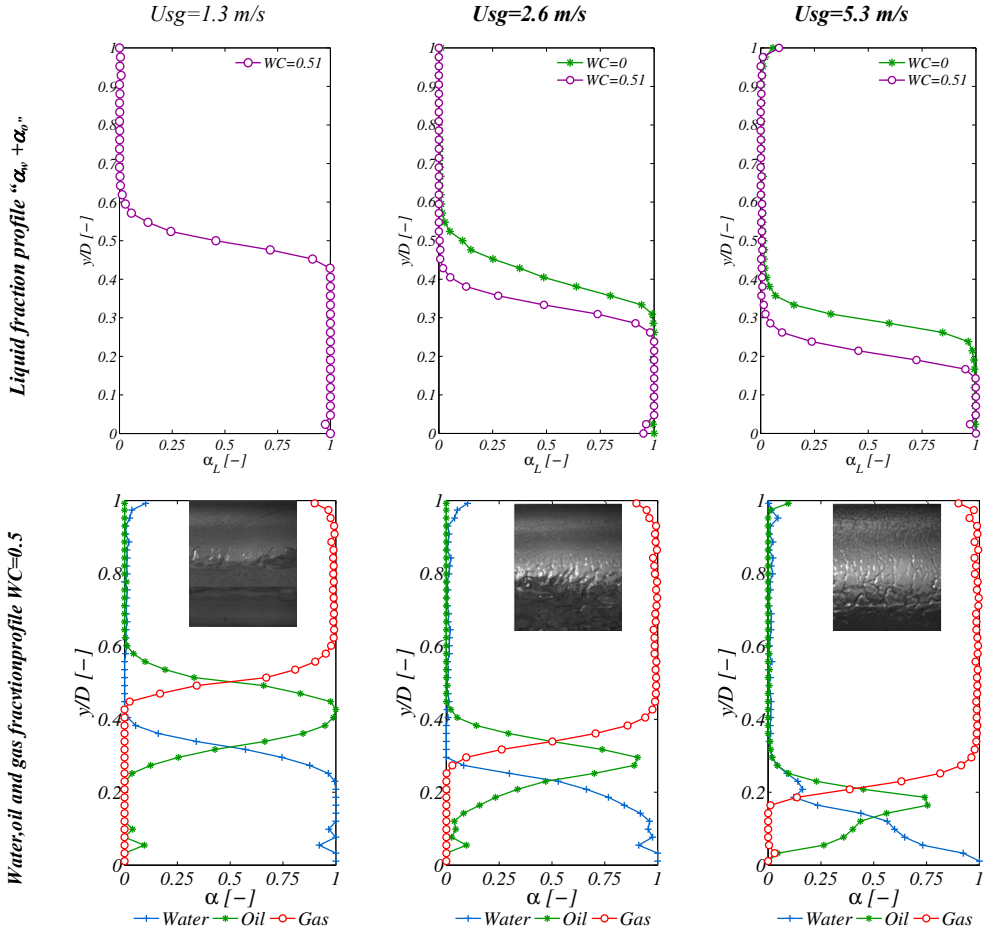

***Nexbase 3080(100 cP) 7 bara, Usl=0.8 m/s, WC=0.5***

*Usg=1.3 m/s* *Usg=2.6 m/s* *Usg=8.0m/s*

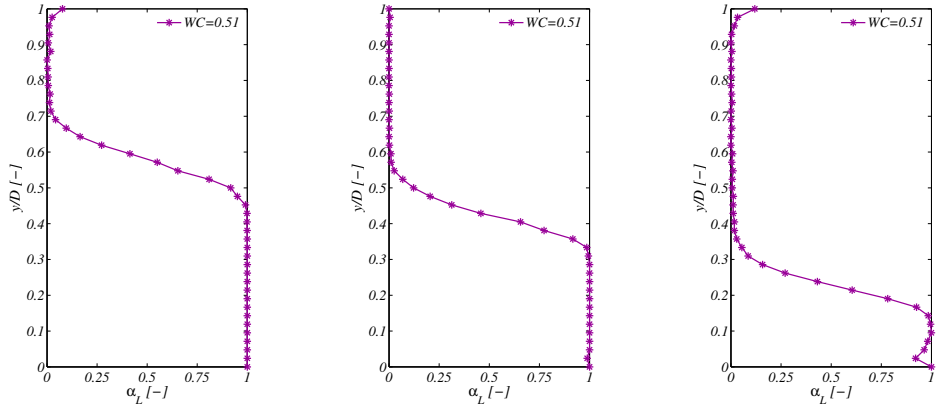


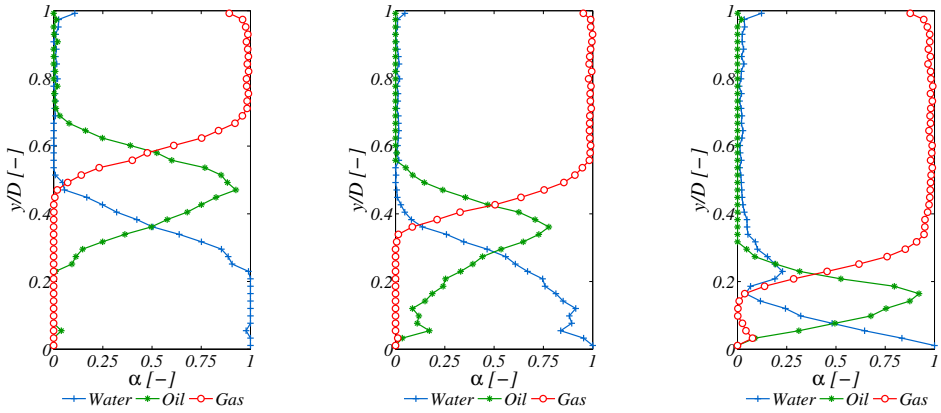


***Nexbase 3080(100 cP) 7 bara, Usl=0.1 m/s, WC=0.75***

*Usg=0.7 m/s* *Usg=2.6 m/s* *Usg=5.3 m/s* *Usg=8.0 m/s*

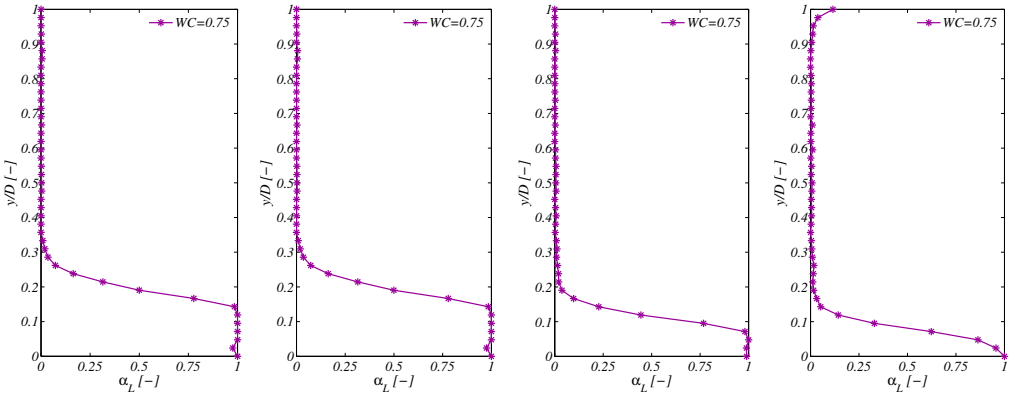

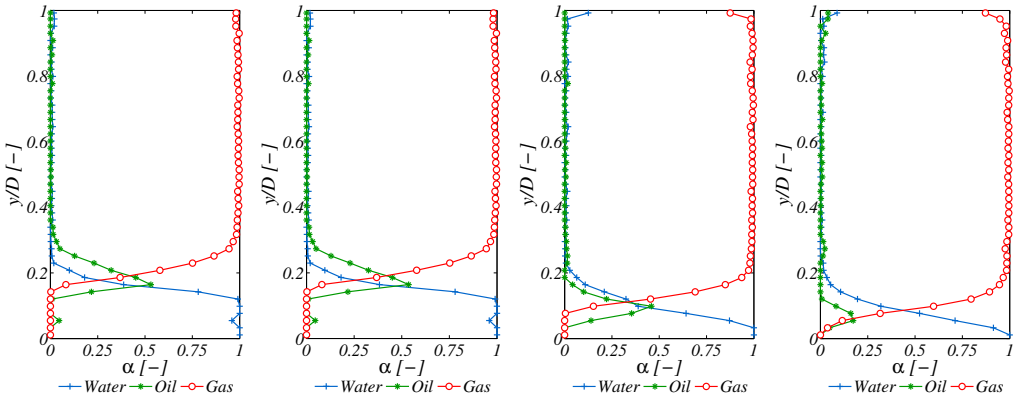


***Exssol D80-Water-SF6: Usl=0.2 m/s***

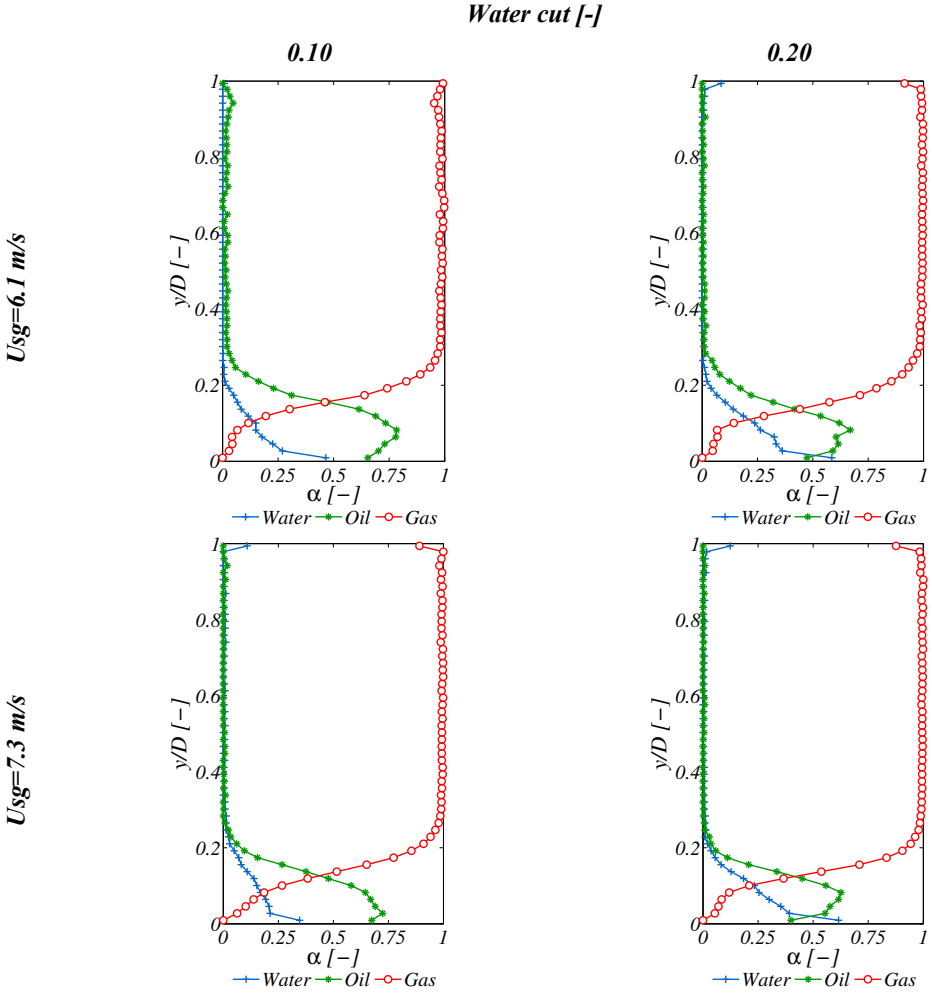

***Exxsol-Water-SF6 Usg=8.9 m/s Usl=0.2 m/s***

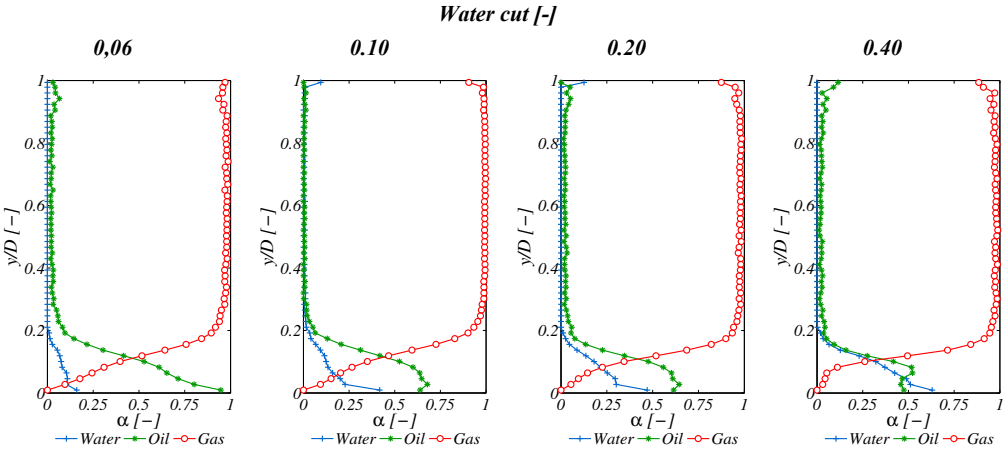


***Exxsol-Water-SF6 Usg=8.8 m/s Usl=0.1 m/s***

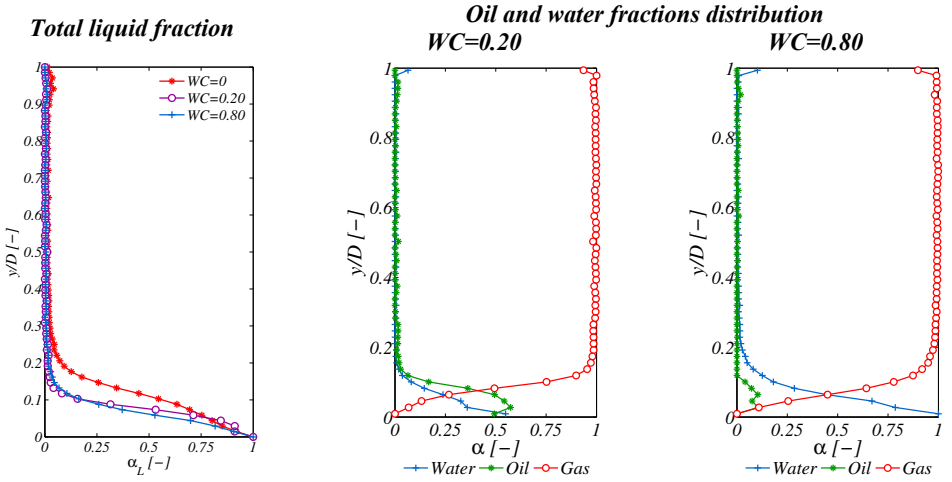

# Appendix C-Summary of sampling experiments:

**Exxsol D80-water-$SF_6$**

| Usg | Usl | WC | $P_{probe}$ | $\rho_g$ | $\rho_o$ | dp/dx | $\alpha_g$ | $\alpha_o$ | $\alpha_\omega$ | 1D integration | | | 2D integration |
|---|---|---|---|---|---|---|---|---|---|---|---|---|---|
| | | | | | | | | | | fe | $Fe_w$ | $fe_o$ | fe |
| (m/s) | (m/s) | (-) | (bar) | ($kg/m^3$) | ($kg/m^3$) | (Pa/m) | (-) | (–) | (–) | (-) | (-) | (-) | (-) |
| 6.04 | 0.2 | 0 | 4.51 | 27.04 | 813 | 330.9 | 0.882 | 0.118 | 0 | 0.051 | 0 | 0.051 | 0.046 |
| 6.1 | 0.2 | 0.05 | 4.48 | 26.81 | 812.7 | 353.2 | - | - | - | - | - | - | - |
| 6.09 | 0.2 | 0.1 | 4.49 | 26.96 | 813.1 | 355.1 | 0.867 | 0.117 | 0.016 | 0.047 | 0.004 | 0.043 | 0.041 |
| 6.12 | 0.2 | 0.2 | 4.48 | 26.97 | 813.6 | 340.1 | 0.89 | 0.082 | 0.028 | 0.047 | 0.007 | 0.04 | 0.043 |
| 7.53 | 0.2 | 0 | 4.45 | 26.76 | 813.7 | 484.7 | 0.91 | 0.09 | 0 | 0.057 | 0 | 0.057 | 0.053 |
| 7.54 | 0.2 | 0.1 | 4.46 | 26.76 | 813.7 | 491.7 | 0.911 | 0.066 | 0.024 | 0.114 | 0.057 | 0.057 | 0.053 |
| 7.53 | 0.2 | 0.2 | 4.46 | 26.79 | 813.6 | 466.3 | 0.912 | 0.057 | 0.031 | 0.055 | 0.009 | 0.046 | 0.041 |
| 8.85 | 0.2 | 0 | 4.47 | 26.76 | 813.6 | 632.8 | 0.923 | 0.077 | 0 | 0.131 | 0 | 0.131 | 0.087 |
| 8.94 | 0.2 | 0.05 | 4.42 | 26.45 | 812.7 | 653.9 | 0.909 | 0.083 | 0.009 | 0.137 | 0.007 | 0.129 | - |
| 8.84 | 0.2 | 0.1 | 4.49 | 26.89 | 813.5 | 639.7 | 0.903 | 0.083 | 0.014 | 0.117 | 0.011 | 0.106 | 0.074 |
| 8.86 | 0.2 | 0.2 | 4.48 | 26.83 | 813.5 | 650 | 0.912 | 0.065 | 0.023 | 0.111 | 0.019 | 0.092 | 0.064 |
| 8.93 | 0.2 | 0.4 | 4.41 | 26.39 | 812.7 | 666.2 | 0.907 | 0.06 | 0.033 | 0.122 | 0.043 | 0.079 | - |
| 8.83 | 0.1 | 0 | 4.49 | 26.85 | 813.7 | 513.6 | 0.953 | 0.047 | 0 | 0.108 | 0 | 0.108 | - |
| 8.85 | 0.1 | 0.2 | 4.48 | 26.79 | 813.7 | 500.4 | 0.953 | 0.03 | 0.017 | 0.079 | 0.012 | 0.067 | - |
| 8.89 | 0.1 | 0.8 | 4.47 | 26.67 | 813.7 | 679 | 0.956 | 0.006 | 0.038 | 0.087 | 0.079 | 0.008 | - |

| Usg (m/s) | Usl (m/s) | WC (-) | $P_{probe}$ (bar) | $\rho_g$ ($kg/m^3$) | $\rho_o$ ($kg/m^3$) | dp/dx (Pa/m) | $\alpha g$ (-) | $\alpha o$ (-) | $\alpha \omega$ (-) | $fe_o$ (-) | $fe_w$ (-) | fe (-) |
|---|---|---|---|---|---|---|---|---|---|---|---|---|
| 6.48 | 0.1 | 0 | 4.27 | 25.7 | 844.5 | 391.4 | 0.88 | 0.12 | 0 | 0.037 | 0 | 0.04 |
| 6.47 | 0.1 | 0.1 | 4.26 | 25.8 | 844.5 | 298 | 0.92 | 0.05 | 0.03 | 0.014 | 9E-05 | 0.01 |
| 6.47 | 0.1 | 0.2 | 4.27 | 25.8 | 844.5 | 287.4 | 0.93 | 0.04 | 0.03 | 0.0056 | 0.0002 | 0.01 |
| 6.47 | 0.1 | 0.7 | 4.28 | 25.8 | 844.5 | 305.8 | 0.92 | 0.03 | 0.05 | 0.0004 | 0.006 | 0.01 |

# Appendix D- Element classification algorithm

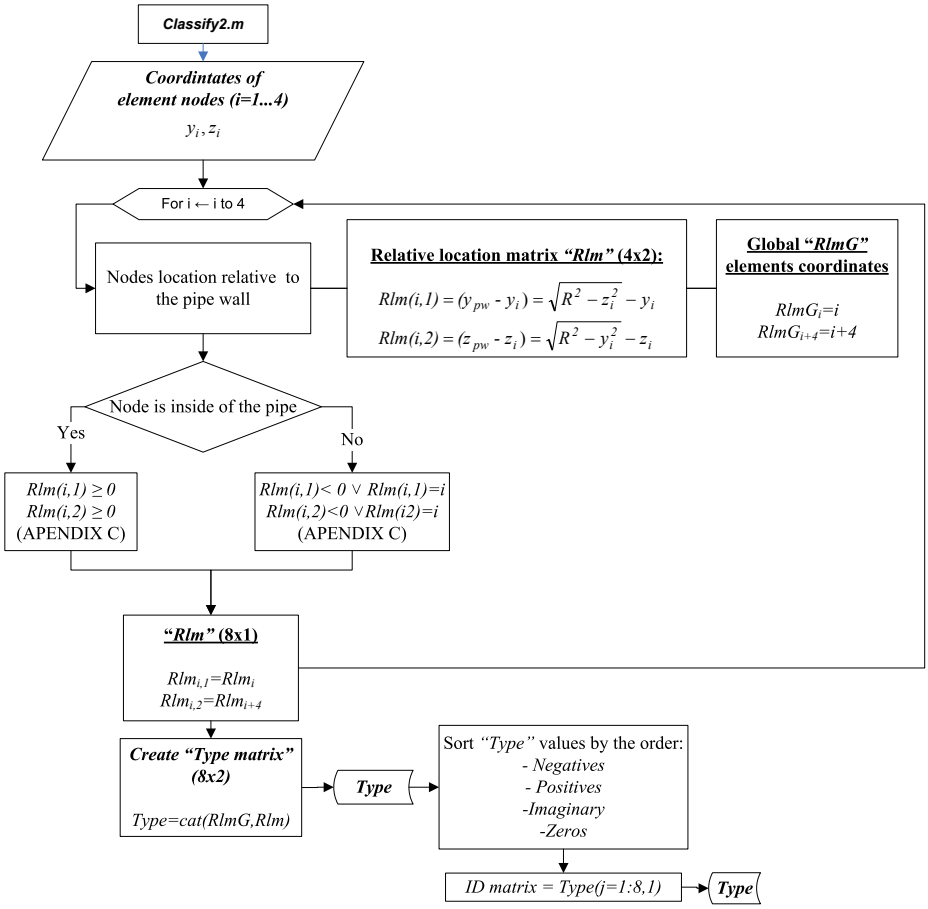


Example

***Element type 1a***

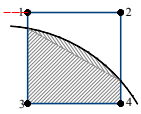


***Rlm matrix***

$$\begin{bmatrix} (\sqrt{R^2 - z_1^2} - y_1) & (\sqrt{R^2 - y_1^2} - z_1) \\ (\sqrt{R^2 - z_2^2} - y_2) & (\sqrt{R^2 - y_2^2} - z_2) \\ (\sqrt{R^2 - z_3^2} - y_3) & (\sqrt{R^2 - y_3^2} - z_3) \\ (\sqrt{R^2 - z_4^2} - y_4) & (\sqrt{R^2 - y_4^2} - z_4) \end{bmatrix} = \begin{bmatrix} i & - \\ i & - \\ + & + \\ + & + \end{bmatrix}$$

***RlmG vector***

$$\begin{bmatrix} 1 \\ 2 \\ 3 \\ 4 \\ 5 \\ 6 \\ 7 \\ 8 \end{bmatrix}$$

***Type matrix***

$$\begin{bmatrix} 1 & i \\ 2 & i \\ 3 & + \\ 4 & + \\ 5 & - \\ 6 & - \\ 7 & + \\ 8 & + \end{bmatrix}$$

***Type matrix sorted***

$$\begin{bmatrix} 5 & - \\ 6 & - \\ 3 & + \\ 4 & + \\ 7 & + \\ 8 & + \\ 1 & i \\ 2 & i \end{bmatrix}$$

***ID Vector (type 1a)***

$$\begin{bmatrix} 5 \\ 6 \\ 3 \\ 4 \\ 7 \\ 8 \\ 1 \\ 2 \end{bmatrix}$$

# Appendix E-Droplet concentration profiles predictions

**Predicted oil and water concentration profiles using the correlation from Pan and Hanratty (2002) for the droplet diameter for the current experiments**

**Usg= 6.1 m/s, Uso= 0.2 m/s**

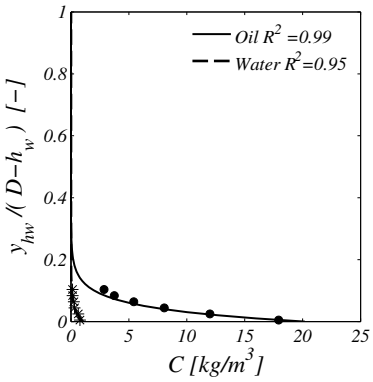


***WC=0.05***

**Usg= 7.3 m/s, Uso= 0.2 m/s**

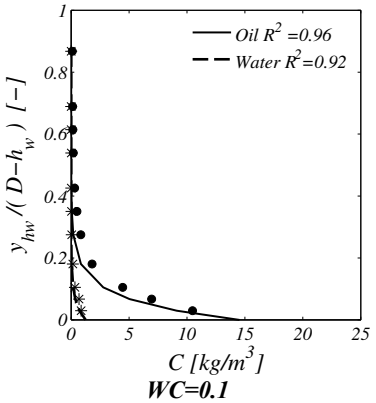


***WC=0.1***

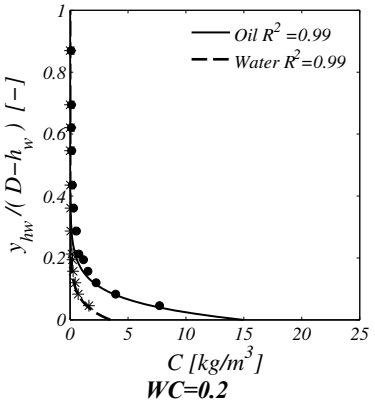


***WC=0.2***

**Usg= 8.9 m/s, Uso= 0.2 m/s**

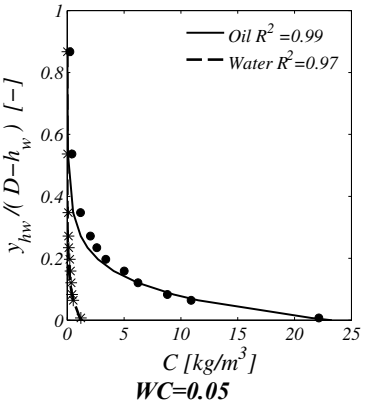


***WC=0.05***

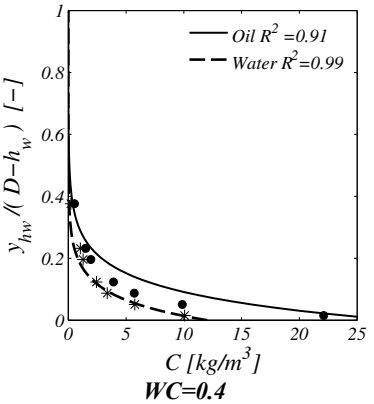


***WC=0.4***

**Predictions with the correlation for Co and λ**

**Usl=0.2 m/s, Usg=6.1 m/s**

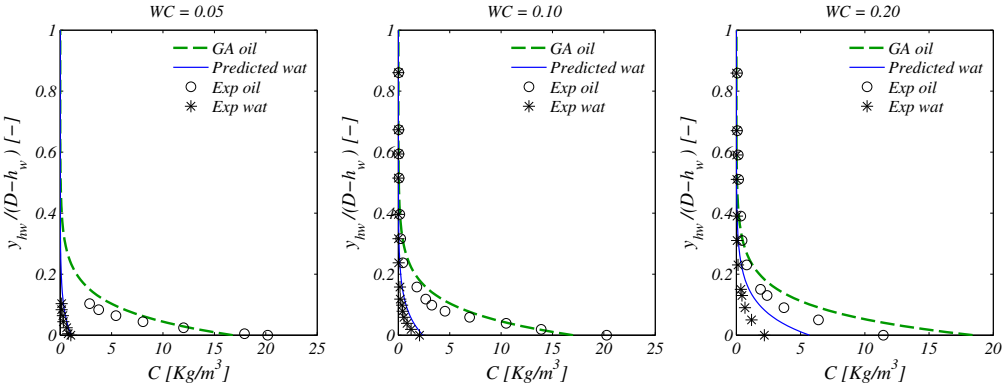


**Usl=0.2 m/s, Usg=7.3 m/s**

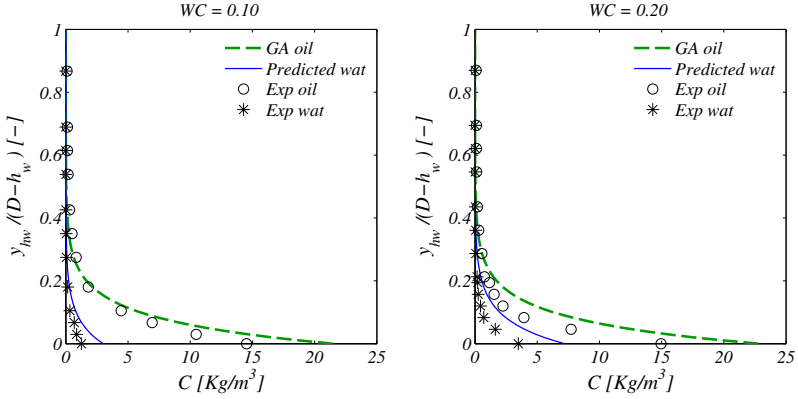


**Usl=0.1, Usg=8.9 m/s**

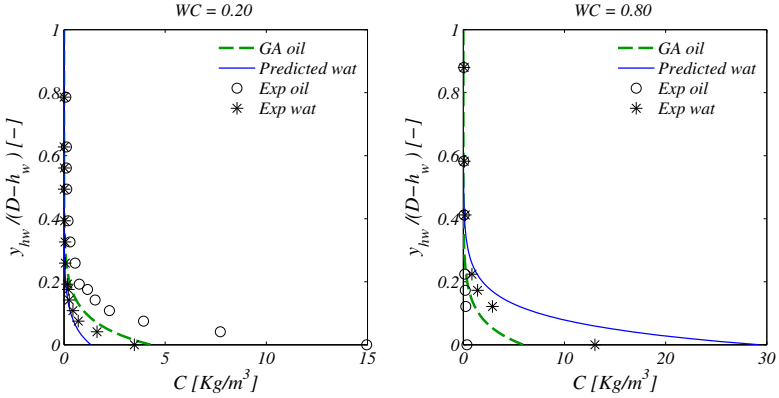

# Apendix F- 5 beams gamma densitometer shielding calculations

***Source properties (from supplier Ritverc)***

| Source | Photon flux (s·sr)$^{-1}$ | | Activity (MBq) |
|---|---|---|---|
| | 59.5 keV | 17.8 keV | |
| Am-241 | $6.7 \cdot 10^8$ | $10^7$ | 3700 |

The properties of the Am-241 provided by the supplier (Cerca-Lea) are shown in Table 3. The shielding needs to be calculated under the Norwegian law regulations for handling radiation which states:

-Less than 0.5 mSv/h at 5 cm from the instrument

-Less than 7.5 μSv/h at 1 m from the instrument

-Dose rate less than 85 μSv/h/GBq at 1m from the instrument (1).

*Source properties (from supplier Cerca-Lea)*

| ***Source*** | ***Photon flux (s·sr)$^{-1}$*** | | ***Activity (MBq)*** |
|---|---|---|---|
| | *59.5 keV* | *17.8 keV* | |
| *Am-241* | *$6.7 \cdot 10^8$* | *$10^7$* | *3700* |

***Dose rates***

$$Intensity\ (x = 1m) = 85 \frac{\frac{\mu Sv}{h}}{GBq} \cdot 3.7 GBq = 314.5\ \frac{\mu Sv}{h}$$

To calculate the intensity at 5 cm from the instrument the Inverse square law is used:

$$\frac{I2}{I1} = \frac{D1^2}{D2^2} \rightarrow I2 = \frac{D1^2}{D2^2} \cdot I1 = \left(\frac{1\ m}{5e-2\ m}\right)^2 \cdot 314e-3\ \frac{mSv}{h} = 125.8\ \frac{mSv}{h}$$

The intensity exponential decay is expressed by the Lambert's Law and it can be written as:

$$I = Io \cdot e^{-\mu \cdot d}$$

Where I is the intensity at distance "d", Io is the original intensity and μ is the linear attenuation coefficient.

***Half value layer***

Thickness required to reduce the exposure rate to a half of its value

$$I = 0.5 \cdot Io = Io \cdot e^{-\mu \cdot HVL}$$

$$HLV = \frac{\ln(2)}{\mu}$$

***Tenth value layer***

Thickness required to reduce the exposure rate to a tenth of its value

$$I = 0.1 \cdot Io = Io \cdot e^{-\mu \cdot TVL}$$

$$TVL = \frac{\ln(10)}{\mu}$$

The linear attenuation coefficient for different materials is shown below together with the calculation of their respective HVL and TVL values.

| | ***μ [1/m]1*** | ***Density (g/cm3)*** | ***HVL [mm]*** | ***TVL [mm]*** |
|---|---|---|---|---|
| *Iron (Fe) (60 keV)* | *950.39* | *7.87* | *0.73* | *2.42* |
| *Aluminium (Al) (60 keV)* | *74.196* | *2.70* | *9.34* | *31.0* |
| *Lead (Pb) (60 keV)* | *5557.5* | *11.34* | *0.13* | *0.42* |
| *Tungsten (60 keV)* | *5662.75* | *15.63* | *0.12* | *0.41* |

[1] *McCrary, 1966*

The required intensity dampening calculations are shown in the table below.

| ***Distance from instrument*** | ***Requirement*** | ***Intensity without shielding*** | ***Required Dampening (times)*** |
|---|---|---|---|
| *5 cm* | *0.5 mSv/h* | *125.8 mSv/h* | *251.6* |
| *1 m* | *7.5 μSv/h* | *314 μSv/h* | *41.9* |

Using the exponential decay equation is possible to calculate the required shielding thickness:

$$I = \frac{1}{requiered\ dampening} \cdot Io = Io \cdot e^{-\mu \cdot t}$$

$$t = \frac{\ln(requiered\ dampening)}{\mu}$$

| ***Distance from instrument*** | ***Shielding material*** | ***Thickness [mm]*** | ***times·TVL*** |
|---|---|---|---|
| *5 cm* | *Aluminium* | *74.5* | *2.4* |
| | *Pb* | *0.99* | |
| | *Iron* | *5.82* | |
| | *Tungsten* | *0.98* | |
| *1 m* | *Aluminium* | *50.34* | *1.6* |
| | *Pb* | *0.68* | |
| | *Iron* | *3.92* | |
| | *Tungsten* | *0.66* | |

Photon Flux Calculation

It will be considered that the photon fluxes should be less than 200000 photons/second

| | | | |
|---|---|---|---|
| *Distance Source-Detector "$x_{s-d}$" (mm)* | | *160* | |
| *Collimator diameter on detector side (mm)* | | *8.5* | |
| *Active area of detector "$A_{act}$" ($mm^2$)* | | *113.1* | |
| *Total Activity of the source (GBq)* | | *3.7* | |
| *Source Yield (%)* | *@13.9 KeV* | | *28* |
| | *@59.5 KeV* | | *36.3* |
| *Attenuation Coefficient "$\mu$"* | *Air* | *@13.9 KeV* | *0.00019* |
| | | *@59.5 KeV* | *0.00017* |
| | *Plexiglass* | *@13.9 KeV* | *1.6* |
| | | *@59.5 KeV* | *0.23* |

The source will spread photons in all directions however the detected photon flux will be constrained to the open area fraction of the collimated detector

$$A_{frac} = \frac{A_{act}}{A_{sph}} = \frac{A_{act}}{4 \cdot \pi \cdot x^2_{source-det}}$$

The initial intensity from a source by energy level can be expressed as the total activity multiplied by the yield percentage at a specific energy level. The photon flux without attenuation can be expressed as

$$I_o = Activity_{@energy} \cdot A_{frac}$$

The measured intensity from a source will be attenuated by the traversed medium. Considering an empty pipe, photons should travel through air and plexiglass. For a specific energy level the attenuated intensity can be written as:

$$I_m = I_0 \cdot e^{-\mu_{pw} \cdot Z_{pw}} \cdot e^{-\mu_{air} \cdot Z_{air}}$$

Where μ and Z are the attenuation coefficient and the travelled distance through a medium respectively. In this case it is considered $Z_{air}$=9 cm and $Z_{pw}$=1 cm. The total attenuated photon flux is 73502 counts/s and 375700 counts/s for 13.9 KeV and 59.5 KeV respectively. The photon flux is lower when the 90 mm ID pipe configuration is in place.

# Apendix G- 5 beams gamma densitometer drawings

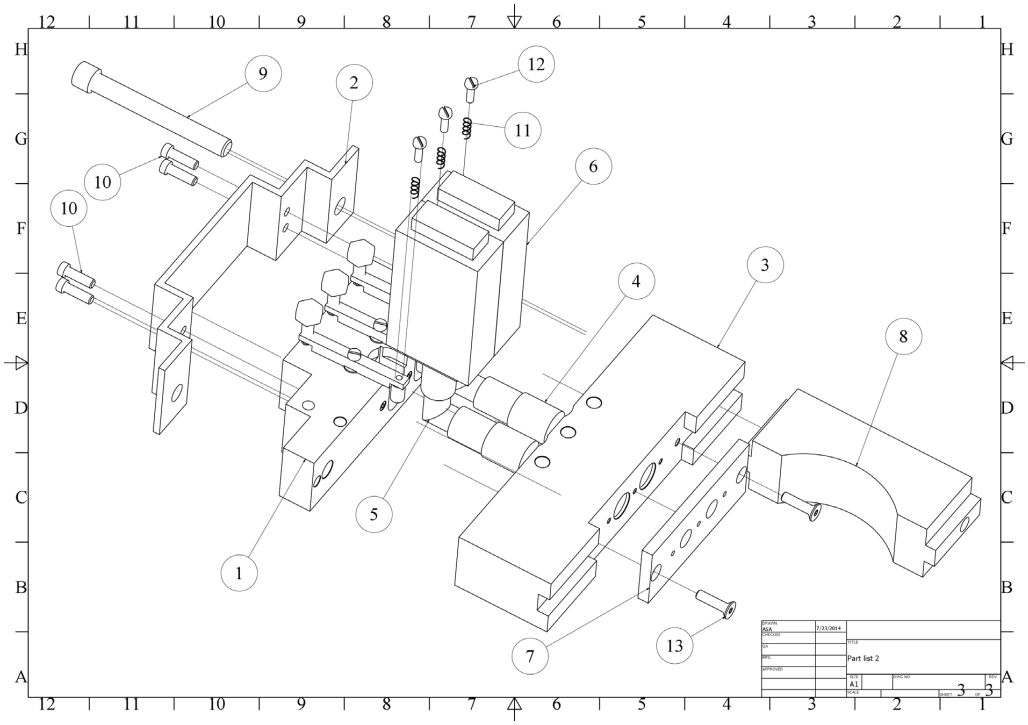


| *Part #* | *Quantity* | *Description* | |
|---|---|---|---|
| *1* | *2* | *Source holders* | *(See drawing)* |
| *2* | *2* | *Safety back plates* | *(See drawing)* |
| *3* | *2* | *Detector holders* | *(See drawing)* |
| *4* | *5* | *CdTe detectors S.5.5.2.U* | *Mounted in an aluminum box with a BNC connector (See datasheet)* |
| *5* | *5* | *90° BNC connectors* | |
| *6* | *5* | *Preamplifiers PR16-H* | |
| *7* | *2* | *Detector collimator plate* | *(See drawing)* |
| *8* | *1* | *Spacer and pipe center alligment tool* | *(See drawing)* |
| *9* | *4* | *M8x65 Hex bolt (reduced head size to 11 mm)* | |
| *10* | *8* | *M4x13 Hex bolt (reduced head size 6 mm)* | |
| *11* | *5* | *Springs $\phi o$=4.1 mm, $\phi i$=3.4 mm, t=0.35 mm, Lcompressed= 5.3 mm* | |
| *12* | *5* | *M3x10 Flat head bolt* | |
| *13* | *4* | *M4x16 Flat head bolt* | |

**Source holders (three sources side)**

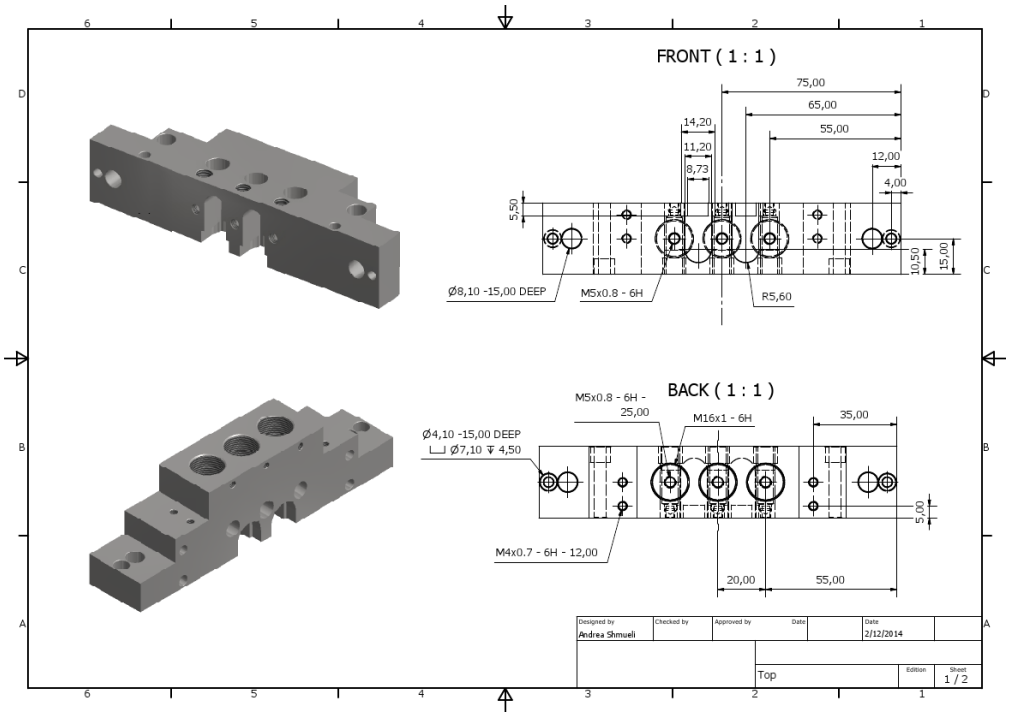


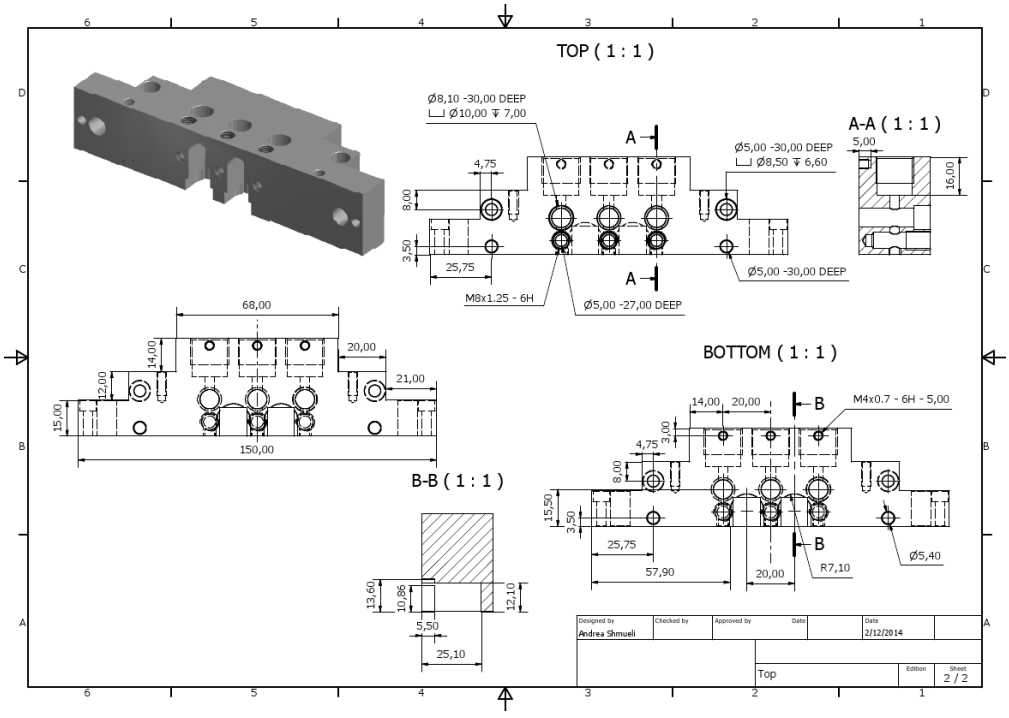

**Safety mechanisms tungsten pins**

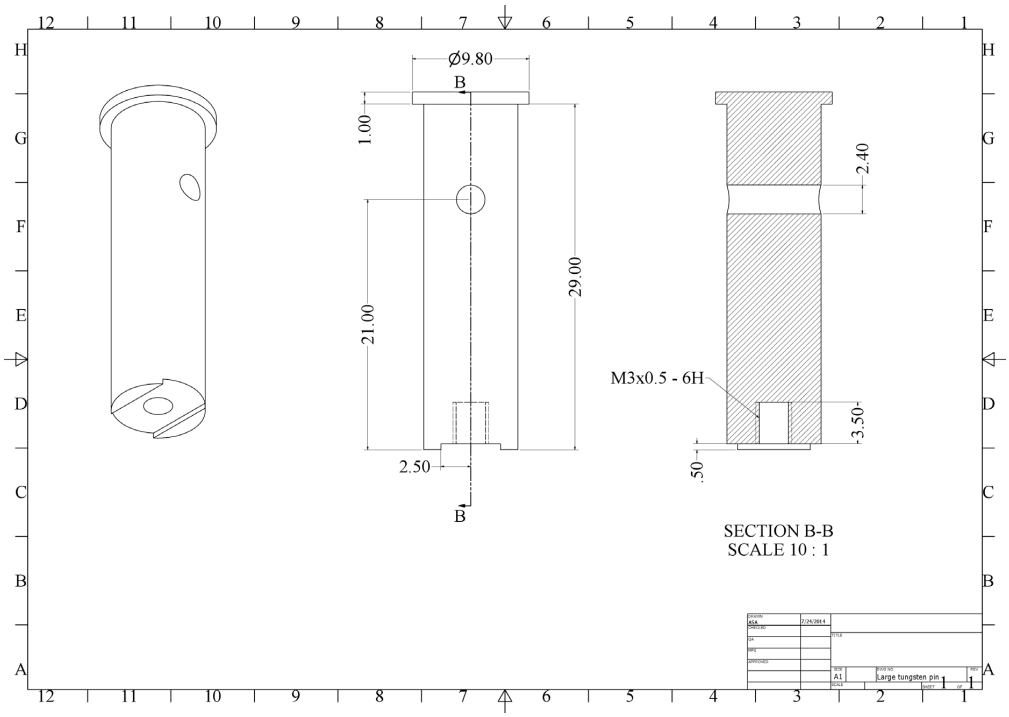


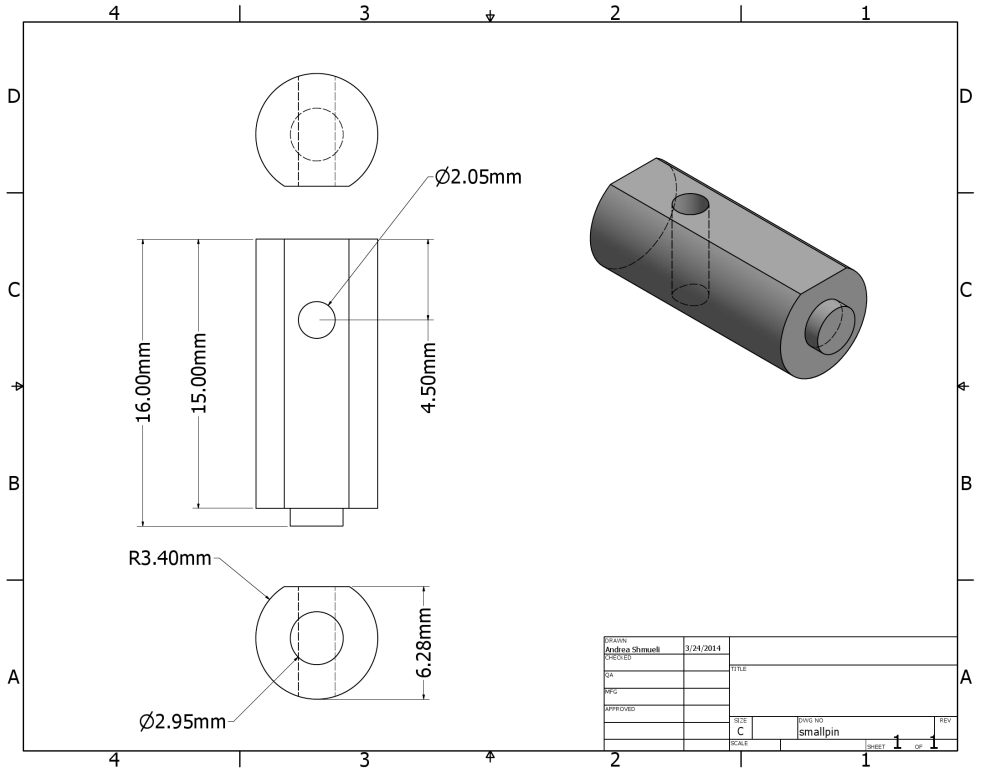

**Detector holder (three sources side)**

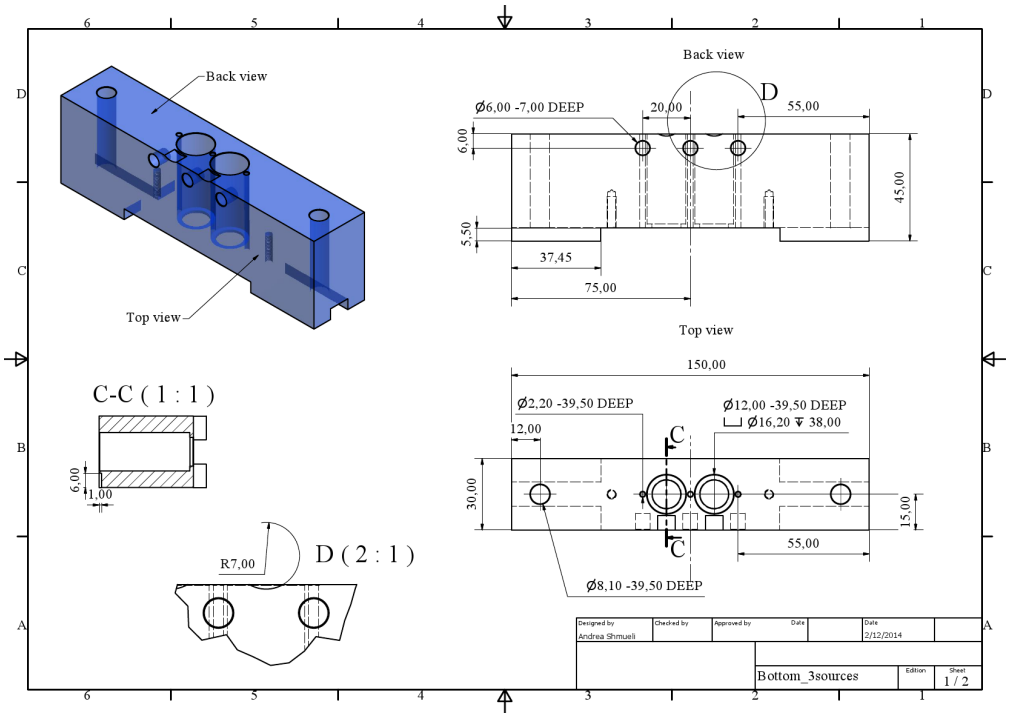


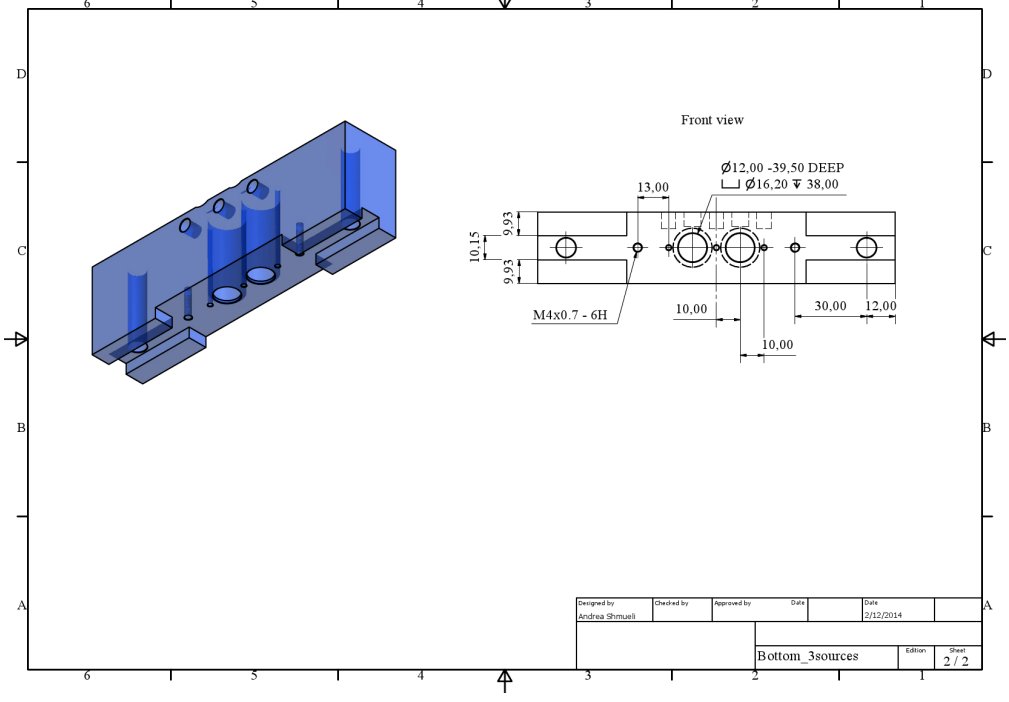

# Apendix H- Paper 4

*Shmueli, A. Nydal, O.J, Djoric, B. Unander, T.E*

## Oil and water droplet entrainment in horizontal gas liquid flows

Proc 8th North American Conference on Multiphase Flow. BHR Group. Cranfield, U.K pp 199-210International Conference on Multiphase Flow.

# Oil and water droplet entrainment in horizontal gas liquid flows

*A Shmueli, O J Nydal*
*Norwegian University of Science and Technology, Norway*
*B Djoric*
*Stavanger Research Centre, Total EP, Norway*
*T E Unander*
*SINTEF Petroleum Research, Norway*

**ABSTRACT**

Three oil-water-gas flows experiments have been carried out in a 68 mm ID pipe with a dense gas (simulating high pressure flows) and with oils of different viscosities (1.8-100 cP). Measurements include pressure drop and liquid entrainment using an isokinetic sampling probe. The flow is recorded with a high speed video camera. The tested gas velocities (1-4 m/s) did not give large entrained droplet fractions. The effect of water is to reduce the entrainment and pressure drop. OLGA predicts the pressure drop quite well.

## 1. INTRODUCTION

In order to design multiphase transport lines it is important to predict the transport of each phase in the pipeline in particular the liquid accumulation and the pressure drop. In separated flows, droplets can be torn off the liquid layer and be transported as a droplet field in the gas. There are two major flow effects coming from an entrained droplet field in the gas. Firstly, the droplet flow can represent a very large fraction of the liquid transport. Secondly, even when the entrained fraction is low, the droplets can cause wall wetting and thus contribute increasing the pressure drop.

1D flow requires closure relations related to the droplet field and these are usually calibrated to experimental measurements under controlled laboratory conditions. Some of the relevant published works are show in Table 1. Most of these experiments were done using water and air at atmospheric pressure where high gas velocities are needed to obtain liquid entrainment in the gas phase. However, the public domain experimental data available for three phase flow is scarce. The present experiments focus in three phase flow at elevated gas densities.

There are several methods proposed to calculate the pressure gradient for stratified wavy flow with droplets entrainment. Some of them are based on a simplified approach were the liquid droplet atomization and deposition are neglected. Vlachos *et al.* (1999) proposed a model that takes into account the gas/liquid interface and a procedure to calculate the liquid to wall shear stress considering a circumferential variation of it. The comparison between the predicted and experimental values (Paras *et al (1994),* Vlachos *et al* (1997)) shows a good agreement (max error 20%).

**Table 1. Previous experimental published works**

| Author | Year | Fluids | D [cm] | Usg [m/s] | WL [kg/s] | WC [%] | ρg [Kg/m$^3$] |
|---|---|---|---|---|---|---|---|
| **Dallman** | 1978 | Air-Water | 2,31 | 15,0-88,0 | 0,003–0,250 | 100 | 1,26–2,75 |
| **Laurinat** | 1982 | Air-Water | 5,08 | 11,0-131,0 | 0,033–0,970 | 100 | 2,05 |
| **Williams** | 1986-1990 | Air-Water | 9,53 | 26,0-88,0 | 0,12–0,86 | 100 | 1,3–1,85 |
| **Paras & Karabelas** | 1991 | Air-Water | 5,08 | 31,0-66,0 | 0,04–0,39 | 100 | 1,3–2,3 |
| **Tayebi** | 2000 | SF6-Water SF6-Exxsol D80 | 10,0 | 3,5-7,0 | 1,960 | 0/100 | 22-47 |
| **Mantilla** | 2008 | Air-Water Air-Water/ Butanol Air-Water/ Glycerin | 5,08 | 20,0-80,0 | 0,0035 -0,1 | 100 | 100 |
| **Boulesteix** | 2010 | Air-Water | 5,0 | 4,5-30,0 | 0,04-1,38 | 100 | 1,18-1,23 |
| **Skartlien** | 2011 | SF6-Water-Exxsol | 10,0 | 5,0-9,5 | 0,031-3,275 | 5/20/ 40/60 | 54 |

Some models for calculating the entrained fraction require estimating the pressure drop as a step in the computing procedure. Mantilla (2008) proposed a model to calculate the entrainment fraction for gas-liquid stratified flow. The pressure gradient calculation is based on the flow pattern (stratified or annular). For stratified flow the model of Hart *et al* (1989) takes into account the shape of the interface but not the atomization of droplets. However, there is a very good agreement between the experimental and predicted entrained fraction values. Meng *et al.* (2001) proposed a model to calculate the pressure drop for low liquid loading gas liquid stratified flow. The entrained liquid droplets were considered in the interfacial friction term for the pressure drop calculation. The interface shape was also taken into account using the double circle model proposed by Chen *et al.* (1997). There is an agreement within the 20% between experimental and predicted entrainment. For these models the experimental and predicted pressure gradient values are not compared.

The present work is part of a study on the effect of the water cut on the liquid entrainment and on the wall wetting for three phase flows systems. This will be done by starting from the two-phase flow (oil-gas) system and then adding water at a constant liquid superficial velocity. The experiments will include three main measurements: visual observation of the phenomenon, isokinetic sampling of the droplet stream along the vertical diameter and pressure gradient.

## 2. EXPERIMENTAL SETUP

The experiments were performed in the medium-scale flow loop located at SINTEF Multiphase Flow laboratory in Trondheim, Norway The facility consists of a 69 mm inner diameter, 53 m long pipeline. The pipeline can be tilted ±4° from the horizontal. In this study only a horizontal configuration was used. There is a transparent 1,95 m section

that was used to visualize the flow. The test section is located about 580D downstream the mixing point.

## 2.1 Instrumentation

### *2.1.1 Pressure gradient calculation*

The pressure gradient is calculated from the measurement of five pressure cells that are connected along the loop. The associated uncertainty of the pressure cells and the pressure gradient calculation are 6 Pa and 1-4Pa/m respectively. Following Smith *et al.* (2011), the uncertainty for the pressure drop is estimated as the uncertainty in the slope from regression of the dp-cells and respective positions.

### *2.1.2 Isokinetic sampling probe*

The liquid droplets entrained in the gas phase were sampled using an isokinetic probe. An isokinetic probe is a pitot type sampling tube that is designed to operate under isokinetic conditions where the pressure at tip of the probe is equal to the static pressure at the probe position. The probe has a 4 mm inner diameter, a 0,2 mm wall thickness and it extends 50 mm upstream. It was possible to collect droplets within 4,2 mm of the pipe wall. A traversing mechanism was used to cross the vertical diameter of the pipe.

The sampled flow goes through the probe to a gas-liquid transparent separator. The sampled liquid will be accumulated then in a clear vessel and the gas will flow through a flow meter and then to a control valve. The uncertainty associated with the measurement of the liquid droplet flow is $9 \cdot 10^{-9}$ $m^3/s$. The uncertainty was estimated by the error propagation using partial derivatives method. Figure 1 shows schematically of the probe module used during this study.

### *2.1.3 Traversing gamma densitometer*

To estimate the liquid layer height and the hold-up a narrow-beam traversing gamma densitometer (TGD) was used together with the visual support from the recorded videos. The TGD was located on the transparent section of the pipe. It is installed such that the beam which contains the collimated gamma emission crosses the pipe horizontally while it is transported from the bottom to the top of the pipe.

### *2.1.4 High-speed video camera*

Visual observations were performed in order to classify each flow pattern and to determine the height of the liquid layer (together with the traversing gamma densitometer). All the videos were recorded at 2500 frames per second in order to capture important characteristics of the flow such as the movement of the liquid droplets entrained in the liquid.

## 2.2 Fluid system

Three set of experiments were carried out using three oils, Nexbase 3080 (N3080), Exxsol D80 (ED80) and a mixture of both of them (Moil), water as liquid phase and sulphur hexafluoride ($SF_6$) as gas phase. The properties of the fluids at 20°C and 8 bar are shown in Table 2.

Smith *et al.* (2011), presented a relation for the viscosity of N3080 (in cP) as function of the temperature at atmospheric pressure. In the same way, a relation for the mixed oil (Moil) viscosity as function of temperature was obtained and presented below:

$$\mu_{N3080} = 89e^{-0.054\cdot(T-22.5)}$$

$$\mu_{Moil} = 63.57 - 1.39 \cdot T$$

Where T is the temperature in ºC. The densities for all the tested oils were measured online using a coriolis meter and it was found that the values were relatively constant during all experiments.

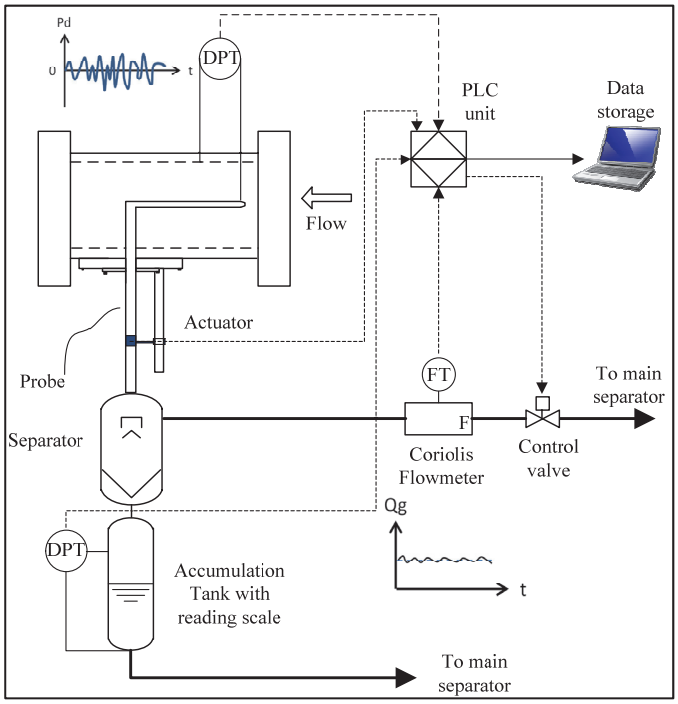


**Figure 1. Isokinetic probe module**

**Table 2. Oil and Gas Properties @ 20 °C**

| Fluid | Pressure [bara] | Density [Kg/m$^3$] | Viscosity [cP] |
|---|---|---|---|
| Nexbase 3080 | 7,0 | 847,9 | 101,9 |
| Exxsol D80 | 7,6 | 824,0 | 1,8 |
| Mixed oil | 4,3 | 844,5 | 35,9 |
| | 7,0 | 46,16 | |
| $SF_6$ | 7,6 | 50,58 | 0,015 |
| | 4,3 | 27,17 | |

### 2.3 Test Points

The flow pattern in a pipe depends on the liquid properties, geometry and superficial gas and liquid velocities used. Stratified flow with liquid entrainment is the flow pattern of interest in this study. For every fluid system and experimental condition, different combinations of liquid and gas superficial velocities were tested in order to determine the required flow range to obtain the desired flow patterns. Every point was classified from visual observations.

The test matrix of this study contains 3 fluids. The water cut has been changed at a constant superficial liquid velocity starting from oil-gas flow (WC=0%) and increasing as it is shown in Table 3.

**Table 3. Test points**

| Fluids | Pressure [bar] | Usl [m/s] | Uso [m/s] | Usw [m/s] | Usg [m/s] | WC [%] | Type of experiment |
|---|---|---|---|---|---|---|---|
| *(N3080/W/SF6)* Nexbase 3080 Water $SF_6$ | 7.0 | 0,2 | 0.2 | 0 | 1.3 | 0 | Qualitative |
| | | | 0.1 | 0.1 | | 50 | |
| | | | 0 | 0.2 | | 100 | |
| | | | 0.2 | 0 | 2.6 | 0 | |
| | | | 0.1 | 0.1 | | 50 | |
| | | | 0 | 0.2 | | 100 | |
| | | | 0.2 | 0 | 5.2 | 0 | |
| | | | 0.1 | 0.1 | | 50 | |
| | | | 0 | 0.2 | | 100 | |
| *(ED80/W/SF6)* Exxsol D80 Water $SF_6$ | 7,6 | 0,25 | 0.25 | 0 | 5.0 | 0 | Qualitative |
| | | | 0.20 | 0.05 | | 20 | |
| | | | 0.15 | 0.1 | | 42 | |
| *(MO/W/SF6)* Mixed oil Water $SF_6$ | 4.3 | 0.1 | 0.1 | 0 | 6.49 | 0 | Qualitative/ Quantitative |
| | | | 0.0923 | 0.0077 | | 7.7 | Qualitative |
| | | | 0.09 | 0.01 | | 10 | Qualitative/ Quantitative |
| | | | 0.08 | 0.02 | | 20 | Qualitative/ Quantitative |
| | | | 0.03 | 0.07 | | 70 | Qualitative/ Quantitative |

## 3. RESULTS AND DISCUSSION

### 3.1 Qualitative Measurements

Video recordings for superficial gas velocity and water cut for a constant liquid superficial velocity and for N3080/W/SF6 and ED80/W/SF6 are shown in the matrix at Figure 2 and Figure 3.

Figure 2 shows that the liquid droplet entrainment is strongly dependent of the gas velocity. For constant water cut the entrainment will increase with increasing velocity (Tayebi *et al.* (2000), Ishii & Mishima (1989), Paras & Karabelas (1991), among others).The liquid layer thickness reduces its size as the gas velocity increases. At higher gas velocities more liquid goes from the layer to the gas core and pipe walls.

From the pictures it is observed that the liquid droplet entrained fraction decreases when water is added to an oil-gas system at the same gas and liquid velocities. There is less droplet entrainment for a 100% water cut (water-gas flow) than for 0% water cut (oil-gas flow). A thin liquid film covering partially or in some cases the whole perimeter of the pipe can make the visualization of droplets harder. When water is added to the system the film starts to become thinner and gradually disappear.

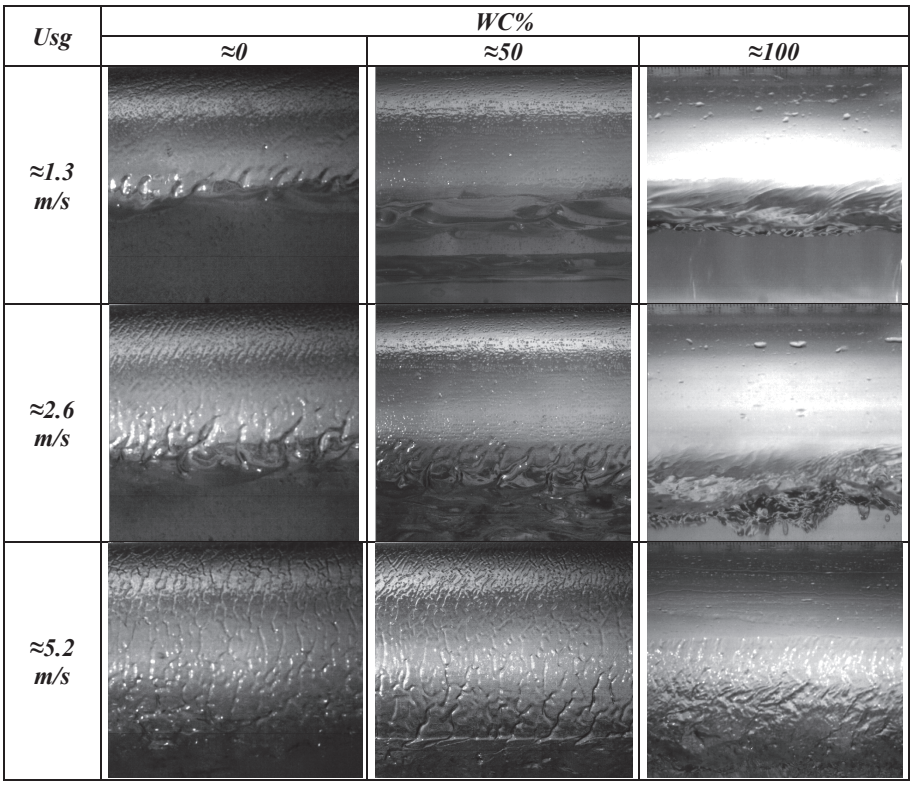


**Figure 2. Variation of the Usg and water cut at a constant Usl≈0,2 m/s**
**Fluids: Nexbase 3080/Water/$SF_6$**

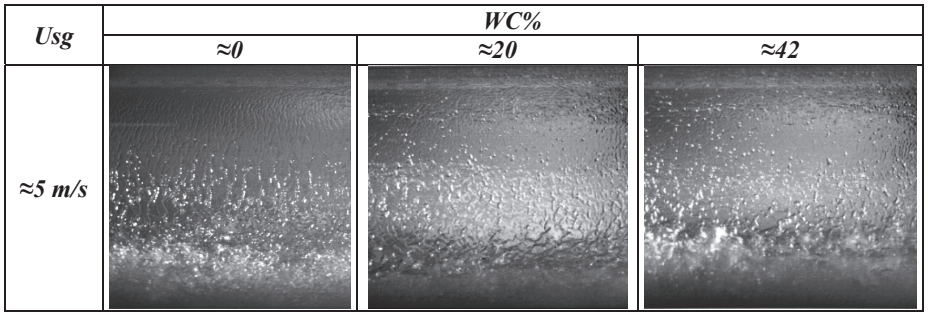


**Figure 3. Variation of the water cut at a constant Usl≈0,25 m/s**
**Fluids: Exxsol D80/Water/$SF_6$**

In order to show visually the effect of the water cut on the wall wetting phenomenon, pictures of the top and front side of the pipe have been taken for WC=0% and WC=7.7% using the Mixed oil as an Oil phase. These pictures are shown in Figure 4. For the two-phase flow system it is possible to see that the liquid film is covering the entire pipe perimeter while after adding a small water fraction (0.028 Kg/s), the top of the pipe is not covered by liquid. After making the comparison of all the videos from the experiments it was observed that as the viscosity of the oil is higher, more water should be added to the system in order to decrease the liquid layer thickness.

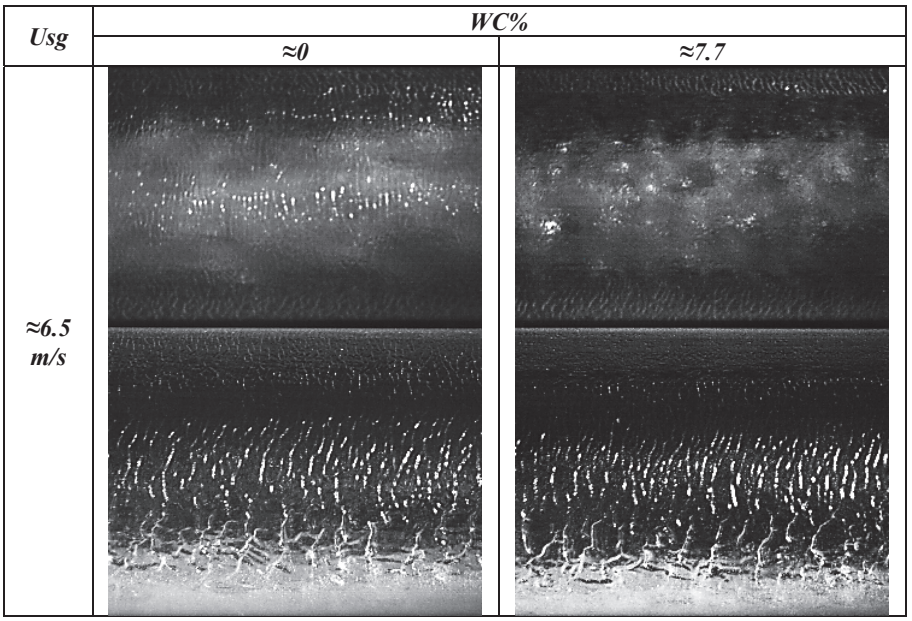


**Figure 4. Variation of the water cut at a constant Usl≈0,25 m/s Fluids: Mixed oil/Water/$SF_6$ (Top and side view of the pipe)**

Figure 5 shows a summary of the expected behavior of the liquid film on the pipe wall and droplets entrained when the water cut is increasing at constant liquid and gas superficial velocities. The added water will help to reduce the entrainment and the liquid film thickness.

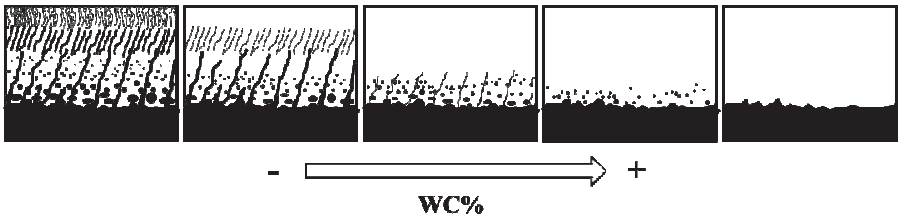


**Figure 5. Summary of the behavior of the liquid film on the pipe wall and droplets entrained**

### 3.2 Quantitative Measurements

#### *3.2.1 Liquid entrained fraction*

From the visual observations two main phenomena were noted when the water cut increases at constant superficial gas and liquid velocities: the liquid droplet entrainment and the wall wetting decrease. Using an isokinetic sampling probe the droplet flux in the gas is measured along the vertical diameter. The tested fluid system was MO/W/S as it was shown in Table 3.

As found previously from Tayebi *et al*. (2000) an exponential liquid droplet distribution in the vertical diameter of the pipe for both liquid phases (oil and water) was successfully

fitted to the experimental data. The local volume flux of droplets will then have the shape:

$$q = A \cdot exp(-B \cdot z) + C \cdot exp(-D \cdot z)$$

Where A, B, C, D are the fitting constants and z is the height measured from the gas-liquid interface. The interface position was visually estimated from the pictures and measurements on the pipe diameter on the clear section. There is an important uncertainty in the measurements related to the definition of this interface. The total liquid that is transported as droplets is calculated by integrating the local liquid flow of droplets from the gas liquid interface to the top of the pipe. The droplet entrainment fraction is defined by the total liquid mass flow rate ($W_{tl}$), the entrained oil droplet mass flow rate ($W_{oe}$) and the entrained water droplet mass flow rate ($W_{we}$) as follows:

$$E = \frac{W_{le}}{W_{tl}} = \frac{W_{oe} + W_{we}}{W_{tl}}$$

Figure 6 shows the liquid entrainment fraction obtained for different water cuts. As it was observed from the pictures on Figures 2 to 4 the entrained fraction decreases when the water cut increases. The most important decrease occurs when a small water fraction is added to the oil system (between WC=0% and 10%). For this case as the liquid flow rate is so small, it was not possible to quantify the amount of water for WC=10%, so the entrained fraction shown for that specific point is calculated just with the oil droplets flow. However from Figure 7 we can approximate the percentage of the water entrained droplets from the total entrainment at WC=10% (≈5% of the total liquid entrained droplets).

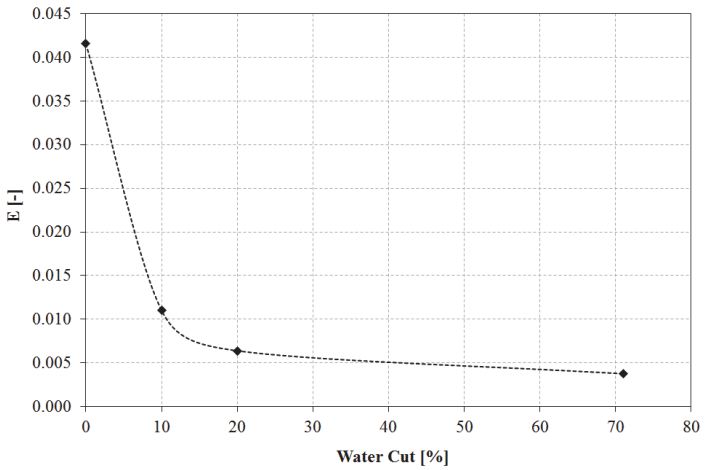


**Figure 6. Entrainment fraction vs. Water cut for fluid system MO/W/S**

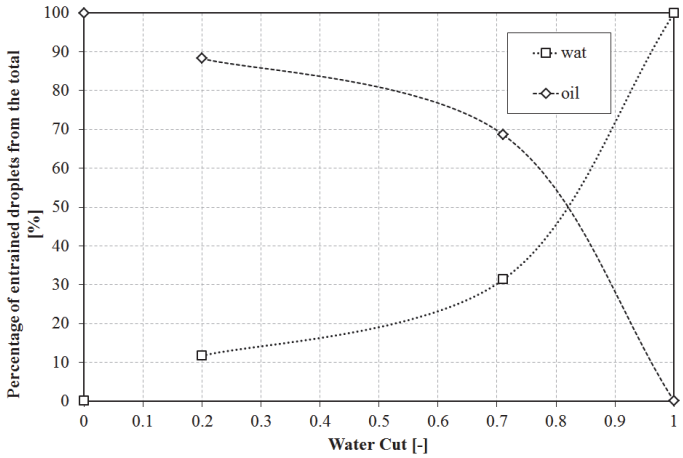


**Figure 7. Percentage of the entrained droplet of a phase from the total liquid entrainment**

### *3.2.2 Axial pressure drop*

The axial pressure drops at different water cuts for all the studied fluid systems and operational conditions are shown at Figures 8 to 10.

The pressure gradient decreases when the water fraction increases. The biggest drop of the pressure gradient occurs at low water cut values. As it was shown in sections 3.1 and 3.2.1 adding a small amount of water to a gas-oil flow system working under entrainment conditions can cause a decrease in the droplets atomization and on the wall wetting. For the mixing oil case it was observed a slightly increment on the pressure drop at 70% water cut. More experiments are needed to confirm this trend. For the Nexbase 3080 case, the global pressure gradient values increase while the superficial gas velocity does it also at constant pressure, liquid velocity and water cut.

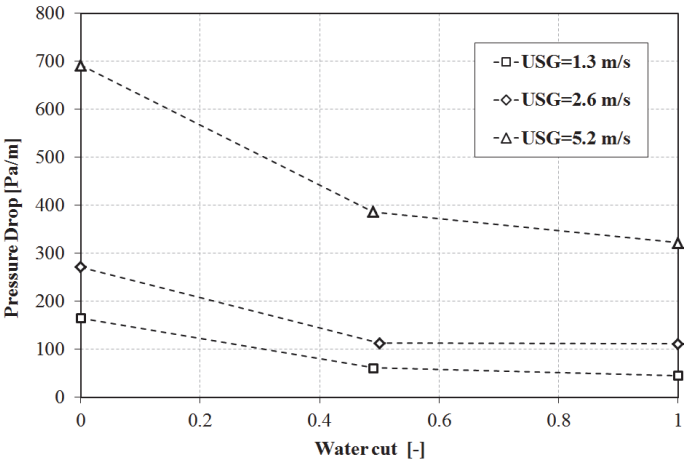


**Figure 8. Pressure drop vs. Water cut at a constant Usl≈0,2 m/s Fluids: Nexbase 3080/Water/$SF_6$**

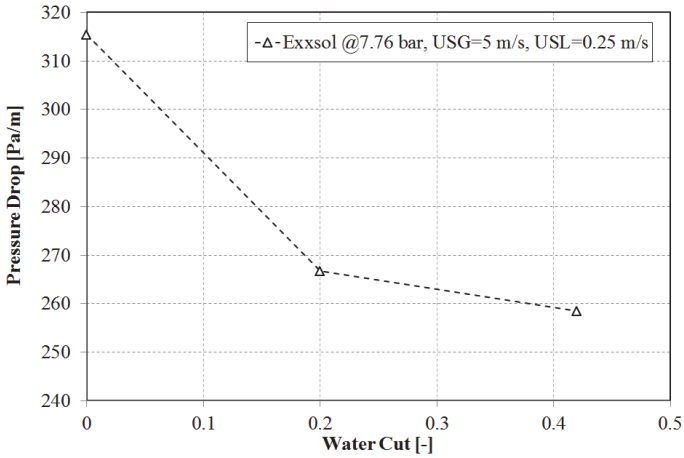


**Figure 9. Pressure drop vs. Water cut at a constant Usl≈0,25 m/s Fluids: Exxsol D80/Water/$SF_6$**

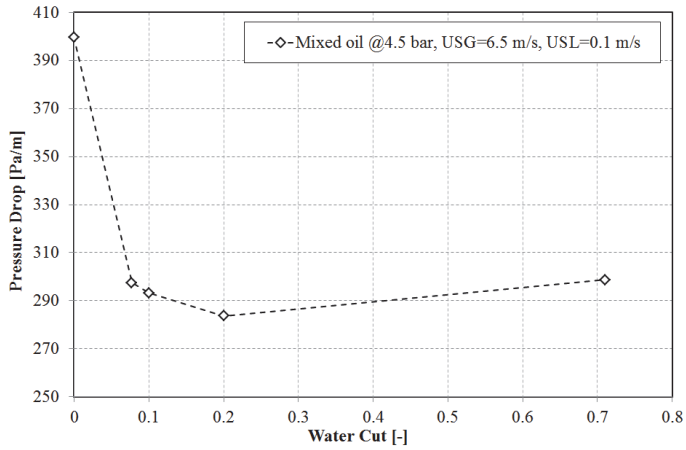


**Figure 10. Pressure drop vs. Water cut at a constant Usl≈0,1 m/s Fluids: Mixed oil /Water/$SF_6$**

*3.2.2.1 Comparison with pressure gradient models*

Some models for the pressure drop are compared with the experimental data sets in this study, Paras *et al* (1994) and Tayebi *et al.* (2000) oil data. The experimental conditions are shown in Table 1. The selected models for comparison are the Hart *et al* (1989) model and OLGA 7.1.3 point model.

The Hart *et al* (1989) model (Figure 11) gives fairly good predictions for the data from Paras *et al* (19940) but for high pressure conditions the model over predicts the pressure gradient. This correlation is based on experiments with low viscosity oils carried out at atmospheric pressure. This can be the cause of the weak fitting for high pressure viscous oils. The OLGA point model (Figure 12) shows a fairy good agreement with the experimental pressure gradient values. For the data of this study, the predicted pressure drop from both models decreases with the water cut.

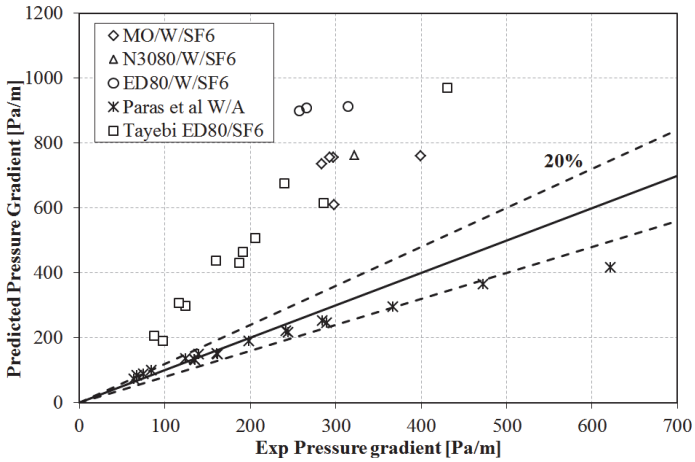


**Figure 11. Comparison between the Predicted and experimental Pressure drop. Model: Hart *et al* (1989)**

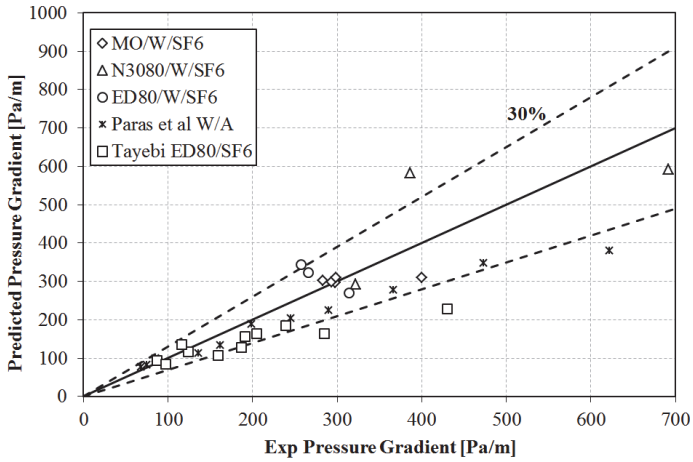


**Figure 12. Comparison between the Predicted and experimental Pressure drop. Model: OLGA point model**

## 4 CONCLUSION

An experimental campaign on droplet flux measurement has been started and some initial experimental results are presented for flows using Exxsol D80, Nexbase 3080 and a Mixed oil as oil phase together with water and $SF_6$. An isokinetic sampling probe has been used.

For the studied conditions, the liquid droplet entrained fraction and the wall wetting decrease when water is added to an oil-gas system at the same gas and liquid velocities. While the entrainment and the wall wetting become smaller the pressure gradient will decrease.

The experimental pressure gradient results from this study and other studies from the literature were compared with a simplified correlation from the literature and OLGA point model.

The predictions of Hart *et al* (1989) show a good agreement with data at atmospheric pressure but fails for high pressure systems. The OLGA point model shows a good agreement in general.

## REFERENCES


Boulesteix, S. (2010).Cisaillement d'une interface gaz-liquide en conduit et entraînement de goutelletes. *PhD Thesis*. *University of Toulouse.*

Chen, X.T., Cai, X.D., and Brill, J.P.,(1997). Gas Liquid Stratified Wavy Flow in Horizontal Pipelines. *ASME J* 119(4) 209-216

Dallman, J. (1978). Investigation of Separated Flow Model in Annular Liquid Two-Phase Flows. *PhD Thesis. University of Illinois at Urbana-Champaign*

Falcone, G., Hewitt, G., Alimonti, C. (2009) Multiphase flow metering "principles and applications", *Developments in petroleum science*, volume 54 Elsevier, Great Britain.

Hart, J., Hamersma, P.J., Fortuin, J.M.H., (1989). Correlations predicting frictional pressure drop and liquid holdup during horizontal gas-liquid pipe flow with a small liquid holdup. *IJMF* 15(6), 947-964

Ishii, M., Mishima, K., (1989) Droplet Entrainment Correlation in Annular Two-Phase Flow. *IJHT* 32(10), pp 1835-1846.

Laurinat, J.E. (1982) Effect of Pipe Size on Horizontal Annular Two-Phase Flows. *PhD Thesis. University of Illinois at Urbana-Champaign.*

Mantilla, I. (2008). Mechanistic Modeling of Liquid entrainment in Gas in Horizontal Pipes. *PhD Thesis. University of Tulsa.*

Meng, W., Chen, X.T., Kouba, G., Sarica, C., and Brill, J.P. (2001). Experimental study of low liquid loading gas liquid flow in near Horizontal Pipes. *SPEPF* 16 (4). 240.249. SPE-74687-PA.

Paras, S., Karabelas, J. (1991). Droplet Entrainment and Deposition in Horizontal Annular Flow. *IJMF* 17(4), pp 455-468.

Paras, S., Vlachos, N.A., Karabelas, J. (1994). Liquid Layer Characteristics in Stratified-Atomization Flow. *IJMF* 20(5), pp 939-956.

Skartlien , R., Nuland, S., Amundsen, J. (2011). Simultaneous Entrainment of Oil and Water Droplets in High Reynolds Number Gas Turbulence in Horizontal Pipe Flow. *IJMF* 37 pp 1282-1293.

Smith, I.E., Krampa, F.N, Fossen, M., Brekken, C., Unander, T.E. (2011) Investigation of Horizontal Two-Phase Gas-Liquid pipe flow using High Viscosity Oil and Simulations. Proc. 15th International Conference on Multiphase Production Technology. BHR Group, Cranfield, U.K. pp 293-307.

Tayebi, D., Nuland, S., Fuchs, P. (2000) Droplet Transport in Oil/Gas and Water/Gas at High Densities. IJMF. 26. Pp 741-761.

Vlachos, N.A, Paras, S., Karabelas, J. (1999) Prediction of holdup, axial pressure gradient and Wall shear stress in wavy stratified and stratified/atomization gas/liquid flow. IJMF 25 pp 365-376.

Williams, L. (1990). Effect of Pipe Diameter on Horizontal Annular Two-Phase Flow. PhD Thesis. University of Illinois at Urbana-Champaign.

# Apendix I- Paper 5

*Shmueli, A.,Unader, T.E., Nydal, O.J.*

## Liquid droplet entrainment in horizontal three-phase flow

Proc 8th International Conference on Multiphase Flow. ICMF 2013. Jeju, Korea.

# Liquid droplet entrainment in horizontal three-phase flow

Andrea Shmueli[1], Tor Erling Unander[2], Ole Jørgen Nydal[1]

[1]*Department of Energy and Process Engineering, Norwegian University of Science and Technology, Trondheim, Norway*
[2]*Department of Petroleum Research, SINTEF, Trondheim, Norway*

**Keywords**: Entrainment, Droplet transport, Isokinetic sampling, stratified flow, three phase flows

## Abstract

Liquid entrainment experiments have been performed in a horizontal, 69 mm ID pipe. Exxsol D80 and water were used as liquid phases and $SF_6$ was used as gas phase in order to simulate high pressure flows. A new 4mm ID isokinetic sampling probe was designed to traverse the cross section of the pipe in high pressure systems. This probe has the capability of simultaneous droplet flux sampling and gas mass flow measurement. Two water cuts were tested. A global reduction in the entrainment was observed when the water cut increases when comparing droplet fluxes contour plots. Non uniformities of the droplet profiles on the pipe cross section were found suggesting the existence of secondary flows.

## Introduction

Gas-liquid flows are very common in the industry and in many cases the liquid phase is hydrocarbons and water. The droplet entrainment in the gas phase and the pressure drop in the pipeline are important variables to predict when designing multiphase flow lines and equipment.

In separated flows, droplets can be entrained from the liquid layer and transported as a droplet field in the gas phase. There are two major flow effects from an entrained droplet field in the gas phase. The droplet flow can represent a very large fraction of the liquid transport. Even when the entrained fraction is low, the presence of droplets can be important because droplets cause wall wetting and thus contribute to increased pressure drop.

It is common practice to use 1D flow models to describe the behavior of multiphase flow. These models require closure relationships related to the droplet field. These relationships are usually obtained from experimental measurements under controlled operating conditions.

Most of the experimental work in the past has been done using water and air at atmospheric pressure. All of these previous studies provide important information about liquid droplets entrainment. However there is still a lack of experimental data in three phase flow and at high pressures.

There are a limited number of experiments of the droplet entrainment over the entire pipe cross-section. The uniformity of the droplet flux distribution on the pipe cross section is one assumption in most of the current models. One objective of this study is to quantify and understand cross sectional distributions effect.

Paras & Karabelas (1991) measured water and air droplet flux over the cross section of a 50.88 mm ID pipe in annular horizontal flow using an isokinetic probe. The fluid system was air and water at atmospheric conditions. They managed to measure the droplet fluxes along both axis of the pipe cross section. Entrainment is fairly constant along the horizontal axis for low liquid rates. However there is no uniformity of the droplet concentration distribution at high liquid rates and the authors attribute this non uniformity to the measuring technique uncertainty.

Williams et al (1996) measured the liquid droplet flux in the pipe cross section using the experimental setup explained in Williams (1990). The local droplet flux was sampled with an isokinetic probe. Two cases where studied: stratified flow with dry top wall and stratified-annular flow. On his cross section measurements he found a non uniformity along the horizontal direction in the droplet concentration profiles. He proposed that this non uniformity could be caused by a secondary flow. In their study, the secondary flow will appear when the concentration of droplets was high. This fact is consistent with the observations from Westende which state that the existence of secondary flows in the gas core of stratified-annular flow can modify the droplet distribution and its deposition on the wall (Westende, 2007).

In addition to Williams et al (1996) measurements, Dykhno et al (1994) and Flores et al. (1995) have supported the existence of secondary flows.

Dykhno et al. (1994) performed axial gas velocity measurements on the pipe cross section using the isokinetic probe from Williams (1990) as a Pitot tube. This flow helps the transport of the liquid droplets to the wall and therefore increases the wall film thickness.

Westende (2007) studied the effect of the dispersed liquid phase on the secondary flow in stratified-annular flow. He performed large eddy simulations (LES) of air-water horizontal-annular flow and compared the results with experiments he carried out using Phase Doppler Anemometry (PDA) and with the gas velocity profiles displayed by Dykhno et al. (1994).

The present work is part of an ongoing study on the effect of the water cut on the liquid entrainment and on the wall wetting for three phase flows systems. The experiments presented in this paper include isokinetic sampling of the droplet stream and gas phase along the pipe cross section for two and three phase flows at pressure conditions higher than atmospheric.

## Nomenclature

| | |
|---|---|
| D | Pipe Diameter (m) |
| U | Axial Velocity (m/s) |
| R | Pipe radius (m) |
| n | Fitting parameter (-) |
| P | Pressure (bar) |
| K | Velocity correction factors due to droplets (-) |
| q | Local flow rate ($m^3$/s) |
| A | Area ($m^2$) |
| N | Number of measured points |
| Re | Reynolds number (-) |
| WC | Water cut (%) |
| *Greek letters* | |
| ρ | Density (Kg/$m^3$) |
| μ | Dynamic viscosity (Pas) |
| ψ | Wave velocity parameter (-) |
| *Subsripts* | |
| g | Gas |
| o | Oil |
| w | Water |
| l | Liquid |
| s | Superficial |
| m | mixture |
| max | Maximum |
| d | dynamic |
| p | Probe |

## Experimental setup

The experiments were performed in the medium-scale flow loop located at SINTEF Multiphase Flow laboratory in Trondheim, Norway. A horizontal 49m long steel pipeline with an internal diameter of 69mm was used. There is transparent 1,95 m section that was used to visualize the flow. The isokinetic probe test section is located about 470D downstream the mixing point.

The sampling experiments were carried out using Exxsol D80 (ED80) and water as liquid phase and sulphur hexafluoride ($SF_6$) as gas phase. $SF_6$ is a high density gas that can reproduce relevant field conditions at high pressures. All the experiments were run at 4.7 bara. The physical properties of the fluids are shown in Table 1. Due to the pressure drop in the pipe, the gas density is corrected for the calculations at the probe location.

The pressure gradient is calculated from the measurement of five pressure cells that are connected along the loop (at 430D, 633D, 865D, 1071D and 1274D). The associated uncertainty of the pressure cells and the pressure gradient calculation are 6 Pa and 1-4Pa/m respectively. The uncertainty for the pressure drop is estimated as the uncertainty in the slope from regression of the dp-cells and respective positions (Smith *et al.* 2011).

**Table 1** Fluid Properties

| Fluid | Density [Kg/$m^3$] | Viscosity [cP] |
|---|---|---|
| Exxsol D80 | 813 | 1.8 |
| Water | 998 | 1.0 |
| $SF_6$ | 27.8 | 0.0151 |

The gas liquid interface location was measured on the outer pipe perimeter at the clear section using a scale attached to the pipe surface. In addition, a traversing gamma densitometer was available to measure the phase fractions. High speed videos of the flow side and top view of the pipe were recorded. The sampling frequency was set at 2500 frames/sec.

The liquid droplets entrained in the gas phase were sampled using an isokinetic probe. An isokinetic probe is a Pitot type sampling tube that is designed to operate under isokinetic conditions. Isokinetic conditions are achieved when the total pressure at tip of the probe is equal to the static pressure at specific probe location and at a constant gas mass flow.

A new 4mm ID. Isokinetic sampling probe was designed and built to either sample isokinetically or to work as a Pitot tube. The probe can be positioned at different locations inside the pipe using simultaneously a linear and a rotary actuator. A real picture of the probe with a description of its components is shown on Figure 1. The operating principle of the probe moving system is described on Figure 2.

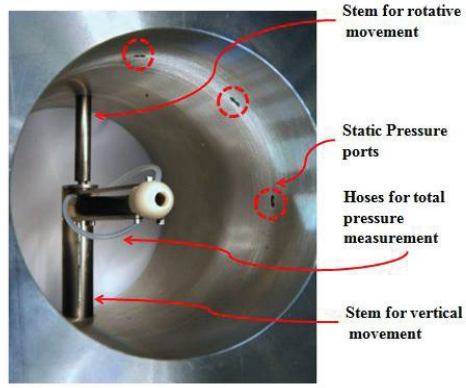


**Figure 1** Isokinetic probe

The measurement of the total and static pressure are made at the probe tip and at the inner pipe wall respectively. The sampled flow goes through the probe to a gas-liquid transparent separator. The sampled gas will flow through a coriolis flow meter and then to a control valve. The liquid will be accumulated in a clear vessel. Two clear vessels with 69mm and 17mm ID were used. The pressure difference between the test section and the separator was too low to generate sufficient suction to obtain the isokinetic condition. For this purpose, two gas compressors connected in parallel between the control valve and the flow meter were used. Figure 3 shows schematically of the probe module used during this study.

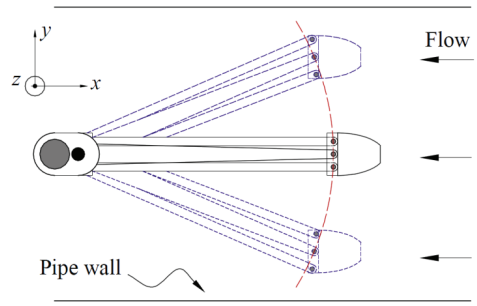


**Figure 2** Probe operating principle

All the signals from the pressure transmitter, the valve, coriolis flow meter and the actuators are sent to a PLC unit with a built-in HMI operator panel. On the screen is possible to set the desired probe location and to visualize the signals from the instrumentation at the probe module. The pressure signal from the probe, gas flow rate, valve opening and tank pressure is plotted in real time on the screen. Using the PLC unit was possible to control automatically the isokinetic condition.

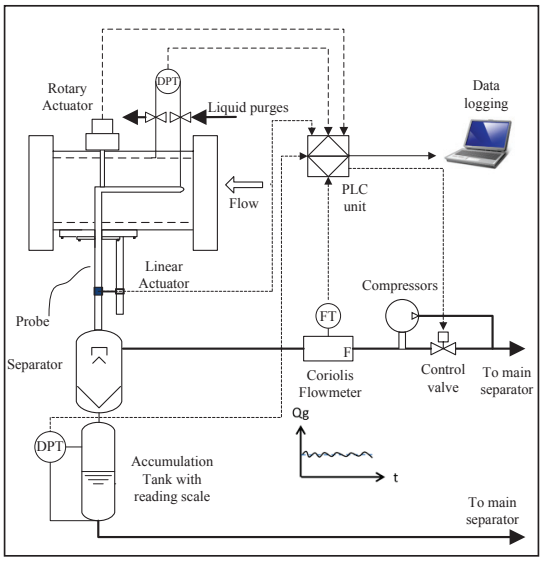


**Figure 3** Isokinetic probe module

The total pressure sensing hoses can be blocked by oil after certain sampling time and wrong pressure values would be sensed. For this reason, the little hoses were flushed and cleaned with pressurized $SF_6$ at the beginning of each sampling measurement.

## Probe Measurements Validation:

The probe was designed to work as a sampling probe and as a Pitot tube. The local gas velocity is necessary to determine the local droplet concentration (Tayebi, 2000) and to understand the flow physics. Two kinds of experiments were run to guarantee the results from the probe. Single phase isokinetic sampling experiments using $SF_6$ were carried out at 8 m/s to verify the velocity profiles. Secondly, sampling and Pitot experiments using two phase oil and gas were done along the vertical pipe diameter using Exxsol D80 and $SF_6$ at 0.2m/s and 5.9 m/s respectively and compared.

- *Gas single phase velocity profiles*

The power law velocity profile for fully developed turbulent pipe flow can be written as:

$$\frac{U}{U_{\max}} = \left(1 - \frac{r}{R}\right)^{1/n} \quad (1)$$

$$r = \sqrt{y^2 + z^2} \quad (2)$$

The value of the exponent $n$ will depend and increase with the Reynolds number (Cengel, 2004). There are many suggested empirical values for this coefficient and a summary of most of them are shown in Afzal et al (2007). The value of $n$ which fits the experimental data the best was found to be 8.8.

Pitot measurements were carried out in half of the pipe cross section and the profiles are plotted against the Power-law profile on Figure 4. There is a good agreement between the experimental data and the proposed theoretical profile.

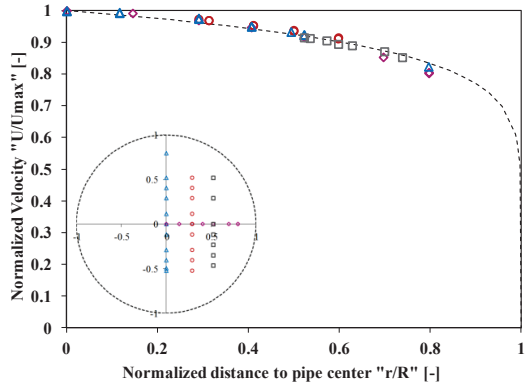


**Figure 4** Comparison between Power-law velocity profile and the local gas velocity profiles at 8 m/s.

- *Oil and gas stratified flow gas velocity profiles*

In order to measure the local gas velocity using the probe as a Pitot tube it is assumed that the stagnation pressure will be the same as the kinetic energy of the mixture. Following Skartlien (2011),

$$U_g = \sqrt{\frac{2 \cdot P_d}{\rho_m}} \quad (3)$$

$$\rho_m = K_o \cdot \rho_o + K_w \cdot \rho_w + K_g \cdot \rho_g \quad (4)$$

The value for the constants $K_i$ will correct the velocity profile distortion due to the existence of liquid droplets.

As it was mentioned before, the isokinetic probe module has a Coriolis gas flow meter downstream of the gas liquid separator (Figure 2). The local gas velocity can be calculated using the sampled gas flow rate in Equation 5.

$$U_g = \frac{q_g}{A_p' \cdot \rho_g} \quad (5)$$

When sampling liquid and gas simultaneously using the probe, the liquid will tend to stick to the probe walls and therefore the gas flow effective area will be less than when it is flowing alone. Therefore it is required to obtain the effective gas flowing area *"$A'_p$"*. This area will be estimated by tuning the gas mass values to the flow using the Pitot tube measurements until the average deviation between them was less than 1%. The average deviation is defined as in Equation 6. Different experiments changing Usg at Usl=0.2 m/s confirm that the value obtained for the effective

flowing area is valid for all the tested conditions.

$$Average\ dev = \left( \frac{1}{N} \sum_{i=1}^{N} \left| \frac{U_{Sampled} - U_{Pitot}}{U_{Pitot}} \right| \right) \cdot 100 \qquad (6)$$

N… Number of measured points

The velocity profiles obtained from both proposed methods are displayed in Figure 5. Both methods had shown an agreement regarding the gas velocity profile shape. Using the probe module is therefore possible to measure simultaneously the gas local velocity and sampling the liquid droplets entrained in the gas core.

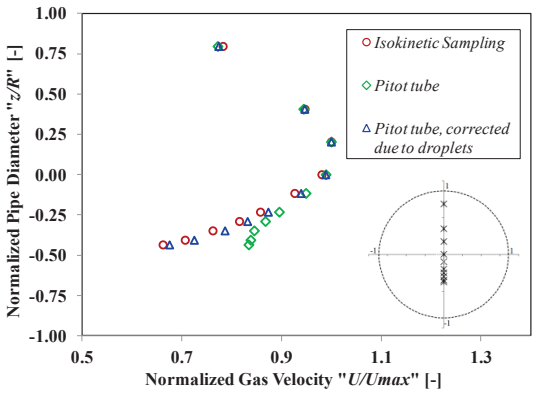


**Figure 5** Comparison between the velocity profiles obtained using the sampling and Pitot tube method.

## Test points

The cross section sampling experiments were conducted starting from an oil-gas system. The water cut has been changed at a constant superficial liquid velocity as it is shown in Table 1.
Two flow patterns were identified during this study: Stratified-annular flow (Cases 1, 3 and 4) and stratified flow with atomization (Case 2). A thin liquid film was present in all the studied cases. However the top of the pipe was not wetted in case 2.

**Table 1** Test points matrix

| Case | Usg [m/s] | WC [%] | Uso [m/s] | Usw [m/s] | Wetted top of pipe |
|---|---|---|---|---|---|
| 1 | 5.9 | 0 | 0.2 | 0 | Wet |
| 2 | | 20 | 0.16 | 0.04 | Non Wet |
| 3 | 8.5 | 0 | 0.2 | 0 | Wet |
| 4 | | 20 | 0.16 | 0.04 | Wet |

## Results and Discussion

In this section, the results of the sampled liquid entrained droplets and gas flow rate profiles are shown for the selected test conditions and fluids.

- *Gas axial velocity*

Two boundary conditions were imposed to the gas velocity data from experiments. These were, the waves celerity, using Kumar et al. (2002) model (Equation 7) and zeros velocity values on the pipe wall above the liquid film.

$$V_{waves} = \frac{\Psi \cdot U_{sg} + U_{sl}}{\Psi} \qquad (7)$$

Where

$$\Psi = 5.5 \cdot \left( \frac{\mathrm{Re}_{sl}}{\mathrm{Re}_{sg}} \right)^{0.25} \cdot \sqrt{\frac{\rho_g}{\rho_L}} \qquad (8)$$

The oil-water liquid layer in three-phase flow experiments was completely mixed. For this reason mixture properties of oil and water where used. The viscosity of the liquid mixture was considered as the continuous phase viscosity (oil).
The velocity contours for all the tested conditions are normalized by the maximum velocity value and shown in Figure 6. All the sampled points are shown as a red cross on the plot.

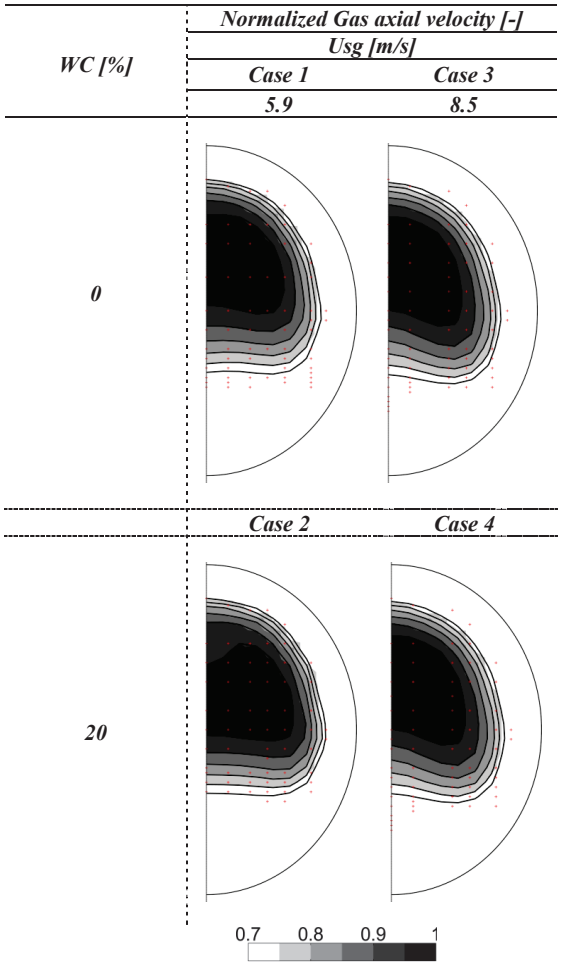


**Figure 6** Normalized Gas velocity contours.

An upwards shifting in the maximum axial velocity location was observed by Dykhno et al. (1994) when increasing the superficial gas velocity. This shift was not clearly detected on the velocity contours for this study at the selected conditions. The tested conditions shown in the contour plots are from stratified flow with atomization to stratified annular flow.
There is a distortion on the profiles when increasing the velocity. This can be caused by secondary flows that ha been enlarged due to the increment of liquid droplets. For Case 2 this distortion on the lower side of the gas core become smaller compared to Case 1. Maybe caused by the reverse effect where the secondary flow gets weaker when the entrained droplets are reduced. This behaviour is not observed in Case 4.
The shape of velocity contour of Case 2 is similar to the ones found by Dykhno et al. (1994) for no or small amount of atomization. From visual observations it has been seen that the liquid droplet flux for this case was less than for Case 1 but still considerable.

- *Liquid particle fluxes and distribution*

The normalized local oil and water droplet fluxes for the pipe cross section are shown in Figure 7 for the cases 1-4. The values of the droplet fluxes were divided by the maximum value of the two-phase condition (Case 1,3). This was done following the observations of Shmueli et al. (2011) where the liquid entrained will decrease when increasing the water cut. On the contour plots a reference value of the gas liquid interface is shown. However this value does not correspond to the exact experimental value. All the sampled points are displayed as blue crosses on the contour plots. There is a significant decrease on the droplet flux magnitude for all the tested cases along the vertical diameter. The local flux of droplets increased when increasing the gas velocity at constant water cut. These observations are in agreement to previous studies (Ishii & Mishima (1989), Williams et al. (1996), Tayebi et al. (2000), Shmueli et al. (2011) among others).
It is also observed that the magnitude of the droplet flux decrease when increasing the water cut. This is consistent with the visual observations shown by Shmueli et al. (2011). However it is necessary to perform the integration of the droplet fluxes profiles on the pipe cross section to conclude if the added water will have a significant reduction on the total liquid entrained fraction. A thorough estimation of the gas-liquid interface will be required when doing the integration.
The contours of the water and oil droplets flux are not uniform on the horizontal axis for all the studied cases. The shapes of the contours are similar to the ones displayed by Williams (1996) and with the simulation results by Westende (2007). The non uniform contours on the horizontal axis can be explained by the existence of secondary flows on the gas core. Secondary flows can transport particles (counter clockwise) from the bottom centre to the top of the pipe due to the roughness effect or can transport particles clockwise from the bottom centre due to the film atomization (Belt, 2007).
There is a redistribution of the droplets when water is added at constant gas velocity. In Cases 1-2 there is a reduction on the liquid film at the wall when adding water from Case 1 to Case 2. This might be translated as a reduction on the secondary flow roughness effect. The bigger particles will not be transported to the top of the pipe with the same intensity as in Case 1. The pulling effect from the liquid film may have less opposition in this Case and a clockwise droplet particles transport may be promoted.
This phenomenon is not so significant in Cases 3-4. This could be due the existence of the liquid film for Case 4 even tough the amount of liquid droplets entrained seems to be reduced.

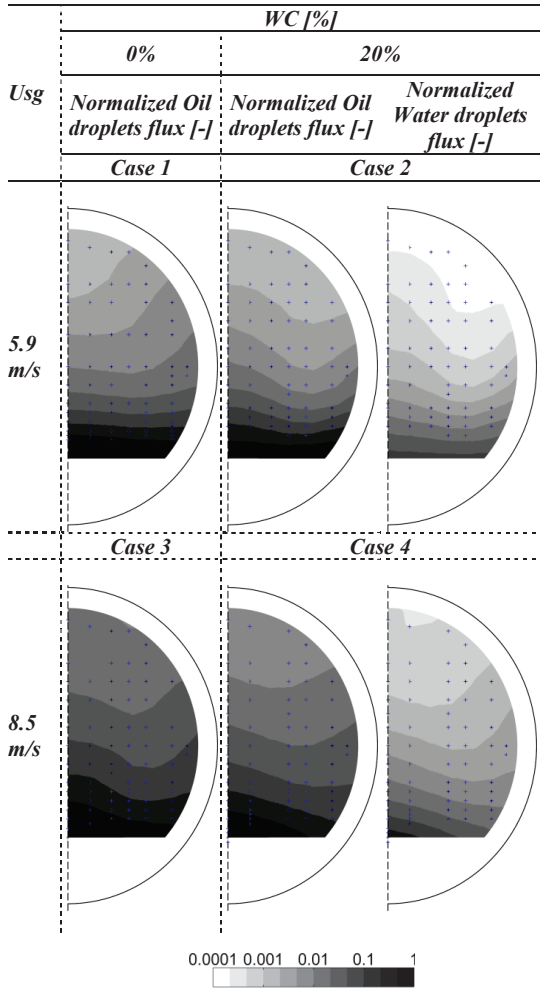


**Figure 7** Normalized contours of water and oil droplet flux at tested conditions.

## Conclusions

New instrumentation was designed and built for isokinetic sampling of droplets and gas in high pressurized systems. The measurements can be done over the pipe cross section.
Using the new 2D probe it is therefore possible to measure simultaneously the gas local velocity and sample the liquid droplets entrained in the gas core.
An experimental campaign on droplet flux measurement was carried out and results for the gas axial velocity profiles

and liquid droplet local fluxes are presented for two and three phase flows.

Accurate position of the gas-liquid interface is important in order to get accurate values from the integration process.

A general increment of the droplet fluxes were observed when the gas velocity increases at constant water cut.

Secondary flows were observed at the selected conditions on the gas velocity and droplets contour plots.

The addition of water modifies the distribution of droplets inside the pipe caused by a modification of the secondary flows nature in the gas core.

Non uniformities on the droplet profiles over the horizontal axis were observed for all the tested conditions.

Appropriate integration of the droplet profiles over the pipe cross section should be done in order to get a conclusion on the effect over the total entrained fraction.

## References

Afzal,N. Seena, A. and Bushra, A. Power Law Velocity Profile in Fully Developed Turbulent Pipe and Channel Flows. Journal of hydraulic engineering. Pp 1080-1086. (2007)

Belt, R,J. On the liquid film in inclined annular flow. PhD Thesis. Delft University. (2007)

Cengel, Y.A. Fluid Mechanics : Fundamentals and applications. McGraw-Hill Science. Chapter 8. (2004)

Dykhno, L.A.. Maps of mean gas velocity for stratified flows with and without atomization. IJMF.20(4), pp 691-702.(1994)

Flores, A.G., Crowe, K.E., Griffith, P., Gas-phase secondary flow in horizontal, stratified and annular two-phase flow. IJMF 21(2), pp. 207-221. (1995)

Ishii, M., Mishima, K., Droplet Entrainment Correlation in Annular Two-Phase Flow. IJHT 32(10), pp 1835-1846. (1989)

Kumar, R., Gottman, M. Sridhar, K.R. Film thickness and wave velocity measurements in a vertical duct. Transactions os ASME 124(September), pp 634-642. (2002)

Mantilla, I. Mechanistic Modeling of Liquid entrainment in Gas in Horizontal Pipes. PhD Thesis. University of Tulsa. (2008).

Meng, W., Chen, X.T., Kouba, G., Sarica, C., and Brill, J.P.. Experimental study of low liquid loading gas liquid flow in near Horizontal Pipes. SPEPF 16 (4). 240.249. SPE-74687-PA. (2001)

Paras, S., Karabelas, J. Droplet Entrainment and Deposition in Horizontal Annular Flow. IJMF 17(4), pp 455-468. (1991).

Paras, S., Vlachos, N.A., Karabelas, J. Liquid Layer Characteristics in Stratified- Atomization Flow. IJMF 20(5), pp 939-956. (1994).

Shmueli, A. Nydal, O.J, Djoric, B. Unander, T.E. Oil and water droplet entrainment in horizontal gas liquid flows. Proc. 8th North American Conference on Multiphase flow. BHR Group. Cranfield, U.K pp 199-210. (2012)

Skartlien , R., Nuland, S., Amundsen, J. Simultaneous Entrainment of Oil and Water Droplets in High Reynolds Number Gas Turbulence in Horizontal Pipe Flow. IJMF 37 pp 1282-1293. (2011).

Smith, I.E., Krampa, F.N, Fossen, M., Brekken, C., Unander, T.E. Investigation of Horizontal Two-Phase Gas-Liquid pipe flow using High Viscosity Oil and Simulations. Proc. 15th International Conference on Multiphase Production Technology. BHR Group, Cranfield, U.K. pp 293-307. (2011)

Tayebi, D., Nuland, S., Fuchs, P. Droplet Transport in Oil/Gas and Water/Gas at High Densities. IJMF. 26. Pp 741-761. (2000)

Williams, L. Effect of Pipe Diameter on Horizontal Annular Two-Phase Flow. PhD Thesis. University of Illinois at Urbana-Champaign. (1990).

Williams. L.R. Dykhno, L.A., Hanratty. T.J. Droplet flux distribution and entrainment in horizontal gas-liquid flows. IJMF. 22(1), pp 1-18. (1996)

Westende, J. M. Droplets in annular-dispersed gas-liquid pipe-flows. PhD Thesis. Delft University. (2007)

# Apendix J- Paper 6

*Shmueli, A.,Unader, T.E., Nydal, O.J.*

## Experimental and numerical evaluation and optimization of a non standard Pitot/sampling probe

Engineering. Vol 5 No. 12. Pp 967-974. 2013

*Engineering*, 2013, 5, 967-974
Published Online December 2013 (http://www.scirp.org/journal/eng)
http://dx.doi.org/10.4236/eng.2013.512118

Scientific Research

# Experimental and Numerical Evaluation and Optimization of a Non Standard Pitot/Sampling Probe

**Andrea Shmueli[1], Tor Erling Unander[2], Ole Jørgen Nydal[1]**
[1]Norwegian University of Science and Technology, Department of Energy and Process Engineering, Trondheim, Norway
[2]Department of Petroleum Research, SINTEF, Trondheim, Norway
Email: andrea.shmueli@ntnu.no

Received September 4, 2013; revised October 4, 2013; accepted October 11, 2013



## ABSTRACT

An isokinetic sampling probe is designed and constructed to measure entrained liquid droplet fluxes in separated gas-liquid pipe flows. This probe also has the capability of working as a non-standard Pitot tube when the sampling is stopped. CFD simulations using the commercial software Ansys CFX were carried out for single phase gas flow to analyze the non-standard design. Pitot tube velocity calculations and isokinetic sampling conditions were studied. The predicted results were compared against theoretical velocity profiles from the literature and with gas single phase experimental data acquired in a horizontal 49 m long steel pipeline with an internal diameter of 69 mm. The experiments were done by using a dense gas (SF6) at 7 bara. An asymmetry of the experimental velocity profiles reproduced with the numerical simulations. The CFD simulations made it possible to verify the design and predict and correct an installation problem.

**Keywords:** Isokinetic Probe; Pitot Tube; CFD; Flow; Installation Effects

## 1. Introduction

Pitot probes are devices which are commonly used in the industry to measure the local velocity in gases flowing in pipes or ducts. The dynamic pressure $\left(P_d = P_t - P_s\right)$ of the fluid stream is measured by the Pitot probe and the velocity can be calculated from it. When the gas compressibility effect can be neglected, the local velocity can be calculated from:

$$U_g = C \cdot \sqrt{\frac{2 \cdot P_d}{\rho_g}} \quad (1)$$

where $C$ is a calibration constant.

The Pitot tubes have been used for measuring the gas dynamic pressure in gas-liquid flows [1-4]. However, the calculation of the velocity from the pressure values is not straightforward and will depend upon the flow regime [5]. In gas flow with liquid droplet entrainment, it is a common practice to use isokinetic sampling probes to extract flow from the main stream in order to get the local dispersed droplet flux. These probes are designed to have a Pitot-like geometry and pressure tapings and can be designed to measure the local velocity when the sampling is stopped. The probes are generally not standard so their design must be tested and validated. Two aspects that should be taken into account when designing a new Pitot probe are the velocity measured by the Pitot probe in an ideal flow and the effect of the probe presence on the upstream flow [6]. Due to the complexity of multiphase flows, the probe design and installation are evaluated by using single phase gas conditions.

In this paper, a design and installation assessment of the non standard Pitot/sampling probe is done by the analysis of single phase gas experimental data and simulation of the probe current design using CFD tools.

## 2. Probe Design

The sampling/Pitot probe is designed to be able to sample a liquid flux. Some authors have demonstrated that the effect of the sampling tube diameter and length of the probe on the measured droplet flux is negligible [7,8]. However in this study the criteria used to select the probe diameter was associated with the maximum possible droplet size. Two correlations were used: one for gas/liquid systems and another one for liquid/liquid systems. Kocamustafaogullari *et al.* (1994) [9] presented a correlation for the maximum droplet diameter in annular flows.

The correlati on is a function of the fluid properties and of the local energy dissipated by the turbulence.

$$\frac{d_{\max}}{d_h} = 2.609 \cdot C_w^{-4/15} \cdot We_m^{-3/5} \cdot \left(\frac{\mathrm{Re}_g^4}{\mathrm{Re}_l}\right)^{1/15} \cdot \left[\left(\frac{\rho_g}{\rho_l}\right) \cdot \left(\frac{\mu_g}{\mu_l}\right)\right]^{4/15} \quad (2)$$

$$Cw = \begin{cases} 0.028\left(N\mu\right)^{-4/5} & \text{for } N\mu \le 1/15 \\ 0.25 & \text{for } N\mu > 1/15 \end{cases} \quad (3)$$

The viscosity number is defined by,

$$N\mu = \frac{\mu_f}{\sqrt{\rho_l \cdot \sigma \cdot \sqrt{\frac{\sigma}{g} \cdot \Delta\rho}}} \quad (4)$$

Kubie and Gardner (1997) [10] developed a correlation for maximum droplet size in liquid/liquid systems.

$$\left(\frac{d_{\max} \cdot \rho_c \cdot \bar{U}^2}{\sigma}\right) \cdot \left(\frac{f \cdot d_{\max}}{D}\right)^{\frac{2}{3}} = 0.369 \quad (5)$$

$$f = 0.076 \cdot \left(\mathrm{Re}\right)^{-0.25} \quad (6)$$

The probe diameter should allow for measurements in oil-water-gas flow systems. The probe has a 4 mm inner diameter, a 0.2 mm wall thickness. It is possible to measure within 4.2 mm of the pipe wall. To avoid disturbing the flow, the opening of the sampling probe extends 50 mm upstream (≈11.4$d_p$). The dynamic pressure is read at 3.75$d_p$ and the static pressure sensed at the pipe wall on the probe stem plane. Two hoses were connected to transmit the dynamic pressure from the holes to the differential pressure transducer. The probe can traverse the vertical pipe diameter using a linear actuator and has the ability to work as a sampling and Pitot probe when a manual ball valve connected to the sampling line is closed. The non standard Pitot probe used in this study is schematically shown in **Figure 1**.

## 3. Experiments

### 3.1. Experimental Setup

The experiments were carried out in the medium-scale flow loop at SINTEF Multiphase Flow laboratory in Trondheim, Norway. The facility consists of a horizontal 69 mm inner diameter, 50 m long pipeline. The probe test section is located about 580D downstream the mixing point.

### 3.2. Experimental Measurements

Pitot measurements on the vertical diameter were carried out using single gas phase SF6 (Sulphur hexafluoride) at 7 bara and 20˚C. Three experimental gas velocities were tested 4, 6 and 8 m/s. The measured gas density and dynamic viscosity from the experiments are $\rho_g$ = 41.91 Kg/m$^3$ and $\mu_g$ = 1.5e – 05 Pa·s respectively.

The measurements are compared against two theoretical velocity profiles. Following [11] the velocity distribution in the main body of flow can be written as shown in Equation (2), where $\alpha$ is a power law constant that in this case is 0.111 as is proposed by [12].

$$\frac{U_g\left(y\right)}{U_{\max}} = \left(\xi\right)^{\alpha} \quad (7)$$

where $\xi = y/R$ is the normalized distance from the wall to the pipe center. The second profile is obtained by following the modified log-wake model [13] for turbulent pipe flow:

$$\frac{U_{\max} - U}{U^*} = -\frac{\sqrt{3}e}{2}\ln\xi + \left(2 - \frac{\sqrt{3}e}{6}\right) - 6\xi^2 + \left(4 + \frac{\sqrt{3}e}{6}\right)\xi^3 \quad (8)$$

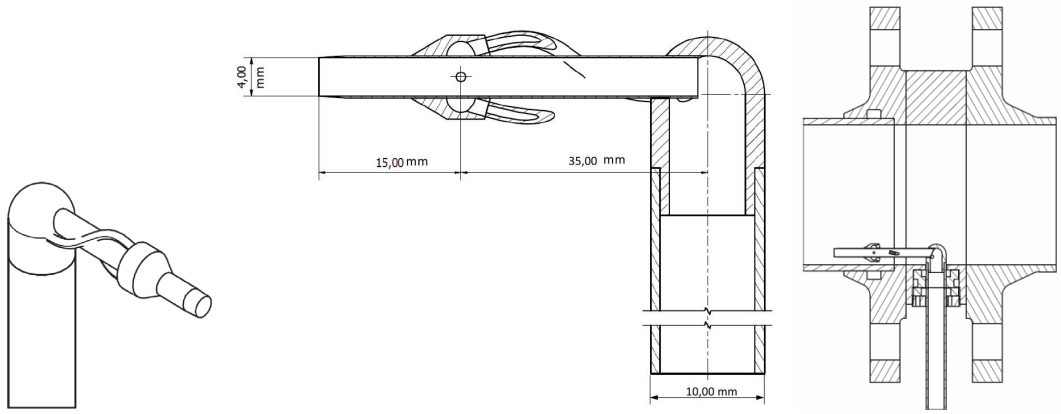


**Figure 1. Pitot probe geometry.**

The local gas velocity measurements and the theoretical profiles are normalized by their maximum value and shown in **Figure 2**. The experimental velocity profiles for all the tests are not symmetric and a systematic error is shown for all of them on the upper half section of the pipe. However, there is a good fitting between the experimental velocity profile and the theoretical one on the bottom part on the pipe.

## 4. CFD Model Details

3D CFD simulations of the flow around a non standard Pitot probe were developed using the commercial software ANSYS-CFX© (V-13) which employs the finite volume method for solving the conservation equations.

### 4.1. Cases under Study

The simulations were carried out using single gas phase SF6 (Sulphur hexafluoride) at 7 bara, 20˚C and 4 m/s. The calculated Mach number for the tested conditions is lower than 0.3 and thereby the fluid is considered as incompressible on the simulations [14]. The goal of the model is to simulate the flow around the designed non standard Pitot probe in order to find the origin of the experimental velocity profile asymmetry, predicting a possible installation effect on the gas velocity calculation and afterwards improving the current design. Two locations of the Pitot probe above the pipe center were numerically studied (See **Table 1**).

### 4.2. CFD Model General Settings

The turbulence model was a homogeneous K-$\varepsilon$ model. All the simulations were considered as steady state conditions. For all the simulations, the convergence was reached when the maximum and RMS residual error for any parameter was reduced to less than 4e−04 and 4.2e−05 respectively.

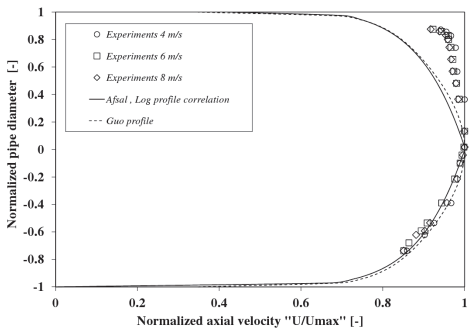


**Figure 2. Experimental and theoretical normalized gas velocity profiles for 4, 6 and 8 m/s.**

**Table 1. Simulated cases.**

| Case | Location of the probe opening from the bottom of the pipe [mm] |
|---|---|
| 1 | 51 |
| 2 | 59 |

### 4.3. Boundary Conditions and Simulation Domain

The simulated domain consists of the probe and a section of the pipe (3.8 m upstream of the probe and 314 mm downstream of it). The hoses used for the total pressure sensing were not included on the model. The imposed boundary conditions were total pressure at the inlet (Upstream Boundary) and uniform mass flow at the outlet boundary condition (Downstream Boundary). All the walls were treated as no-slip walls.

### 4.4. Mesh

The fluid domain was meshed using the commercial Workbench CFX© Mesh Module. The created meshes were non-structured formed by tetrahedral, wedge and pyramid elements. A grid dependence procedure was carried out in order to select the right mesh (see **Table 2**).

Four parameters were compared in order to select the right mesh for the simulations: The pressure loss on the pipe segment, maximum Y+ value, the gas velocity on the probe opening calculated from Equation (1) using the static pressure value at the current location Ps-1 (See **Figure 3** and **4**).

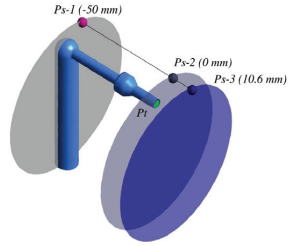


**Figure 3. Location of the specific calculated parameters in the domain.**

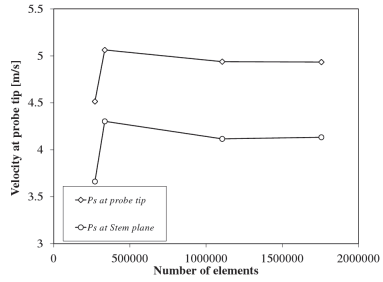


**Figure 4. Mesh dependency study. Variable: velocity at Pitot opening.**

The velocity profile on a line is located on the probe opening Ps-2, (See **Figure 5**). A percent error lower than 3% between each mesh and the finest one of every physical variable compared was used as selection criteria. There are some qualitative differences between all the meshes especially close to the probe tip. The biggest difference between Mesh 1 and Mesh 4 is 7%. The selected mesh for the simulations was Mesh 3.

## 5. Results

### 5.1. Pitot Geometry Effect

One possible cause of the asymmetry in velocity profiles around the pipe centerline is a blockage effect of the stem in the flow upstream the probe tip. For this reason, the vertical velocity profiles in different locations downstream and upstream the probe tip are plotted in **Figures 6** and **7**. The profiles from the pipeline inlet to the probe location are compared (**Figure 6**) showing symmetry with respect to the pipe axis. The flow in the pipe is developed before 20D. There are no upstream disturbances on the profiles due to the presence of the Pitot. However, the probe stem has a blockage effect on the profiles downstream the tip of the probe, mainly due to the reduction of the flow area (**Figure 7**). This behavior

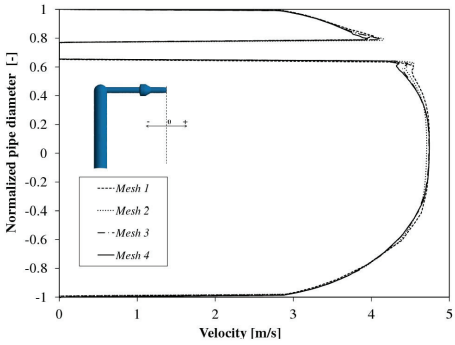


**Figure 5. Mesh dependency study variable: velocity profile on a line located at the probe opening.**

**Table 2. Generated meshes for case 1.**

| Mesh | 1 | 2 | 3 | 4 |
|---|---|---|---|---|
| Max Y+ | 13.27 | 13.52 | 13.56 | 13.55 |
| Connectivity number | 3 - 46 | 3 - 46 | 2 - 44 | 2 - 50 |
| Element vol ratio | 1 - 52 | 1 - 48 | 1 - 93 | 1 - 82 |
| Min face angle | 18 - 84 | 17 - 86 | 16 - 86 | 12 - 87 |
| Max face angle | 65 - 130 | 66 - 136 | 66 - 131 | 64 - 134 |
| Edge length ratio | 1 - 43 | 1 - 43 | 1 - 16 | 1 - 16 |
| Elements | 270,328 | 334,852 | 1,105,596 | 1,756,149 |
| Nodes | 92,570 | 111,118 | 383,564 | 600,838 |

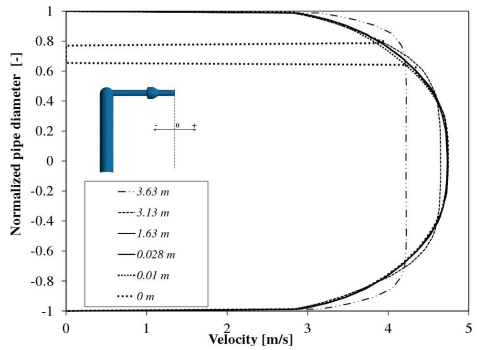


**Figure 6. Velocity profiles from the pipe inlet. Case 1.**

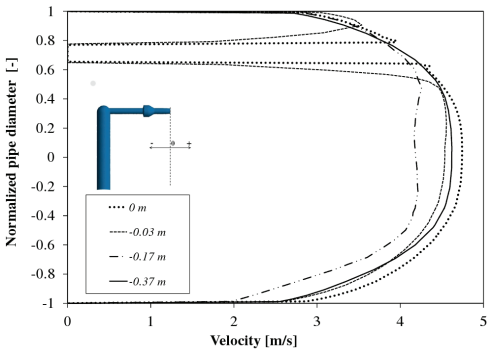


**Figure 7. Velocity profiles downstream the probe tip. Case 1.**

was expected as the ratio of the Pitot tube diameter to the pipe diameter does exceed 0.02 [14].

### 5.2. Pitot Vertical Location

Two cases were studied as presented in **Table 1**. The vertical location of the probe has a qualitative and quantitative effect on the static pressure distribution around the Pitot. The closer the Pitot is to the upper side of the pipe the lower is the pressure on the probe plane (See **Figure 8**). Near the top of the pipe the probe disturbs the flow and accelerates it creating a low pressure area on the top of the probe caused by the area reduction between the stem of the probe and the pipe.

The velocity at the probe opening (**Table 3**) is calculated using Equation (1) with the total pressure value at the probe tip and the static pressure values at Ps-1, Ps.2 and Ps-3 (See **Figure 3**). The percentage errors in the velocity calculation using Ps-1 or Ps-2 are 10% and 17 for Cases 1 and 2 respectively. The percentage errors when sensing the static pressure in front the Pitot tip (Ps-3) are 0.5% and 0.7% for Cases 1 and 2 respectively.

A comparison of the calculated velocity values and the

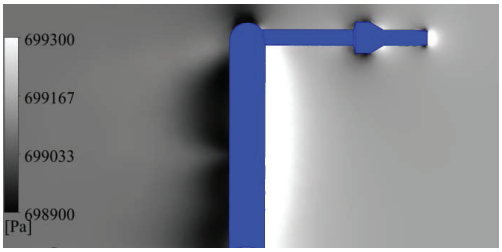


**Figure 8. Static pressure contour case 2.**

**Table 3. Velocity at the probe opening calculated with total pressure and static pressure at point 1 and 2.**

| Case | Location | Static Pressure [Pa] | Total Pressure [Pa] | Velocity at the probe opening [m/s] |
|---|---|---|---|---|
| 1 | Ps-1 | 699,344 | - | 4.92 |
| | Ps-2 | 699,428 | - | 4.49 |
| | Ps-3 | 699,434 | | 4.46 |
| | Pt | | 699,851 | |
| 2 | Ps-1 | 699,003 | - | 4.89 |
| | Ps-2 | 699,151 | - | 4.10 |
| | Ps-3 | 699,156 | | 4.08 |
| | Pt | - | 699,504 | - |

experimental one is made in **Figure 9**. Using the static pressure at the probe tip plane to calculate the local velocity shows a better fit with the theoretical profiles.

### 5.3. Pitot Probe Sampling under an Isokinetic Condition

The main goal of this simulation was to obtain the pressure loss inside the probe working under isokinetic condition. It is important to establish the pressure loss between the probe tip and the dynamic pressure ports inside it. For this simulation just Case 2 was analyzed.

The simulation and mesh selection was done following the steps explained on section 4. The flow conditions and fluid are the same as in the previous simulations. The imposed boundary conditions were total pressure at the inlet (Upstream Boundary), uniform mass flow at the outlet of the probe (calculated from the isokinetic condition) and uniform mass flow at the outlet boundary condition (Downstream Boundary). All the walls were treated as no-slip walls. The k-ε turbulence model was used on the simulations.

The streamlines approaching the probe opening and inside it are plotted in **Figure 10**. All the streamlines are undisturbed as the probe is not present and the velocity of the flow entering the probe is the same as in the main body of the flow so the conditions for isokinetic sampling are accomplished.

The total pressure is averaged on planes perpendicular to the flow inside the probe (See **Figure 11**). The total pressure holes are currently located on the position marked by the dotted line. The pressure loss between the probe opening and the total pressure holes is 33 Pa.

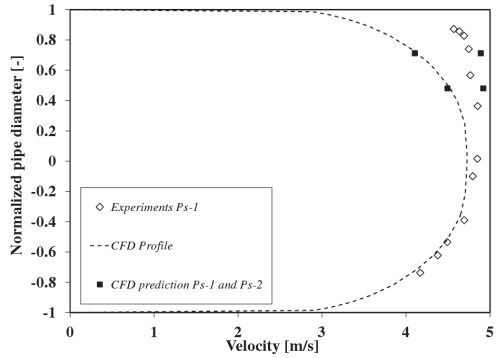


**Figure 9. Comparison between experimental, theoretical and CFD normalized gas velocity profile at 4 m/s.**

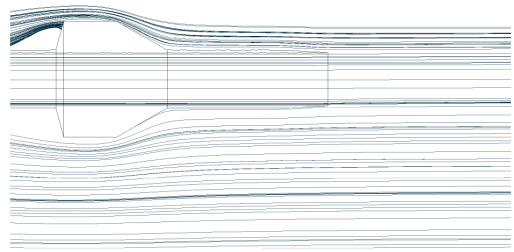

**Figure 10. Streamlines entering the probe.**

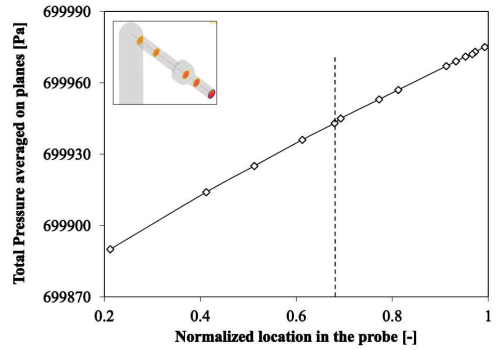


**Figure 11. Total pressure averaged on planes inside the probe where location 1 is the probe opening.**

## 6. Experiments on the Upgraded Installation

New experiments at 4 m/s were developed using an upgraded setup in which the static pressure tap was located on the same plane of the probe tip. The velocity profiles are symmetric in accordance to the pipe axial direction. The experiments are compared against the CFD profile showing an agreement and improvement in comparison with the previous setup (See **Figure 12**).

## 7. Conclusions and Remarks

A non-standard Pitot/sampling probe was experimentally tested and simulated using Ansys CFX (V13) to validate its accuracy and to determine any design or installation problem. The current experimental setup caused asymmetries on the measured gas velocity profiles.

The experiments were conducted for 3 velocities while the numerical simulations were carried out for one velocity. The obtained experimental asymmetries show a systematic behavior so the numerical results are extrapolated to other flow conditions.

The CFD simulations were concentrated on two probe vertical locations where the velocity profiles present the asymmetry. The effect of the probe location on the vertical pipe diameter, static pressure port location on the pipe wall, probe stem location and dynamic pressure ports location was studied. The location of the static pressure tap at either the probe tip plane or upstream of it will give more real and accurate velocity values.

As a result from the simulations, the static pressure tap at the top of the pipe was relocated in order to have a real and accurate reading of the static pressure. The probe itself generates disturbances of the flow downstream of it but not upstream of it.

A simulation of the isokinetic sampling probe was carried out to obtain the pressure drop inside the probe. It was recommended for further probe designs to place the dynamic pressure holes on the probe closer to the probe tip in order to avoid the pressure losses and have a better reading of the pressure.

Experiments with a new configuration with the static pressure tap on the same plane as the probe tip were carried out at 4 m/s showing an improvement on the measurements with symmetric velocity profiles which agreed with the theoretical predictions.

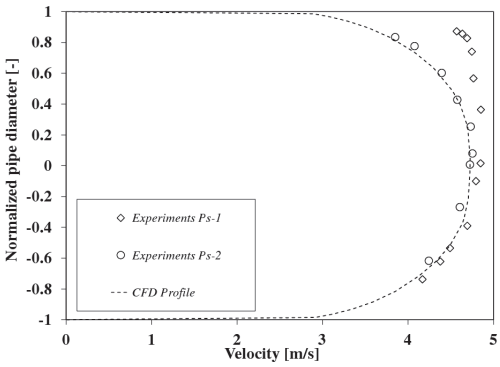


**Figure 12. Comparison of the experiments carried out the upgraded facility at 4 m/s with previous experiments and CFD profile.**

## 8. Acknowledgements

The financial and research support from Total E&P and Sintef Petroleum Research are greatly appreciated.

## REFERENCES

[1] L. A. Dykhno, "Maps of Mean Gas Velocity for Stratified Flows with and without Atomization," *International Journal of Multiphase Flow*, Vol. 20, No. 4, 1994, pp 691-702. http://dx.doi.org/10.1016/0301-9322(94)90039-6

[2] F. M. White, "Fluid Mechanics," 4th Edition, McGraw-Hill, New York, 1999.

[3] D. Tayebi, S. Nuland and P. Fuchs, "Droplet Transport in Oil/Gas and Water/Gas at High Densities," *International Journal of Multiphase Flow*, Vol. 26. 2000, pp. 741-761. http://dx.doi.org/10.1016/0301-9322(94)90039-6

[4] R. Skartlien, S. Nuland and J. Amundsen, "Simultaneous Entrainment of Oil and Water Droplets in High Reynolds Number Gas Turbulence in Horizontal Pipe Flow," *International Journal of Multiphase Flow*, Vol. 37 2011, pp. 1282-1293. http://dx.doi.org/10.1016/j.ijmultiphaseflow.2011.07.006

[5] G. Falcone, F. Hewitt and C. Alimonti, "Multiphase Flow Metering: Principles and Applications," Elsevier, Amsterdam, 2009.

[6] R. C. Baker, "Flow Measurement Handbook: Industrial Designs, Operating Principles, Performance and Applications," Cambridge University Press, New York, 2000. http://dx.doi.org/10.1017/CBO9780511471100

[7] M. Wicks and A. E. Dukler, "Entrainment and Pressure Drop in Concurrent Gas-Liquid Flow: Air-Water in Horizontal Flow," *American Institute of Chemical Engineers*, Vol. 6, No. 10, 1960, pp. 463-468. http://dx.doi.org/10.1002/aic.690060324

[8] L. Williams, "Effect of Pipe Diameter on Horizontal Annular Two-Phase Flow," PhD Thesis, University of Illinois at Urbana-Champaign, 1990.

[9] G. Kocamustafaogullari, S. R. Smits and J. Razi, "Maximum and Mean Droplet Sizes in Annular Two-Phase Flow," *International Journal of Heat and Mass Transfer*, Vol. 37, No. 6, 1994, pp. 955-965. http://dx.doi.org/10.1016/0017-9310(94)90220-8

[10] J. Kubie and G. C. Gardner, "Drop Sizes and Drop Dispersion in Straight Horizontal Tubes and Helical Coils," *Chemical Engineering Science*, Vol. 32, No. 2, 1977, pp. 195-202.

http://dx.doi.org/10.1016/0009-2509(77)80105-X

[11] N. Afzal, A. Seena and A. Bushra, "Power Law Velocity Profile in Fully Developed Turbulent Pipe and Channel Flows," *Journal of Hydraulic Engineering*, Vol. 133, No. 9, 2007, pp. 1080-1086. http://dx.doi.org/10.1061/(ASCE)0733-9429(2007)133:9(1080)

[12] W. J. Duncan, A. B. Thorn and A. D. Young, "Mechanics of Fluids," ELBS Edward Arnold, 1967.

[13] J. Guo and P. Juliem, "Modified Log-Wake Law for Turbulent Flow in Smooth Pipes," *Journal of Hydraulic Research*, Vol. 41, No. 4, 2003, pp. 493-501. http://dx.doi.org/10.1080/00221680309499994

[14] ISO, "Measurement of Fluid Flow in Closed Conduits-Velocity Area Method Using Pitot Static Tubes," ISO 3966, 1977, pp. 146-183.

**Appendix**

**Nomenclature**

| | |
|---|---|
| $\rho$ | Density |
| $P$ | Pressure |
| $d$ | Diameter |
| $D$ | Pipe diameter |
| $C$ | Pitot calibration constant $\approx 1$ |
| $U$ | Velocity |
| $R$ | Pipe radius |
| $U_{max}$ | Velocity at the pipe center |
| $d_{max}$ | Maximum droplet size |
| $d_h$ | Hydraulic diameter |
| $d_p$ | Pitot diameter |
| $C_w$ | Coefficient in Kocamustafaogullari correlation |
| $y$ | Distance from the wall |
| $\xi$ | Normalized distance from the wall to the pipe center |
| $\mu$ | Dynamic viscosity |
| $\alpha$ | Power law constant |
| Re | Reynolds number |
| $f$ | Friction factor |
| $We_m$ | Modified Weber number |
| $N\mu$ | Viscosity number |
| $\sigma$ | Surface tension |
| $g$ | Gravity |
| ***Subscripts*** | |
| $c$ | Core |
| $d$ | Dynamic |
| $s$ | Static |
| $t$ | Total |
| $g$ | Gas |
| $l$ | Liquid |
| $p$ | Probe |

# References


Açikgöz, M., França, F., & Lahey Jr, R. T. (1992). An experimental study of three-phase flow regimes. *International Journal of Multiphase Flow, 18*(3), 327-336. doi: http://dx.doi.org/10.1016/0301-9322(92)90020-H

Afzal, N., Seena, A., & Bushra, A. (2007). Power Law Velocity Profile in Fully Developed Turbulent Pipe and Channel Flows. *Journal of Hydraulic Engineering, 133*(9), 1080-1086. doi: doi:10.1061/(ASCE)0733-9429(2007)133:9(1080)

Al-Sarkhi, A., & Hanratty, T. J. (2002). Effect of pipe diameter on the drop size in a horizontal annular gas–liquid flow. *International Journal of Multiphase Flow, 28*(10), 1617-1629. doi: http://dx.doi.org/10.1016/S0301-9322(02)00048-4

Andreussi, P. (1983). Droplet transfer in two-phase annular flow. *International Journal of Multiphase Flow, 9*(6), 697-713. doi: http://dx.doi.org/10.1016/0301-9322(83)90117-9

Asali, J. C., Hanratty, T. J., & Andreussi, P. (1985). Interfacial drag and film height for vertical annular flow. *AIChE Journal, 31*(6), 895-902. doi: 10.1002/aic.690310604

Azzopardi, B. J. (1985). Drop sizes in annular two-phase flow. *Experiments in Fluids, 3*(1), 53-59. doi: 10.1007/BF00285271

Azzopardi, B. J. (1997). Drops in annular two-phase flow. *International Journal of Multiphase Flow, 23*(7), 1-53. doi: http://dx.doi.org/10.1016/S0301-9322(97)90087-2

Barnea, D., Shoham, O., Taitel, Y., & Dukler, A. E. (1980). Flow pattern transition for gas-liquid flow in horizontal and inclined pipes. Comparison of experimental data with theory. *International Journal of Multiphase Flow, 6*(3), 217-225. doi: http://dx.doi.org/10.1016/0301-9322(80)90012-9

Belt. (2007). *On the Liquid Film in Inclined Annular Flow*.

Belt, Van't Westende, J. M. C., & Portela, L. M. (2009). Prediction of the interfacial shear-stress in vertical annular flow. *International Journal of Multiphase Flow, 35*(7), 689-697. doi: http://dx.doi.org/10.1016/j.ijmultiphaseflow.2008.12.003

Binder, J. L., & Hanratty, T. J. (1992). Use of lagrangian methods to describe drop deposition and distribution in horizontal gas—liquid annular flows. *International Journal of Multiphase Flow, 18*(6), 803-820. doi: http://dx.doi.org/10.1016/0301-9322(92)90060-T

Borregales, M., Capelleto, J., Nuñez, G., & Asuaje, M. (2014). *Genetic algorithms applied to flow estimation in a two-phase flow with a venturi meter.* Paper presented at the International Mechanical Engineering Congress & Exposition, Canada.

Borregales, M., Cappelletto, J., Asuaje, M., Shmueli, A., & Stanko, M. (2014). *MODEL BUILDING USING GENETIC ALGORITHM FOR DATA FITTING*. Paper presented at the Cimenics 2014, Venezuela.

Boulesteix, S. (2010). *Cisaillement d'une interface gaz-liquide en conduite et entraînement de gouttelettes*.

Cengel, Y. A., & Cimbala, J. M. (2004). *Fluid Mechanics: Fundamentals and Applications*: McGraw-Hill Higher Education.

Chen, X. T., Cal, X. D., & Brill, J. P. (1997). Gas-Liquid Stratified-Wavy Flow in Horizontal Pipelines. *Journal of Energy Resources Technology, 119*(4), 209-216. doi: 10.1115/1.2794992

Chupin, G. (2003). *An experimental investigation of multiphase gas-liquid pipe flow at low liquid loading.* (Ph.D.), Norwegian university of science and technology, Norway.

Clift, R., Grace, J. R., & Weber, M. E. (1978). *Bubbles, Drops, and Particles*: Academic Press.

Dallman, J. (1978). *Investigation of Separated Flow Model in Annular Liquid Two-Phase Flows.* University of Illinois at Urbana-Champaign, USA.

Darling, R. S., & McManus, H. N. (1968). *Flow patterns in circular ducts with circumferential variation in roughness: a two-phase flow analog*. Paper presented at the Dev. in Mech. Proc. 11th Mid- Western Mech. Conf.

Dykhno, L. A., Williams, L. R., & Hanratty, T. J. (1994). Maps of mean gas velocity for stratified flows with and without atomization. *International Journal of Multiphase Flow, 20*(4), 691-702. doi: http://dx.doi.org/10.1016/0301-9322(94)90039-6

Flores, A. G., Crowe, K. E., & Griffith, P. (1995). Gas-phase secondary flow in horizontal, stratified and annular two-phase flow. *International Journal of Multiphase Flow, 21*(2), 207-221. doi: http://dx.doi.org/10.1016/0301-9322(94)00072-R

Fore, & Dukler. (1995). Droplet deposition and momentum transfer in annular flow. *AIChE Journal, 41*(9), 2040-2046. doi: 10.1002/aic.690410904

Fore, L. B., Beus, S. G., & Bauer, R. C. (2000). Interfacial friction in gas–liquid annular flow: analogies to full and transition roughness. *International Journal of Multiphase Flow, 26*(11), 1755-1769. doi: http://dx.doi.org/10.1016/S0301-9322(99)00114-7

Gawas, K. (2013). *Studies in low-liquid loading in gas/oil/water three phase flow in horizontal and near horizontal pipes.* (PhD), Tulsa, US.

Gilmore, G. R. (2008). Front Matter *Practical Gamma-Ray Spectrometry* (pp. i-xix): John Wiley & Sons, Ltd.

Gokcal, B., Wang, Q., Zhang, H.-Q., & Sarica, C. (2008). Effects of High Oil Viscosity on Oil/Gas Flow Behavior in Horizontal Pipes. doi: 10.2118/102727-PA

Gorelik, D., & Brauner, N. (1999). The interface configuration in two-phase stratified pipe flows. *International Journal of Multiphase Flow, 25*(6–7), 977-1007. doi: http://dx.doi.org/10.1016/S0301-9322(99)00038-5

Hanratty, T. (1991). Separated flow modelling and interfacial transport phenomena. *Applied Scientific Research, 48*(3-4), 353-390. doi: 10.1007/BF02008206

Hart, J., Hamersma, P. J., & Fortuin, J. M. H. (1989). Correlations predicting frictional pressure drop and liquid holdup during horizontal gas-liquid pipe flow with a small liquid holdup. *International Journal of Multiphase Flow, 15*(6), 947-964. doi: http://dx.doi.org/10.1016/0301-9322(89)90023-2

Henstock, W. H., & Hanratty, T. J. (1976). The interfacial drag and the height of the wall layer in annular flows. *AIChE Journal, 22*(6), 990-1000. doi: 10.1002/aic.690220607

Hewitt, G. F., & Govan, A. H. (1990). Phenomenological modelling of non-equilibrium flows with phase change. *International Journal of Heat and Mass Transfer, 33*(2), 229-242. doi: http://dx.doi.org/10.1016/0017-9310(90)90094-B

Hoffmann, R., & Johnson, G. W. (2011). Measuring phase distribution in high pressure three-phase flow using gamma densitometry. *Flow Measurement and Instrumentation, 22*(5), 351-359. doi: http://dx.doi.org/10.1016/j.flowmeasinst.2011.02.005

Hoogendoorn, C. J. (1959). Gas-liquid flow in horizontal pipes. *Chemical Engineering Science, 9*(4), 205-217. doi: http://dx.doi.org/10.1016/0009-2509(59)85003-X

Ishii, M., & Mishima, K. (1989). Droplet entrainment correlation in annular two-phase flow. *International Journal of Heat and Mass Transfer, 32*(10), 1835-1846. doi: http://dx.doi.org/10.1016/0017-9310(89)90155-5

Khor, S. H. (1998). *Three-phase Liquid-liquid-gas Stratified Flow in Pipelines*: University of London.

Kjølaas, J., Johansen, S. T., Ladam, Y., Belt, R., Danielson, T., & Stinessen, M. (2011). *Modeling of the droplet field in near-horizontal low liquid loading flows.* Paper presented at the Multiphase production technology conference, Cannes, France.

Kocamustafaogullari, G., Smits, S. R., & Razi, J. (1994). Maximum and mean droplet sizes in annular two-phase flow. *International Journal of Heat and Mass Transfer, 37*(6), 955-965. doi: http://dx.doi.org/10.1016/0017-9310(94)90220-8

Kubie, J., & Gardner, G. C. (1977). Drop sizes and drop dispersion in straight horizontal tubes and in helical coils. *Chemical Engineering Science, 32*(2), 195-202. doi: http://dx.doi.org/10.1016/0009-2509(77)80105-X

Kumar, R., Gottmann, M., & Sridhar, K. R. (2002). Film Thickness and Wave Velocity Measurements in a Vertical Duct. *Journal of Fluids Engineering, 124*(3), 634-642. doi: 10.1115/1.1493808

Laurinat, J. E. (1982). *Studies of the Effects of Pipe Size on Horizontal Annular Two-phase Flows*: University of Illinois at Urbana-Champaign.

Lin, P. Y., & Hanratty, T. J. (1986). Prediction of the initiation of slugs with linear stability theory. *International Journal of Multiphase Flow, 12*(1), 79-98. doi: http://dx.doi.org/10.1016/0301-9322(86)90005-4

Mantilla, I. (2008). *Mechanistic Modeling of Liquid Entrainment in Gas in Horizontal Pipes*: The University of Tulsa.

Meng, W., Chen, X. T., Kouba, G. E., Cem, S., & Brill, J. P. (2001). Experimental Study of Low-Liquid-Loading Gas-Liquid Flow in Near-Horizontal Pipes. doi: 10.2118/74687-PA

Mols, B., & Oliemans, R. V. A. (1998). A turbulent diffusion model for particle dispersion and deposition in horizontal tube flow. *International Journal of Multiphase Flow, 24*(1), 55-75. doi: http://dx.doi.org/10.1016/S0301-9322(97)00043-8

NTNU HSE division (2014, 04/11/2014). [Control measurement of radiation from Gamma densitometer]. 2014/21823.

Nuland, S., Skarsvåg, K., Sæther, G., & Fuchs, P. (1993). *Phase tractions in three-phase gas-oil-water flow.* Paper presented at the 5th International Conference in Multiphase Production, Cannes, France.

Pan, L. (1996). *High pressure three-phase /gas/liquid/liquid) flow.* (Ph.D.), University of London, UK.

Pan, L., & Hanratty, T. J. (2002). Correlation of entrainment for annular flow in horizontal pipes. *International Journal of Multiphase Flow, 28*(3), 385-408. doi: http://dx.doi.org/10.1016/S0301-9322(01)00074-X

Paras, S. V., & Karabelas, A. J. (1991). Droplet entrainment and deposition in horizontal annular flow. *International Journal of Multiphase Flow, 17*(4), 455-468. doi: http://dx.doi.org/10.1016/0301-9322(91)90042-2

Paras, S. V., Vlachos, N. A., & Karabelas, A. J. (1994). Liquid layer characteristics in stratified—Atomization flow. *International Journal of Multiphase Flow, 20*(5), 939-956. doi: http://dx.doi.org/10.1016/0301-9322(94)90103-1

Parker, J. (1991). *Instrumentation for gamma-ray spectroscopy. In: Passive Nondestructive Assay of Nuclear Materials*. USA: The Commission.

Plasencia, J. L. (2013). *Experimental study on two phase oil-water dispersed flow.* (Doktoravhandlinger ved NTNU), Norwegian University of Science and Technology, Norway.

Rivkind, V. Y., & Ryskin, G. M. (1976). Flow structure in motion of a spherical drop in a fluid medium at intermediate Reynolds numbers. *Fluid Dynamics, 11*(1), 5-12. doi: 10.1007/BF01023387

Shmueli, Nydal, O. J., Djoric, B., & Unander, T. E. (2012). Oil and water droplet entrainment in horizontal gas liquid flows. 8th North American Conference on Multiphase Technology 2012 (Vol. Language: eng, pp. 199-210): BHR Group.

Shmueli, A., Unander, T. E., & Nydal, O. J. (2013). Experimental and Numerical Evaluation and Optimization of a Non Standard Pitot/Sampling Probe. *Engineering, 5*, 967-974.

Skartlien, R., Nuland, S., & Amundsen, J. E. (2011). Simultaneous entrainment of oil and water droplets in high Reynolds number gas turbulence in horizontal pipe flow. *International Journal of Multiphase Flow, 37*(10), 1282-1293. doi: http://dx.doi.org/10.1016/j.ijmultiphaseflow.2011.07.006

Smith, I. E., Krampa, F. N., Fossen, M., Brekken, C., & Unander, T. E. (2011). *Investigation of Horizontal Two-Phase Gas-Liquid Pipe Flow Using High Viscosity Oil: Comparison with Experiments Using Low Viscosity Oil and Simulations*.

Sobocinski, D. P. (1955). *Horizontal, Co-current Flow of Water, Gas-oil and Air*: University of Oklahoma.

Tatterson, D. F., Dallman, J. C., & Hanratty, T. J. (1977). Drop sizes in annular gas-liquid flows. *AIChE Journal, 23*(1), 68-76. doi: 10.1002/aic.690230112

Tayebi. (1994). *Måling av dråpefraksjon og væskefilmtykkelse ved bruk av en isokinetisk probe i horisontal annulær-/lagdeltstrømming avolje/gass og vann/gass ved bruk av tung gass*. Oslo: [D. Tayebi].

Tayebi, Nuland, S., & Fuchs, P. (2000). Droplet transport in oil/gas and water/gas flow at high gas densities. *International Journal of Multiphase Flow, 26*(5), 741-761. doi: http://dx.doi.org/10.1016/S0301-9322(99)00054-3

Tzotzi, C., Bontozoglou, V., Andritsos, N., & Vlachogiannis, M. (2011). Effect of Fluid Properties on Flow Patterns in Two-Phase Gas−Liquid Flow in Horizontal and Downward Pipes†. *Industrial & Engineering Chemistry Research, 50*(2), 645-655. doi: 10.1021/ie100239v

Vames, J. S., & Hanratty, T. J. (1988). Turbulent dispersion of droplets for air flow in a pipe. *Experiments in Fluids, 6*(2), 94-104. doi: 10.1007/BF00196459

Van 'T Westende, J. (2007). *Droplets in annular-dispersed gas-liquid pipe-flows*.

Vlachos, N. A. (2003). Studies of Wavy Stratified and Stratified/Atomization Gas-Liquid Flow. *Journal of Energy Resources Technology, 125*(2), 131-136. doi: 10.1115/1.1576265

Wallis, G. B. (1969). *One-dimensional two-phase flow*: McGraw-Hill.

Weisman, J., Duncan, D., Gibson, J., & Crawford, T. (1979). Effects of fluid properties and pipe diameter on two-phase flow patterns in horizontal lines. *International Journal of Multiphase Flow, 5*(6), 437-462. doi: http://dx.doi.org/10.1016/0301-9322(79)90031-4

Wicks, M., & Dukler, A. E. (1960). Entrainment and pressure drop in concurrent gas - liquid flow: I. Air - water in horizontal flow. *AIChE Journal, 6*(3), 463-468. doi: 10.1002/aic.690060324

Williams. (1990). *Effect of pipe diameter on horizontal annular two-phase flow*: University of Illinois at Urbana-Champaign.

Williams., Dykhno, L. A., & Hanratty, T. J. (1996). Droplet flux distributions and entrainment in horizontal gas-liquid flows. *International Journal of Multiphase Flow, 22*(1), 1-18. doi: http://dx.doi.org/10.1016/0301-9322(95)00054-2

Zhang, & Ziada, S. (2000). PDA measurements of droplet size and mass flux in the three-dimensional atomisation region of water jet in air cross-flow. *Experiments in Fluids, 28*(1), 29-35. doi: 10.1007/s003480050004

Zhang, G. J., & Ishii, M. (1995). Isokinetic sampling probe and image processing system for droplet size measurement in two-phase flow. *International Journal of Heat and Mass Transfer, 38*(11), 2019-2027. doi: http://dx.doi.org/10.1016/0017-9310(94)00314-L